UNIVERSITY OF SOUTHAMPTON

FACULTY OF ENGINEERING AND THE ENVIRONMENT

INSTITUTE OF SOUND AND VIBRATION RESEARCH

MODELLING OF TRACK SOUND RADIATION

by

Xianying Zhang

Thesis for the degree of Doctor of Philosophy

May 2016

UNIVERSITY OF SOUTHAMPTON

ABSTRACT

FACULTY OF ENGINEERING AND THE ENVIRONMENT

INSTITUTE OF SOUND AND VIBRATION RESEARCH

Thesis for the degree of Doctor of Philosophy

MODELLING OF TRACK SOUND RADIATION

Xianying Zhang

In most situations the dominant source of noise from the railway system for conventional speeds is rolling noise. This is radiated by the wheels, the rails which dominate the important mid-frequency region between 400 and 2000 Hz, and, at low frequencies, also the sleepers. The acoustic properties of the rails, sleepers and ballast are investigated in this thesis.

The sound radiation of a rail in close proximity to a ground (both rigid and absorptive) is predicted by the boundary element method (BEM) in two dimensions (2D). Results are given in terms of the radiation ratio for both vertical and lateral motion of the rail, when the effects of the acoustic boundary conditions due to the sleepers and ballast are taken into account in the numerical models. Allowance is made for the effect of wave propagation along the rail by applying a correction in the 2D modelling. The numerical predictions of the sound radiation from a rail are verified by comparison with experimental results obtained using a 1:5 scale rail model in different configurations.

The sound radiation from the sleepers has been calculated using a three-dimensional boundary element model including the effect of both reflective and partially absorptive ground. When the sleeper flexibility and support stiffness are taken into account, it is found that the radiation ratio of the sleeper can be approximated by that of a rigid half-sleeper. When multiple sleepers are excited through the rail, their sound radiation is increased as they form a composite source. This effect has been calculated for cases where the sleeper is embedded in a rigid or partially absorptive ground. It is shown that it is sufficient to consider only three sleepers in determining their radiation ratio when installed in track. At low frequencies the vibration of the track is localised to the three sleepers nearest the excitation point whereas at higher frequencies the distance between the sleepers is large enough compared with the acoustic wavelength for them to be treated independently. Measurements on a 1:5 scale model railway track are used to verify the numerical predictions with good agreement being found for all configurations.

Not only can ballast absorb noise to some extent due to the gaps between the ballast particles but it can also vibrate and reradiate noise during a train pass-by. Experiments have been performed using 1:5 scale ballast to investigate this. The basic properties of the ballast, as a porous material, are measured initially, in particular the flow resistivity and porosity. The modelling of the ballast absorption is then implemented based on the corresponding measured parameters and this is compared with the measured absorption. The effects of ballast absorption on the rail and sleeper radiation are also measured, and are compared with the numerical predictions. Moreover, the vibration of the ballast is obtained experimentally. The influence of the ballast vibration on the sleeper radiation is then estimated and shown to increase the noise radiation below 200 Hz.

Finally, the sound radiation from the whole track is predicted, and compared with the corresponding measured results on the 1:5 scale model. The sound radiation models for the rail and the sleeper, are used with the TWINS software to give revised predictions of the track sound radiation. Prediction differences are shown between the original TWINS and the updated models.

Contents

List of Tables

List of Figures

Declaration of Authorship

I, Xianying Zhang, declare that this thesis entitled MODELLING OF TRACK SOUND RADIATION and the work presented in it are my own and has been generated by me as the result of my own original research.

I confirm that:

1. This work was done wholly or mainly while in candidature for a research degree at this University;
2. Where any part of this thesis has previously been submitted for a degree or any other qualification at this University or any other institution, this has been clearly stated;
3. Where I have consulted the published work of others, this is always clearly attributed;
4. Where I have quoted from the work of others, the source is always given. With the exception of such quotations, this thesis is entirely my own work;
5. I have acknowledged all main sources of help;
6. Where the thesis is based on work done by myself jointly with others, I have made clear exactly what was done by others and what I have contributed myself;
7. Parts of this work have been published. A full list of these publications is given in Appendix A.

Signed: ....

Date: ....

Acknowledgements

Finishing the research for a PhD degree has been a challenging journey for me. During this journey, there are many people who helped me in one way or another.

First and foremost, wholehearted gratitude goes to my supervisor, Professor David Thompson. I wish to thank him for his consistent guidance, support and friendship in these three and a half years. No matter what difficulties I encountered in the work, he is always kind and patient to give me his explanations, ideas and suggestions. I learned a lot from his supervisions: from English writing to a broader range of academic knowledge. He has been a wonderful supervisor for me. I am really impressed by his erudite academic knowledge, rigorous way to conduct scientific research and hard working. He has set a good example for me to follow in the academic field.

I am greatly indebted to my second brilliant supervisor, Dr Giacomo Squicciarini. Great thanks for his help and guide for my PhD research, especially for his support during the measurements for the current work: from setting up the experiments to assisting in carrying out the measurements. When it comes to the difficulties in the measurements, he is always kind and patient to help me analyse and solve the problems. My experimental skills improved a lot under his supervision. The time spent working together with him is unforgettable.

I gratefully acknowledge the help of people with the measurements. From the technical staff, Phil Oxborrow helped me a lot with the test rigs and constructing some facilities needed for this research. John Fithyan was greatly supportive for the arrangements of the availability of the large reverberation chamber. I also appreciated the ‘labour’ support from Andrea Ricci, Bo Ding, Hongseok Jeong and Jin Zhang during the measurement of the ballast absorption. Many thanks to Jack Lewis, David Milne and Martin Toward for sharing results of their measurements.

Sincere thanks to all my former and current colleagues in the Dynamics Group, especially Dr Eduardo Iglesias, Jou-Yi Shih, Xiaowan Liu, Dimitris Kostovasilis and Qiyun Jin, the fun we had together will be memorable. I am also grateful to all my friends for the friendship and help during these years.

Greatest gratitude to my family, especially my parents, my sister and my brother for unconditional love and support throughout my life, which is always a source of inspiration whenever I encounter difficulties in life.

Finally, I appreciate the financial support from EPSRC for the research in this dissertation through the Track 21 project.

List of Symbols

A	Cross-sectional area
$A(x_n)$	Measured mobilities or accelerances at the position n for decay rate
$A(x_0)$	Measured mobilities or accelerances at the position 0 for decay rate
$A_1, A_2, A_3, A_4\ A_5, A_6, A_7, A_8$	Amplitudes of the various waves
$[\mathrm{A}]$	Global matrix in the boundary element method
$[\overline{\mathrm{A}}]$	Global matrix in the boundary element method
B	Amplitude of the sound pressure for an oscillating cylinder
$\{\mathrm{B}\}$	Vector in the boundary element method
$[\overline{\mathrm{B}}]$	Global matrix in the boundary element method
D	Distance between centres of the capillaries in a porous medium
$[\mathrm{D}]$	Matrix in the boundary element method
E	Young's modulus
F	Harmonic force
$\overline{F^2}$	Mean-square force
G	Shear modulus
$\mathrm{H}_0^{(2)}$	Hankel function of the second kind and order 0
$\mathrm{H}_1^{(2)}$	Hankel function of the second kind and order 1
$\mathrm{H}_2^{(2)}$	Hankel function of the second kind and order 2
$H(\omega)$	Point accelerance of the sleeper
I	Sound intensity
I_s	Second moment of area of the cross-section
K_e	Effective or dynamic bulk modulus of the air
L	Length
$[\mathrm{M}]$	Matrix in the boundary element method
N	Number of nodes of the whole surface
N_p	Prandtl number

N_s	Number of sleepers included in the multiple sleepers
$[N_a]_e$	Shape function for element in the boundary element method
P	Noise source location
P_0	Atmosphere pressure
P'	Image noise source location
Q	Receiving point
R	Reflection coefficient
S	Surface area of the vibrating structure
S_e	Element *e* on the boundary
S_H	An infinite reflection plane
S_2	Surface area of the acoustic domain
T	Reverberation time
U	Flow velocity
U_0	Velocity amplitude for an oscillating cylinder
U_1	Amplitude of the displacement for the rail
U_2	Amplitude of the displacement for the sleeper
V	Volume
V_n	Normal velocity amplitude of a cylinder surface
V_2	Infinite fluid domain
W	Sound power
W'	Sound power of a cylinder per unit length
a	Radius of a cylinder
$\overline{a_\mathrm{Q}^2}$	Mean-square acceleration
c_0	Speed of sound
d	Capillary diameter
$[\mathrm{d}]$	Matrix in the boundary element method
$[\mathrm{d}]_e$	Matrix for an element in the boundary element method
f	Frequency
f_c	Critical frequency
f_u	Highest frequency measured in a circular tube
f_s	Schroeder frequency
g	Green’s function
g'	Half-space Green’s function

h	Thickness of porous material
i	$\sqrt{-1}$
j	Node at the boundary
k	Wavenumber
k_e	Wavenumber of evanescent waves
k_{fs}	Stiffness of the elastic foundation beneath the sleeper
k_i	Imaginary part of the complex wavenumber for decay rate
k_p	Wavenumber of propagating waves
k_{ps}	Railpad stiffness
k_{we}	Effective wavenumber in the Johnson-Allard model
k_x	Wavenumber in x direction
k_{2D}	Wavenumber in y-z plane
l	Thickness of a rigidly-backed layer
m	Air mass flow rate
m_r	Mass of the rail
m_s	Mass of the sleeper
$m_\mathrm{s}(\omega)$	Apparent mass of the sleeper
m_r'	Mass per unit length of the rail
m_1	Air absorption in the room
$[\mathrm{m}]$	Matrix in the boundary element method
$[\mathrm{m}]_e$	Matrix for an element in the boundary element method
$\mathbf{n}$	Unit normal
p	Complex sound pressure amplitude
p_j	Pressure amplitude at node j
$\overline{p_Q^2}$	Spatially averaged mean-square pressure caused by source Q
q	Tortuosity
r, r'	Distance
(r, ϕ)	Cylindrical polar coordinates
(r, θ, ϕ)	Spherical polar coordinates
s	Scale factor
s_p	Stiffness for per unit length of the sleeper
s_r	Standing wave ratio
t	Time
u	Response amplitude of the Timoshenko beam

u_r	Velocity of an oscillating cylinder
u_1	Vertical complex displacement amplitude of the rail
u_2	Vertical complex displacement amplitude of the sleeper
v	Complex amplitude of the velocity
v_n	Surface normal velocity
$\overline{v^2}$	Mean squared velocity
$\mathbf{x}$	Points in the acoustic domain
(x, y)	Cartesian coordinate system
$\mathbf{y}_j$	Points $\mathbf{y}$ at node j
y_0	Distance from one end of the Timoshenko beam
$\mathbf{y}$	Points on the surface of the structure
$\mathbf{y}'$	Points on the boundary of the structure
z	Impedance of a rigidly-backed layer
z_n	Specific normal acoustic impedance
z_n'	Normalized ground impedance
z_c	Characteristic impedance
Γ	Coefficient in the effective bulk modulus
Δ	Decay rate
ΔL	Level difference between sound pressure levels
Δp	Pressure drop
Δx	Distance between two microphone points in the impedance tube
Λ	Viscous characteristic length
Λ'	Thermal characteristic length
Ω	Porosity
α	Absorption coefficient
α_s	Absorption coefficient of the sample
α_0	Absorption coefficient of the empty room
γ	Ratio of specific heats
γ_p	Propagation coefficient
ε	Coefficient for the surface integral equation
η	Viscosity of the air
θ	Incident angle
κ	Shear coefficient

λ	Wavelength
ρ	Density
ρ_e	Effective density
ρ_0	Density of air
$\rho_0 c_0$	Specific acoustic impedance of air
σ	Radiation ratio
σ_e	Effective flow resistivity
σ_f	Flow resistivity
τ	Constant factor for the viscous characteristic length
φ	Rotation of the cross-section
ψ	Ratio of the rotation of cross-section to the deflection
ω	Angular frequency

Abbreviation

BE	Boundary element
BEM	Boundary element method
CHIEF	Combined Helmholtz Integral Equation Formulation
EPSRC	Engineering and physical sciences research council
FE	Finite element
FLOSS	Finite Line of Simple Sources
K-HIE	Kirchhoff-Helmholtz integral equation
LUL	London Underground Limited
MATLAB	A mathematical software package
SPL	Sound pressure level
SYSNOISE	Boundary element software
TWINS	Track-Wheel Interaction Noise Software
WANDS	Wave Number Domain Software
2D	Two dimensions
3D	Three dimensions

Chapter 1 Introduction and literature review

1.1 Background and motivation

Environmental noise has become an increasingly important issue in the last fifty years. With the development of society, noise is often viewed as a source of dissatisfaction with the living environment by residents. This is true with railway noise as well. Railways are generally viewed as an environmentally-friendly and sustainable means of transportation, and as a popular means of transportation in daily life. However, opposition to new railway developments is often focussed on the noise impact on local residents and this can lead to increased cost for the inclusion of noise barriers or other counter-measures. It is necessary therefore to reduce the railway noise at source. The sources of environmental noise from railways are generally classified into rolling noise, curve squeal, bridge noise, aerodynamic noise, ground vibration and ground-borne noise; more details can be found in [1]. In each case, it is necessary to understand thoroughly the mechanisms of sound generation before implementing strategies of noise control in the railway system.

The most important source of railway noise, however, is rolling noise, which is caused by wheel and rail vibrations induced at the wheel/rail contact area. Figure 1.1, taken from [1], shows the mechanism visually, whereas Figure 1.2 demonstrates this in the form of a flowchart. The roughness on the wheel and rail running surfaces makes the wheel and rail systems vibrate according to their dynamic properties; in turn, they radiate sound, producing noise at the wayside. Figure 1.2 also indicates that sleeper vibration is induced by the rail vibration, and this leads to the sleeper radiation.

Based on the predicted vibration levels on wheels, rails and sleepers, obtained using the Track-Wheel Interaction Noise Software (TWINS, [2, 3]), an example prediction of the contributions of the wheel, rail and sleeper to the total noise generated in the railway system is shown in Figure 1.3 [1]. As can be seen, the sleepers are important sources at low frequencies. The rail becomes the dominant source especially in the mid frequency range, while the wheel radiates most noise at high frequency. In order to implement effective noise control measures on the railway, therefore, it is necessary to investigate the structural vibration and sound radiation of the sleeper, rail and the wheel. This research focuses on the sound radiation caused by the vibration of the railway track. In comparison with this, the vibration and radiation of the wheel are better understood [4] and therefore are excluded from the scope of the current research.

Railway tracks are usually constructed with ballast. Its primary function is to support the track vertically and to provide lateral stability. Also, it is a porous material, which provides drainage, and it therefore also has sound absorption properties. For slab track or 'ballast-less track', the noise levels are typically 2-3 dB higher, which is partly due to the absence of the absorption of the ballast [1]. It is therefore important that the effects of vibration and absorption of the ballast on the sound radiation of the rail and sleeper are investigated as well.

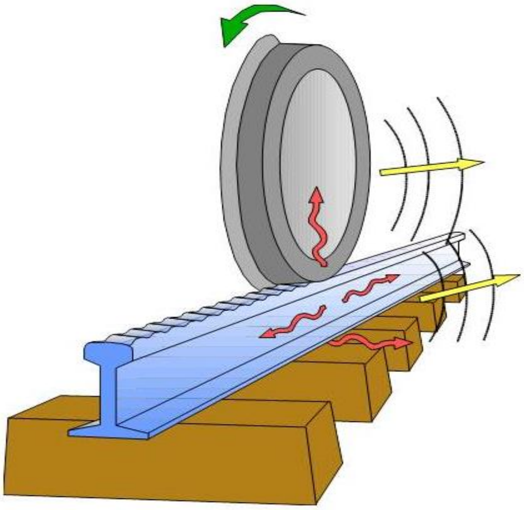

Figure 1.1 Illustration of the mechanism of generation of rolling noise [1]

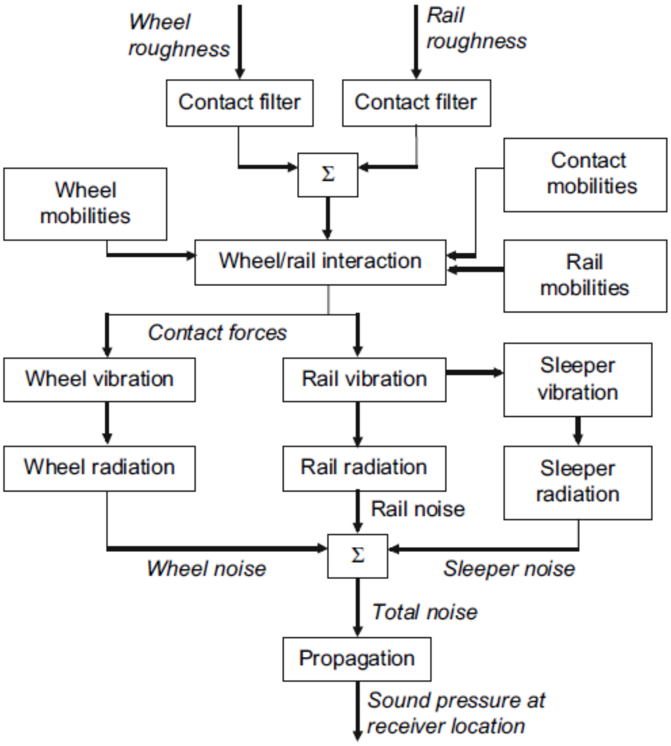

Figure 1.2 Model for rolling noise generation forming the basis for the TWINS software [1]

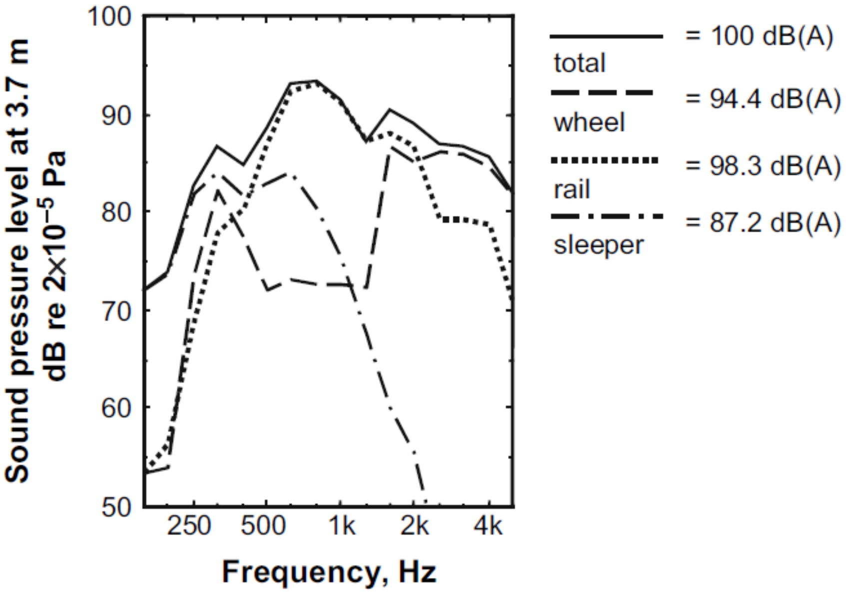

Figure 1.3 Prediction of contribution of rail, sleeper and wheel noise to total noise using TWINS model [1]

In the reminder of this chapter, an extensive literature review is presented for the acoustic behaviour of railway track and associated topics. This is followed by a presentation of the objectives and scope of thesis, and a list of original contributions.

1.2 Track vibration

As Figure 1.2 shows, the noise radiated by the track greatly depends on the track vibration. It is therefore necessary to give a brief review of track vibration first.

The Euler-Bernoulli beam equation has been used for simple models of the rail response [5, 6]. This theory assumes that plane sections of the beam remain plane and perpendicular to the neutral axis. When the wavelength of a beam is shorter than about six times its height, shear deformation and rotational inertia play a role and should be included in the description of the beam [7]. Therefore, more accurate beam equations, known as a Timoshenko beam which includes these effects, are used. Besides, the equations should consider the effects of the support, including ballast, sleepers and the railpads inserted between the rails and concrete sleepers. For example, in reference [8], such track models were developed and validated by experiments. For vertical vibration, the effects of discrete supports were also studied theoretically and found to affect the frequency response only at certain frequencies. Grassie *et al.* showed that the Timoshenko beam is required for a typical rail above about 500 Hz.

Another model of the vertical vibration of the track was developed by Clark et al [9], including the discrete nature of the support of the rail. A modal sum for a finite length of track was used. Tassilly [10] modelled the track as a periodically supported Euler-Bernoulli beam, and presented dispersion diagrams of wavenumber against frequency, showing stop and pass bands. Ono and Yamada [11] also modelled the rail as an Euler-Bernoulli beam, and the propagation of vibration in the roadbed was included in their model. Also, in order to account for the discrete location of the sleeper supports in the railway track, Nielsen's model was based on Timoshenko beam in a finite element model [12].

However, these models could not be used reliably for the study of rolling noise generation, because at high frequencies the rail no longer behaves as a simple beam in which the cross-section remains plane, instead cross-sectional deformation occurs. This was shown by experiments performed by British Rail [13], in which it was shown that the cross-section deformed significantly above about 1500 Hz. In 1991, considering these deformations, Thompson [14] modelled the vibration of an infinite rail beam by using periodic structure theory, based on a finite element model of an arbitrary period length of 10 mm. It was found that wavenumber results agreed well with conventional finite element results, and with results derived from experimental data. Also, a supported rail (on ballast, sleepers and railpads) was considered within the same basic model, by using an equivalent continuous support. However, the periodic nature of the support of the rail was not considered. It was found that the damping properties of the railpads, introducing a decay with distance, required further study, especially their frequency-dependence.

Knothe and Grassie [15] presented a review of theoretical dynamic modelling of railway track. Models of sleepers and the wheelset were also available for the whole frequency range of interest. Moreover, it was pointed out that the dynamic behaviour of the railpad and ballast was a promising area for future development. According to the categories of track models in [15], Thompson and Vincent [16] discussed three alternative theoretical models of the dynamic behaviour of railway track in the frequency range 50~6000 Hz, including the model from [14]. The three track models are presented in Figure 1.4. Various physical phenomena of importance to rolling noise generation were pointed out by using these models. Advantages and disadvantages of the three models were also compared. Meanwhile, in another paper by Vincent and Thompson [17], experimental data of several European tracks was presented. The validity of the three models was assessed by means of comparisons between experiments and simulations. It was shown that a generally good agreement was obtained. Also, it was found that the measured decay rate could be correctly predicted by the rail model including cross-section deformation for vertical and horizontal directions. Moreover, it was pointed out that measurements of the sleeper behaviour by using an impact excitation on the rail does not fully represent its actual behaviour during train operation, which needed to be improved for further investigation.

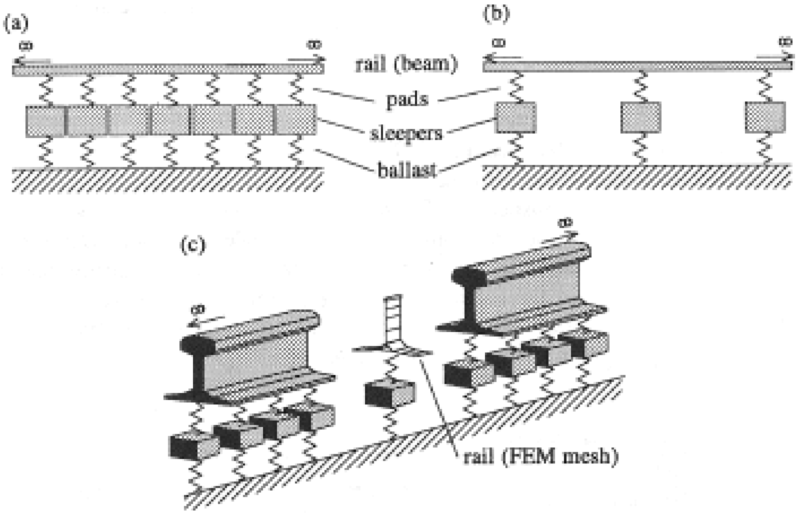

Figure 1.4 Models for track vibration [16]; (a) continuously supported beam model, (b) periodically supported beam model, (c) rail model including cross-sectional deformation

In [18], Thompson developed a new experimental analysis method for analysing propagating waves in effectively infinite structures. The various propagating vibrational waves in the rail were identified in terms of their complex propagation coefficients and their corresponding deformed shapes. These waves were separated based on fitting a series of complex exponential functions to the measured data using a Prony series. The effects of cross-sectional deformation was also demonstrated using finite element results fora finite length of UIC54 rail as well as experimentally. It was found that for lateral vibration of the rail, web bending occurs above about 1.5 kHz, whereas foot flapping motion occurs progressively above around 2 kHz for vertical motion of the rail.

Simplified theoretical models to study the cross-sectional deformation of the rail were developed by Wu and Thompson in [19] and [20]. The vertical motion was represented by two Timoshenko beams, as shown in Figure 1.5, which were coupled by a continuous layer of springs. It was found that this model included the essential cross-sectional deformation of a rail vibrating vertically at high frequencies. The dispersion relation of propagating waves in a free and a continuously supported rail was also studied using this model. Moreover, vertical vibration frequency responses of the rail were obtained by continuously and discretely supported models. The results were found to have good agreement with an FE model and with experimental data.

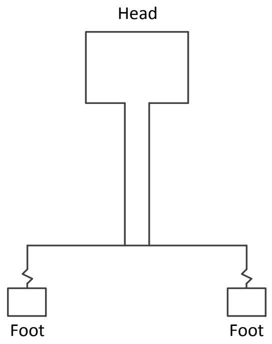

Figure 1.5 Cross-section of the double beam model for the rail vibrating vertically. The two beams representing the foot are assumed to have the same vibration

With regard to the lateral direction, it is necessary to include bending and torsion from low frequencies, as well as web bending and second-order web bending at high frequencies. Such a model was formed by two beams including torsion, which were linked by an array of vertical beams representing the web [20]. It omitted the twisting stiffness of the web, but it was shown that this can be ignored compared with the other stiffness in the rail. The corresponding model is presented in Figure 1.6. The subscripts h, f, and w represent the rail head, foot, and web, respectively. The whole rail is divided into three parts: the head and the foot are represented by two infinite Timoshenko beams and the web is replaced by numerous beams along the rail which connect the head and foot in Figure 1.6(a). The isolated diagrams for the three components are shown in Figure 1.6(b), where v_h and θ_h represent the head lateral displacement and rotation about the rail axis respectively, v_f and θ_f are the foot lateral displacement and rotation about the rail axis. This model was also applied to study the lateral vibration behaviour related to the discrete supports [21]. Using a Green's function matrix and the superposition principle, the lateral vibration of a discretely supported rail was investigated in detail. The prediction was found to have good agreement with measured data in terms of its frequency response.

In recent years, some new approaches have been developed to study the vibrational properties of the track. Heckl presented a new approach to model the free propagation of coupled waves on a periodically supported Timoshenko beam [22]. It was based on Hamilton's principle, the superposition principle and Bloch's theorem. A waveguide finite element was used by Nilsson et al. [23] to calculate the rail vibration, which was combined with the wavenumber boundary element to predict the rail radiation by considering the characteristics of radiation from waves in rails. This wavenumber finite element method was also utilised by Ryue et al. [24] to investigate the propagating wave types in railway tracks at high frequencies.

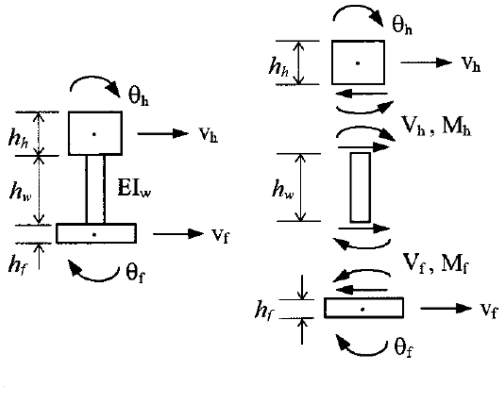

(a) (b)

Figure 1.6 Multiple beam model for lateral vibration of the rail [20]

As well as the frequency response, decay rate is an important parameter to describe properties of a track. The decay rate of vibration along the rail controls the effective radiating length of the rail, the noise performance of a track could, therefore, be linked to the decay rate. This parameter could also be measured to test and improve the accuracy of prediction models. A direct and automated method was proposed to calculate the decay rate from frequency response measurements by Jones et al. [25], which became incorporated in the European Standard EN 15461:2008+A1:2010(E) [26]. This can be used to calculate an equivalent vertical and lateral wave decay rate for the track. The track noise could then be predicted by these wave decay rates.

1.3 Sound radiation from a rail

The sound field induced by a vibrating structure can be described in terms of the distribution of sound pressure or the sound power. The former parameter is related to the distance and orientation of the receiver to the source. The latter one shows the total rate of sound energy produced by a source, and is independent of the receiver location.

The sound power *W*, radiated by a vibrating object, can be written as [27]

$$W = \rho_0 c_0 S \left\langle \overline{v^2} \right\rangle \sigma \qquad (1.1)$$

where ρ_0, c_0 are the density of air and the speed of sound, respectively. *S* is the surface area of the vibrating structure and $\left\langle \overline{v^2} \right\rangle$ is the squared velocity normal to the surface in the frequency band of interest, which is averaged both over time $\left(\overline{\ }\right)$ and over the surface area $\left(\langle\ \rangle\right)$. For sinusoidal motion with complex amplitude *v*, the mean-square corresponds to $\overline{v^2} = \frac{1}{2}|v|^2$.

The parameter σ is called the radiation ratio or radiation efficiency. It expresses the ratio of the sound power actually produced to that which would be produced in an idealized case producing plane waves. The reference case can be considered as a piston in a tube. If the piston has the same area *S* and mean-square velocity amplitude $\overline{v^2}$ as the actual source, it radiates a sound power of $\rho_0 c_0 S\overline{v^2}$.

In terms of rolling noise in the railway system, both the wheels and the track radiate significant components of noise (see Figure 1.3). Their relative importance depends on details of the design, the roughness spectra and the train speed [23, 28, 29]. Nonetheless, the component of noise from the rail is often the highest.

The role of the rail in rolling noise was studied by Bender and Remington as early as 1974 [30]. Measurements of the radiation efficiency of an AREA rail (50 kg/m) were carried out, which were compared with an analytical formulation for a cylinder. The radiation efficiency of the rail was modelled by the uniform motion of simple cylindrical beams.

To calculate the rail radiation efficiency for the horizontal forcing of the rail, the cylinder diameter was set equal to the rail height, whereas for the vertical forcing of the rail, the rail was treated as two cylinders vibrating independently such that the total radiated power was the sum of that radiated by each cylinder. However, there were several factors, which were not considered in the paper. Both the length of the rail that effectively radiates sound when excited by the wheel and the directivity pattern of the radiation were unknown. Also, measurements of the roughness spectra of wheels and rails were unavailable. In reference [5], Remington measured the directivity of rail radiation for vertical motion, and compared this with analytical models. The conclusion was reached that the vertical directivity of the rail radiation can be taken as uniform for estimations of wayside noise. The directivity of rail radiation for horizontal motion, however, was not mentioned in this paper.

In 1976, analytical formulas for the prediction of wheel/rail rolling noise in urban rail transit systems were developed by Remington [31]. The analytical formulas were obtained based on the characterization of the wheel/rail dynamic system in [5] and the roughness spectra on the contact surface of wheels and rails. These formulas were verified by comparing the predictions with field measurements both from a full-scale transit system and a small-scale engineering test vehicle. It was shown that the size of the contact patch at the wheel/rail interface has an important effect on the magnitude of the noise radiated. The rail was found to be the major radiator over a broad frequency range. Although the model showed reasonable agreement with measured data, there were still improvements that were required in the analytical model. For example, the rail radiation was based on a model in free field without taking into account reflections from the ground plane.

Remington [6] presented a comprehensive analytical model to predict wayside noise generated by wheel/rail rolling noise based on the models presented in the earlier study [5, 31]. In order to obtain a better analytical model, the following modifications were made: inclusion of the contact stiffness in the wheel/rail interaction model; improvement of the wheel/rail contact area filter model; improvement of the wheel impedance model; inclusion of ground effects in the sound propagation model; and prediction of the average wayside noise during a train pass-by rather than the noise at a particular train position during the pass-by. However, the model ignored the sound radiation from lateral motion of the rail and from the sleepers, because preliminary estimates of sound radiation indicated that sound radiation from the other wheel/rail components was more significant than that from these components. The ground was modelled as a finite impedance plane using the approach of Chessell [32]. Comparison of analytical results and field measurements showed, however, that the predicted results ‘without ground’ agreed much better with the measured data than the results including the ground effect. It was concluded that this may be because of the omission of absorptive ballast in the model.

In a companion paper by Remington [33], the verification of the analytical model was performed. Predictions from the analytical model were compared with field measurements. It was shown that, within the limitations of the model, predictions and measurements agreed reasonably well. Furthermore, areas for further development were identified. For example, the model of the contact patch filter attenuation needed to be improved to agree better with field and laboratory measurements. For the exact way to implement this, however, the author only pointed out possible factors essential to an analytical determination of the filter attenuation, such as the roughness correlation perpendicular to the direction of rolling, the proper weighting of the roughness within the patch, etc. Also, the periodic supports were not included in the rail impedance model. Moreover, it was stated that the model of rail radiation efficiency should be improved and rail directivity in the plane perpendicular to the rail axis should be taken into account in future development.

In 1993, Thompson extended these engineering methods of predicting rolling noise [34]. A software package, known as TWINS (‘Track-Wheel Interaction Noise Software’), was produced [2, 3]. The model in TWINS provides a way to predict the noise for particular designs of wheel and track and allow noise reduction technologies to be assessed.

Experimental validation is also described in [2, 3]. TWINS is currently by far the most widely used rolling noise prediction model. Within TWINS, the track vibration can be calculated using the models described in [16]. Regarding the sound radiation in TWINS, it can be calculated either in terms of sound power or the average sound pressure during the passage of a train at specified positions at the trackside from various vibrating components of the track. In the case of the sound radiation from the rail, a module supplied by TU Berlin [35] was applied. It used a series of multipole sources contained within the geometry of the rail cross-section to replace the vibrating rail. Specifically, it is a two-dimensional model in which the cross-section of the rail is approximated by four rectangular boxes containing the equivalent sources along their centrelines. It was used to predict the radiated power due to normalized motions of the cross-sectional deformation of the rail in each wave. One of the assumptions in the model, as in Bender and Remington [30], is that the rail radiates sound in a free field.

A two-dimensional boundary element model of rail radiation was described in [36]. A UIC 60 rail cross-section was modelled, which was constructed in the proprietary boundary element package, SYSNOISE. The model included just half of the cross-section by using the vertical line of symmetry of the rail. Moreover, the ‘CHIEF’ method (Combined Helmholtz Integral Equation Formulation) [37] was applied to overcome the non-uniqueness of the solutions due to modes of the equivalent internal problem for exterior radiation problems when using the boundary element method. The radiation efficiencies for rigid-body vertical and lateral motions of the rail cross-section in free space were calculated. It was shown that the rail in free field had the acoustic properties of a simple line dipole source.

A three-dimensional model was also presented in [36]. The model was based on an array of simple sources, and known as FLOSS (Finite Line of Simple Sources). This model was developed to study the three-dimensional effects. According to the various simplifying assumptions, the rail cross-section was replaced by a simple equivalent rectangle. Then, the equivalent rectangular cross-section was replaced by equally spaced dipole and/or quadrupole sources placed along its central axis. The distances between sources had to be close compared with the wavelength in air and the wavelength in the structure. The source strengths should also be suitably chosen, allowing for the wavelength and decay rate in the rail.

Results were presented in [38] showing the different conditions under which 2D and 3D models for sound radiation from railway track are applicable. It was shown that, if the decay rate of vibration along the rail becomes large or the wavelength in the rail becomes small compared with the acoustic wavelength in the air, it is necessary to consider three-dimensional radiation effects. The two-dimensional model, however, was shown to give satisfactory results in most practical cases for frequencies above about 250 Hz.

Nilsson et al. introduced a novel approach to calculate the vibration and sound radiation from a rail [23]. A combination of waveguide finite elements and wavenumber boundary elements was used to avoid several of the simplifying assumptions in the established methods. This takes advantage of the 2D geometry of a rail to give efficient numerical results, while also considering the 3D nature of the vibration and sound field and the infinite extent of the rail.

Recently, the directivity of noise radiated by a rail has been investigated by several authors. The horizontal directivity of rail radiation was investigated by Kitagawa and Thompson using a model similar to FLOSS [39]. The structural waves propagating along a railway trail forms an extended source of sound radiation. The distribution of this sound in the horizontal plane has been shown to consist of sound propagating at a specific angle to the normal. This direction depends on the ratio of the wavenumbers in the rail and in air. It cannot, therefore, be treated simply as a directivity. A survey of the directivities of all railway noise types and components, including rolling noise and aerodynamic noise, was discussed extensively and systematically by Zhang and Jonasson [40]. In reference [41], a model of a straight line of perpendicular dipole pairs was proposed for the vertical directivity of rail radiation. It was found to have good agreement with measurements of the directivity characteristic of rail radiation. A horizontally vibrating rail section could be modelled as a line of dipoles, which was shown to agree well with the measured horizontal directivity. However the effect of the ground on the directivity was neglected in the work described above.

1.4 Validation measurements for the rolling noise model

Experiments have been performed along with the development of railway noise theory; these are briefly summarized here. Two extensive acoustic measurements of the railway system were conducted by TNO and Vibratec in the early 1990s. Their main purpose was to validate the TWINS model, with the main outcome of the validation published in [2, 3]. It was found that the model gave reliable results, provided that care was taken with the input data, especially the roughness data and the attenuation of vibration along the rail. Also, the overall noise predictions were found to be on average 2 dB(A) above the measured values. This may be due to the simplifications in the model of propagation of sound from source to receiver.

The validation was later extended with measurement data from the Silent Track and Silent Freight EU projects [42]. In these projects, new designs of wheel and track were produced including wheel and rail dampers and they were tested in a combined experiment in 1999 at Velim in the Czech Republic. In addition, various improvements were included in the prediction model. It was found that the improved sound propagation model gave better agreement in terms of spectra. However, the predictions were on average 1-2 dB below the experimental data of these new experiments. The possible reasons were the omission of the wheel roughness and differences between the freight wagons measured here, compared with the passenger vehicles used in the previous validation. During the two validation measurement campaigns, a mean sound pressure level was used which was averaged over three microphones located 3 m away from the track with different heights. Therefore, any variations in directivity were averaged out, which improved the agreement between measurements and predictions.

More recent measurements were made by TNO in 2010 of Thalys trains on the Dutch high speed line. Another extensive field measurement campaign was conducted by SNCF within the STARDAMP project in 2012 for the purpose of comparison with a prediction model, although this project mainly aimed at defining laboratory methods for evaluation of the efficiencies of rail and wheel dampers. In both cases, TWINS was used to make corresponding predictions of acoustical parameters. The experimental data and comparisons are summarized in [43].

1.5 Vibration and sound radiation from a sleeper

1.5.1 Sleeper vibration

Early track vibration models represented the rail as a beam and the sleepers by a layer of independent rigid bodies (mass). It was shown that the dynamic response to forces at the railhead was well represented up to 1 kHz by using this sleeper model [15].

A simple uniform Timoshenko beam for the sleepers was proposed by Grassie and Cox to study the dynamic response of railway track with flexible sleepers to high frequency vertical excitation [44]. This Timoshenko beam was used again by Grassie for a freely suspended sleeper [45]. Quite reasonable agreement was found with measurements in terms of natural frequencies, apart from the first mode, where the effect of the non-uniform profile is greatest.

In TWINS a way of modelling the sleeper, and including ballast underneath, was proposed in terms of sleeper vibration modes [46]. Another approach based on the wave propagation, was developed later by Thompson [1]. In both cases, the sleeper was represented as a finite beam on a continuous elastic foundation, and the ballast was represented as an elastic layer. Measurements were taken to verify the response [47]. Reasonable agreement was found between the analytical prediction and the experimental results in terms of natural frequencies.

Moreover, it was pointed out this model could give better predictions of sleeper radiation than the mass-spring model.

1.5.2 Sleeper radiation

Few references have been found with respect to the acoustic properties of the sleeper. The sound radiation was explored numerically in terms of radiation ratio in [1], when the sleeper is embedded in a rigid ground. The sound radiation from a single sleeper was viewed as that from a flat rectangular surface located in a plane baffle, with its lower surface neglected. The Rayleigh integral was used to calculate the sound radiation of sleepers with various dimensions by assuming the sleeper vibration was uniform. It was found that the radiation ratio would depend on the sleeper width in the frequency range 300 ~ 800 Hz, while it would be determined also by the length of the sleeper at low frequency.

A preliminary investigation of the sound radiation from multiple sleepers was also presented in [1]. The Rayleigh integral approach was used again to calculate the radiation ratios of three adjacent sleepers with vibration amplitudes in the ratio 0.5:1:0.5. The multiple sleepers were again assumed to be embedded in rigid ground. It was shown that the proximity of the three sleepers would amplify the sound radiation at low frequency, where the three sleepers form a single composite source. For the estimation of sound radiation from multiple sleepers, it was found to be sufficient to consider only three sleepers, although more sleepers fall within the range defined by the acoustic wavelength at low frequency. This was because the vibration is sufficiently localized along the rail that other additional sleepers have negligible source strength. Moreover, although more sleepers vibrate at high frequencies, where waves propagate along the rail, they can be considered to radiate independently.

Some work has been done on reducing the sleeper noise. In the theoretical optimization of track components by Vincent et al. [48], it was concluded that the sound power radiated by sleepers can be minimized in three ways: reducing rail pad stiffness; increasing sleeper mass and reducing the area of the upper side of the sleeper.

Acoustic optimization of railway sleepers was investigated by Nielsen [49]. A mathematical model [50] was developed to minimize the sound power generated by railway sleepers. By using the model, the effects of some parameters, including the sleeper material properties, sleeper shape, ballast properties and rail pads, on the sleeper sound power were assessed [51]. It was pointed out that the most important parameters determining the sound radiation from sleepers were the rail pad stiffness and ballast properties. Also, it was found that a bi-bloc design would reduce the sound power from the sleeper bending modes. In order to investigate the effects of the sleeper shape on the radiation ratio from the sleeper, the commercial software SYSNOISE [52] was used to model a single mono-bloc and bi-bloc sleeper. From a comparison between mono-bloc and bi-bloc designs in the boundary element simulations, it was shown that the influence of sleeper shape on its radiation ratio was negligible.

1.6 Ground impedance model

The acoustic properties of the ground, including the ballast, can be represented by its acoustic impedance. A phenomenological model was first developed by Zwikker and Kosten as early as 1949 [53]. It was shown that the acoustic behaviour of rigid-porous materials could be determined from three parameters: flow resistivity, porosity and tortuosity. In this model, adiabatic conditions were assumed in the pores. It has been common to use this model for time-domain computations because of its straightforward time-domain implementation. Later, another model was proposed by Biot [54, 55]. It used the dynamic density function given by Biot, the Zwikker and Kosten expression for the dynamic bulk modulus, and a frequency-independent shape factor. It was shown that the material could be described by four parameters: flow resistivity, porosity, tortuosity and shape factor.

A simple semi-empirical model was proposed by Delany and Bazley [56], in which the acoustical properties of porous materials are specified by their characteristic impedance and propagation coefficient. The semi-empirical model obtained by Delany and Bazley was based on impedance tube measurements on fibrous materials. They showed that the characteristic impedance and propagation coefficient can be obtained as a function of frequency normalised by the flow resistivity σ_f and can be represented by simple power-law functions. This model has also been widely used to predict acoustical behaviour of outdoor ground surfaces. The model has some limitations: it was based on data limited to a range $10 \le f/\sigma_f \le 1000$, the porosity of the materials tested was close to 1 and the model can result in unphysical predictions, particularly at low frequency.

Miki modified the Delany-Bazley model [57]. From the viewpoint of physical realizability, the characteristic impedance and propagation constant of porous materials were discussed. New regression models were presented based on the original experimental data by Delany and Bazley as well as more recent data. The new models were found to be useful for the prediction of the acoustical behaviour of porous materials, especially for double-layer materials. Besides, they were valid outside the range of the original models. Nonetheless, the models still had the restriction that the porosity of the material must be near unity. The empirical models were further generalized by Miki with respect to the porosity, the tortuosity and the pore shape factor ratio [58]. Compared with the original Delany-Bazley models, the new models had more applicability to various kinds of porous materials. In addition, it was shown that the models had good agreement with Attenborough’s models, discussed below, and therefore, they could be used to predict the acoustical behaviour of various kinds of ground surfaces. Furthermore, the impedance and the propagation constant could be evaluated by using only two parameters.

A theoretical impedance model was proposed by Attenborough for outdoor ground surfaces [59]. It was proposed that the acoustical characteristics of rigid porous materials could be predicted by using four physical parameters: flow resistivity, porosity, grain shape factor and pore shape factor ratio. The predictions were found to have good agreement with measurements of surface normal impedance for grass-covered ground, bare ground and layered forest floor. Additionally, it was shown that the agreement with experimental acoustical data was superior to that obtained by the Delany-Bazley model, even when the single parameter was adjusted for best-fit.

Based on Biot theory for the acoustic properties of porous media, Johnson presented a model in terms of frequency-dependent tortuosity and frequency-dependent permeability [60]. There are basically four parameters in the model: flow resistivity, porosity, tortuosity and viscous characteristic length. The viscous characteristic length was first introduced into modelling of porous material here. This model was later developed by Allard [61]. More detailed information of other parameters (the effective density of a porous material and effective bulk modulus, for example) are presented in the model of propagation of sound in porous media.

A relaxation model was given by Wilson [62], which was also determined by four parameters: viscous and thermal relaxation times for low and high frequencies. The viscous and thermal dissipation of an acoustic wave propagating through a porous medium was shown to be characteristic of a relaxation process. This model was based on approximating the relaxational characteristics, as opposed to previous models based on matching low- and high-frequency asymptotic behaviour. The relaxation model was found to be physically realistic for all frequencies, unlike the Delany-Bazley empirical equations.

To predict the acoustical properties of porous asphalt, a new phenomenological model was proposed by Berengier et al. in 1997 [63], which was also known as the Hamet and Berengier model [64], based on a modified form of the Zwikker and Kosten model. The model treated the porous medium as a globally compressible fluid in which dissipation occurs. The mathematical expressions are simple enough that the effects of the various physical parameters on the impedance values can be analysed. In addition, it included both viscous and thermal dissipation within the porous medium. The impedance was characterized by three parameters: porosity, flow resistivity, structure factor. The theoretical predictions demonstrated good agreement with experimental results in laboratory conditions as well as in situ.

A new one-parameter model for outdoor ground impedance was developed by Taraldsen [65], based on Darcy’s law. This model removed the unphysical results obtained by the Delany-Bazley model in some cases. It has been demonstrated that the two models give very similar predictions of the ground effect in typical cases. This one-parameter model was generalized by Taraldsen and Jonasson [66], into a two-parameter model, which depended on an effective flow resistivity and an effective layer depth. Extensive field measurements of the acoustic impedance of various ground types were carried out in the frequency range of 200 Hz ~ 2.5 kHz. This model gave an improved fit to the measurements compared to the Delany-Bazley model. Also, it corresponded to a proper causal time-domain model. Attenborough et al. [67] summarized some of the ground impedance models described above. Advantages and disadvantages of the models in different environments are given, compared with the measurement data.

Some of the measurement campaigns mentioned in Section 1.4 also took ground effects, including reflection and absorption, into account. For example, the TWINS model did so using the Delany and Bazley model [56]. However, the ACOUTRAIN project, which commenced in 2011, investigated this in more detail. Acoustic impedance measurements were carried out of a grass surface and a ballast surface, from which attempts were made to determine the acoustic impedance of these two kinds of common surfaces around the railway [68]. The Delany-Bazley model [56] was used as an impedance model to give analytical predictions. The measured complex pressure ratio at two positions was compared with the calculated ones to find the parameters of the impedance model, which could make the modelled and experimental data fit best.

1.7 Vibration and absorption of ballast

1.7.1 Vibration of ballast

Ballast is an important component in the railway system. However, it is difficult to analyse the vibration of ballast due to its granular configuration and special mechanism of action [69]. The dynamic effect of the ballast is usually viewed as a series of springs and dampers under sleepers in the analysis of track dynamics [70]. Ahlbeck et al. [71] conducted some theoretical work on the ballast vibration, assuming that the load was transmitted within a cone region in the ballast, and the relative measurements of ballast accelerations was carried out by Sato et al. [72]. Zhai et al. [73] proposed a detailed model for exploring dynamic interactions between vehicles and tracks, in which Ahlbeck's hypothesis was used to establish the ballast vibration model. Later, Zhai et al. improved the ballast vibration model [69]. A five-parameter ballast vibration model was proposed based on the hypothesis that the transmission of the load from a sleeper to the ballast approximately coincides with a cone distribution. Effects of shear stiffness and shear damping of ballast were considered in the ballast model, and a full scale field experiment was performed to verify the model. Moreover, it was pointed out that, for the analysis of track dynamics, it was necessary to consider the ballast shearing effect between adjacent ballast masses to model the continuity and the coupling effects of the interlocking ballast granules.

Note that the ballast stiffness used in above literature was constant. However, measurements of ballast stiffness have shown it is strongly frequency dependent above 100 Hz [74]. This frequency dependent stiffness is also the stiffness used in TWINS for the ballast.

1.7.2 Acoustic absorption of ballast

As early as 1940, the absorption of ballast was measured in reverberation chamber by Kaye and Evans [75]. It was shown that the absorption increased with frequency. It was also indicated that proper choice of ballast materials may usefully contribute to noise reduction in the railway system.

In [76], in order to calculate the sound propagation attenuation in models such as e.g. Harmonoise, it was recommended that the ballast area was viewed as a locally reacting surface with a comparably low flow resistivity. A typical flow resistivity of 50 kPa s/m^2 can be obtained by using the Delany and Bazley model [56]. However, it is unknown whether this impedance model is applicable for the ballast. Also, the local reaction assumption for very low flow resistivity material is questionable as there may be relevant sound propagation in the medium itself [61, 77, 78].

Non-acoustic measurements were made of flow resistivity, stone density and porosity of ballast by Attenborough et al. [79]. The Johnson-Allard-Umnova model [80] was used to deduce the tortuosity of the ballast. It was shown that the measured low flow resistivity of railway ballast, with a value of 200 Pa.s/m^2, suggested that its acoustic properties exhibited extended reaction allowing for propagation in the material itself. Also, it was mentioned that the surface impedance of the ballast depended on its depth. Moreover, for the assumed track profile, by using the boundary element method, the ballast was predicted numerically to improve the A-weighted broadband SPL attenuation by 10 dB compared to levels predicted for a hypothetical ‘flattened’ track profile with grass edges.

The ballast as an extended reaction medium was considered by Heutschi in [81] based on a network of spheres and tubes. It was found that the sound propagating over a ballast bed had to be calculated with an extended reaction approach, which was confirmed by measurements in terms of excess attenuation. Also, both measurements and calculations confirmed a pronounced sensitivity of the ground effect to the thickness of the ballast bed. It was pointed out, therefore, that this sensitivity should be measured in situations where there was significant reflection over ballast.

By using a very large impedance tube (7.3 m × 0.76 m), experiments were performed by Swenson et al. to measure the various sound-wave propagation parameters of two kinds of gravel (a crushed gravel and a stream-formed ‘pea gravel’) at frequencies between 25 and 200 Hz [82]. The sound wave was found to be attenuated in the gravel, which indicated that it may be better to treat the ballast as a medium with extended reaction.

The acoustic properties of railway ballast were investigated by Broadbent et al. in terms of absorption coefficient and excess attenuation at the receiver [83]. Measurements were carried out both in a diffuse field and a free field environment to obtain the complex impedance and diffuse field sound absorption coefficient of a layer of ballast. The ballast was found to have negligible absorption at low frequency, but moderate absorption at mid and high frequency. It could also be modelled as a three-layer porous material using a locally reacting surface assumption. Reasonable agreement could be seen between the experimental results and the analytical prediction.

1.8 Vibro-acoustic scale modelling

The measurements in this thesis make use of a 1:5 scale track, which is based on scaling by dimensions; therefore vibro-acoustic scale models are briefly reviewed here.

If all dimensions are reduced by a scale factor, the dynamic behaviour remains the same but corresponding frequencies are increased by the scale factor [84, 85, 86]. In [84], a 1:8 scale model was used for the experimental validation in the vibro-acoustic research of multi-path sound transfer from resiliently mounted shipboard machinery. The scale model experiments indicated that the measuring (direct and reciprocal) methods were feasible. It was also pointed out that the reciprocal method could circumvent some practical difficulties when strong background noise at distant receiver locations existed in many practical shipboard situations. This reciprocal method is also the basis of the current measurement method, which will be discussed in detail in Chapter 6.

Ver et al. used both a reduced scale and full scale model to study experimentally the impact noise generation caused by rail discontinuities [85]. The scale model facility consisted of a 1:8 scale three-axle bogie with standard (rigid) wheels and aluminium-magnesium alloy rails. The peak sound pressure level of impact noise was measured when the train travelled in step-up and step-down directions with different speeds for both models. Agreement between the measurements and the analytical results was good. The major parameters influencing the generation of impact sound were identified. It was shown that scale models could be worthwhile to test the parameters identified first, then followed by the measurements at full-scale.

Both full scale and smaller scale roller rigs have also been used to study railway vehicle dynamics [87]. Detailed information on rolling rigs and scale models in railway research was also briefly summarised in this paper. In addition, some suggestions on the designs of different test rigs were given based on practical purposes.

A 1:8 scale single wheel and track model [88] was used by London Underground Limited (LUL) to investigate whether a scale model could be used to represent rolling noise and to study the effects of roughness on the wheel and rail vibration. The LUL test rig was later developed by Armstrong and Thompson, but with a 1:5 scale factor [86]. The wheel/rail interaction, where surface roughness and discontinuities are present on the railhead, was predicted by linear and non-linear wheel/rail contact models. Reasonable agreement was seen between the predictions and the corresponding measurements obtained from the 1:5 scale rig.

Recently, a 1:5 scale model track, including scale rails, sleepers and ballast, was constructed by Lawrence in an undergraduate project [89] for the purpose of modelling and software validation. The radiation ratio of the scale rails and scale sleepers in free space and the effects of the ground plane on the acoustic behaviour of the rails and sleepers have been preliminarily measured by using this 1:5 scale model facility. The agreement between the measured results and the numerical predictions was poor. It is pointed out that the radiation ratio of the rails and sleepers needed further investigation and a more effective constrained layer damping treatment should be applied to the rail. Measurements of the absorption of the 1:5 scale ballast in this scale model was presented in another undergraduate project by Lewis [90].

In terms of the scaling law for sound absorptive material, according to Junger [91], it is different from the conventional scaling law for the dynamic scaling. Figure 1.7 shows a scale model for a layer of porous material. A Rayleigh solid is a kind of simplification for a solid embodying a regular array of parallel fluid-filled capillaries [91]. As it is shown, in order to ensure the invariance of the layer impedance, if the thickness *L* is scaled down by a factor of *s*, the intersticial dimensions should be scaled down as $s^{1/2}$. This scaling law will also be studied in this thesis.

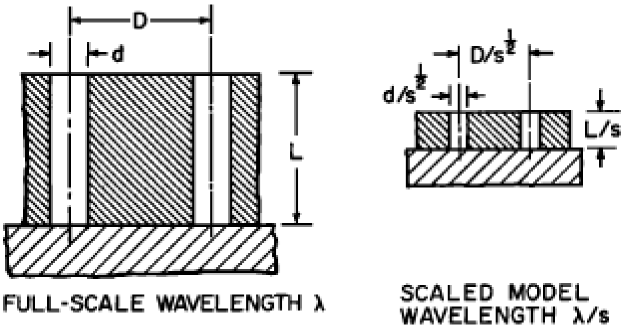

Figure 1.7 Scaled model of a layer of Rayleigh solid designed to display an invariant specific acoustic impedance [91]

1.9 Methods to reduce rolling noise from the track

A promising means to reduce the noise radiated by the track was presented by Thompson et al. [92]. The noise radiated was reduced by increasing the damping of the rail, which increased the attenuation with distance of vibration transmitted along the rail. To achieve this, a tuned, damped mass-spring absorber system was designed. Multiple tuning frequencies were used along with a material with a high damping loss factor in order to cover a wide range of frequencies. The rail damper effectiveness was assessed by measuring the rolling noise at 100 km/h for a vehicle fitted with noise reducing wheels. Adoption of rail dampers resulted in a reduction of the track component by about 6 dB.

During the period 2005-2008, pass-by measurements were performed by DB near Gersthofen, Germany, within the SILENCE project. Their main purpose was to assess the efficiency of rail dampers which were installed on a portion of the test site. It was shown that the noise emission from the railway could be reduced by about 4 dB by increasing the damping of the rail [93]. Also, predictions were found to have good agreement with measured data [94].

The influence of porous concrete sleepers on rail noise was predicted by Attenborough et al. [79] using a boundary element code. It was found that, for the assumed track profile, in a vertical plane through the sleepers, replacing acoustically hard sleepers by porous concrete sleepers could reduce the A-weighted SPL. It was also found that a porous slab track was predicted to yield up to 6 dB reduction in A-weighted SPL compared with an acoustically hard slab track.

There are also other solutions to reduce the rolling noise. One possible option is the optimum of rail pad stiffness [48]. Low height barriers are a choice for the reduction of the track noise as well, which has been tested in Silent track project [1].

1.10 Gaps between knowledge

It is shown in previous sections that few work has been carried out concerning the basic issues of rolling noise in the railway track system: particularly the acoustic properties of the rail and the sleeper. Also, as an important component in the railway track, the ballast will affect their sound radiation. This thesis focuses on these three aspects.

The TWINS model for rolling noise has been validated by means of field measurements during train passby [2, 3, 42]. This showed reasonably good agreement between measurements and predictions over a wide range of conditions. Particularly where the noise was predicted directly from the measured vibration the agreement was good; larger uncertainty was found in the prediction of the vibration from the surface roughness. Despite its widespread use, there remain areas for improvement in this model.

One of the assumptions in this model, as in Bender and Remington [30], was that the rail radiation could be modelled using a rail in free field. In practice, however, the rail is not located in free space but is in close proximity to the ground. This consists of ballast, which is partially absorptive, and sleepers (or cross ties) which are reflective. This is expected to influence the results at low frequency, but since the sleepers dominate the radiated noise below about 400 Hz [1], this effect has been neglected up to now. In order to propose a more realistic model to predict the noise from the rail at low frequencies, the effects of acoustic boundary conditions due to the sleeper and ballast should be taken into account in the prediction models.

Regarding the sleeper radiation, it is also found that the agreement between predictions and field measurements of the track sound radiation is often less satisfactory at low frequencies (below 300 Hz), where the sleepers radiate most of the noise. The sleeper acoustic power is currently predicted in TWINS by adopting a simplified formulation for its radiation efficiency [46]. The model in TWINS [46] is based on an approximate relation for the radiation from a rectangular piston set in an infinite baffle. However, this is modified at low frequencies to allow for the fact that multiple sleepers are close together compared with the acoustic wavelength and therefore can be considered to form a single composite source. The increase in the radiation efficiency compared with that of a single sleeper is estimated using a heuristic approach [46], and has not been validated, so a rigorous way to estimate this effect is required.

Some initial predictions for the sound radiation of a single sleeper as well as multiple sleepers, embedded in a rigid ground, are presented in [1]. These were obtained using the Rayleigh integral approach [95], which is based on the assumption that the vibrating surface is flush with a rigid ground. Apart from the above references, however, very little work has been carried out into the acoustic characteristics of the sleepers.

Another limitation in the TWINS model is that the effect of ballast vibration and absorption on the track radiation is not considered. On one hand, during a train pass-by, the ballast can vibrate, leading to reradiated noise. On the other hand, from an acoustical point of view, the gaps between the stones make it behave as a porous material, absorbing noise to some extent. It is not clear, however, to what extent these two effects contribute to the noise radiated to the side of the track and how much the mechanical and acoustical properties of the ballast modify the radiation from the sleeper and the rail.

1.11 Objectives and scope of work for this thesis

The main objective of this thesis is to improve the complete prediction of the track sound radiation compared with the TWINS software by improving the sound radiation models for the rail and sleeper, particularly at low frequencies. The effects of the ballast on the track sound radiation will also be considered in the numerical models. This research aims ultimately at proposing a feasible control strategy for the noise from a railway track after understanding the mechanisms of sound radiation by the rail, sleeper and ballast.

The scope of work in the current research can be specifically summarized in three main aspects:

1. Sound radiation from the rail. Two-dimensional boundary element method (BEM) predictions of the sound radiation from a rail in different situations (in free space, attached to a ground and above a ground) are explored in terms of the radiation ratio, when the rail vibrates vertically and horizontally. Moreover, the effects of an

absorptive ground on the sound radiation of the rail are investigated for the rail vibrating both vertically and horizontally. Measurements have been carried out to verify the numerical predictions.

2. Sound radiation from the sleeper. The work concentrates on concrete monobloc sleepers which are the most common form used in modern ballasted track. The sound radiation of the sleeper (a single sleeper and multiple sleepers) in proximity to rigid and absorptive ground is predicted numerically using a three-dimensional boundary element model, when the sleeper vibrates vertically. Experiments have been conducted to verify the modelling.
3. Absorption and vibration of ballast. A 1:5 scale ballast is studied in this thesis for convenience. The flow resistivity and porosity of the ballast have been measured. Modelling of ballast absorption is then implemented based on the corresponding measured parameters for the ballast, which is also compared with the measured absorption. The effects of ballast absorption on the rail and sleeper radiation are also measured. In addition, the vibration of the ballast is obtained experimentally; the influence of the ballast vibration on the sleeper radiation is then estimated.

Finally, the models for the sound radiation from the rail and the sleeper are implemented with the TWINS software to give a complete prediction of the track sound radiation, including the influence of the ballast. These predictions are compared with field measurements from an operational railway track. Differences are also shown between the predictions using the original TWINS model and the new models.

It is necessary to point out that the scale track model used for the measurements in this thesis is basically the one constructed by Lawrence [89]. Some of the current measurements are, therefore, further and more comprehensive investigations of issues in that project [89].

1.12 Original contributions

The main original contributions of the current work are identified as follows:

1. Using the boundary element method (BEM) in two dimensions (2D), for both vertical and horizontal vibration, the effects of an absorptive ground in close proximity to the rail on its sound radiation have been determined using an impedance model for the absorptive ground. Allowance has also been made for the effect of wave propagation

along the rail by applying a wavenumber correction in the 2D modelling of the sound radiation from the rail.

2. The influence of ground absorption on the sound radiation from the sleeper (a single sleeper and multiple sleepers) has been explored by using the three-dimensional boundary element method. The numerical results include the effects of the flexible behaviour of the sleeper.
3. Extensive measurements have been carried out to verify the numerical predictions for the sound radiation from the rail and the sleeper in different configurations by using a 1:5 scale rail and sleeper model.
4. The basic properties of a 1:5 scale railway ballast have been measured: the flow resistivity, the porosity and the acoustic absorption. A locally reacting model of ballast absorption is then investigated based on these measured parameters. The effects of the ballast absorption on the rail and sleeper radiation have also been measured and compared with the corresponding numerical results.
5. In order to check the scaling law for ballast as a porous material, the absorption of 1:√5 scale ballast has been measured. Additionally, the effects of a different ballast gradation on the absorption of scale ballast have been measured.
6. The influence of the ballast vibration on the sleeper radiation has been estimated by using the measured vibration of the ballast, when the ballast is excited by the sleeper vibration.
7. The updated models are implemented together with the TWINS model giving improved predictions for rolling noise.

1.13 Layout of thesis

The present thesis is structured as follows:

Chapter 1 gives an introduction of the research background, aims and scope of the current work. Previous work has also been summarized by reviewing related literature, and gaps in existing knowledge are pointed out.

The theory of the boundary element method is introduced in Chapter 2. Some test cases are shown to verify the boundary element program used in the current research in both 2D and 3D.

Chapter 3 presents predictions of the sound radiation from a rail in different conditions (in free space, attached to a rigid ground and above the rigid ground) in 2D, when the rail vibrates either vertically or laterally. Effects of an absorptive ground on the rail radiation are also explored. Finally, allowance is made for the effect of wave propagation along the rail by applying a correction in the 2D modelling.

Chapter 4 describes the modelling of the sleeper radiation. Specifically, a 3D boundary element model is used to investigate the sound radiation of the sleeper (a single sleeper and multiple sleepers) embedded in a rigid ground and an absorptive ground when vibrating vertically.

Chapter 5 presents the measurements of acoustic properties for a melamine foam and 1:5 scale ballast. In order to test the accuracy of the measurement methods, a melamine foam is measured first. The flow resistivity and porosity of the ballast were then measured. Modelling of ballast absorption is finally implemented based on the corresponding measured parameters for the ballast.

Experimental validation of models for the sound radiation from the rail and the sleeper is presented in Chapter 6 using a 1:5 scale rail and sleeper. For the rail radiation, tests have been carried out for both vertical and lateral excitation, when the rail is in free space and above both rigid and absorptive ground. The sleeper radiation has been measured for vertical excitation when a single sleeper is in free space and on an absorptive ground. The sound radiation from multiple sleepers is also measured, when they are resting on an absorptive ground. Besides, the effects of the ballast absorption on the rail and sleeper radiation are investigated experimentally using 1:5 scale models, and the results are compared with the corresponding numerical predictions. Moreover, the ballast vibration is measured when the sleeper (a single sleeper and multiple sleepers) is embedded in the ballast. The effect of the ballast vibration on the sleeper radiation is then evaluated based on the measured vibration level of the ballast.

In Chapter 7 the models are combined to give the prediction of the sound radiation from the whole track. Comparison is also made with the corresponding measured results from the 1:5 scale model. The new sound radiation models for the rail and the sleeper, are combined with the TWINS software to give the prediction of the full track sound radiation, including the influence of ballast. Besides, the differences are shown between the original TWINS models and the updated predictions.

Finally, Chapter 8 presents a summary of the conclusions obtained, and gives an outline of the suggested future work.

Chapter 2 Boundary element method

The boundary element method (BEM) is a numerical method, which can be used to determine the acoustic field inside a cavity or the sound radiation from a vibrating surface. There are two forms of the BEM generally available for acoustical analysis [96]. One is the direct boundary element method, which is based on the classical Helmholtz integral equation. It solves the Helmholtz equation in either an interior domain or an exterior domain. The other is the indirect BEM, which solves the Helmholtz equation in both the interior domain and the exterior domain simultaneously, even though one of the domains may not be needed for analysis and may not contain fluid. The indirect BEM approach can also handle boundaries that are not closed.

In the present work the direct BEM is used. Here, a summary is given of the direct BEM formulation in both two dimensions and three dimensions for the case of an exterior domain. Further details can be found in [96, 97]. A few simple test cases are then given to verify the BEM program used.

2.1 The boundary integral equation

The starting point for the BEM is a surface integral equation [96], which is known as Kirchhoff-Helmholtz integral equation (K-HIE). Assuming harmonic motion at frequency *ω*, for a volume *V* enclosed by a surface *S*, as shown in Figure 2.1, the equation can be written as

$$\varepsilon p(\mathbf{x}) = \int_S \left\{ g(\mathbf{x},\mathbf{y}) \frac{\partial p(\mathbf{y})}{\partial n} - p(\mathbf{y}) \frac{\partial g(\mathbf{x},\mathbf{y})}{\partial n} \right\} \; \mathrm{dS} \tag{2.1}$$

The vector notation is used to denote the co-ordinate positions of the points **x** and **y**, where **x** is in the acoustic domain and **y** is on the surface *S*. The term $g(\mathbf{x},\mathbf{y})$ is the Green’s function, **n** is the unit normal on the surface, pointing away from the acoustic domain in Figure 2.1, *p* is the complex sound pressure amplitude. ε can be calculated by the integration over a spherical volume or surface enclosing **x** in the limit of very small volume [96]. It is ½ for a point on a smooth surface, 1 for a point within the domain and 0 for a point outside the domain.

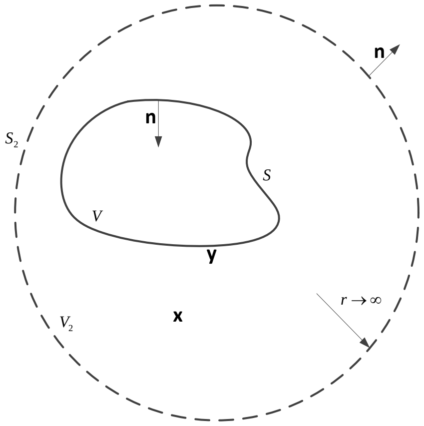

Figure 2.1 Radiation from a vibrating surfaces, based on [96]

For two-dimensional problems, the free field Green's function is

$$g(\mathbf{x},\mathbf{y}) = -\frac{i}{4}\mathrm{H}_0^{(2)}(kr) \tag{2.2}$$

where $\mathrm{H}_0^{(2)}$ is the Hankel function of the second kind and order 0, k is the wavenumber and $r = |\mathbf{x}-\mathbf{y}|$.

For three-dimensional problems, the corresponding free field Green's function is

$$g(\mathbf{x},\mathbf{y}) = \frac{e^{-ikr}}{4\pi r} \tag{2.3}$$

For an exterior problem, the objective is to solve the Helmholtz equation in an infinite fluid domain V_2 due to the sound radiation from a vibrating structure with boundary surface S, as shown in Figure 2.1. It can be seen that the volume V_2 is bounded by two surfaces S and S_2. The outer surface may be enlarged and taken in the limit to infinity. In the far field, the sound pressure must satisfy

$$p \to \frac{e^{-ikr}}{r} \quad \text{as} \quad r \to \infty \tag{2.4}$$

where $k = \omega/c_0$ is the wavenumber. A corresponding limit applies in 2D. This is a statement of the Sommerfeld radiation condition. It can be shown that

$$\lim_{r\to\infty}\int_{S_2}\left\{g(\mathbf{x},\mathbf{y})\frac{\partial p(\mathbf{y})}{\partial n} - p(y)\frac{\partial g(\mathbf{x},\mathbf{y})}{\partial n}\right\}\,\mathrm{dS}_2 = 0 \tag{2.5}$$

That is, the outer part of the surface that has been taken to infinity contributes nothing to the integral, and therefore the integral surface in the boundary integral equation (2.1) can be taken as the surface *S*.

In order to derive the boundary element formulation, the first main step is to consider a point **x** on the boundary *S*. If the point **x** becomes the boundary point **y**′, then the integral equation is written as

$$\frac{1}{2}p(\mathbf{y}') = \int_S \left\{ g(\mathbf{y}',\mathbf{y})\frac{\partial p(\mathbf{y})}{\partial n} - p(\mathbf{y})\frac{\partial g(\mathbf{y}',\mathbf{y})}{\partial n} \right\} \, \mathrm{dS} \tag{2.6}$$

Here, for simplicity, it is assumed that the boundary is smooth at **y**′, so that ε=1/2. It should be noted that when **y**′ and **y** coincide, both terms of the integrand are singular. As *r* goes to zeros, the singularity due to *g* is in the order of *O* (1/*r*), whereas the singularity due to $\partial g/\partial n$ is in the order of *O* (1) because $\partial r/\partial n$ is in the order of *O* (*r*). Therefore, the singularity is weak and both integrals converge in the regular sense [96].

Noting that

$$\frac{\partial p}{\partial n} = -i\omega\rho_0 v_n \tag{2.7}$$

where v_n is the surface normal velocity, it is clear that the first term in the integrand of Equation (2.6) is specified for an acoustic radiation problem by the vibration of the surface and thus the equation relates pressures at all points **y** on the surface to that at the surface point **y**′.

Therefore, the boundary integral formulation of Equation (2.6) can be given by

$$\frac{1}{2}p(\mathbf{y}') = -\int_S \left\{ i\omega\rho_0 v_n g(\mathbf{y}',\mathbf{y}) + p(\mathbf{y})\frac{\partial g(\mathbf{y}',\mathbf{y})}{\partial n} \right\} \, \mathrm{dS} \tag{2.8}$$

2.2 Half-space problems

It can be found in many applications that the acoustic domain *V* is bounded by an infinite reflection plane, S_H, as shown in Figure 2.2. The reflection plane, for example, can represent a rigid ground, on which the normal velocity is zero. Modelling of this infinite reflection plane can be avoided by using a half-space Green’s function.

This can be derived by using the method of images. As Figure 2.2 shows, the noise source *P* has an image *P′* with respect to the reflection plane. The distances between the original and image sources and the receiving point *Q* are denoted by *r* and *r′*, respectively. Accordingly, taking the image point source solution into account, the half-space Green's function in the presence of the reflection plane can be given in 3D as

$$g'(\mathbf{x},\mathbf{y}) = \frac{e^{-ikr}}{4\pi r} + \frac{e^{-ikr'}}{4\pi r'} \tag{2.9}$$

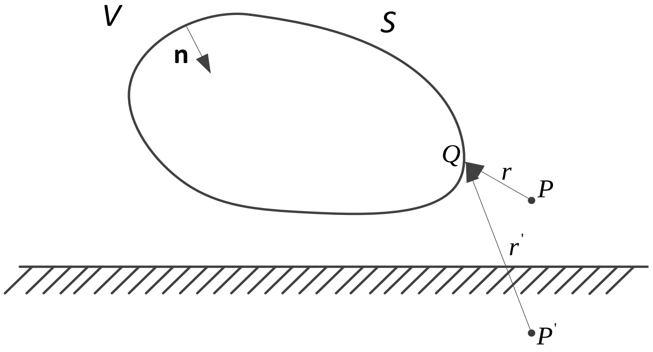

Figure 2.2 Image method for the half-space Green's function

Figure 2.2 shows the image source *P′* is outside the acoustic domain. The half-space Green's function $g'(\mathbf{x},\mathbf{y})$ therefore has only the same singularity as $g(\mathbf{x},\mathbf{y})$ in the acoustic domain *V*. Thus, $g'(\mathbf{x},\mathbf{y})$ can be used in the Helmholtz integral equation to replace $g(\mathbf{x},\mathbf{y})$. The corresponding boundary integral formulation with the half-space Green's function can be written as

$$\frac{1}{2} p(\mathbf{y}') = -\int_{S+S_{\mathrm{H}}} \left\{ i\omega\rho_0 v_n g'(\mathbf{y}',\mathbf{y}) + p(\mathbf{y}) \frac{\partial g'(\mathbf{y}',\mathbf{y})}{\partial n} \right\} \, \mathrm{dS} \tag{2.10}$$

where the reflection plane S_{H} is temporarily included in the integral equation because it is part of the boundary of the acoustic domain.

For *Q* on S_{H}, it is known that $r = r'$ and $\frac{\partial r}{\partial n} = -\frac{\partial r'}{\partial n}$. Therefore, on a rigid reflection plane, it is found that

$$v_n = 0 \quad \text{and} \quad \frac{\partial g'(\mathbf{x},\mathbf{y})}{\partial n} = 0 \tag{2.11}$$

The integral over S_H is therefore zero and the half-space boundary integral equation becomes

$$\frac{1}{2}p(\mathbf{y}') = -\int_S \left\{ i\omega\rho_0 v_n g'(\mathbf{y}',\mathbf{y}) + p(\mathbf{y})\frac{\partial g'(\mathbf{y}',\mathbf{y})}{\partial n} \right\} \mathrm{dS} \tag{2.12}$$

2.3 Boundary element discretization

To solve the Helmholtz integral equation numerically, it is necessary to discretize the boundary into a number of elements; more details can be found in [96]. For the BEM, only one-dimensional elements are required for the analysis of a two-dimensional domain, whereas for the analysis of a three-dimensional domain, two-dimensional elements are used to represent ‘patches’ of the surface. Node points are defined at the ends or corners of these elements and in some cases also at internal points.

Within each element, the sound pressure can be given by

$$p = \left[N_a\right]_e \left\{p\right\}_e \tag{2.13}$$

and

$$\frac{\partial p}{\partial n} = \left[N_a\right]_e \left\{\frac{\partial p}{\partial n}\right\}_e \tag{2.14}$$

where $\left[N_a\right]_e$ is a row matrix of shape functions for a single element, and $\{\}_e$ denotes a vector of pressures or pressure gradients at the node points of the element. The two vectors $\left\{p\right\}_e$ and $\left\{\partial p/\partial n\right\}_e$ represent the unknown pressure and normal velocities at the nodes of the element.

Substituting these expressions into the surface integral Equation (2.6), the results can be obtained for the point $\mathbf{y}' = y_j$ located at node j by the piece-wise approximation method. The pressure is written as

$$p_j = \sum_e [\mathrm{m}]_e \left\{\frac{\partial p}{\partial n}\right\} - \sum_e [\mathrm{d}]_e \left\{p\right\}_e \tag{2.15}$$

where

$$[\mathrm{m}]_e = 2\int_{S_e} g\left(\mathbf{y}_j,\mathbf{y}\right)\left[N_a\right]_e \mathrm{dS} \tag{2.16}$$

$$\left[\mathrm{d}\right]_e = 2\int_{S_e} \frac{\partial g\left(\mathbf{y}_j, \mathbf{y}\right)}{\partial n} \left[N_a\right]_e \mathrm{dS} \tag{2.17}$$

It should be noted that expressions (2.16) and (2.17) are evaluated over the element S_e. The terms in $\left[\mathrm{m}\right]_e$ and $\left[\mathrm{d}\right]_e$ can be calculated by Gauss-Legendre quadrature [97].

In Equation (2.15), it is implied that the integral over the whole surface has been replaced by the summation over all the elements. Therefore, Equation (2.15) can be expressed as the following row-matrix equation

$$p_j = \left[\mathrm{m}\right]\left\{\frac{\partial p}{\partial n}\right\} - \left[\mathrm{d}\right]\left\{p\right\} \tag{2.18}$$

where the two vectors $\{p\}$ and $\partial p/\partial n$ are the pressure and normal velocity amplitudes at the nodes of the global system, respectively, and [m] and [d] are assembled from the element matrices $[\mathrm{m}]_e$ and $[\mathrm{d}]_e$.

Then setting the node j to each of the N nodes of the whole surface in turn, a square set of equations can be produced in the following form

$$\left\{p\right\} = \left[\mathrm{M}\right]\left\{\frac{\partial p}{\partial n}\right\} - \left[\mathrm{D}\right]\left\{p\right\} \tag{2.19}$$

$$\text{or } \left(\left[\mathrm{D}\right] + \left[\mathrm{I}\right]\right)\left\{p\right\} = \left[\mathrm{M}\right]\left\{\frac{\partial p}{\partial n}\right\} \tag{2.20}$$

where [M] and [D] are $N \times N$ matrices.

According to Equation (2.19), a boundary condition must be known for each part of the boundary for either p or $\partial p/\partial n$ or the relation between them. The pressure or the normal velocity may be prescribed. For example, for the radiation from a vibrating surface, v_{n} is known and hence $\partial p/\partial n$. Or, it may be that both the pressure and the normal velocity on the boundary are unknown, but that a relationship between them, known as an impedance boundary condition, is given. According to the boundary conditions specified at each node of the surface, the Equation (2.19) may be rearranged so that the unknowns are collected in a single column vector $\left\{\hat{p}\right\}$ and the matrix multiplication with the vector of known boundary condition values is on the right-hand side. This can be written as

$$\left[\mathrm{A}\right]\left\{\hat{p}\right\} = \left\{\mathrm{B}\right\} \tag{2.21}$$

Once the boundary unknowns are solved, the Helmholtz integral equation (2.6) can be integrated again to obtain the sound pressure at any field point in the acoustic domain from the pressure and pressure gradient on the boundary.

2.4 Non-uniqueness problem

One problem occurring for the direct BEM in acoustics is that the integral Equation (2.6) has a non-unique solution for exterior problems at some characteristic frequencies. The reasons are as follows. The integral terms in Equation (2.6) are common to both the interior and exterior problems. For interior problems, if p=0 or v_{n}=0 at all points on S, a non-zero solution can still occur at the undamped modes of the cavity, and Equation (2.6) becomes singular at the corresponding frequencies. However, for exterior problems, no such modes exist, so this is just a breakdown of the solution at these frequencies. This problem is purely mathematical.

The simplest way to overcome the non-uniqueness problem is to use the CHIEF method proposed by Schenck [37]. This introduces additional constraint equations at a number of points $\mathbf{x}_j$ located inside the body, where a zero pressure is enforced. That is, for $\mathbf{x}_j$ in the interior domain,

$$0=\int_S \left\{ g\left(\mathbf{x}_j,\mathbf{y}\right)\frac{\partial p\left(\mathbf{y}\right)}{\partial n}-p\left(\mathbf{y}\right)\frac{\partial g\left(\mathbf{x}_j,\mathbf{y}\right)}{\partial n}\right\} \mathrm{dS} \tag{2.22}$$

When Equation (2.22) is discretized, it becomes

$$0=\sum_e \left[\mathrm{m}_j\right]_e \left\{\frac{\partial p}{\partial n}\right\}_e -\sum_e \left[\mathrm{d}_j\right]_e \left\{p\right\}_e \tag{2.23}$$

where

$$\left[\mathrm{m}_j\right]_e=\int_{S_e} g\left(\mathbf{x}_j,\mathbf{y}\right)\left[N_a\right]_e \ \mathrm{dS} \tag{2.24}$$

$$\left[\mathrm{d}\right]_e=\int_{S_e} \frac{\partial g\left(\mathbf{x}_j,\mathbf{y}\right)}{\partial n}\left[N_a\right]_e \ \mathrm{dS} \tag{2.25}$$

When a number M of interior points are chosen, the set of equations can be combined into matrix form

$$0=\left[\mathrm{M}_j\right]\left\{\frac{\partial p}{\partial n}\right\}-\left[\mathrm{D}_j\right]\left\{p\right\} \tag{2.26}$$

The combination of the global matrix equation for prescribed surface velocity (Equation (2.19)) and Equation (2.26) representing the interior points, gives

$$\left[\bar{\mathrm{A}}\right]\{p\}=\left[\bar{\mathrm{B}}\right] \tag{2.27}$$

where

$$\left[\bar{\mathrm{A}}\right]=\begin{bmatrix}\mathrm{D}+\mathrm{I}\\ \mathrm{D}_j\end{bmatrix}, \text{ and } \left[\bar{\mathrm{B}}\right]=\begin{bmatrix}\mathrm{M}\\ \mathrm{M}_j\end{bmatrix}\left\{\frac{\partial p}{\partial n}\right\}.$$

In Equation (2.27), for M interior points and N surface points, the dimensions of the matrices $\left[\bar{\mathrm{A}}\right]$ and $\left[\bar{\mathrm{B}}\right]$ are both $(M+N) \times N$, that is, there are more equations than unknowns. It can be solved by a least squares method. Similarly, for other forms of boundary condition Equation (2.21) can be extended in the same way.

As for the number or the locations of the CHIEF points used in the models, there are no rules. Nevertheless, in defining the positions of CHIEF points, the locations of nodal pressure surfaces of possible mode shapes should be avoided. Also, generally speaking, the models will need more CHIEF points at high frequencies. On the other hand, if too many points are used, it can lead to the solution becoming distorted. Thus, in order to get more accurate numerical results, it is necessary to test different numbers or positions of CHIEF points.

2.5 Numerical examples

The direct boundary element method is used for the prediction of sound radiation from a simple vibrating structure in this section. Comparisons are made with the corresponding analytical results. The numerical calculations in the following sections make use of a Matlab program called BEARS[1]. In the current work the program has been verified and also modifications have been made to implement the frequency-dependent impedance boundary conditions needed for the current research. Moreover, symmetry planes have been added in the modified program.

Four test cases are presented for the verification of the BEM program. Specifically, the sound radiation from a pulsating cylinder and an oscillating cylinder, as simple line sources, are predicted in 2D BEM. The effects of different element size and type in the modelling on the numerical results are also demonstrated, followed by the influence of different CHIEF points.

---

[1] This program was written by Dr C.J.C Jones based on [96].

The verification of the programming of impedance is next carried out in both 2D and 3D by using the corresponding test cases from reference [96]. Finally, the implementation of symmetry planes in the modified program is presented in both 2D and 3D.

2.5.1 Pulsating cylinder

For a cylinder of radius *a* and infinite length that is uniformly pulsating with velocity amplitude V_n at frequency ω with assumed time dependence $e^{i\omega t}$, then the amplitude of the sound pressure radiated from the cylinder is [98]

$$p = \frac{i\rho_0 c_0 V_n}{\mathrm{H}_1^{(2)}(ka)} \mathrm{H}_0^{(2)}(kr) \tag{2.28}$$

Where ρ_0, c_0 are the density of the air and speed of sound in the air, respectively. *r* is the distance from the centre of the cylinder, $\mathrm{H}_1^{(2)}$ is a Hankel function of the second kind and order 1, *k* is the wavenumber, given by $k = \omega / c_0$.

The sound power radiated by the cylinder can be determined in two ways: far field integration and surface integration. The method of surface integration is presented here. The sound intensity at the surface of the cylinder can be expressed as

$$I = \frac{1}{2} \mathrm{Re}\left(V_n^* p\right) \tag{2.29}$$

where V_n is the normal velocity amplitude of the cylinder surface, *p* is the sound pressure amplitude at the corresponding location, and * indicates complex conjugate.

Therefore, the sound power of the cylinder per unit length, W', is given by

$$\begin{aligned} W' &= \int_0^{2\pi} Ia d\phi \\ &= \int_0^{2\pi} \frac{1}{2} \mathrm{Re}\left(V_n^* p\right) a d\phi \\ &= \pi a \rho_0 c_0 \left|V_n\right|^2 \mathrm{Re}\left(\frac{i\mathrm{H}_0^{(2)}(ka)}{\mathrm{H}_1^{(2)}(ka)} \right) \end{aligned} \tag{2.30}$$

where ϕ is the azimuthal angle.

Then, the radiation ratio is

$$\sigma = \frac{W'}{\rho_0 c_0 \left\langle v^2 \right\rangle \bullet 2\pi a} = \mathrm{Re}\left(\frac{i\mathrm{H}_0^{(2)}(ka)}{\mathrm{H}_1^{(2)}(ka)} \right) \tag{2.31}$$

A pulsating cylinder with radius 0.1 m is used here, with a normal velocity amplitude of 1 m/s. Figure 2.3 presents the corresponding radiation ratio obtained by the analytical method described above. It can be seen that the pulsating cylinder, behaving as a line monopole, has a radiation ratio proportional to *f* at low frequencies (10 dB/decade), but tends to unity (0 dB) at high frequencies.

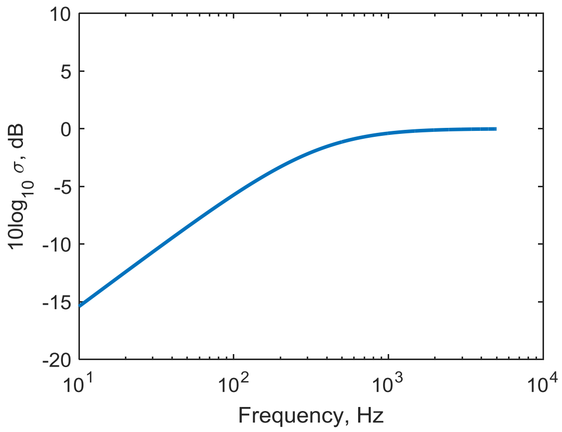

Figure 2.3 Radiation ratio of a pulsating cylinder of radius 0.1 m from analytical results

The same pulsating cylinder is next implemented in BEM. Figure 2.4 shows the cylinder model used with 32 quadratic elements, each with 3 nodes. The element size here is 0.0195 m, which is no more than one sixth of the smallest wavelength in the frequency range considered [97]. A normal velocity amplitude of 1 m/s is applied to every node point as the boundary conditions. Figure 2.5 presents the results for BEM models with different numbers and types of element. The same single CHIEF point is applied in these models.

The differences between the analytical and numerical results can be seen more clearly by using the following ratio of radiation efficiencies

$$err = 10\log_{10}\frac{\text{Boundary element result}}{\text{Analytical result}} \quad \text{dB} \tag{2.32}$$

Figure 2.6 shows the corresponding differences of the results for the element sizes and types tested, when the same single CHIEF point is used in the models. It can be seen that quadratic elements can give better results. In the remainder of this section, 32 quadratic elements are used in the cylinder model.

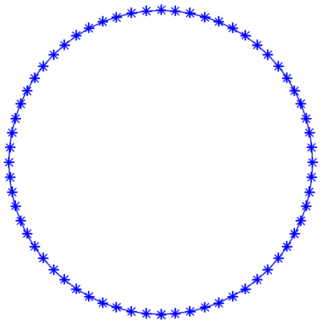

Figure 2.4 Cylinder model with 32 quadratic elements

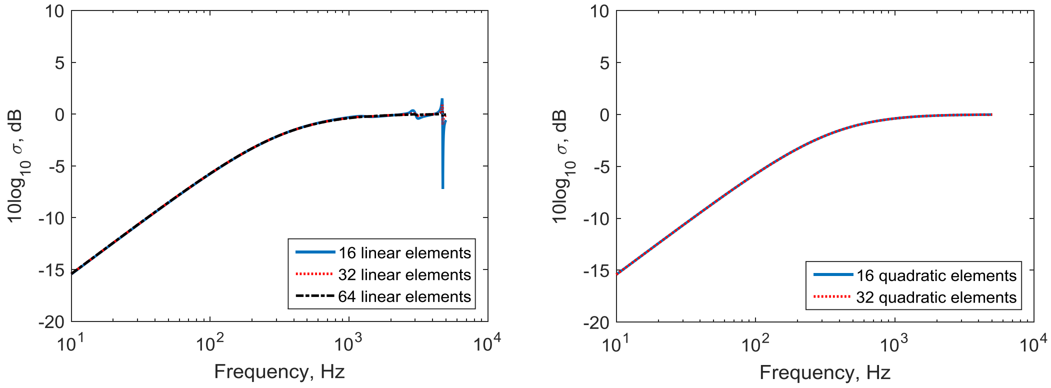

(a) Linear elements
(b) Quadratic elements

Figure 2.5 Tests of element size and type for pulsating cylinder

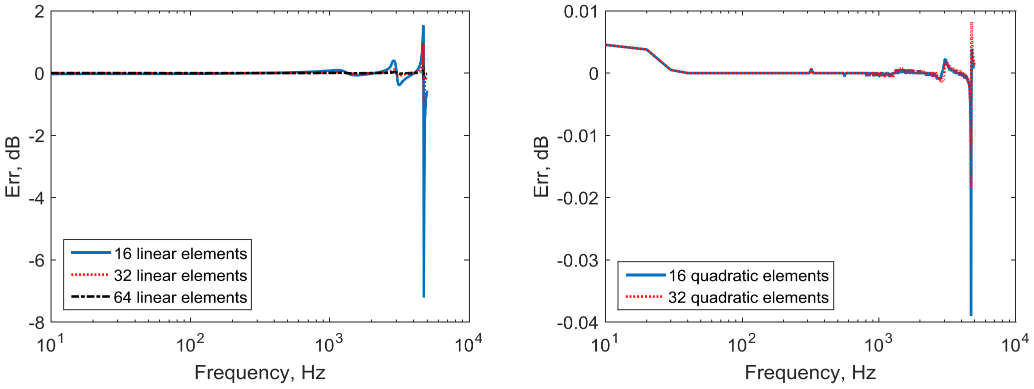

(a) Linear elements
(b) Quadratic elements

Figure 2.6 Differences of the results using different element sizes and types for pulsating cylinder

Figure 2.7 compares the analytical results obtained by the surface integral method and numerical ones using 32 quadratic elements for the radiation ratio of the pulsating cylinder. It is clear that the two solutions are nearly the same, which directly verifies the correctness of the BEM code. Also, results are shown for 0, 1 and 5 CHIEF points. It can be seen that different choices of CHIEF points cause little variations of the results.

Figure 2.8 illustrates the differences between the results obtained with different numbers of CHIEF points and the analytical solution. It is clear that the use of different CHIEF points has some influence on the results at high frequencies. The errors will be larger when no CHIEF points are used, especially at certain frequencies which can be identified as the eigenfrequencies of the interior problem. Nevertheless the errors here are all less than 0.02 dB. They could be larger if the frequency points were closer to the eigenfrequencies.

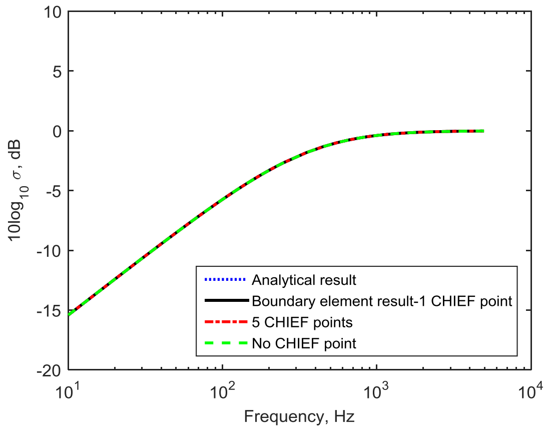

Figure 2.7 Radiation ratio of analytical model and BEM for pulsating cylinder of radius 0.1 m

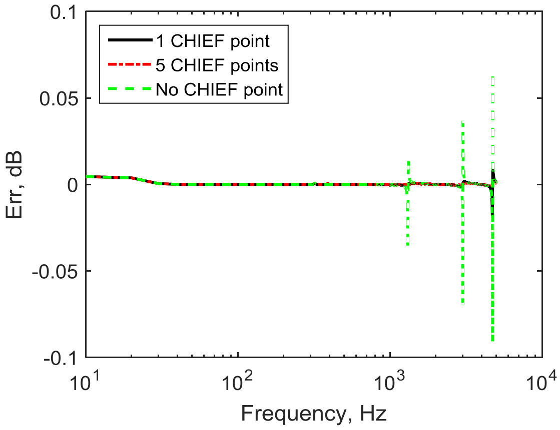

Figure 2.8 Differences of the results using different number of CHIEF points

2.5.2 Oscillating cylinder

In this section, the sound radiation from an oscillating cylinder is considered. For a cylinder with vibration velocity $U_0 e^{i\omega t}$, the normal velocity is $U_0 \cos\phi e^{i\omega t}$; the sound pressure radiated is [99]

$$p = B\cos\phi \mathrm{H}_1^{(2)}(kr)e^{i\omega t} \tag{2.33}$$

where (r,ϕ) are cylindrical polar co-ordinates with the origin at the centre of the cylinder, B is the amplitude of the sound pressure, and $\mathrm{H}_1^{(2)}$ is a Hankel function of the second kind and order 1. To determine B, consider the motion of the boundary of the cylinder, which has a radius of a. Its velocity is written as

$$\begin{aligned} u_r &= \frac{1}{i\rho_0\omega}\frac{\partial p}{\partial r}\bigg|_{r=a} \\ &= \frac{1}{i\rho_0\omega}B\cos\phi\frac{\mathrm{H}_0^{(2)}(ka)-\mathrm{H}_2^{(2)}(ka)}{2} \\ &= U_0\, e^{i\omega t}\cos\phi \end{aligned} \tag{2.34}$$

Thus

$$B = \frac{2i\rho_0\omega U_0}{\left[\mathrm{H}_0^{(2)}(ka)-\mathrm{H}_2^{(2)}(ka)\right]k} \tag{2.35}$$

Then the sound intensity at the surface of the $I = \frac{1}{2}\mathrm{Re}\left(V_n^* p\right)$ cylinder can be obtained. According to Equations (2.30) and Equation (2.31), the radiation ratio can also be calculated as

$$\sigma = 2\,\mathrm{Re}\left[\frac{i\mathrm{H}_1^{(2)}(ka)}{\mathrm{H}_0^{(2)}(ka)-\mathrm{H}_2^{(2)}(ka)}\right] \tag{2.36}$$

The BE model used here is the same as that for the pulsating cylinder. However, 64 linear elements are used, as it is easier to introduce the different normal velocity at every nodal point. A unit velocity vertical motion of the cylinder is defined as the boundary condition. The normal velocity at each node is determined from $U_0\cos\phi$. Figure 2.9 compares the analytical and numerical results of the radiation ratio of the oscillating cylinder. It is clear that the numerical solution again agrees well with the analytical one. This again verifies the correctness of the BEM code. Also, it can be seen that the radiation ratio of the oscillating cylinder, which behaves as a line dipole, is proportional to f^3 (30 dB/decade) at low frequencies, and tends to unity (0 dB) at high frequencies.

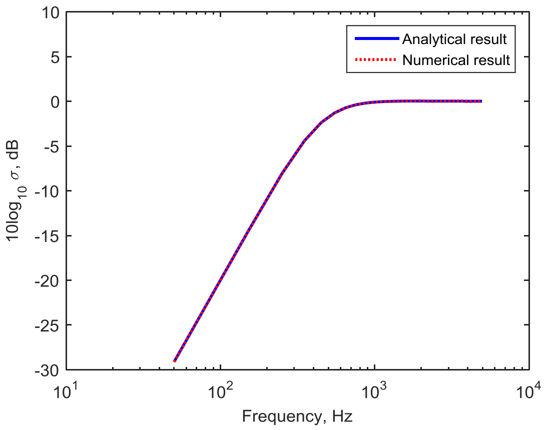

Figure 2.9 Radiation ratio of oscillating cylinder of radius 0.1 m

Figure 2.10 shows the locations of different numbers of CHIEF points used within the cylinder and Figure 2.11 shows their effects on the radiation ratio compared with the analytical results. In Figure 2.11(b), the constant number 0.03 or 0.01 refers to the distance (in m) of four CHIEF points from the origin, where one CHIEF point is located, as seen for the cases of d-h in Figure 2.10. These configurations all use five CHIEF points. It can be seen that the results differ greatly when using different CHIEF point configurations. Also, using more CHIEF points cannot guarantee increased accuracy of the results. For example, in Figure 2.11(a), the case of four random CHIEF points gives larger errors than that with 1 CHIEF point. Actually, 1 CHIEF point can achieve sufficient accuracy of results (see black line), when it is selected properly. Therefore, this implies that tests of different points are necessary in order to get satisfactory results.

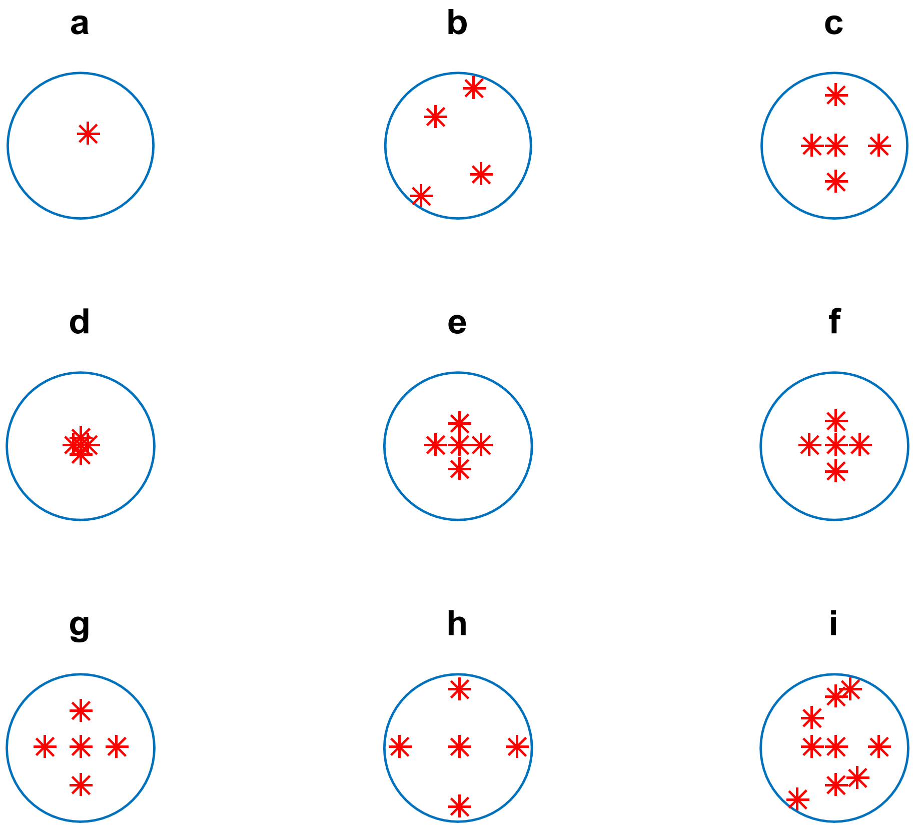

Figure 2.10 Locations of different CHIEF points in the oscillating cylinder

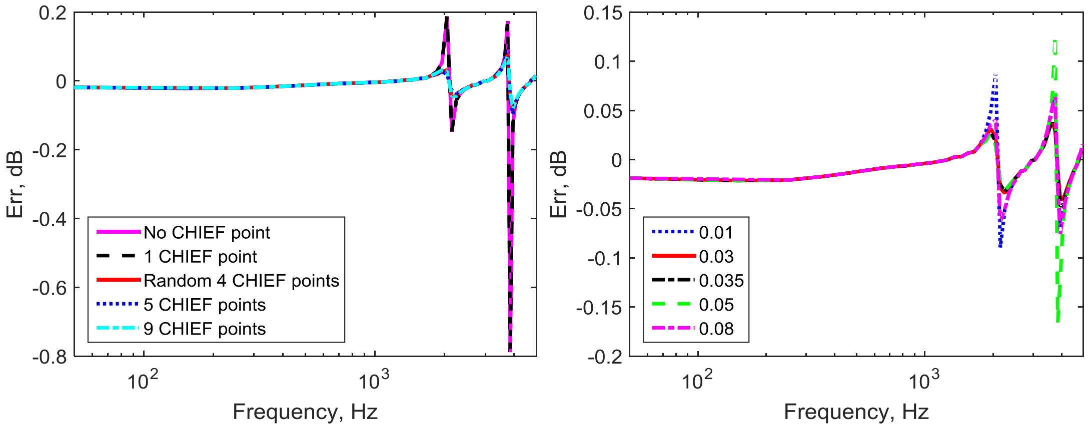

(a) Random positions of CHIEF points

(b) Regular positions of 5 CHIEF points

Figure 2.11 Differences between using different CHIEF points for oscillating cylinder

2.5.3 Test cases for the verification of the programming of impedance

The surface impedance will be applied in the numerical models in the current research. Therefore, it is necessary to verify the programming of the impedance in the BEM calculations, which are carried out in both 2D and 3D.

2.5.3.1 *Straight duct in 2D*

The model used in 2D is a straight duct, which has the boundary conditions of a unit normal velocity at the inlet (x=0) and an anechoic termination at the outlet (x=10 m), as shown in Figure 2.12. The anechoic termination means no reflection of sound, which is implemented by an impedance of $\rho_0 c_0$=415 Ns/m^3. More details are available in [96]. At the frequency of 54.5901 Hz, the real and imaginary parts of the sound pressure amplitude inside the duct are calculated using the modified program, and then compared with those obtained in reference [96]. Figure 2.13 shows the results. It is clear that the results calculated agree well with those in [96]. It is found the error for the real part of the sound pressure is less than 0.06 dB, whereas its counterpart is less than 0.04 dB for the imaginary part of the sound pressure. This directly verifies the correctness of the programming of the calculation with impedance in 2D.

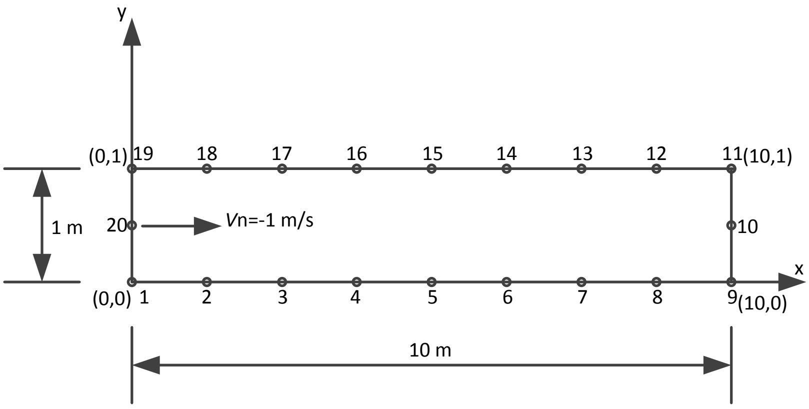

Figure 2.12 Mesh for the straight duct

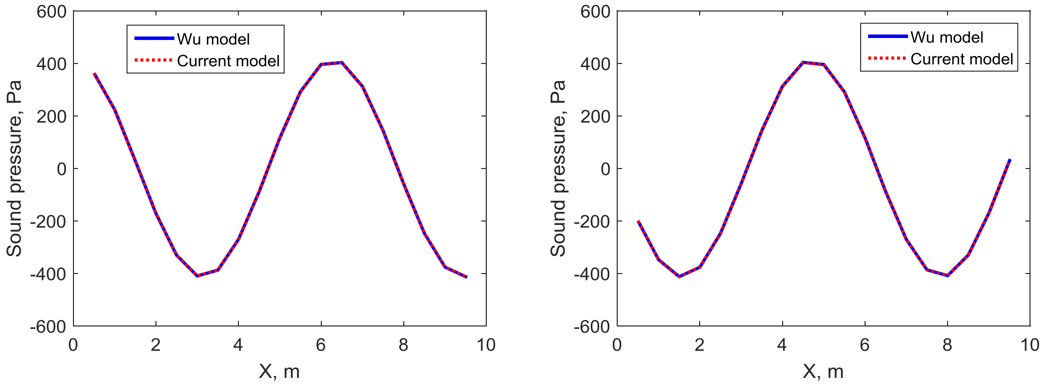

(a) Real part of sound pressure (b) Imaginary part of sound pressure

Figure 2.13 Verification of the programming of implementing the impedance boundary condition: sound pressure on the centreline of a duct with an impedance termination, compared with results from [96]

2.5.3.2 *One-dimensional plane wave in a box in 3D*

The case study for the verification of the BEM program in 3D is a 1 m × 1 m × 1 m box with the boundary conditions of a unit-amplitude normal velocity on one side (*x*=0) and an anechoic termination on the opposite side (*x*=1 m). Further details can again be found in [96]. As Figure 2.14 shows, 26 nodes and 24 four-node linear surface elements are used to model the box. At the frequency of 5.45901 Hz, the real and imaginary parts of the sound pressure amplitude at specified field points inside the box are calculated by the BEM program, and are compared with both analytical and numerical results presented in reference [96]. Table 2.1 shows the results. It is shown that the numerical predictions agree well with the analytical solution. This directly presents the correctness of the 3D BEM program.

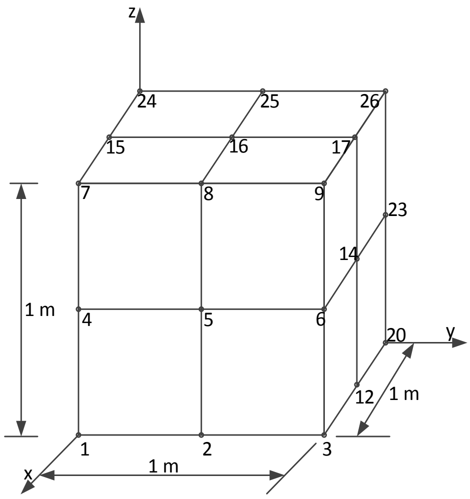

Figure 2.14 Mesh of the box

Table 2.1 Complex sound pressure amplitude (Pa) at two field points in the box

Field Point (m)	Analytical [96]	Wu Solution [96]	Current Solution
(0.25, 0.5, 0.5)	(414.900, -10.375)	(414.797, -9.216)	(414.800, -9.211)
(0.5, 0.5, 0.5)	(414.511, -20.743)	(414.533, -19.584)	(414.500, -19.580)

2.5.4 Test cases for symmetry used in boundary element method

In order to save calculation time in the BEM, especially in 3D, modifications are made in the original Matlab codes to introduce symmetry planes. The theory of the half-space problem in the boundary element method, as described in section 2.2, can be extended to implement one or more symmetry planes in the models. Specifically, the corresponding Green's function should be modified to include the corresponding image sources. The test cases described above for the pulsating cylinder and one-dimensional plane wave in a box will be used again here to verify the BEM program including symmetry planes in both 2D and 3D.

The first case studied is the pulsating cylinder. As shown, both its geometry and boundary conditions are symmetrical. Therefore, two kinds of symmetry are taken into account: one symmetry axis (half of the cylinder will be modelled) and two symmetry axes (one quarter of the cylinder will be modelled). The corresponding boundary meshes are shown in Figure 2.15. These models are recalculated in the updated BEM program. The results are shown in Figure 2.16 including the results from the model without symmetry. As can be seen, the results are the same, indicating that the program including the symmetry planes is correct. The maximum differences for the radiation ratio from the half model and the one-quarter model compared with that from the full model are 0.02 dB and 0.01 dB, respectively.

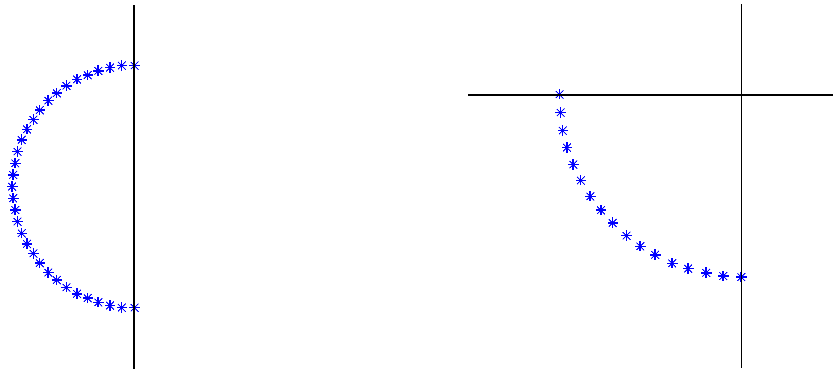

(a) Mesh of half the cylinder

(b) Mesh of one quarter of the cylinder

Figure 2.15 Symmetry models for the pulsating cylinder

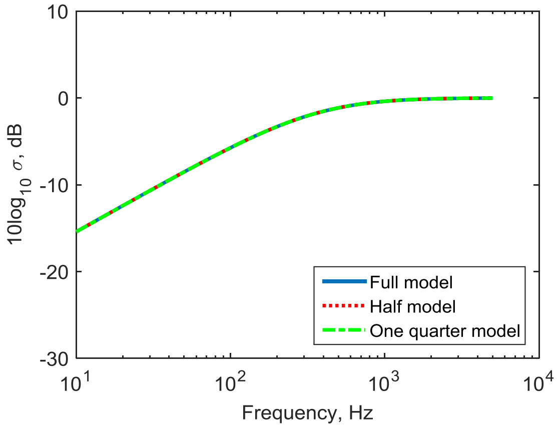

Figure 2.16 Comparison of the numerical results for sound radiation of the pulsating cylinder calculated with and without symmetry axis

The test case considered in 3D is the box with a plane wave from the section 2.5.3.2. The mesh for one quarter of the box is shown in Figure 2.17. The planes shown are the corresponding symmetry planes in the model. Table 2.2 presents the numerical results which are identical to those for the model without symmetry.

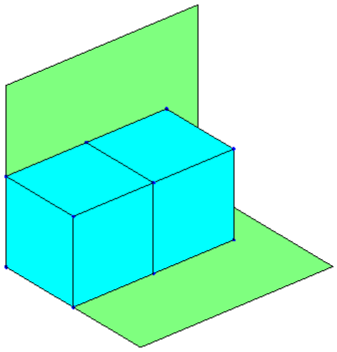

Figure 2.17 Mesh of one quarter box

Table 2.2 Complex sound pressure (Pa) at the two field points in the box

Field point (m)	Without symmetry	With symmetry
(0.25, 0.5, 0.5)	(414.8, -9.211)	(414.8, -9.211)
(0.5, 0.5, 0.5)	(414.5, -19.58)	(414.5, -19.58)

2.6 Summary

The theory of the direct boundary element method has been summarised for exterior domain problems in both 2D and 3D. Following the mathematical derivation of this numerical method, some simple test cases have been presented to verify the BEM program, including the implementation of impedance boundaries and symmetry planes. In the next chapters this will be used for studying the radiation of the rail and the sleepers.

Chapter 3 Modelling the sound radiation from the rail

The geometry of a rail can be considered as two-dimensional, with the third dimension being effectively infinite. Expressing Equation (1.1) for the radiation ratio in 2D, W becomes the power per unit length and S becomes the perimeter length. As the wavelength of rail vibration is generally large compared with the acoustic wavelength, the radiated sound field can be approximated as two-dimensional, allowing it to be calculated using a two-dimensional boundary element model. The validity of such an approach has been considered in [38] and shown to be valid in practical situations for a rail in situ above about 250 Hz, giving results within approximately 2 dB of that for the three-dimensional case.

In this chapter, the effect of the ground on the sound radiation from the rail is studied using two-dimensional boundary element methods. Cases are considered of a free rail, a rail in proximity to a rigid ground and to an absorptive ground. Results are presented in terms of the radiation ratio for both vertical and lateral motion of the rail. In order to understand more clearly how the rail radiates sound, the effects of geometrical parameter modifications of the rail on the sound radiation in free space have also been studied. Finally, allowance is made for the effect of wave propagation along the rail by applying a correction in the 2D modelling.

3.1 Sound radiation of the rail in free space

The sound radiation for a CEN60E1 rail is investigated here using a two-dimensional boundary element model based on the direct BEM approach as described in Chapter 2. Initially, a simplified rail section is considered in free space and this is compared with the actual geometry. Following this, the effects of geometrical parameter modifications on the rail radiation are considered.

3.1.1 Sound radiation of a simplified rail

A simplified rail, as shown in Figure 3.1, is studied initially. Comparison is also made with the cross-section of CEN60E1. For the simplified rail model in free space, 73 two-noded linear elements are used to represent the rail with a maximum element size of 0.01 m, which means there are at least 7 elements per wavelength at the maximum frequency of 5 kHz used in the prediction. A single CHIEF point is also applied in the model. In the calculations, it is assumed, for simplicity, that the rail vibrates with a unit amplitude rigid body motion either vertically or horizontally. This neglects cross-sectional deformation which is reasonable for frequencies below about 2 kHz for vertical motion and about 1 kHz for lateral motion [18]. To find the boundary condition for all the nodes when the rail vibrates vertically and horizontally, the normal velocity on each element is determined from its angle to the vertical or horizontal direction. Figure 3.2 presents a comparison of the radiation ratio from the simplified rail and that from the CEN60E1, when they are located in free space vibrating vertically or laterally. As can be seen, the radiation ratios of these two rails are nearly the same as each other. The differences of the predicted radiation ratio between these two rails are presented in Figure 3.3. As can be seen, it is less than 0.3 dB for lateral motion, whereas less than 1.2 dB for the rail with vertical motion. Actually, the differences for the vertical motion are generally less than 0.5 dB. The error has the maximum value of 1.2 dB at 4350 Hz. This is probably because this frequency is close to one of the eigenfrequencies of the rail cross-section. Nonetheless, this simplified rail section will be used in current research to represent the CEN60E1 rail.

For both vertical and lateral motion, Figure 3.2 also shows that the radiation ratio of the rail in free space is proportional to f^3 (30 dB/decade) at low frequency, which is characteristic of a line dipole. Based on the acoustic properties of an oscillating cylinder in Chapter 2, equivalent cylinders can be found for the rail vibrating vertically or laterally in free space. More details will be discussed in Section 3.2. For vertical motion, above around 1 kHz the radiation ratio oscillates around unity (0 dB). Peaks and dips are exhibited which are due to the shape of the rail. It can be suggested that constructive and destructive interference between the sound radiation from the rail head and the rail foot cause these fluctuations in the radiation ratio. Taking the dip at 1 kHz, for example, the distance between the centre of the rail head and the rail foot is approximately half the acoustic wavelength at this frequency. Thus a dip occurs at this frequency because of destructive effects, whereas at 2 kHz the distance is equal to the wavelength and a peak occurs. This will be investigated further in the next section.

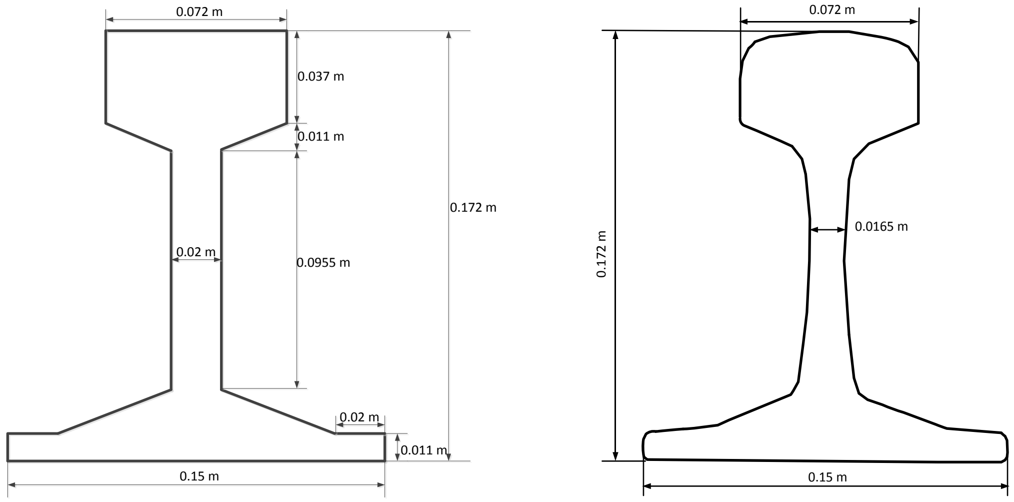

(a) Simplified rail (b) CEN60E1 rail

Figure 3.1 Comparison of simplified and CEN60E1 rail cross-section

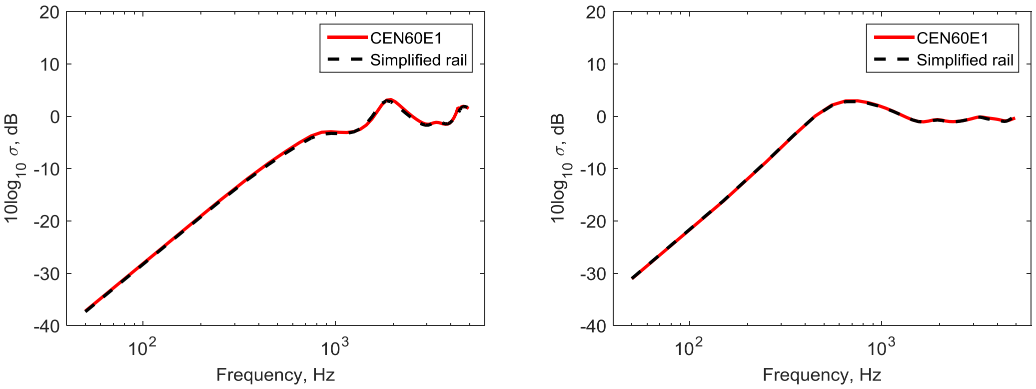

(a) Vertical motion (b) Lateral motion

Figure 3.2 Comparison of the radiation ratio between the simplified rail and CEN60E1 rail in free space

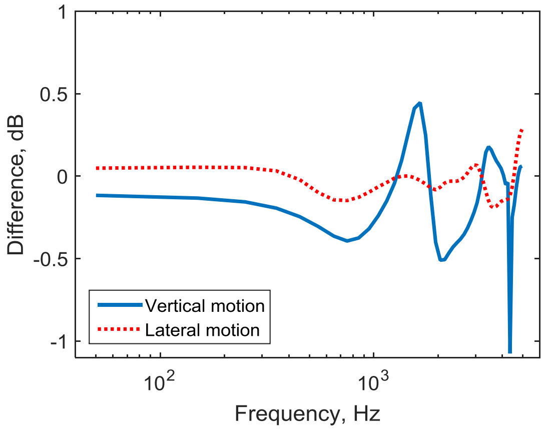

Figure 3.3 Differences of the radiation ratio between the simplified rail and CEN60E1rail for both vertical and lateral motion

3.1.2 Effects of geometrical modifications on the sound radiation of a rail

In order to understand the acoustic radiation from a rail more clearly, it is beneficial to investigate the effects of geometrical modifications of the rail on the sound radiation. Here, a study is presented to show how the geometry affects the sound radiation of the rail in free space when it vibrates vertically or horizontally.

3.1.2.1 *Modification of web height and width*

Figure 3.4 shows a case in which the length of the rail web is increased by 20 mm. Figure 3.5 presents the radiation ratio for the rail vibrating vertically and horizontally for this case. The peak at 2 kHz shifts to lower frequency for the rail moving vertically. For the rail moving horizontally, when the length of the rail web is enhanced, that means the equivalent cylinder for the rail has a larger radius; thus the radiation ratio increases at lower frequency in Figure 3.5(b).

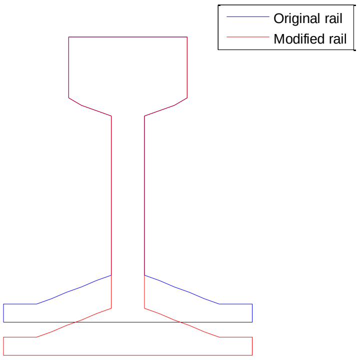

Figure 3.4 Length of rail web

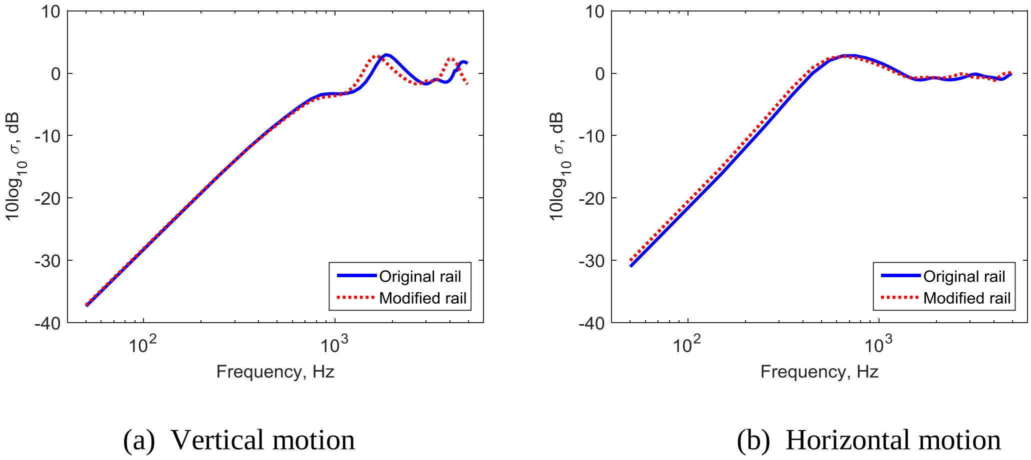

(a) Vertical motion (b) Horizontal motion

Figure 3.5 Radiation ratio of the rail for different web length

Figure 3.6 shows a modified rail in which the web width is equal to that of the rail head. Figure 3.7 presents the corresponding results. For the rail moving vertically, the radiation ratio is enhanced over the whole frequency range except at the peaks. Specifically, the peaks become flatter. For horizontal motion, the effects are smaller, but the modified rail again has less peaks and dips than the conventional rail.

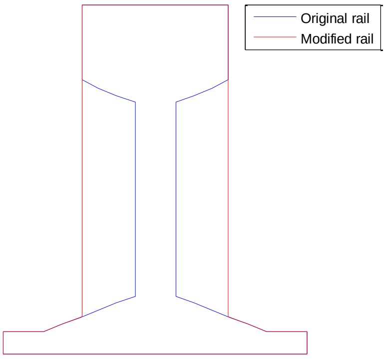

Figure 3.6 Web width equal to the rail head

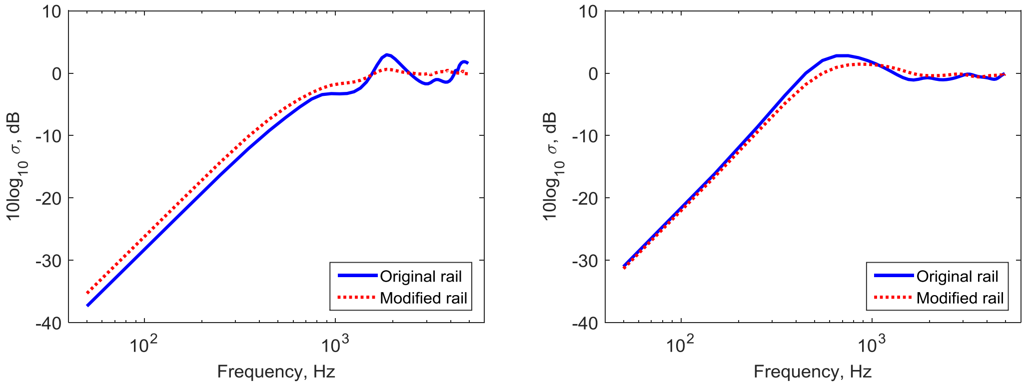

(a) Vertical motion (b) Horizontal motion

Figure 3.7 Radiation ratio of the rail for different web width

3.1.2.2 *Modification of rail foot*

Figure 3.8 shows a modified section in which the thickness of the rail foot is increased by 10 mm while keeping the overall height unchanged. Figure 3.9(a) presents the radiation ratio for the vertical motion of the rail. It can be seen that it is increased a little at low frequencies. Also, the peaks move. The sound radiation for the lateral motion of the rail changes very little over the whole frequency range, as shown in Figure 3.9(b).

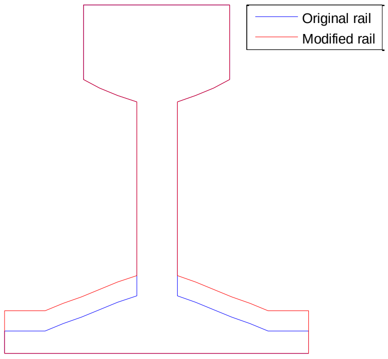

Figure 3.8 Height of rail foot

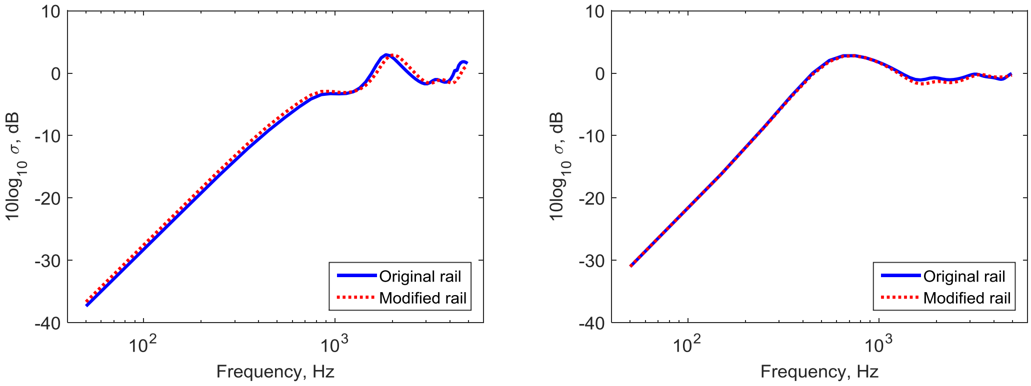

(a) Vertical motion (b) Horizontal motion

Figure 3.9 Radiation ratio of the rail for different heights of foot

Figure 3.10 shows two cases in which the width of the rail foot is increased or reduced by 20 mm (10 mm on each side). Figure 3.11(a) presents the results for the rail with vertical motion. It can be seen that the radiation ratio changes much at low frequency, but little at high frequency. This can be interpreted as a change in the radius of the equivalent cylinder for the rail. However, the radiation ratio for the rail vibrating horizontally changes little over the whole frequency range. In this case, the radius of the equivalent cylinder remains the same and it may be concluded that the width of the rail foot does not significantly affect the sound radiation for the rail moving laterally.

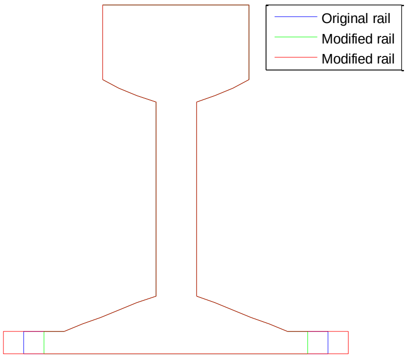

Figure 3.10 Width of rail foot

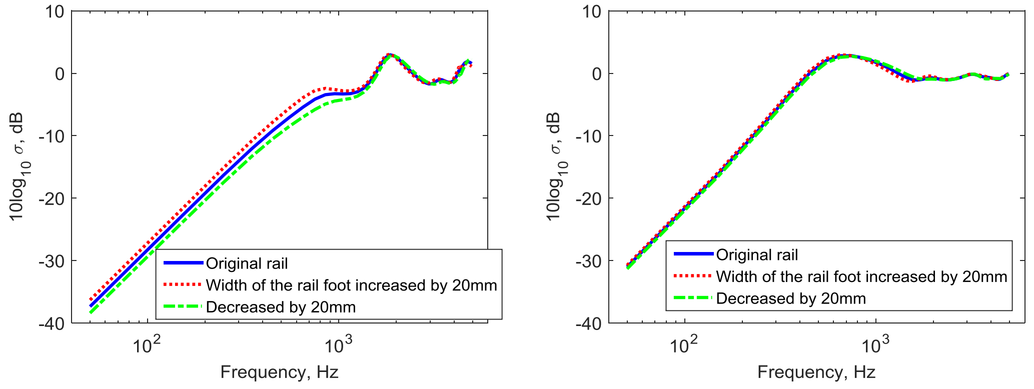

(a) Vertical motion (b) Horizontal motion

Figure 3.11 Radiation ratio of the rail for different widths of foot

3.1.2.3 *Modification of rail head*

Figure 3.12 shows a modified rail in which the height of the rail head is increased by 10 mm while keeping the overall height unchanged. Figure 3.13(a) presents the radiation ratio for the rail vibrating vertically. It can be seen that it is unchanged at low frequency; however, the peaks shift to higher frequency. For the rail vibrating horizontally, Figure 3.13(b) shows that the radiation ratio changes little over the whole frequency range.

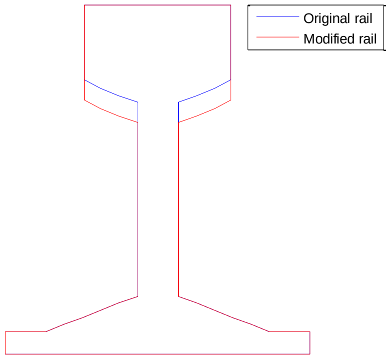

Figure 3.12 Height of rail head

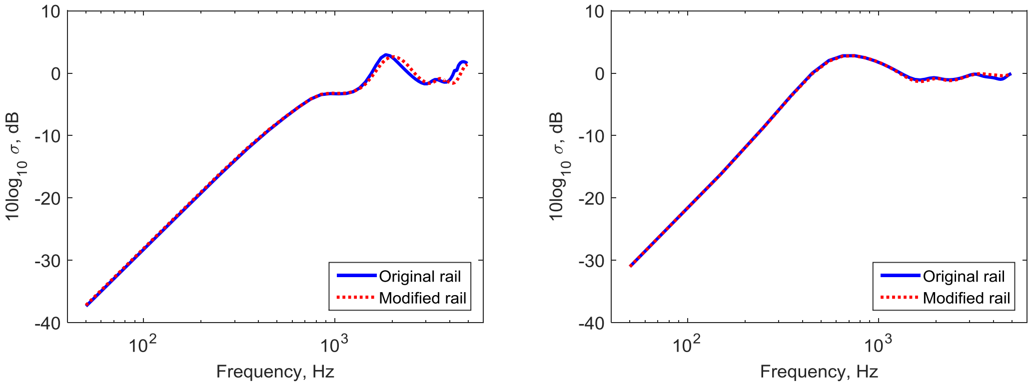

(a) Vertical motion (b) Horizontal motion

Figure 3.13 Radiation ratio of the rail for different heights of head

3.1.2.4 *T sections*

Figure 3.14 shows three cases, in which the modified rail takes the form of a T-section, with different widths of ‘web’, denoted T1, T2, T3. They have the decreasing web widths of 0.11 m, 0.072 m and 0.02 m. Figure 3.15(a) presents the radiation ratio of these sections for vertical motion. It can be seen that the cancellation of the sound radiation between the top surface of the rail head and the bottom surface of the rail foot has an impact on the results, as can be seen by comparing the curves for the modified rail. The wider T1 has the largest radiation at low frequency, whereas the narrow T3 has a result similar to the rail. The peak at 2 kHz and the dip at 1 kHz seen for the rail are not found for these T sections. Figure 3.15(b) shows the radiation ratio of these sections when they move horizontally. It is clear that the width of the web has an influence on the rail radiation, as can be seen in the peaks at around 800 Hz, which are strongest for the narrow section T3 which is most similar to the rail in this frequency region. At low frequency, the narrowest section, T3, has a lower radiation than the other sections, whereas the widest, T1, has a similar radiation to the rail section.

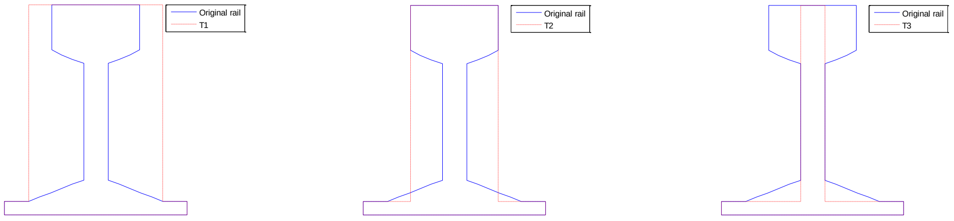

Figure 3.14 T-sections of the rail

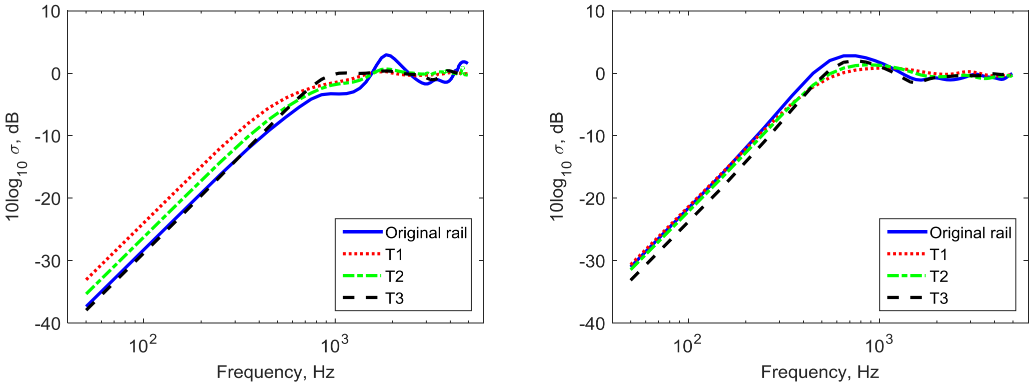

(a) Vertical motion (b) Horizontal motion

Figure 3.15 Radiation ratio of the rail for different T sections

3.1.2.5 *Separated rail head and foot*

In order to investigate these effects further, Figure 3.16 shows two cases with separate rail head and foot: one with a simplified shape and the other with the correct shape used previously. Figure 3.17 and Figure 3.18 present the radiation ratios in different conditions for vertical and horizontal motion. Both head and foot are assumed to have the same velocity amplitudes. In addition, the two components are considered separately.

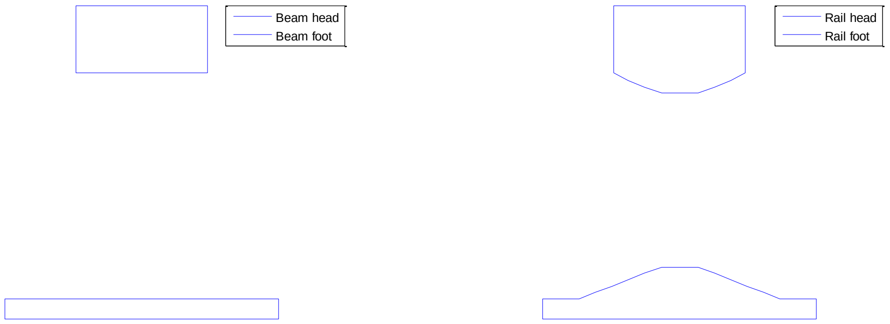

(a) Separated beam head and foot (b) Separated rail head and foot

Figure 3.16 Modification of the rail with separate head and foot

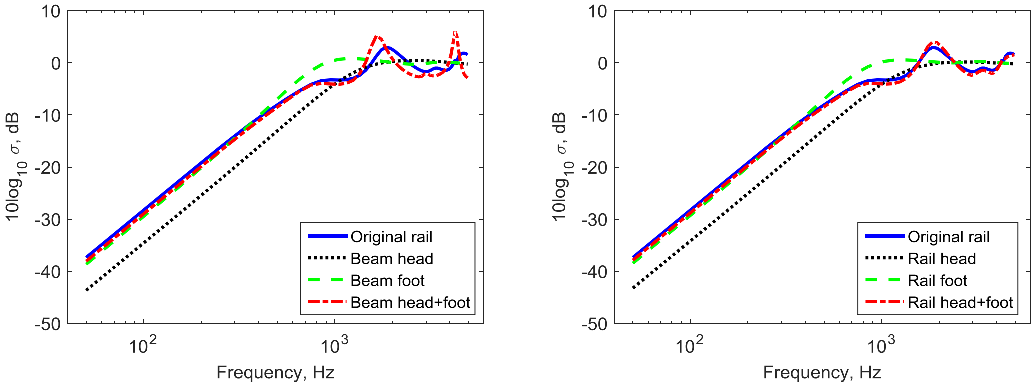

(a) Simplified head and foot (b) Actual shapes of head and foot

Figure 3.17 Radiation ratio of separate head and foot for vertical motion

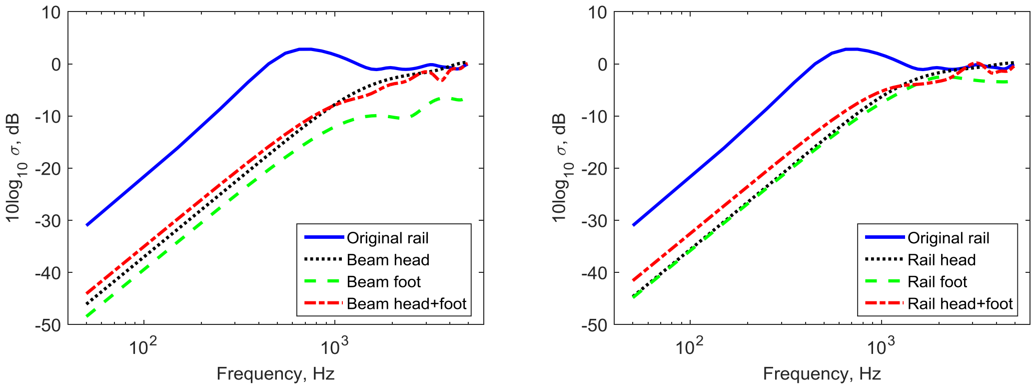

(a) Simplified head and foot (b) Actual shapes of head and foot

Figure 3.18 Radiation ratio of separate head and foot for horizontal motion

With regard to the sound radiation of the rail vibrating vertically, it can be seen in Figure 3.17 that the rail head and foot affect each other when they are put together (see dash-dot red lines). Also, the peaks are at lower frequencies for the simpler head and foot put together, compared with those for the normal rail head and foot together. Moreover, comparing the blue solid curve for the original rail and the red dash-dot curve for the rail head and rail foot together, it can be seen that including the rail web reduces the peak value at around 2 kHz, but enhances the value at the dip at around 1 kHz.

Figure 3.18 shows the corresponding results for the horizontal motion. As can be seen, the shapes of the head and foot have an influence on the sound radiation. Also, the sound radiation from the web has a large influence on the results as can be seen by comparing the blue curve for the original rail and the red dash-dot curve for just rail head and rail foot put together.

3.1.2.6 *Symmetric rail sections*

Figure 3.19 shows two symmetric rail sections in which the overall height of the rail remains unchanged. In Figure 3.19(a) the rail head is replicated at the bottom of the rail whereas in Figure 3.19(b) the foot is replicated at the top of the rail. Figure 3.20(a) shows the radiation ratio for these cases for vertical vibration. It can be seen that the peaks are shifted in these two cases. For the rail vibrating laterally, Figure 3.20(b), the sound radiation is again affected at low frequency although by less than for vertical motion, while the sound radiation is nearly the same at high frequency for the symmetric rails and the original rail.

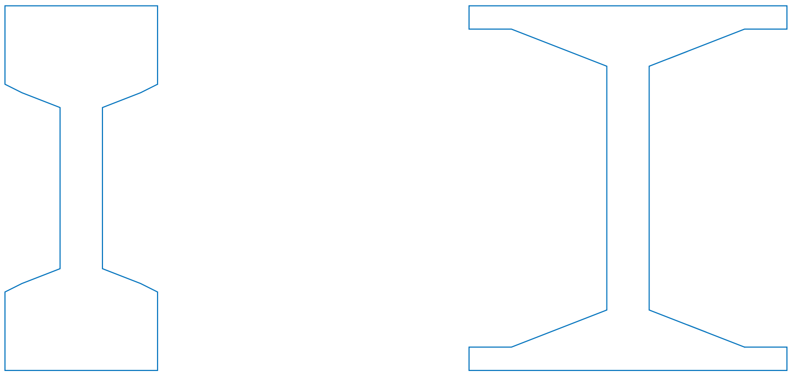

(a) Symmetric rail head (b) Symmetric rail foot

Figure 3.19 Modification of the rail with symmetric rail head and rail foot

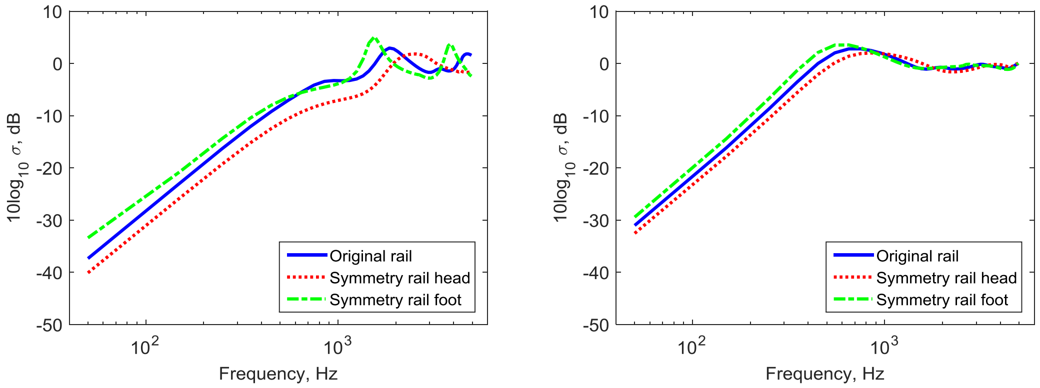

(a) Vertical motion (b) Horizontal motion

Figure 3.20 Sound radiation of the rail for symmetric sections

3.1.2.7 *Discussions of parameter modifications*

For the sound radiation of the rail vibrating vertically, it has been seen that the frequency of the first peak moves up or down compared with that of the original rail, when the modifications are made to the rail, apart from the cases with T sections where there are no larger peaks and dips. This has been attributed to changes in the centre-centre distance between the rail head and the rail foot. Figure 3.17(b) shows that the frequency of the first peak does not move compared with that for the original rail, when there is no rail web between the rail head and rail foot. Thus, in order to demonstrate the relationship between the peak frequencies and the centre-centre distance more clearly, the radiation ratio of two separate boxes, as presented in Figure 3.16(a), with different dimensions and various centre-centre distances are studied here. The detailed information on the boxes is shown in Table 3.1 with the frequencies of the first peak in the radiation ratio for each case.

Table 3.1 Comparison of various boxes with different centre-centre distances

Box dimensions (m)		Centre-centre differences between the two boxes (m)			
		0.07	0.15	0.3	0.6
Upper box	Lower box	Frequency at the first peak (Hz)			
0.03 × 0.03	0.03 × 0.03	4950	2250	1250	650
0.03 × 0.07	0.03 × 0.07	×	2850	1250	650
0.07 × 0.03	0.07 × 0.03	4650	1850	1150	650
0.15 × 0.03	0.15 × 0.03	4450	1650	850	550
0.07 × 0.07	0.07 × 0.07	×	2650	1150	650

The radiation ratio for vertical motion of the various different boxes is shown in Figure 3.21. The frequencies at the first peak in each case have been listed in Table 3.1. Taking the centre-centre distances between different boxes and normalising them by the wavelength at their corresponding peak frequencies, these are plotted against the centre-centre distances in Figure 3.22. The circles correspond to the different boxes with different centre-centre distances from Table 3.1. As can be seen clearly, the peak frequencies are generally related to the centre-centre distance and are less affected by the box sizes.

Figure 3.22 also shows the corresponding results for the different rails from the previous subsections. The marker '*' is for the original rail, whereas '+' represents the cases for the modifications made to the rail. It can be seen that the frequencies are not so obviously related to the centre-centre distance as those for the different boxes. This is because the dimensions of the rail are more complicated and other features also play a role. Nevertheless, it is clear that the first peak frequencies increase when the centre-centre distance between the rail head and the rail foot is reduced.

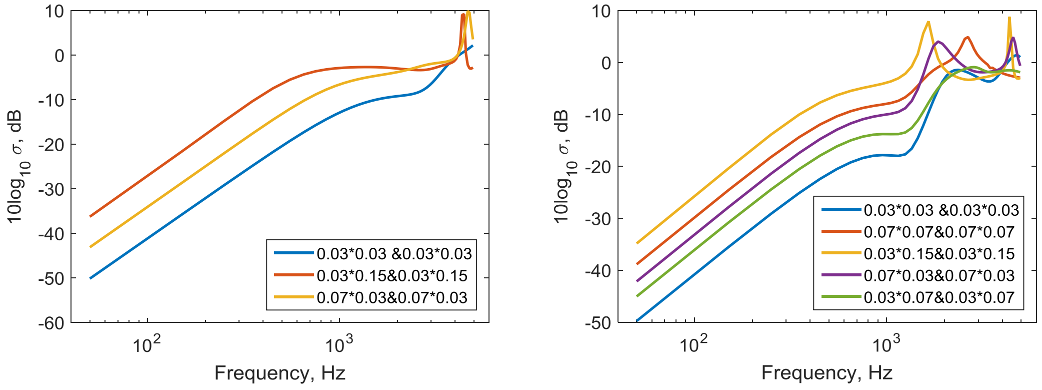

(a) 0.07 m (b) 0.15 m

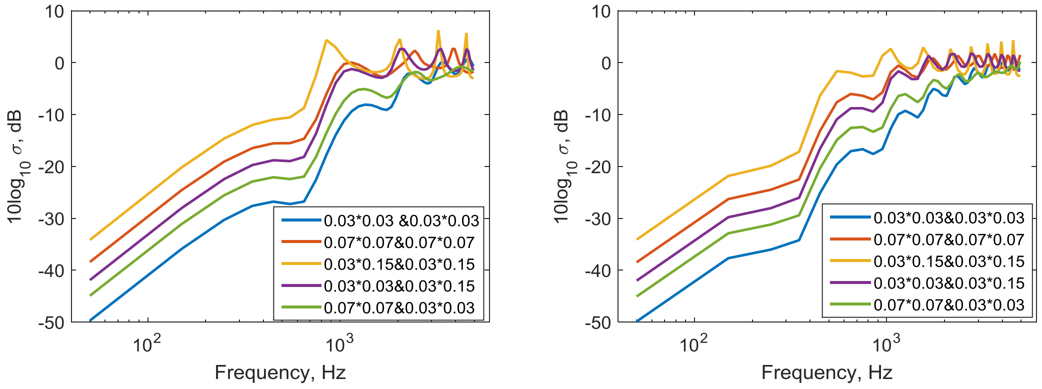

(c) 0.3 m (d) 0.6 m

Figure 3.21 Radiation ratio for various boxes with different central distances

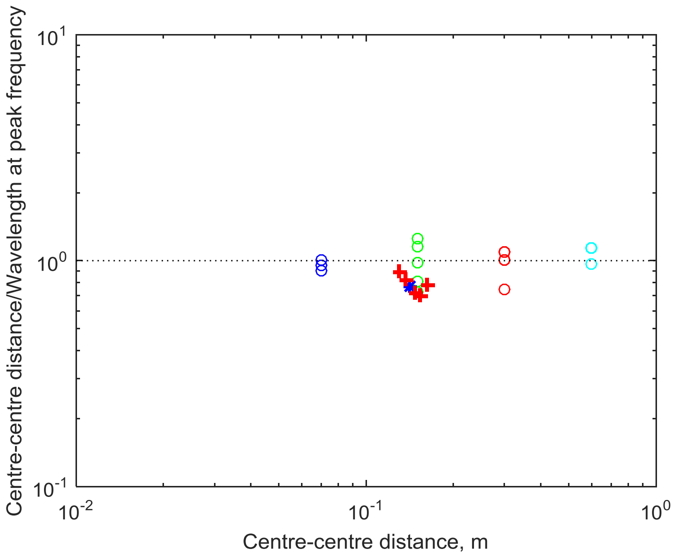

Figure 3.22 Effects of centre-centre distance on the peak frequency

3.2 Sound radiation of the rail with rigid ground

In practice, the rail is usually attached to a sleeper or track slab via a flexible pad, or it is located above the ballast. These two cases are shown schematically in Figure 3.23. For simplicity, the ground is initially considered to be acoustically hard; the case of an absorptive ground is considered in Section 3.3. For the case of a rail above the rigid surface, the sound radiation of the rail also depends on the distance of the base of the rail from the ground; three different heights will be considered: 20, 50 and 100 mm. In all cases the ground is assumed not to vibrate. In all the calculations it is again assumed that the rail vibrates with a rigid body motion either vertically or horizontally. Two methods can be used to represent the rigid ground: a half-space formulation and a rigid box. Further details of modelling the ground are given below.

(a) On rigid ground (b) Located above a rigid ground

Figure 3.23 2D BE models of a rail in proximity to the ground

3.2.1 Half-space model for the rigid ground

The first way of modelling the rigid ground is to use a half space Green's function as described in Chapter 2. The models used in the program have been shown in Figure 3.23. Again, a unit velocity is used to derive the boundary conditions for all the nodes when the rail vibrates vertically or horizontally.

Figure 3.24 shows the radiation ratio of the rail predicted for the two cases shown in Figure 3.23. Comparison is also made with the case of the rail in free space. When the rail is located above the rigid ground, the line dipole source will be reflected in the ground plane, so that for vertical motion a line quadrupole will be formed by the source and its image. This gives a slope proportional to f^5 (50 dB/decade) at low frequency. It can also be seen that a peak occurs at 850 Hz when the rail foot is 0.02 m above the ground. At this frequency the acoustic wavelength is equal to 0.4 m which is twice the distance between the centre of the rail and its image source; hence at this frequency the two dipoles reinforce. For larger distances between the rail and the ground the peak moves to lower frequencies and becomes less pronounced. For the model of the rail attached to the rigid ground, however, the bottom of the rail foot cannot radiate sound, which means that the top and the bottom areas of the rail section are not equal. A net line monopole is present and the radiation ratio increases proportional to f (10 dB/decade) at low frequency. At high frequencies the results are similar for all three cases. However, a sharp peak occurs when the distance between the rail foot and the ground is equal to half a wavelength (3.4 kHz for 50 mm separation, 1.7 kHz for 100 mm) as a narrow cavity is formed beneath the rail foot.

Figure 3.24(b) shows the corresponding results when the rail vibrates laterally. At high frequencies, the radiation ratio again tends to unity, although different peaks and dips occur for the three cases due to the constructive and destructive interference effects of the different parts of the rail. At low frequencies, below a transition frequency, the calculated radiation ratios in these three cases have the same slope, which is again proportional to f^3 (30 dB/decade). Therefore, when the rail moves laterally, the rail source can be treated as a line dipole for all three cases. However, in the presence of the rigid ground, the effective size of the dipole is increased, shifting the transition frequency downwards and increasing the radiation ratio at low frequencies. Note that the distance of 0.02 m will be used for the rest of simulation results.

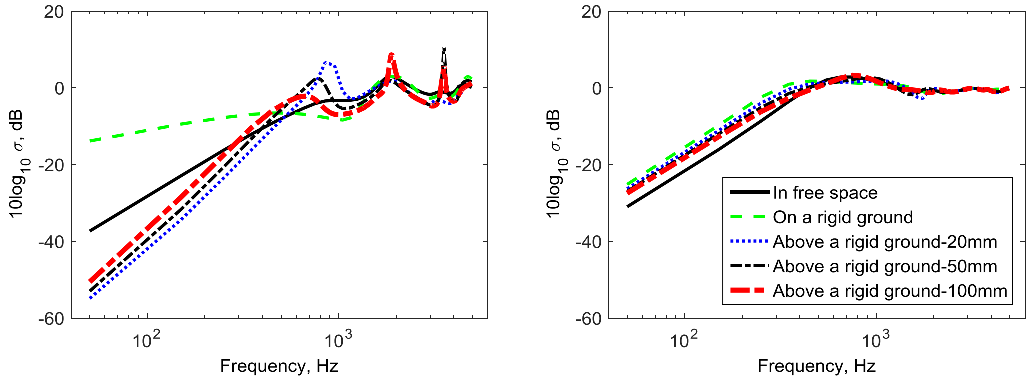

(a) Vertical motion (b) Lateral motion

Figure 3.24 Sound radiation of the rail calculated for free space and in presence of a rigid ground

Figure 3.25 shows results for the corresponding equivalent cylinders calculated for the rail vibrating laterally in three conditions. These are obtained by fitting the radiation for an oscillating cylinder (see Section 2.5.2) to the BEM results at low frequencies. As can be seen, for the radiation of the rail on a rigid ground, the equivalent cylinder has the largest radius with a value of 0.14 m. The equivalent cylinders have a radius of 0.125 m for the case of rail located above a rigid ground and 0.086 m for the rail in free space.

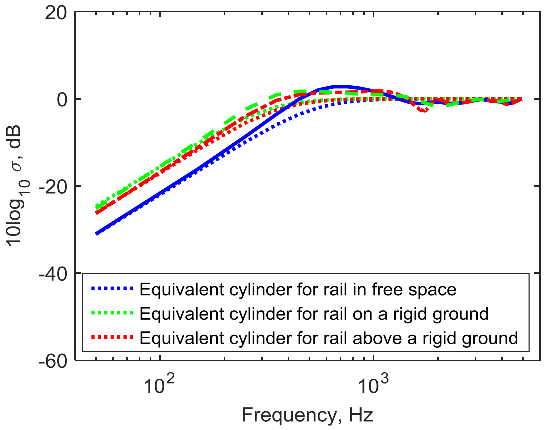

Figure 3.25 Equivalent cylinders for the sound radiation of rail vibrating laterally

3.2.2 Box models of the rigid ground

The half-space models for the rigid ground cannot be extended to an absorptive ground. In order to allow for an absorptive surface later, an alternative approach to modelling the ground is introduced here. A rigid box is included beneath the rail with dimensions chosen to be large enough that the edges have negligible effect on the results. This box has to be closed in the direct BEM method but apart from the top its surfaces are arbitrary. Box models are applied here to represent the ground geometry, as shown in Figure 3.26. The shaded area in the models indicates the surface which is later made absorptive.

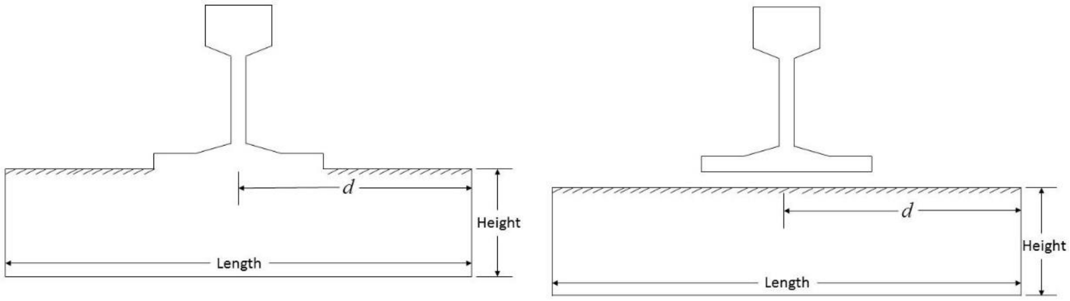

(a) Rail attached to the ground (b) Rail above the ground

Figure 3.26 Box models of the ground

In order to select the dimensions of the boxes, two main rules should be followed. The distance *d* indicated in Figure 3.26 should be larger than the largest wavelength multiplied by a coefficient, which should be at least 0.5, in the frequency range considered. This means the distance is determined by the lower frequency limit. The upper frequency limit will determine the element size, which should ideally be no more than one sixth of the smallest wavelength in the frequency range [97]. According to these rules, different box sizes will be used for different frequency ranges of interest. In the models established, two main frequency ranges are defined: the low frequency range of 50 ~ 500 Hz and the high frequency range of 250 ~ 5000 Hz. The dimensions and the element sizes used will be described in the next sections.

In order to verify the box models, comparisons are made in terms of the results for vertical and horizontal motions with those obtained by the half-space models in Section 3.2.1 for the two-dimensional rail attached to and above the rigid ground. Also, the procedure for establishing the models is explained. For example, the first step is to determine the approximate sizes of the box models at low and high frequencies according to the rules described above. Secondly, different element sizes are used based on the dimensions of the boxes. Thirdly, different CHIEF points are tested.

It should be pointed out that more detail is given here about establishing the box model for the rail vibrating vertically attached to the rigid ground. The establishment of box models for the other cases are the same as this, and therefore the detailed information is omitted.

3.2.2.1 *Rail attached to a rigid ground*

According to the frequency ranges mentioned above, the box model for the frequency range 50 ~ 500 Hz is dealt with first, followed by the model for the high frequency range.

The largest acoustic wavelength in the frequency range is 6.86 m at 50 Hz; therefore, the length of the box should be more than this value. Five different box models are tested here:

10 m × 1 m, 10 m × 3 m, 10 m × 5 m, 20 m × 1.05 m and 20 m × 3 m. As for the rail, two-noded linear boundary elements are used. Figure 3.27 shows results for these five different box models after the corresponding proper CHIEF points are applied in the models. These are shown as the sound power level difference in dB compared with the half-space model of Figure 3.24. It can be seen that the height of the box has little impact on the results in comparison with the width of the box. Taking the 10-metre-long box for example, the results for three heights of 1 m, 3 m and 5 m are similar at low frequencies, but the differences are greater at high frequencies. Comparing the variations of results from the lengths of 10 m and 20 m with the same height, it is clear that the length of 20 m has less difference in this frequency range. Therefore, in the frequency range of interest, the box with the size of 20 m × 1.05 m is ideal for the model, with errors less than 0.1 dB and this will be applied for the ground impedance geometry model later.

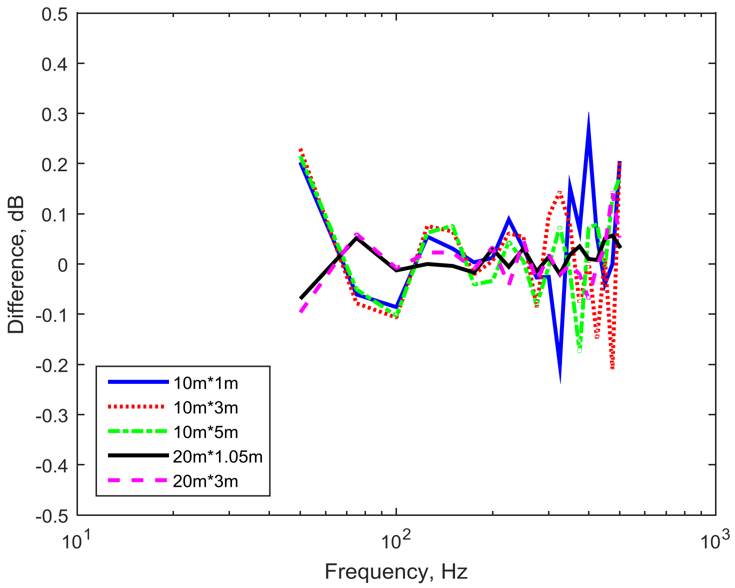

Figure 3.27 Results for different sizes of boxes at low frequency relative to half-space model

Figure 3.28 shows the results for two different element sizes, 0.1 m and 0.15 m. Here, the smallest wavelength in the frequency range of interest is 0.686 m at 500 Hz. Hence, 0.1 m corresponds to 1/6 of the smallest wavelength and 0.15 m to 1/4. As can be seen in Figure 3.28, the different element sizes have a small impact on the errors of the results. Thus, it is recommended that the element size should be no more than 1/6 of the wavelength. For the element size 0.15 m, this is satisfied below 380 Hz.

Figure 3.29 indicates further the influence of different CHIEF points on the accuracy of the numerical results. The different arrangements of CHIEF points are shown in Figure 3.30. It can be seen that the differences are larger when no CHIEF points are used. Considering both calculation time and least errors, 16 CHIEF points are used for the box model.

Figure 3.30 shows the four kinds of CHIEF point arrangement tested in Figure 3.29. Cp is an abbreviation for the CHIEF point.

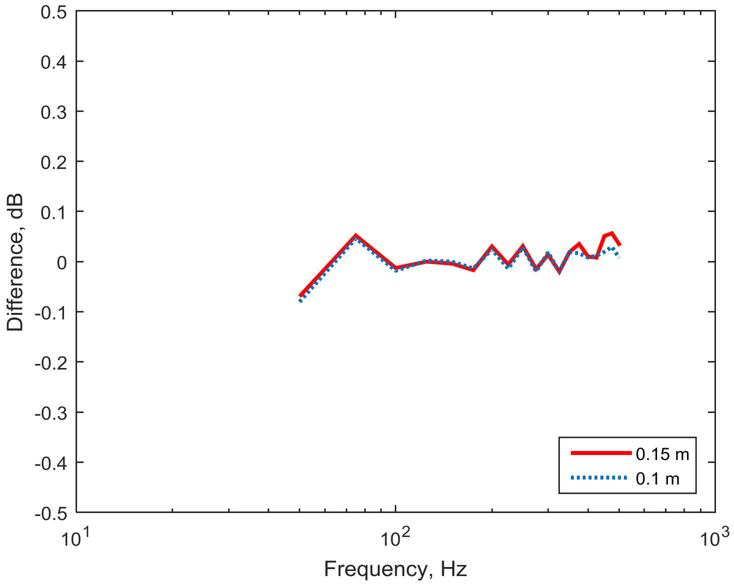

Figure 3.28 Results for different element sizes for low frequency box model relative to half-space model

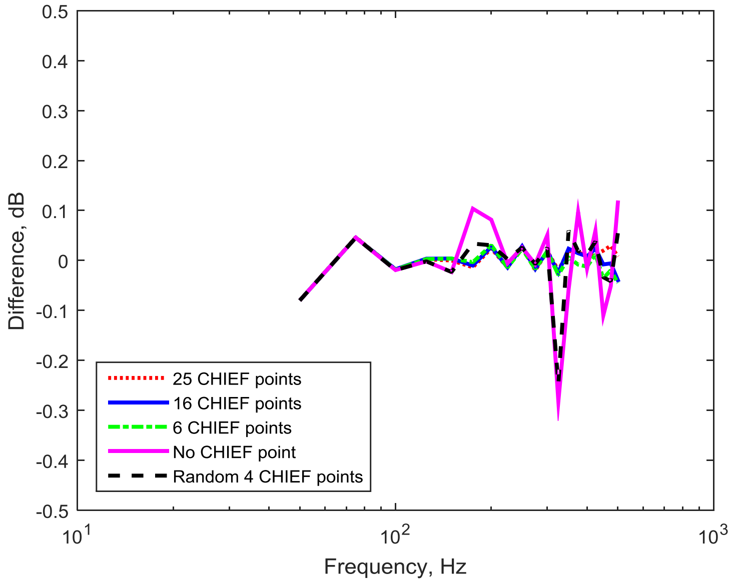

Figure 3.29 Results for different CHIEF points for low frequency box model relative half-space model

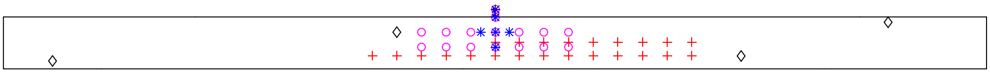

Figure 3.30 Different CHIEF point arrangements used (the rail is very small). +: 25 Cp; o: 16 Cp; ∗: 6 Cp; ◊: Random 4 Cp

With regard to the box model for high frequency, the process followed is similar to that at low frequency. Three different boxes are tested: 1 m × 0.1 m, 2 m × 0.1 m and 3 m × 0.1 m. In order to save the calculation time, the element size is 0.015 m, which is less than one quarter of the smallest wavelength (0.0686 m at 5000 Hz). In the frequency range 250 ~ 5000 Hz, it has been found that the box of dimensions 1 m × 0.1 m has errors less than 0.5 dB, whereas the box with dimensions of 2 m × 0.1 m has less than 0.3 dB. The errors for the box with 3 m × 0.1 m is less than 0.2 dB. Thus, this size of model is used for the ground geometry for the case of a rail attached to the ground at high frequency.

After these two boxes with different dimensions have been defined for the low and high frequency ranges, the next significant step is to deal with the values in the overlapping frequency range 250 ~ 500 Hz, where the two boxes give slightly different results. It is found that the differences between the numerical results from the two different box models in the overlapping frequency range are no more than 0.16 dB. Linear interpolation is applied to avoid a discontinuity. Figure 3.31 shows the sound radiation of the rail attached to the rigid ground using the two box models after interpolation. Comparison is also made with those obtained by using the half-space model. It can be seen they agree very well with each other.

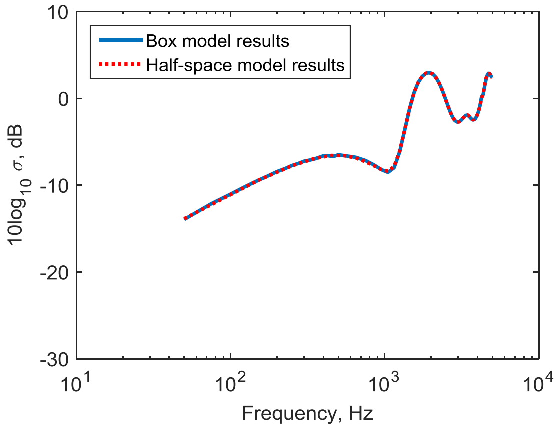

Figure 3.31 Radiation ratio of a rail vibrating vertically attached to rigid ground using two box models after interpolation

These two different box models for different frequency ranges are next used for a rail vibrating horizontally attached to the rigid ground. Again, the linear interpolation is used in the overlapping frequency region 250 ~ 500 Hz. Figure 3.32 compares the results with those from the half-space model. It is found that the differences between the box model results and symmetry model results are less than 0.25 dB. Thus, it can be concluded that the box dimensions used (20 m × 1.05 m at low frequency and 3 m × 0.1 m at high frequency) are sufficient for the accuracy of the numerical results.

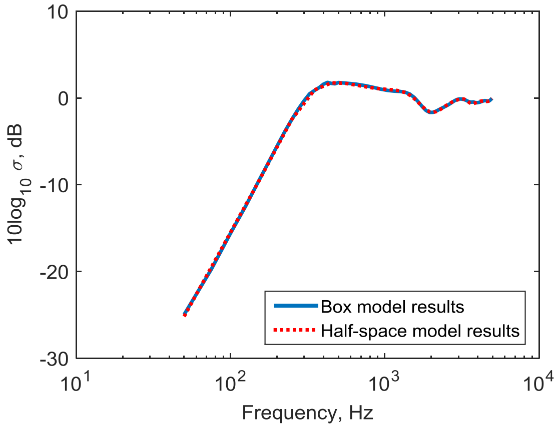

Figure 3.32 Radiation ratio of a rail vibrating laterally attached to rigid ground using two box models after interpolation

3.2.2.2 *Rail above a rigid ground*

In a similar way, box models are established for the case of the rail above the rigid ground. For the rail moving vertically in this case, including the ideal number of 16 CHIEF points, six different boxes are tested: 10 m × 1 m, 15 m × 1 m, 15 m × 3 m, 20 m × 1m, 20 m × 3 m, 20 m × 3 m. It is found in this case the height of the box has an impact on the results of the models, whereas the length of the box has little influence on the results. For example, when the box has the length of 20 m, the errors differ greatly for the boxes with the heights of 1 m, 3 m and 5 m. When the box has a constant height of 1 m, the results for the boxes with the lengths of 10 m, 15 m and 20 m change little especially at low frequencies. Comparing the results for different dimensions of boxes, the box with the size of 15 m × 3 m is employed at low frequency with errors no more than 0.7 dB. At high frequency the box size of 3 m × 0.1 m is used with errors less than 0.16 dB. For the horizontal motion of the rail above the rigid ground, the errors introduced by these two box models over the whole frequency range are less than 0.2 dB. Figure 3.33 shows the comparison of the box model results with those calculated by the half-space models. As it is shown, the results agree well with each other for both vertical and lateral motion of the rail above the rigid ground. Therefore, the box dimensions used (15 m

× 3 m at low frequency and 3 m × 0.1 m at high frequency) are confirmed as sufficient for the accuracy of the numerical results for the rail above a rigid ground.

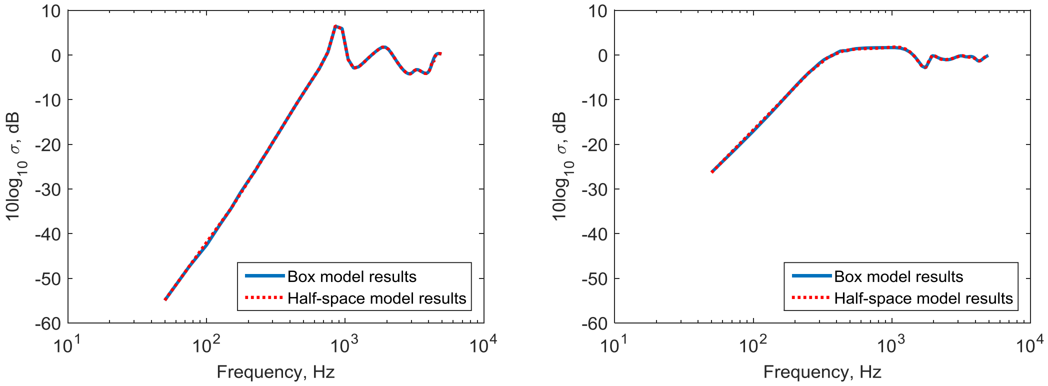

(a) Vertical motion (b) Lateral motion

Figure 3.33 Radiation ratio of rail above rigid ground using two box models after linear interpolation

The dimensions of box models used for corresponding cases of rail are summarised in Table 3.2.

Table 3.2 Dimensions of box models

Case of a rail	Box dimensions (m)	
	Low frequency	High frequency
Attached to a rigid ground	20 m × 1.05 m	3 m × 0.1 m
Above a rigid ground	15 m × 3 m	3 m × 0.1 m

3.3 Sound radiation of the rail with an absorptive ground

In practice, the ground is not rigid but has absorptive properties which can be described by the ground impedance, if the ground can be assumed to be locally reacting. The normalized ground impedance is given by

$$z_n' = z_n / \rho_0 c_0 \tag{3.1}$$

where z_n is the specific normal acoustic impedance of the ground, and $\rho_0 c_0$ is the specific acoustic impedance of air. The method of including impedance boundary conditions in the

BEM is described in Chapter 2 as well as the verification of the programming of the impedance in 2D and 3D.

3.3.1 Theory of the ground impedance model

The ground impedance depends on frequency. Also, different types of ground have different impedances, which can be estimated from their flow resistivity. More detailed information can be found in [100]. In order to obtain simulations close to practical situations, a ground impedance model should be applied.

For engineering outdoor sound propagation problems, a simple and widely used model for ground impedance is that originally proposed by Delany and Bazley [56] for porous materials. This model depends only on a single parameter, the effective flow resistivity, σ_e. For ground with an infinite thickness, its impedance can be given by

$$z_n' = 1 + 9.08\left(\frac{1000f}{\sigma_e}\right)^{-0.75} - 11.9i\left(\frac{1000f}{\sigma_e}\right)^{-0.73} \tag{3.2}$$

This form of the equation applies for flow resistivity in Pa.s/m^2.

The normal incidence absorption coefficient of the ground can then be deduced by using z_n', which is expresses as [101]

$$\alpha = \frac{4\operatorname{Re}(z_n')}{\left(\operatorname{Re}(z_n')+1\right)^2 + \left(\operatorname{Im}(z_n')\right)^2} \tag{3.3}$$

For ground, an equivalent value of flow resistivity can be selected by comparison with a measured impedance. Although more elaborate models are also available, e.g. [61], for simplicity in the present study the Delany and Bazley model is used with a range of values of flow resistivity in order to test the sensitivity of the results to variations in the ground impedance. Figure 3.34 shows the ground impedances obtained with this model for different values of flow resistivity for an infinitely thick layer of material. As can be seen, the normalised impedance $z_n/\rho_0 c_0$ tends to 1 as frequency increases, but at low frequency it has large real and (negative) imaginary parts. It can be expected that as the normalised impedance tends to 1, the surface will be able to absorb sound effectively.

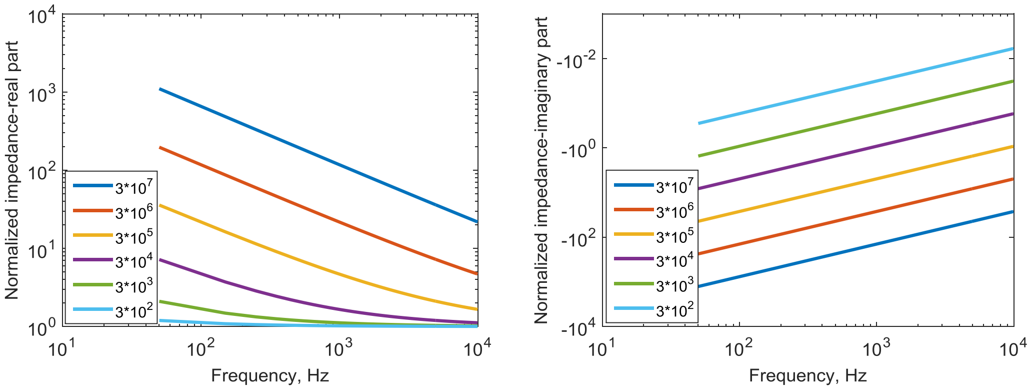

Figure 3.34 Normalised impedances used for the ground obtained using different values of flow resistivity in Pa.s/m^2

The corresponding normal incidence absorption coefficient for the ground with different flow resistivity is also obtained according to Equation (3.3), and demonstrated in Figure 3.35. As can be seen, the impedances obtained using the lower values of flow resistivity correspond to a more absorptive ground.

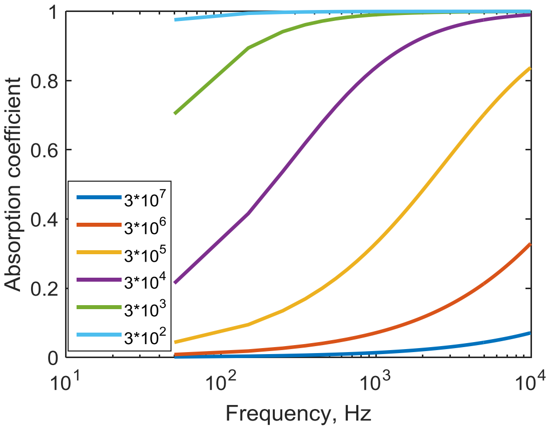

Figure 3.35 Normal incidence absorption coefficient for the ground surface with different values of flow resistivity in Pa.s/m^2

3.3.2 Effects of an absorptive ground on the sound radiation of the rail

This simple model for the impedance of the ground surface has been introduced into the boundary element simulations by using the box models in Table 3.2. Although the normal velocity is non-zero on the impedance boundary, this is not included in the calculation of the radiation ratio in the denominator of Equation (1.1). The result is thus based on the total radiated power normalised by the rail area and velocity.

Figure 3.36 and Figure 3.37 show the calculation results for the rail attached to the ground undergoing vertical and lateral motion. Results are shown for three values of flow resistivity for an infinite layer of absorptive material; the corresponding impedances were shown in Figure 3.34. As can be seen in Figure 3.36 and Figure 3.37, for both vertical and lateral motion, the rail will radiate less noise when attached to an absorptive ground than for a rigid ground, especially at low frequency. As the flow resistivity is lowered the sound radiation is reduced over a wider frequency range. At high frequency, the ground has little influence for the vertical motion, but reduces the sound from lateral motion by 2 dB.

Likewise, the sound radiation of the rail located 0.02 m above an absorptive ground is shown in Figure 3.38 and Figure 3.39. From Figure 3.39, for lateral motion, as the ground becomes more absorptive the rail radiates less noise over the whole frequency range, especially between 200 and 1000 Hz, where reductions of up to 10 dB are obtained. On the other hand, it can be seen in Figure 3.38 that for vertical motion a more absorptive ground causes the rail to radiate more noise at low frequency. This is because the absorptive ground partly destroys the cancellation present for a reflective ground which led to the formation of a quadrupole source. At higher frequency, however, particularly between 600 and 2000 Hz, the absorptive ground causes a reduction in the sound radiation of the rail.

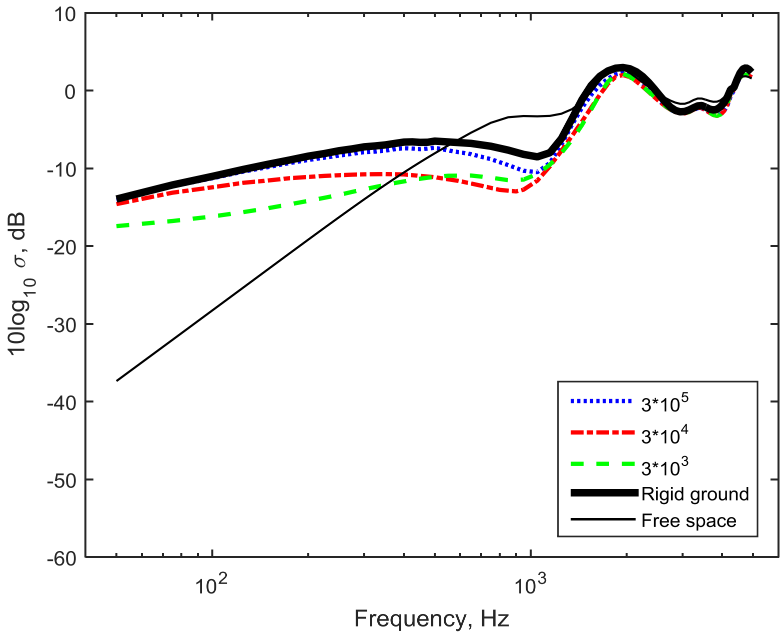

Figure 3.36 Sound radiation of the rail vibrating vertically attached to an absorptive ground with different values of flow resistivity in Pa.s/m^2

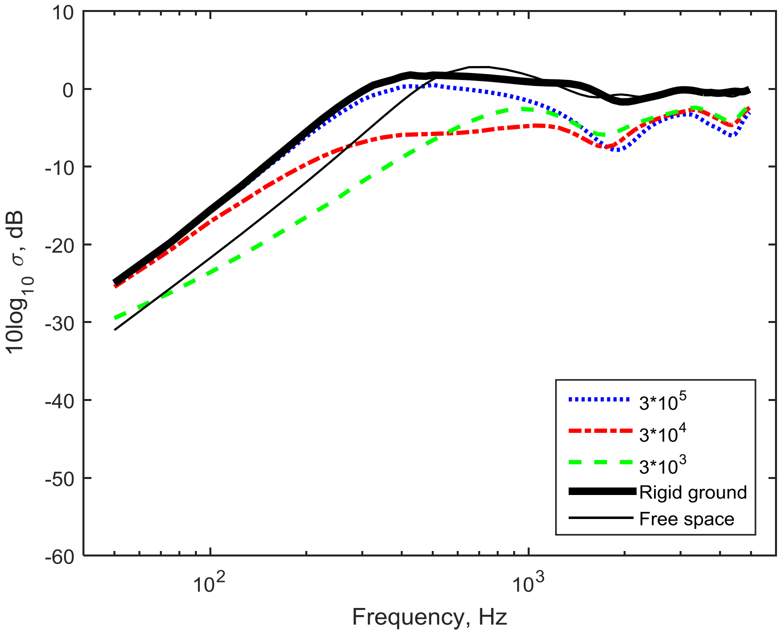

Figure 3.37 Sound radiation of the rail vibrating laterally attached to an absorptive ground with different values of flow resistivity in Pa.s/m^2

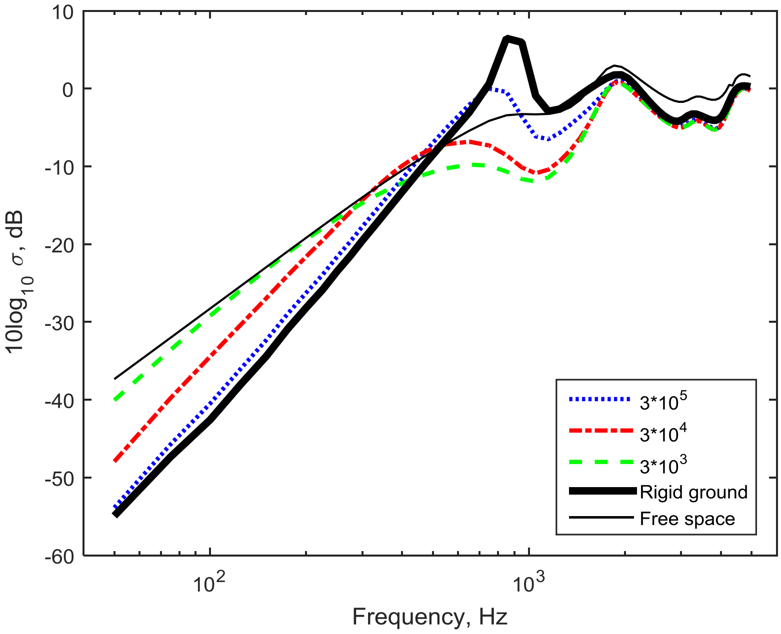

Figure 3.38 Sound radiation of the rail vibrating vertically above an absorptive ground with different values of flow resistivity in Pa.s/m^2

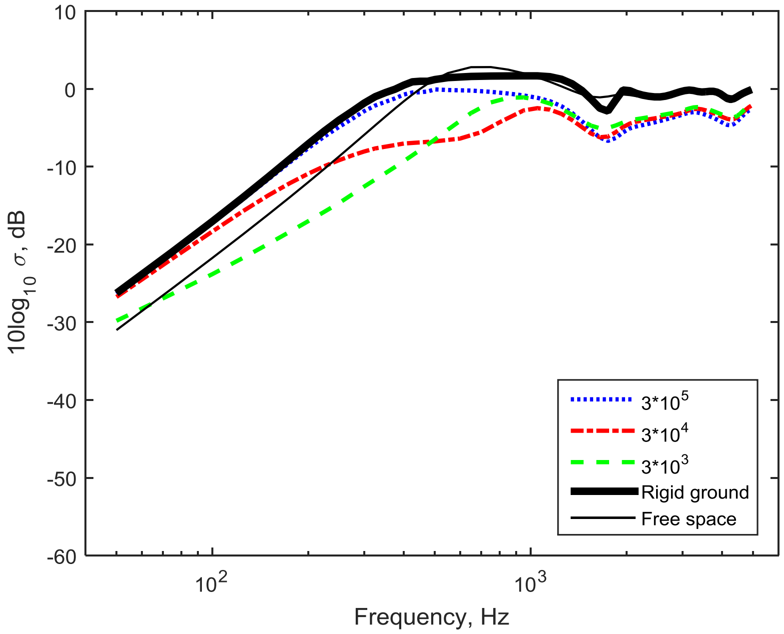

Figure 3.39 Sound radiation of the rail vibrating laterally above an absorptive ground with different values of flow resistivity in Pa.s/m^2

3.4 Sound radiation of the rail allowing for wave propagation

3.4.1 Wavenumbers in a rail

The numerical predictions described above are based on the rigid body motion of the rail cross-section in two dimensions, ignoring variation along the length of the rail. This assumption is valid if the wavenumber in the rail is much smaller than the wavenumber of sound in air [38]. It is no longer valid at low frequency, especially for an unsupported rail for which a critical frequency f_c exists, at which the wavenumber in the rail is equal to that in air.

In order to obtain the wavenumbers of a rail for different wave types, a 2.5D finite element (FE) method has been applied. WANDS [23], a 2.5D FE software, is used here to extract the wavenumber of an unsupported rail. This method allows the eigenvalue problem to be solved to obtain the frequencies corresponding to specified wavenumbers. Figure 3.40(a) presents these dispersion results for the unsupported rail vibrating in vertical/longitudinal waves, while Figure 3.40(b) gives the results for lateral/torsional waves. As can be seen, for both vertical and lateral motion, various wave types occur. More details of the various waves can be found in [18, 23]. The wave type with the highest wavenumber in each case is the bending wave. The second wave type in Figure 3.40(a) is the longitudinal wave, whereas the second wave type in Figure 3.40(b) is the torsional wave. The waves at higher frequencies correspond to higher order waves involving cross-section deformation. Also shown in Figure 3.40 is the acoustic wavenumber. The frequency at which this line crosses the bending wave curve can be identified as the critical frequency. For vertical motion this is 57 Hz; for lateral motion it is 141 Hz.

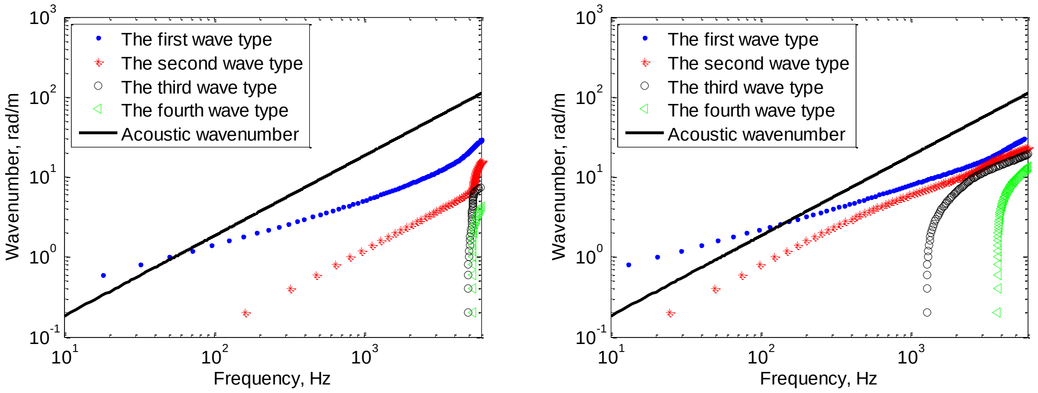

(a) Vertical/longitudinal motion (b) Lateral motion

Figure 3.40 Structural wavenumbers of waves in an unsupported rail

In practice the rail is supported on rail pads. A 2.5D FE model of a supported rail has therefore also been established in the WANDS software. The stiffness of the support per unit length is taken as 200 × 10^6 N/m^2 in the vertical direction and 77 × 10^6 N/m^2 in the lateral direction, corresponding to a soft rail pad. This model corresponds to a continuous support beneath the rail; no damping is included. Moreover the sleepers and ballast beneath the pad are neglected. Figure 3.41 presents the corresponding dispersion curves for both vertical and lateral motion. As can be seen, the various wave types in the supported rail cut on at a non-zero frequency. For the currently used values of support stiffness the vertical bending wave cuts on at 327 Hz and the lateral bending wave at 108 Hz. Compared with the results for the unsupported rail, there are no critical frequencies; all wavenumbers are lower than the corresponding acoustic wavenumber. For a stiffer support the cut-on frequencies would be higher and again there would be no critical frequency.

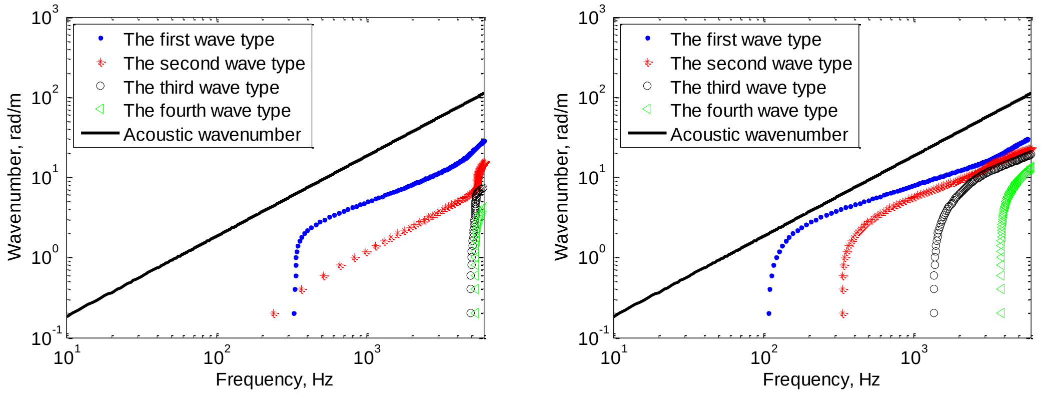

(a) Vertical/longitudinal motion (b) Lateral motion

Figure 3.41 Structural wavenumbers of waves in the supported rail

3.4.2 Corrections to sound radiation to allow for rail wavenumber

When a wave propagates along the rail, it has a wavenumber k_x as shown in Figure 3.40 and Figure 3.41. For an infinite rail with low decay rate, the corresponding sound field will share this wavenumber in the axial *x* direction along the rail. To find the radiation within the *y*-*z* plane, perpendicular to the rail, the wavenumber in this plane should therefore be modified to k_{2D} given by [27]

$$k_{2D} = \sqrt{k^2 - k_x^2} \tag{3.4}$$

where $k = \omega / c_0$ is the acoustic wavenumber at circular frequency ω.

The 2D BEM calculations presented in section 3.3 are based on the assumption that $k_x \ll k$ and hence $k_{2D} \approx k$. If $k_x \approx k$, however, $k_{2D} = 0$; the corresponding frequency is the critical frequency f_c. Below the critical frequency, k_{2D} is imaginary and there is no radiation.

For frequencies below around 2 kHz, the bending waves dominate in the structural vibration of the rail [1]. The wavenumber ratio k_{2D}/k for vertical and lateral bending waves in an unsupported rail up to 2 kHz is presented in Figure 3.42(a) based on the wavenumber k_x in Figure 3.40. The critical frequency is marked by the vertical dotted and dashed lines for vertical and lateral motion, respectively. As can be seen, the ratio k_{2D}/k increases from 0 at f_c and tends to 1 at high frequencies.

For the prediction of the radiation from the unsupported rail at low frequency, it is necessary to use a modified wavenumber in the 2D BE calculation, according to Equation (3.4). This modified wavenumber will be used in the boundary element model to calculate the rail radiation for frequencies above the critical frequency.

For a supported rail, however, no waves propagate below the cut-on frequency of waves in the rail. Below that frequency the waves are strongly attenuated and a point source model is more appropriate than the 2D line source model [1]. The corresponding wavenumber ratio for the supported rail is presented in Figure 3.42(b), which differs from the result for the unsupported rail at low frequencies. For the vertical motion, the wavenumber ratio is close to 1 over the whole frequency range above the cut-on frequency at 327 Hz. This means that the 2D numerical prediction for the sound radiation without wavenumber correction will be valid for the supported rail above the corresponding cut-on frequency.

For the lateral direction, as can be seen, the cut-on frequency of the supported rail is lower than for the vertical direction due to the lower stiffness of the rail pad and the lower bending stiffness of the rail. In addition to the value considered above, a higher rail pad stiffness of 225 MN/m^2 is also considered for the lateral direction. This gives a cut-on frequency of 173 Hz. The ratio k_{2D}/k has minimum values of 0.67 for the soft pad and 0.8 for the stiff one.

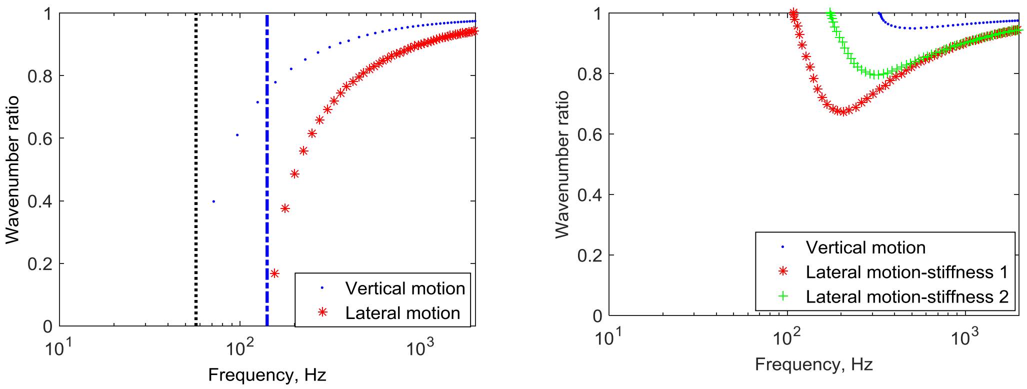

(a) Unsupported rail (b) Supported rail

Figure 3.42 Acoustic wavenumber ratio k_{2D}/k

Figure 3.43 shows a comparison of the 2D numerical prediction of the radiation ratio of an unsupported rail in close proximity to a rigid ground with and without the wavenumber correction ie, using k_{2D} in the BE calculations, when the rail vibrates rigidly. As can be seen, for both vertical and lateral motion, the corrected 2D prediction drops at low frequency, especially close to the corresponding critical frequency. At high frequency, however, the radiation ratios of the rail with and without correction are nearly the same as each other.

For the case of the free space boundary conditions, comparison is also made with the sound radiation of the supported rail in Figure 3.44. As can be seen, for vertical motion, the sound radiation from the supported rail is identical to that for the unsupported rail above the cut-on frequency of 327 Hz. Therefore, no corrections are necessary for the supported rail. For lateral motion, the sound radiation from the supported rail with both soft and stiff rail pads is shown in Figure 3.44(b). It can be seen that with the effect of the rail pad stiffness the radiation ratio increases at low frequency, tending to the 2D result, so the corrections found for the unsupported rail will not be applicable for the supported rail at low frequency. Between approximately 250 and 500 Hz the radiation ratio of the supported rail is up to 5.6 dB lower than that obtained using the 2D analysis for the soft pad and 3.5 dB for the stiffer pad. This means that the numerical correction required in the lateral case at low frequency depends on the rail pad stiffness. At higher frequency, however, the 2D numerical prediction without wavenumber correction can be used for the lateral motion of the supported rail.

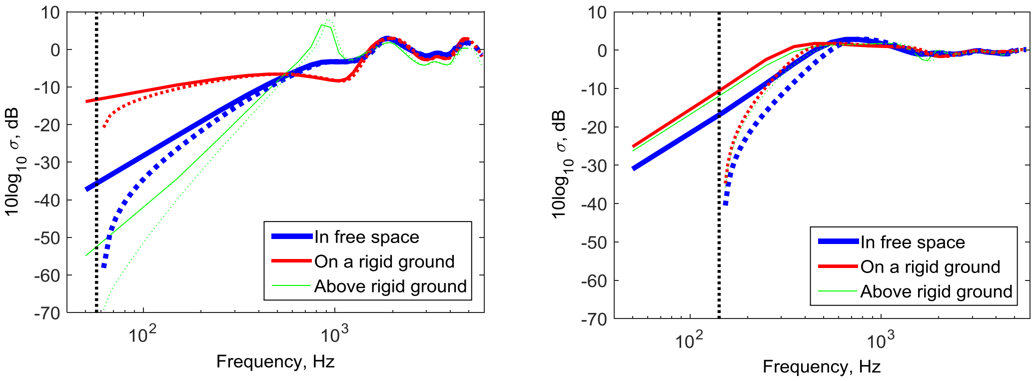

(a) Vertical motion (b) Lateral motion

Figure 3.43 Effects of a rigid ground on the sound radiation of the rail. Solid lines: 2D prediction; dotted lines: corrected 2D prediction

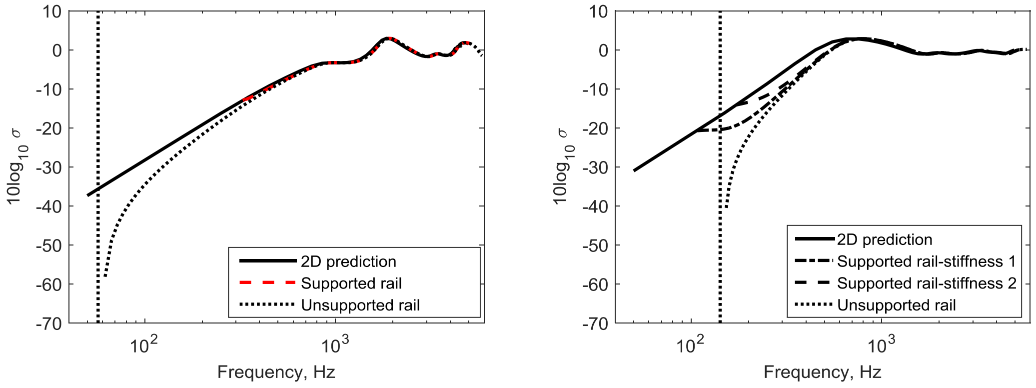

(a) Vertical motion (b) Lateral motion

Figure 3.44 Comparison of sound radiation of the supported rail and unsupported rail in free space

The corresponding results for the rail with an absorptive ground with a flow resistivity of 3×10^5 Pa.s/m^2 are shown in Figure 3.45 for the unsupported rail moving rigidly. Again, when the rail moves either vertically or laterally, the 2D numerical prediction overestimates the rail radiation at low frequency, but gives reasonable results at high frequency.

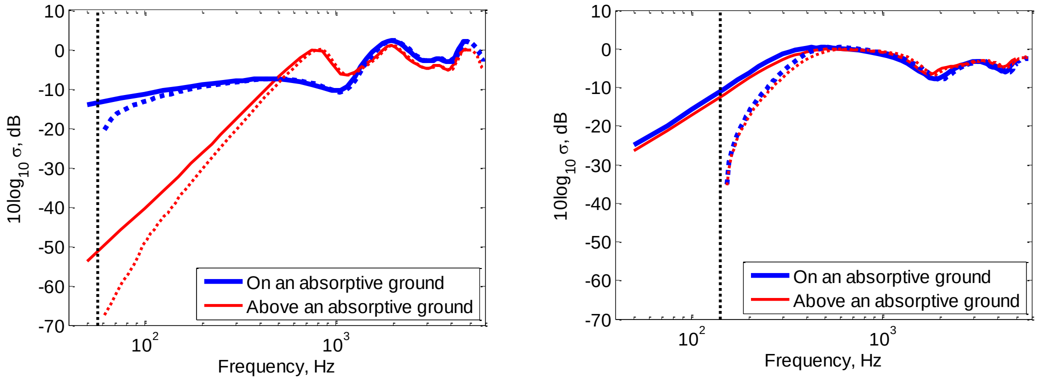

(a) Vertical motion (b) Lateral motion

Figure 3.45 Effects of an absorptive ground on the sound radiation of the rail. Solid lines: 2D prediction; dotted lines: corrected 2D prediction

3.5 Summary

Using a two-dimensional boundary element model, the sound radiation from a rail has been investigated in this chapter in terms of its radiation ratio. Initially, the sound radiation of a simplified rail section in free space is explored and this is shown to be a good approximation to the behaviour of a CEN60E1 rail. It has been shown that the sound radiation of a rail in free space has the behaviour of a line dipole when vibrating vertically or laterally. In order to understand more clearly how the rail radiates sound, the effects of geometrical parameter modifications of the rail on the sound radiation in free space have been studied. It is shown that the peak in the vertical radiation shifts when centre-centre distances between the head and foot change.

The sound radiation of the two-dimensional rail has also been studied in combination with a rigid ground. Both half-space models and box models are used for the rail attached to and above a rigid ground. For vertical motion above a rigid ground the rail radiation is changed to that of a line quadrupole, while it becomes a line monopole when the rail is attached to the rigid ground. For lateral vibration of the rail, however, the radiation follows the characteristics of a line dipole for both cases.

Next, if the rail is attached to an absorptive ground, the noise radiated by the rail reduces as the absorption is increased. For the rail above an absorptive ground, the ground absorption will reduce the sound radiated by lateral motion of the rail over the whole frequency range. For the rail vibrating vertically, however, at low frequency, an absorptive ground will make the rail radiate more noise than above a rigid ground but less than the rail in free space, whereas the rail radiation will be reduced at higher frequencies.

Corrections to the 2D predictions have been introduced to allow for the wavenumber in the rail, which for an unsupported rail are significant in the vicinity of the critical frequency of the rail. However, these corrections are not applicable for a supported rail in track. For vertical motion it is shown that no correction is required whereas for lateral motion, the specific correction required at low frequency will be less than that for an unsupported rail and will depend on the stiffness of the rail pad used in practice.

Chapter 4 Modelling of sleeper radiation

The sleepers supporting the rails of a railway track are an important source of noise at low frequencies. For the numerical prediction of the sleeper radiation, it is important to include their finite length as well as their width. The sound radiation is therefore modelled using a three-dimensional boundary element model.

In this chapter, the vibration of a single sleeper is explored first by using a wave approach in Section 4.1. Calculations of the sound radiation from a single sleeper, obtained by using the boundary element method in three dimensions (3D), are next presented in Section 4.2. Initially, the sleeper is considered to be located in free space. The ground is then introduced, first as a rigid reflecting surface and then as a partially absorptive surface, represented by its impedance, and the effects on the sound radiation are investigated. The fact that multiple sleepers are connected by the rails can lead to a change in their radiation efficiency [1]. This effect is explored in Section 4.3 for sleepers in close proximity to both a rigid and an absorptive ground. The work concentrates on concrete monobloc sleepers which are the most common form used in modern ballasted track.

4.1 Vibration of a single sleeper

Before considering the sound radiation from a sleeper, its vibrational behaviour is considered first. As described in Chapter 1, in track vibration models the rail is often represented as a beam and the sleepers by a layer of independent rigid bodies (masses) [15]. However, such an approach neglects the bending modes that monobloc sleepers exhibit in the frequency range of interest. A simple Timoshenko beam for a freely suspended sleeper was proposed by Grassie [45] who showed that it was sufficient to represent the sleeper as an equivalent uniform beam. This beam model was extended in [1, 46] to include the stiffness and damping of the ballast below the sleeper. In the model presented in [1], the sleeper was represented by a finite length, uniform Timoshenko beam with free ends and the ballast by a continuous elastic layer, the stiffness of which may be frequency-dependent. The forced response was studied using a wave approach. This approach is summarised here, followed by the results obtained for a typical concrete sleeper.

A sleeper, represented as a finite Timoshenko beam with a length L, is assumed to be supported on a continuous elastic foundation (representing the ballast), as shown in Figure 4.1. It is excited at y=0 by a point harmonic force $Fe^{i\omega t}$, where y is the coordinate along the sleeper. The motion of a Timoshenko beam is described by its deflection u and the rotation of the cross-section relative to the undeformed axis, φ. The equations of motion for a Timoshenko beam on an elastic foundation of stiffness s_p per unit length can be written as

$$GA\kappa \frac{\partial}{\partial y}\left(\varphi - \frac{\partial u}{\partial y}\right) + s_p u + m_r' \frac{\partial^2 u}{\partial t^2} = F\delta(y)e^{i\omega t} \tag{4.1}$$

$$GA\kappa \frac{\partial}{\partial y}\left(\varphi - \frac{\partial u}{\partial y}\right) - EI_s \frac{\partial^2 \varphi}{\partial y^2} + \rho I_s \frac{\partial^2 \varphi}{\partial t^2} = 0 \tag{4.2}$$

where ρ is the density, A is the cross-sectional area, $\kappa < 1$ is the shear coefficient and I_s is the second moment of area of the cross-section, E and G are the Young's modulus and the shear modulus, respectively, and m_r' is the mass per unit length of the beam.

When the sleeper is excited, various waves are generated, with wavenumbers, k_p (propagating waves) and k_e (evanescent waves), along with their negative counterparts. Above the cut-on frequency given by $\omega c_0 = \left(s_p / m_r'\right)^{1/2}$, k_p is close to real with a positive real part, whereas k_e is close to imaginary with a negative imaginary part. The beam response amplitude, u, at frequency ω can then be expressed as

$$u(y) = A_1 e^{ik_e y} + A_2 e^{ik_p y} + A_3 e^{-ik_e y} + A_4 e^{-ik_p y} \tag{4.3}$$

where A_n are the amplitudes of the various waves.

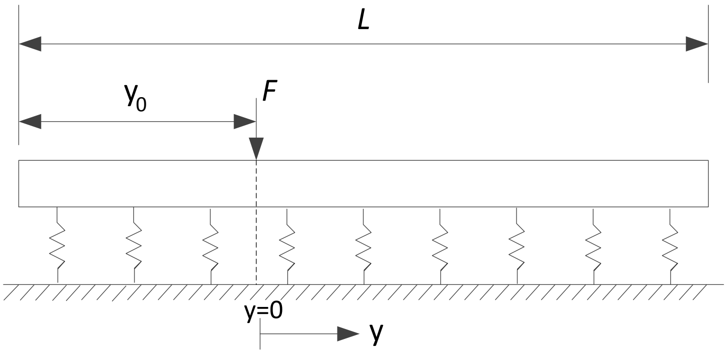

Figure 4.1 Sleeper represented as a finite Timoshenko beam on an elastic foundation (Side view)

The forced response can be determined directly by dividing the beam into two parts as follows:

$$u_-(y) = A_1 e^{ik_e y} + A_2 e^{ik_p y} + A_3 e^{-ik_e y} + A_4 e^{-ik_p y} \qquad \text{for } -y_0<y<0 \qquad (4.4)$$

$$u_+(y) = A_5 e^{ik_e y} + A_6 e^{ik_p y} + A_7 e^{-ik_e y} + A_8 e^{-ik_p y} \qquad \text{for } 0<y<L-y_0 \qquad (4.5)$$

Similarly, the rotation of the cross-section, φ, is given by

$$\varphi_-(y) = A_1 \psi_e e^{ik_e y} + A_2 \psi_p e^{ik_p y} + A_3 \psi_e e^{-ik_e y} + A_4 \psi_p e^{-ik_p y} \qquad \text{for } -y_0<y<0 \qquad (4.6)$$

$$\varphi_+(y) = A_5 \psi_e e^{ik_e y} + A_6 \psi_p e^{ik_p y} + A_7 \psi_e e^{-ik_e y} + A_8 \psi_p e^{-ik_p y} \qquad \text{for } 0<y<L-y_0 \qquad (4.7)$$

where ψ_n are the ratios φ/u in each wave given by $\psi_n = \dfrac{ik_n GA\kappa}{\rho I_s \omega_n^2 - GA\kappa - EI_s k_n^2}$.

The Equation (4.4) and Equation (4.5) can be solved by using the boundary conditions at each end of the beam. Specifically, the shear force is zero at each end:

$$GA\kappa\left(\frac{\partial u}{\partial y} - \varphi\right)\bigg|_{y=-y_0} = 0 \quad \text{and} \quad GA\kappa\left(\frac{\partial u}{\partial y} - \varphi\right)\bigg|_{y=L-y_0} = 0 \qquad (4.8)$$

The bending moment is also zero at each end:

$$EI_s \frac{\partial \varphi}{\partial y}\bigg|_{y=-y_0} = 0 \quad \text{and} \quad EI_s \frac{\partial \varphi}{\partial y}\bigg|_{y=L-y_0} = 0 \qquad (4.9)$$

Moreover, four more conditions exist at y=0: continuity of displacement, rotation, bending moment and equilibrium of forces. The corresponding expressions are

$$u_-(0) = u_+(0) \qquad (4.10)$$

$$\varphi_-(0) = \varphi_+(0) \qquad (4.11)$$

$$EI_s \frac{\partial \varphi_-}{\partial y}\bigg|_{y=0} = EI_s \frac{\partial \varphi_+}{\partial y}\bigg|_{y=0} \qquad (4.12)$$

$$GA\kappa\left(\frac{\partial u_-}{\partial y} - \varphi_-\right)\bigg|_{y=0} - GA\kappa\left(\frac{\partial u_+}{\partial y} - \varphi_+\right)\bigg|_{y=0} = F \qquad (4.13)$$

Equations (4.8)-(4.13) can be written in the form of 8 × 8 matrix equation and solved to give the wave amplitudes A_n. Then the response at a general position y can be obtained.

This model is applied to monobloc concrete sleepers, which usually have a cross-section similar to that shown in Figure 4.2 and a typical length of about 2.5 m. Often they are tapered slightly towards the middle but, for simplicity, this is neglected here and a constant cross-section as in Figure 4.2 is adopted, as used by Grassie [45]. This will also be convenient for comparison with experimental results in Chapter 6, where a 1:5 scale model of a sleeper with this cross-section has been used. The parameters used for this sleeper are listed in Table 4.1.

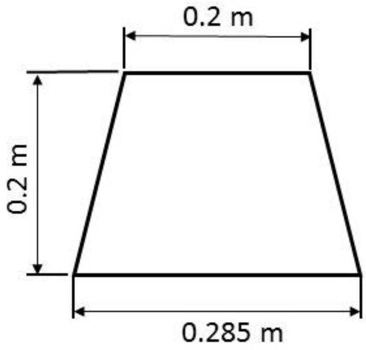

Figure 4.2 Cross-section of the idealised concrete sleeper

Table 4.1 Parameters used to describe a concrete sleeper

Young's modulus (N/m^2)	4.3×10^{10}
Shear modulus (N/m^2)	1.87×10^{10}
Poisson's ratio	0.15
Sleeper damping loss factor	0.01
Density (kg/m^3)	2500
Shear coefficient	0.83
Length, m	2.5
Excitation point, from one end (m)	0.5
Ballast damping loss factor	1.0

Figure 4.3 shows the calculated point mobility of the sleeper when it is excited at the rail seat (mobility is the velocity for a unit force expressed as a function of frequency). For the free sleeper a series of bending resonances can be seen; the first four modes have natural

frequencies of 134, 355, 663 and 1036 Hz. The amplitude of the first (and sixth) mode is much smaller than the adjacent modes as the rail seat is close to a nodal point. The displaced shape (operational deflection shape) at the first two of these frequencies is shown in Figure 4.4. This shows the real part of the response after normalisation to that at the excitation point ($y = 0$).

Figure 4.3 also shows the point mobility obtained in the presence of a frequency-dependent support stiffness, representing the ballast. This has a stiffness per unit length of 48 MN/m^2 up to 100 Hz, above which it increases linearly as shown Figure 4.5 [1]. This is chosen to represent measured stiffness values obtained in field tests [1]. The damping is given by a constant loss factor of 1.0. The fundamental resonance of the beam on the foundation stiffness can be seen in Figure 4.3 at about 100 Hz. Above this frequency the bending resonances can still be seen but with reduced amplitude and increased natural frequency compared with the free beam. Figure 4.6 shows the spatially averaged mobility; this is the square root of the mean square mobility. The sound radiation of a single sleeper can be predicted by using this mobility together with the radiation ratio.

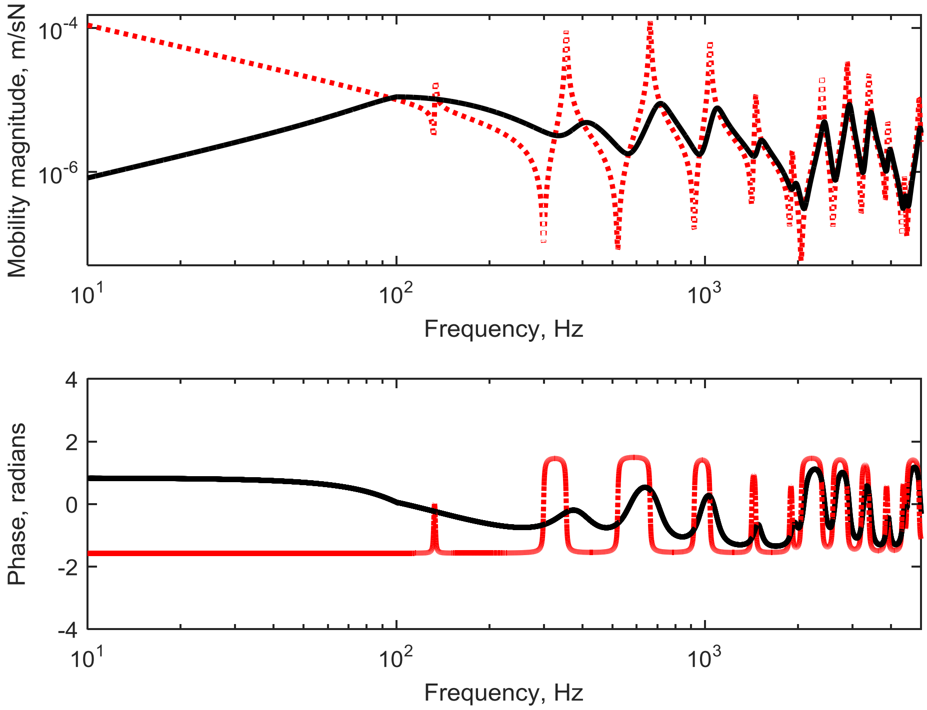

Figure 4.3 Point mobility of the concrete sleeper: ···, freely suspended sleeper; –, supported sleeper with frequency-dependent stiffness

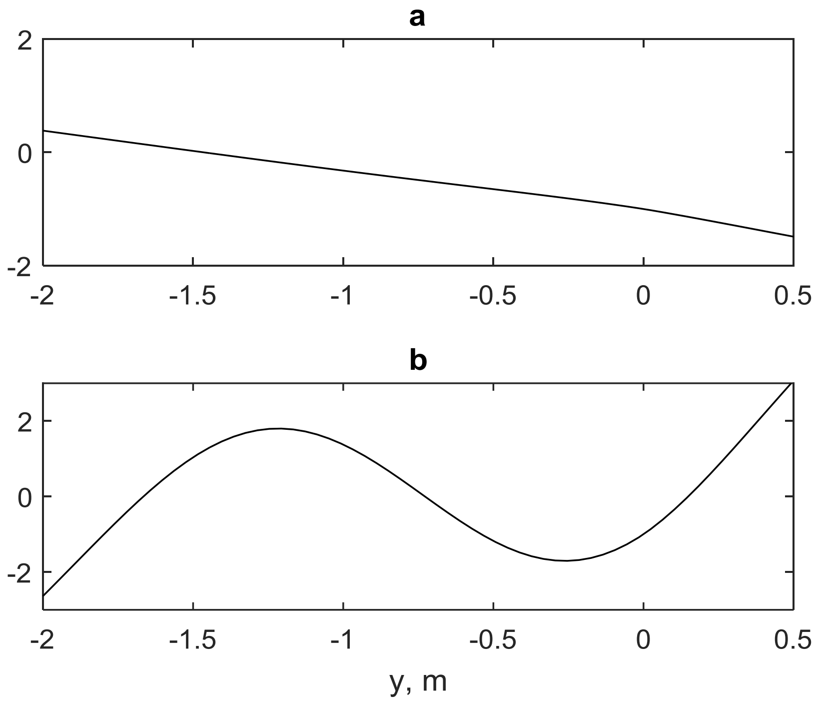

Figure 4.4 Displaced shape versus distance y along sleeper at frequencies corresponding to peaks of the mobility, normalised to response at excitation point. (a) 134 Hz, (b) 355 Hz

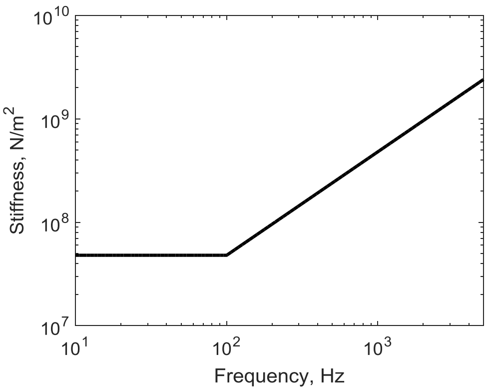

Figure 4.5 Assumed frequency-dependent ballast stiffness (per unit length)

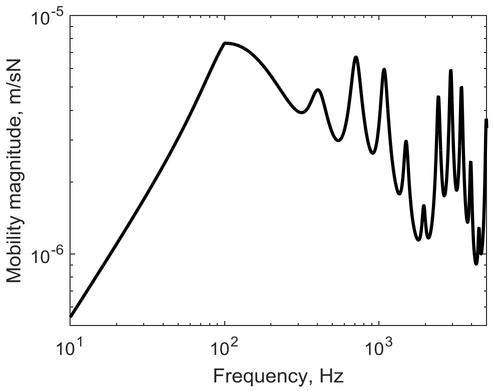

Figure 4.6 Spatially-averaged mobility of sleeper with this ballast stiffness

4.2 Sound radiation from a single sleeper

4.2.1 Radiation in free space

The sound radiation from a sleeper is modelled here using a three-dimensional boundary element model based on the direct BEM approach described in Chapter 2. For simplicity, the bending modes of the sleeper are ignored initially and a rigid body motion is assumed; the bending of the sleeper will be introduced in Section 4.2.2. A sleeper with the geometry given in Figure 4.2 is modelled first in free field by using 4-node linear quadrilateral boundary elements. The element size used is 0.04 m, which is less than ¼ of the smallest wavelength in the frequency range of interest (up to 2 kHz). Taking symmetry in two planes into account, the corresponding mesh for one quarter of the sleeper is shown in Figure 4.7(a). The planes shown are the corresponding symmetry planes in the model. The normal velocity is set equal to the component of the rigid body motion normal to the surface at each node when the sleeper vibrates vertically with unit amplitude.

Figure 4.7(b) presents the radiation ratio obtained. This is compared with the results for an infinitely long sleeper obtained using a two-dimensional (2D) boundary element model of the cross-section. The result from the 2D model has a slope of f^3 (30 dB/decade) at low frequency and tends to unity (0 dB) at high frequency. This behaviour corresponds to that of an oscillating cylinder of radius approximately 0.13 m and may be considered as a line dipole source.

It can be seen there is a clear difference between the 2D and 3D predictions below about 140 Hz, whereas at higher frequency their results are identical. From this it can be seen that the length of the sleeper is important at low frequencies, where the acoustic wavelength is large compared with the length (the acoustic wavelength is equal to 2.5 m at 136 Hz). The slope of the curve below 100 Hz is f^4 (40 dB/decade), corresponding to a point dipole. It follows the slope of f^3 in the intermediate frequency region between about 140 and 350 Hz before tending to unity (0 dB) as for the 2D model.

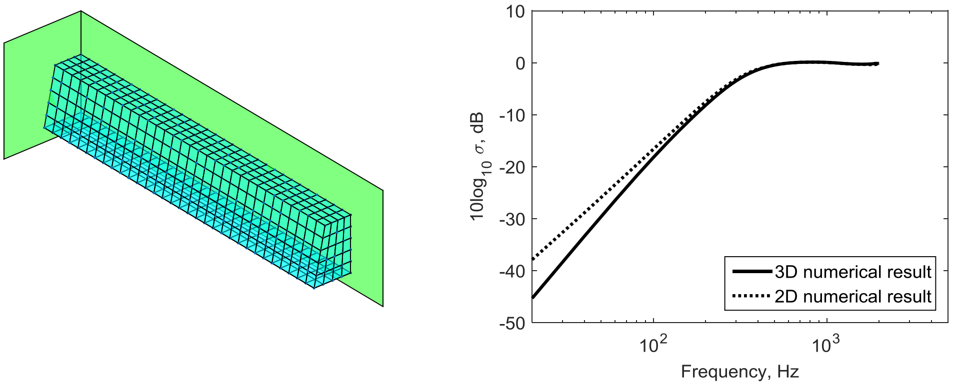

(a) Mesh of one quarter of the sleeper (b) Radiation ratio

Figure 4.7 A 2.5 m long sleeper in free space

4.2.2 Influence of a rigid ground on the sleeper radiation

The sleeper in free space is not a good representation of the actual situation; instead it is usually located on the ground in ballast. It is necessary, therefore, to investigate the effects of the presence of the ground on the sleeper radiation.

For simplicity, the ground is again assumed initially to be rigid. Only the upper surface of the sleeper is assumed to be visible, the remainder being fully embedded in the ground. It is assumed in this situation that only the top surface of the sleeper radiates sound, this being considered flush with the ground surface. The rigid ground can be represented in the boundary element model by an infinite reflecting (symmetry) plane as introduced in Chapter 2. There are now therefore three orthogonal symmetry planes in the model, with the rectangular upper surface of the sleeper represented by boundary elements, as shown in Figure 4.8(a). Figure 4.8(b) shows the radiation ratio of the sleeper in this case. Also, comparison is made with the result obtained by the Rayleigh integral method [95] which can be used when a source is flush with an infinite rigid surface and which will be used for convenience later. Details about implementing this method is in Appendix B. Very good agreement can be seen between the two numerical predictions. This confirms, again, the correctness of the BEM program. As the figure shows, the radiation ratio has a slope of f^2 at low frequency, corresponding to the behaviour of a point monopole. In this region the acoustic wavelength is larger than the sleeper length. Between about 80 Hz and 600 Hz, half the acoustic wavelength is smaller than the sleeper length but greater than its width, and the sleeper has the characteristic of a line monopole with a slope proportional to f. Above 800 Hz, the radiation ratio again tends to unity.

It is also possible to include the effects of the sleeper flexibility in this model. The beam model described in Section 4.1 for the supported sleeper is used to determine the vertical vibration amplitude at each position along the sleeper corresponding to the nodes of the BEM mesh for the full model of the sleeper. The force point is again considered to be at the rail seat. On each cross-section the normal velocity is determined from this vertical amplitude in the same way as before and import to the BE program. The results are shown in Figure 4.9 together with those for the case with rigid body motion. In addition, results are shown for rigid body motion of a sleeper with length 1.25 m. As can be seen, the flexible motion of the sleeper causes it to radiate less noise below about 400 Hz than the full rigid sleeper, whereas the results are the same at higher frequency. Below 100 Hz the sleeper vibration consists of a combination of vertical translation and rotation (see Figure 4.4), and the radiation ratio for the flexible sleeper corresponds closely to that for a rigid sleeper of reduced length 1.25 m. This therefore gives a better approximation of the behaviour of the flexible sleeper than the full length model with rigid motion. Therefore, in the remainder of this chapter the rigid half-sleeper of length 1.25 m will be used for simplicity.

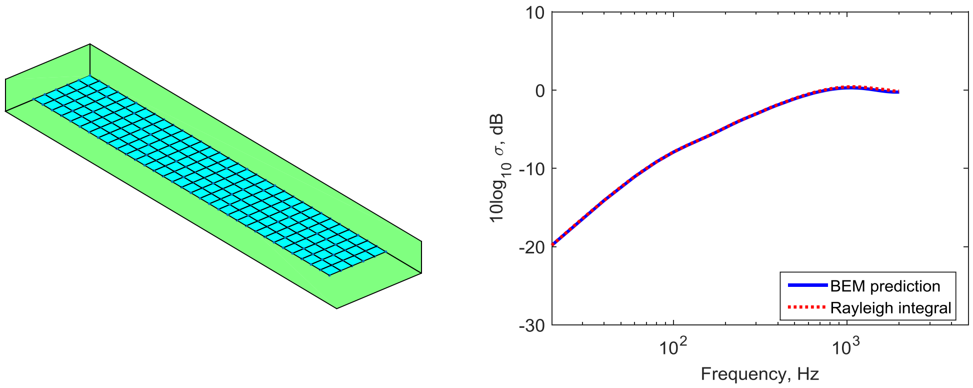

(a) Mesh of one quarter of upper surface of the sleeper

(b) Radiation ratio

Figure 4.8 A single sleeper with dimensions of 2.5 m × 0.2 m completely embedded in a rigid ground with an infinite reflection plane

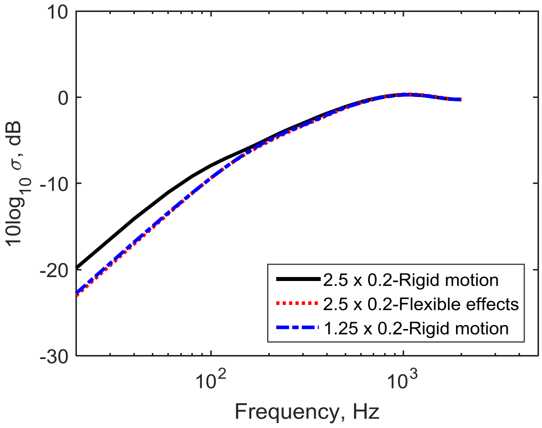

Figure 4.9 Radiation ratio of a single sleeper completely embedded in a rigid ground with an infinite reflection plane

4.2.3 Influence of ground absorption on the sleeper radiation

In practice, the ground is not rigid, but has absorptive properties, which can be described by its acoustic impedance. Therefore, the influence of an absorptive ground on the sleeper radiation is investigated here. Similar to the absorptive ground model used for the rail, the absorptive ground surface is introduced in the boundary element model by a finite box, the upper surface of which has the specified impedance based on the Delany-Bazley model [56]. The height of this box is limited to a single element layer and the symmetry plane is introduced beneath it. The ground region close to the sleeper, which is modelled with boundary elements, should be large enough to avoid the effects of diffraction at the edges of the ground box on the sleeper radiation.

As explained in the previous section, the sleeper has dimensions 1.25 m × 0.2 m and a rigid vertical motion. Before the impedance is added into the ground model, the appropriate dimensions of the ground box should be determined. The two main rules used to determine the parameters of the box models for a rigid ground for the rail in Chapter 3 can be applied here. Different box sizes will be again used for different frequency ranges of interest. For the BEM modelling of the sleeper, three main frequency ranges are defined: the low frequency range of 20 ~ 250 Hz, mid-frequency range of 200 ~ 1000 Hz, and the high frequency range of 800 ~2000 Hz. For the values in the overlapping frequency ranges of 200 ~ 250 Hz and 800 ~1000 Hz where the boxes give slightly different results (no more than 0.3 dB), the results are again smoothed by linear interpolation. The corresponding model information for the three frequency ranges is indicated in Table 4.2. The element sizes used here correspond to one quarter of the smallest wavelength in the corresponding frequency range. The box dimensions given are the full size of the models before dividing by 2 due to the use of symmetry planes.

Table 4.2 Element size and dimensions for the ground box

Frequency range (Hz)	Element size (m)	Box dimensions (m)
20~250	0.3	15 × 15 × 0.3
200~1000	0.075	4.25 × 4.25 × 0.075
800~2000	0.04	2 × 2 × 0.04

Next, the validity of the ground box dimensions is checked. For the sleeper completely embedded in a rigid ground with only its upper surface exposed, the results from the model including a ground box are compared with those obtained by using a ground represented by an infinite reflection plane in Section 4.2.2. One quarter of the corresponding model is shown in Figure 4.10(a), in which the highlighted region is the upper surface of the sleeper. Figure 4.10(b) shows the comparison between the results from the two models. As can be seen, the predictions from these two models agree very well with each other. It is found the maximum difference of the predicted radiation ratios from these two models are less than 0.15 dB.

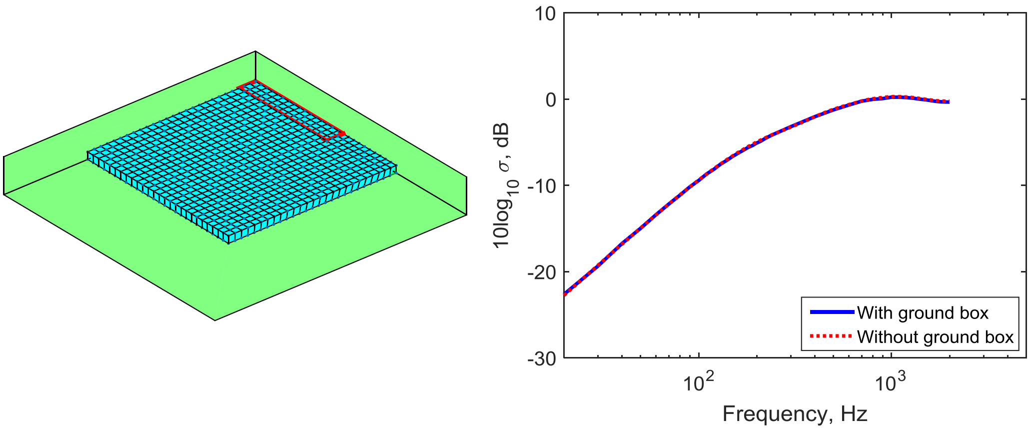

(a) Mesh of one quarter sleeper with ground (high frequency model)

(b) Radiation ratio

Figure 4.10 A single sleeper completely embedded in rigid ground with box model

Next three values of flow resistivity are used to generate the corresponding impedance for the ground based on Delany and Bazley model [56]. This simple model for the impedance of the ground surface has been introduced into the boundary element simulations, and the results are compared with those for the rigid ground. Figure 4.11 shows the radiation ratio and also the level difference compared with the result for a rigid ground. As in Chapter 3 for the rail, although the normal velocity is non-zero on the impedance boundary, this is not included in the calculation of the radiation ratio in the denominator of Equation (1.1). The result is thus based on the sleeper area and velocity. It can be seen that the results for the larger value of flow resistivity, 3×10^5 Pa.s/m^2, are quite close to the extreme case of a rigid ground. This means that the sound will mostly be reflected when the impedance is large. For lower values of flow resistivity, the ground is more absorptive, and the sleeper radiates less noise. As can be seen, the radiation ratio is up to 6 dB lower for the ground with a flow resistivity of 3×10^3 Pa.s/m^2. Nevertheless, at very low frequency the radiation ratio tends to that of the rigid ground as the corresponding impedance differs from that of air even for this low value of flow resistivity (see Figure 3.34); there is thus a transition between the features of a rigid material and an absorptive material.

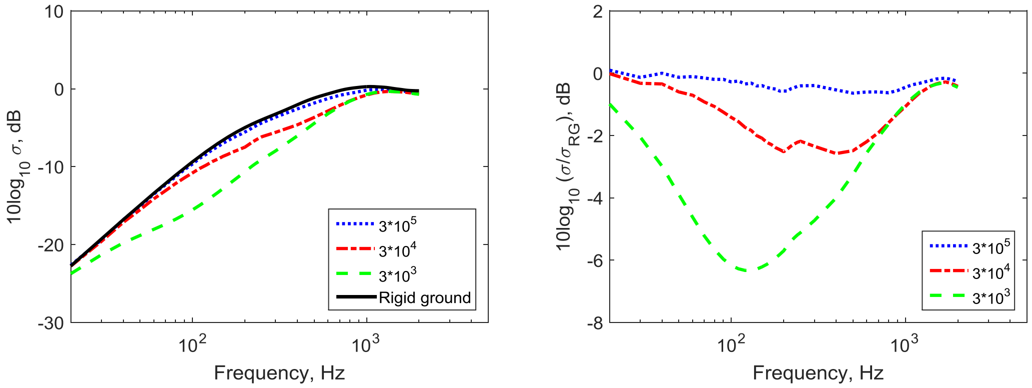

Figure 4.11 Radiation ratio of single sleeper completely embedded in an absorptive ground with different values of flow resistivity

4.2.4 Sound radiation of a single sleeper resting on the ground

A model in which the sleeper, with dimensions 1.25 m × 0.2 m, is resting on a rigid ground is considered here. An infinite reflection plane is again used for the rigid ground. One quarter of the sleeper is modelled, as can be seen in Figure 4.12(a). Figure 4.12(b) presents the corresponding sleeper radiation ratio and a comparison with that of an individual sleeper completely embedded in rigid ground. It can be seen that it again has the acoustic characteristic of a monopole at low frequency. Also, it radiates about 2 dB more noise than the sleeper completely embedded in the rigid ground below 280 Hz, because the projected area is greater due to its tapered shape.

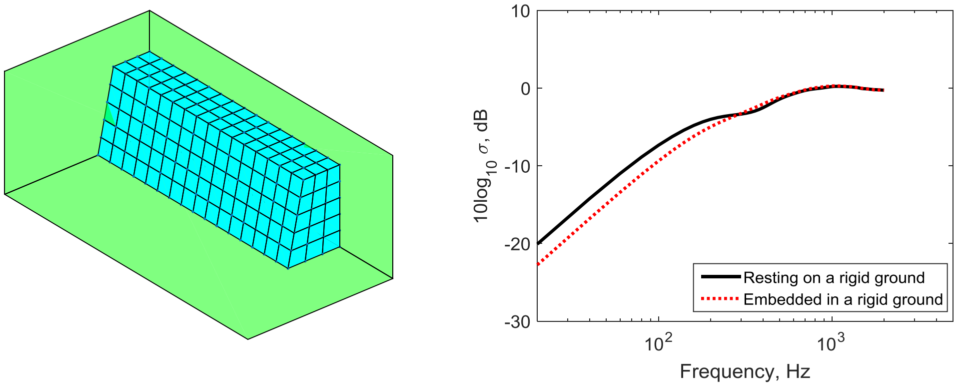

(a) Mesh of one quarter of sleeper resting on rigid ground

(b) Radiation ratio

Figure 4.12 A single sleeper fully resting on a rigid ground with an infinite reflection plane

The effects of the ground absorption on the sleeper radiation are also investigated in this case, and compared with the results for the rigid ground. Figure 4.13 presents the sound radiation ratio of the sleeper resting on the absorptive ground. The results are quite similar to those in Figure 4.11. As before the sleeper radiates about 6 dB less noise compared with that for the sleeper with a rigid ground, when the ground is absorptive with a low flow resistivity.

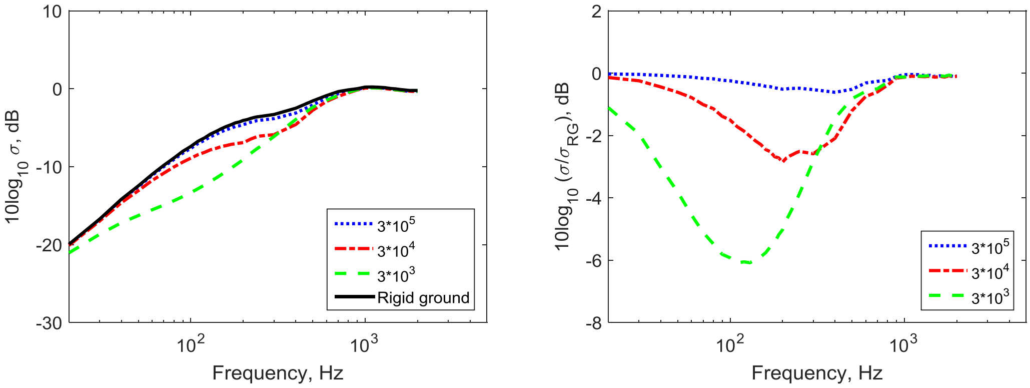

Figure 4.13 Radiation ratio of a single sleeper resting on an absorptive ground with different values of flow resistivity

4.3 Sound radiation from multiple sleepers

4.3.1 Vibration of multiple sleepers

Up to now the radiation from a single sleeper has been considered. In reality, the sleepers are connected to the rails through fasteners and rail pads. When the rail is excited at a point, vibration is transmitted along the rail over a distance that depends on the frequency [1]. At low frequency, due to the track support, wave propagation is inhibited and the rail vibration consists of a near-field region of a certain size. At higher frequency, waves propagate along the rail with a low rate of attenuation; the cut-on frequency of this wave propagation depends on the support stiffness, in particular that of the railpad. The ratio of the sleeper vibration to that of the rail above it is frequency-dependent but is independent of the attenuation of wave propagation in the rail [1]. Thus, if the rail vibrates within a certain distance of the excitation point, all the sleepers within that region also vibrate. The relative amplitude and phase of the various sleepers depends on the corresponding rail vibration. At low frequency, where the acoustic wavelength is large compared with the distance between sleepers, it is expected that multiple sleepers will form a composite source with a modified radiation ratio compared with that for a single sleeper. Initial results were presented in [1] which have been extended here.

To investigate the sound radiation from multiple sleepers, a track vibration model is first used to determine the relative amplitude and phase of the various sleepers. The model used represents the vertical vibration of the track by a continuously supported Timoshenko beam [1, 8], where the sleepers in the track are represented by a layer of mass. Although the discrete sleeper spacing is neglected in this model, the track response is reliably predicted apart from the pinned-pinned frequency region around 1 kHz and the vibration of the sleeper layer at the corresponding distances from the excitation point can be taken as representative of the corresponding sleeper vibration amplitudes. The parameters used for the track are listed in Table 4.3, which represent a track with CEN60E1 rails, concrete monobloc sleepers and relatively soft railpads.

When the force is applied to the rail above a sleeper, as shown in Figure 4.14 the calculated amplitudes and phases of several sleepers are as presented in Figure 4.15 relative to the vibration of sleeper 1, which is directly beneath the excitation point. As can be seen, below about 300 Hz the vibration amplitude of sleeper 2, at 0.6 m away from the excitation point, can be approximated as being half that of sleeper 1 at 0 m, and they are roughly in phase. Subsequent sleepers have a much smaller vibration amplitude in this low frequency region, which is characterised by near-field behaviour in the rail. The vibration ratios become closer to unity and obvious phase changes occur above about 400 Hz, which is the region in which bending waves propagate in the rail. For a track with stiffer railpads, 500 MN/m, for example, the corresponding results are shown in Figure 4.16. As can be seen, the low frequency near-field behaviour of the rail is similar to the case in Figure 4.15 but extends up to a higher frequency (600 Hz).

Table 4.3 Parameters used for vertical motion of the track in the calculations

Rail bending stiffness	6.42 MNm^2
Rail mass per unit length	60 kg/m
Rail shear stiffness	6.17×10^8 N
Rail shear parameter	0.4
Rail rotational inertia	0.24 kgm
Pad stiffness	120 MN/m
Pad damping loss factor	0.2
Sleeper mass (half)	150 kg
Sleeper spacing	0.6 m
Ballast stiffness	100 MN/m
Ballast loss factor	1.0

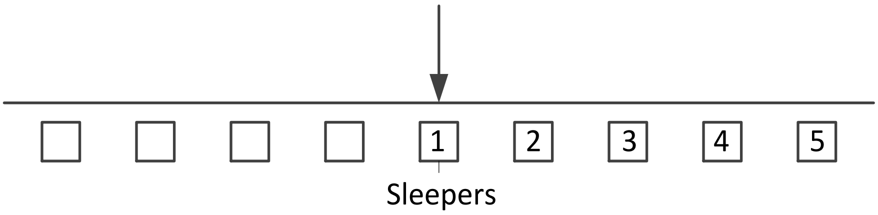

Figure 4.14 Side view of the excited sleepers: the force is above the sleeper

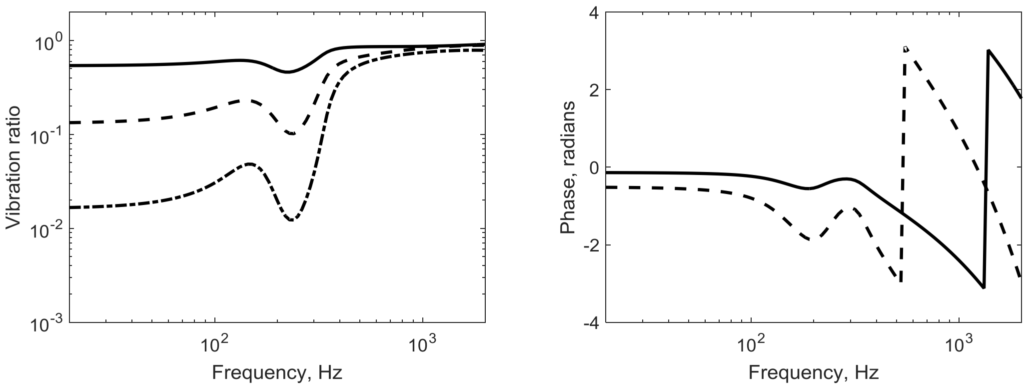

Figure 4.15 Vibration of successive sleepers relative to sleeper 1 at 0 m. –, sleeper 2 at 0.6 m; – – –, sleeper 3 at 1.2 m; – · – ·, sleeper 6 at 3.0 m (amplitude only)

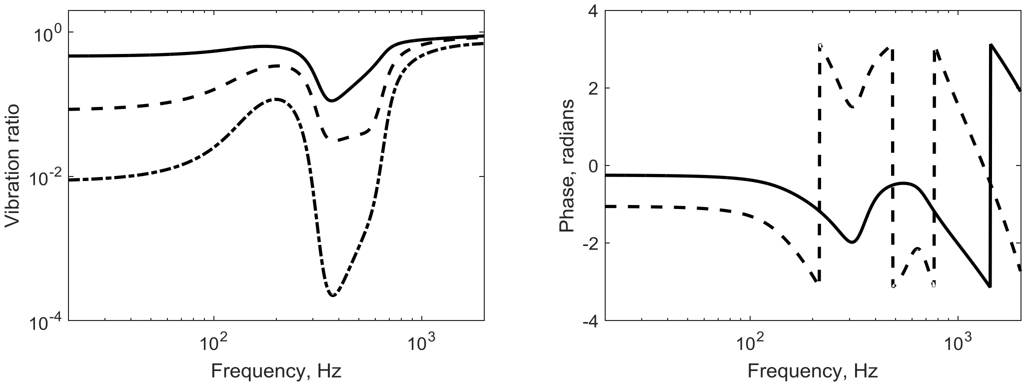

Figure 4.16 Vibration of successive sleepers with stiffer railpads (500 MN/m) relative to sleeper 1 at 0 m. –, sleeper 2 at 0.6 m; – – –, sleeper 3 at 1.2 m; – · – ·, sleeper 6 at 3.0 m (amplitude only)

Next the force is applied to the position mid-way between two sleepers, as shown in Figure 4.17. According to the model in [1, 8], the calculated amplitudes and phases of several sleepers are presented in Figure 4.18 relative to the vibration of sleeper 1, which is now half of the sleeper-sleeper distance from the excitation point. As can be seen, the vibration ratios of the consecutive sleepers are smaller compared with Figure 4.15. However, the trend for both vibration ratio and phase is nearly the same as that in Figure 4.15.

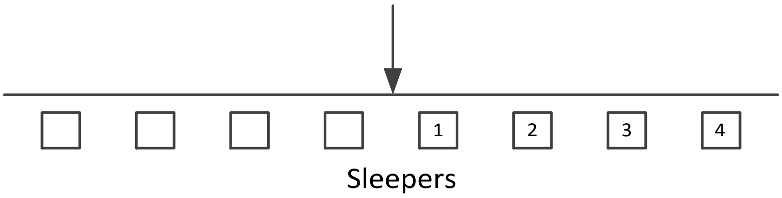

Figure 4.17 Side view of the excited sleepers: the force is between two sleepers

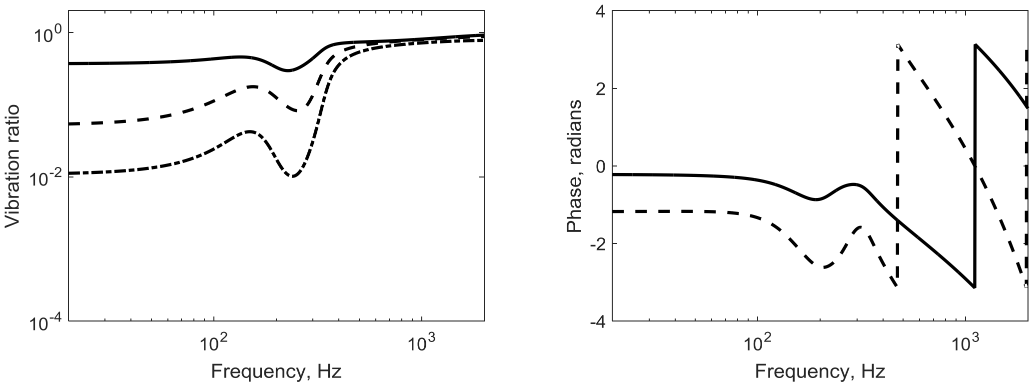

Figure 4.18 Vibration of successive sleepers relative to sleeper 1 at 0.3 m. –, sleeper 2 at 0.9 m; – – –, sleeper 3 at 1.5 m; – · – ·, sleeper 6 at 3.3 m (amplitude only)

4.3.2 Sound radiation of multiple sleepers in rigid ground

The sound radiation from multiple sleepers is calculated first when the sleepers are embedded in a rigid ground. For convenience the Rayleigh integral method has been used as this more readily allows larger models to be considered. In each case the upper surface of the sleepers is assumed to be flush with the rigid ground. The sleepers in the radiation model have a length of 1.25 m and are assigned rigid vertical motion as before.

When three sleepers are excited by the force applied to the rail above a sleeper, as presented in Figure 4.19(a), the sound radiation obtained for these three sleepers is shown in Figure 4.19(b). The outer sleepers are assigned a vibration amplitude of half that of the central one and all are assumed to be vibrating in phase; this corresponds to the low frequency behaviour seen in Figure 4.15. To show the influence of the vibration ratio, results are also shown for three sleepers with equal vibration amplitude; these are very similar to the results obtained for a vibration ratio of 0.5. For comparison the radiation ratio of an individual sleeper in a rigid baffle is also shown (from Figure 4.8). As can be seen, all the results tend to unity at high frequencies. At low frequencies, however, the radiation ratio of the three sleepers is higher than that of the single sleeper by up to 5 dB, indicating that they will radiate more noise than if they were considered separately. A dip is found at around 400 Hz, and a peak occurs at 570 Hz, where the acoustic wavelength equals 0.6 m, the sleeper separation distance.

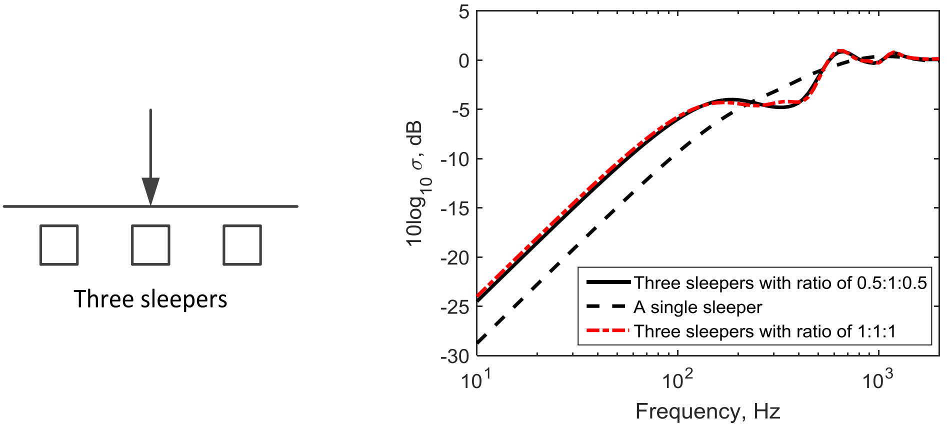

(a) Sketch of three sleepers (b) Radiation ratio of sleepers

Figure 4.19 Three sleepers set in a rigid baffle

Figure 4.20 shows the increase in radiation ratio that occurs when multiple sleepers are considered relative to the result for a single sleeper. Here, results are shown for three, five and nine sleepers, each with identical vibration amplitudes. It can be seen that the results rise to a constant value at low frequency. For three sleepers this is an increase in radiation ratio of 5 dB for frequencies below about 100 Hz. As the number of sleepers increases, the size of the composite source becomes greater so that a higher value is reached at low frequency, but it is not reached until a lower frequency. This increase at low frequency is approximately equal to $10\log_{10}N_s$ where N_s is the number of sleepers included. In the region between 100 Hz and 250 Hz the radiation ratio falls, tending to that of the single sleeper and in this region it is independent of the number of sleepers included in the model. The acoustic wavelength is equal to twice the sleeper spacing (1.2 m) at 285 Hz. Above this frequency the results oscillate within the region ±2 dB, tending to 0 dB at high frequency.

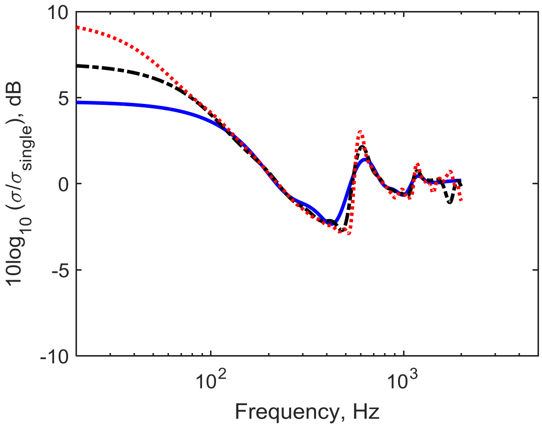

Figure 4.20 Increase in sleeper radiation ratio due to multiple sleepers: –, 3 sleepers with vibration amplitudes in the ratio 1:1:1; – · – ·, 5 sleepers; ···, 9 sleepers

Figure 4.21 shows corresponding results for three sleepers with a vibration ratio of 0.5 between the outer and central sleepers. These are compared with results in which the vibration amplitudes are obtained from the track vibration model, i.e. using the frequency-dependent ratios from Figure 4.15. The increase in the radiation ratio calculated in this way is shown for three sleepers and 15 sleepers. Similar results are found in each of these three cases, especially at low frequency. Below 100 Hz the increase in radiation ratio is approximately constant at 4.5 dB. This increase is now virtually independent of the number of sleepers included in the model due to the fact that the sleepers further from the excitation point on the rail have much lower amplitudes. Between 100 and 250 Hz the radiation ratio again tends to that of the single sleeper; above this frequency the results again oscillate within the region ±2 dB.

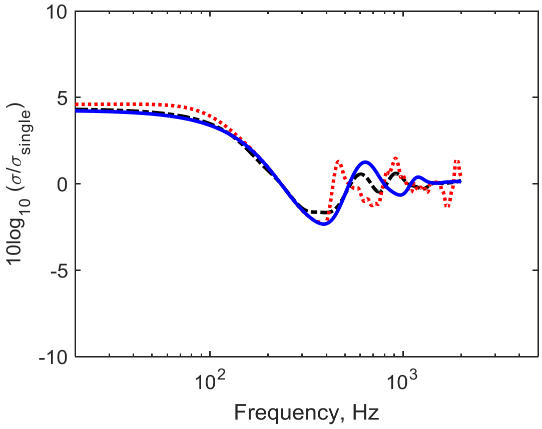

Figure 4.21 Increase in sleeper radiation ratio due to multiple sleepers: –, three sleepers with vibration amplitudes in the ratio 0.5:1:0.5; – · – ·, three sleepers with amplitudes from track vibration model; ···, 15 sleepers with amplitudes from track vibration model

For the sleepers excited by the force at the position between two sleepers, as shown in Figure 4.17, the ratios of the calculated amplitudes of the four consecutive sleepers around the force position to the central sleepers are 0.37:1:1:0.37. The corresponding increase in the radiation ratio is calculated in the boundary element model by using this vibration amplitude ratio, and is presented in Figure 4.22. Comparison is also made with the radiation ratio from three sleepers with vibration amplitude in the ratio of 0.5:1:0.5, as shown in Figure 4.21. As can be seen, the differences of the results between the two kinds of multiple sleepers are less than 1 dB at low frequencies, whereas they are similar to each other at high frequency.

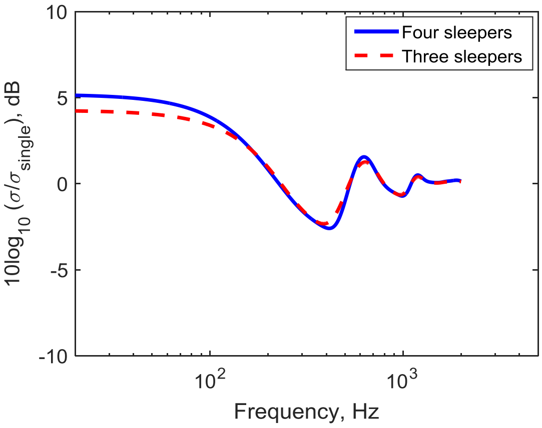

Figure 4.22 Increase in sleeper radiation ratio due to four sleepers with rail excited between two sleepers, compared with the radiation ratio from three sleepers with rail excited above the central sleeper

From these results it can be concluded that it is sufficient to consider only three sleepers in determining the radiation ratio for predicting the noise from the whole track system, no matter where the track is excited. Although more sleepers are contained within the acoustic wavelength at low frequency, the rail vibration is localised so that those additional sources have negligible source strength. At high frequencies, although the rail decay rate drops and many sleepers vibrate together, the acoustic wavelength is shorter and they can be considered as independent sources. Therefore, in the remainder of this chapter, work is focussed on the use of three sleepers to represent multiple sleepers in the track.

4.3.3 Multiple sleepers in absorptive ground

A more realistic ground condition, an absorptive ground, is explored in this section using the BE model. As before, the dimensions of the box representing the ground were determined first using a rigid ground box. The element size and box dimensions of the ground in different frequency ranges are taken to be the same as in Table 4.2. The outer sleepers are then assigned a vibration amplitude of half that of the central sleeper; all three are assumed to be vibrating in phase as above.

Figure 4.23(a) presents the model for the three sleepers embedded in a rigid ground with the ground box for high frequency. Due to symmetry only one and a half sleepers are included with length 0.625 m. Figure 4.23(b) shows the corresponding numerical results from the sleepers with the ground box models compared with those from the sleepers embedded in an infinite rigid ground. As can be seen, the numerical predictions agree very well. The maximum error is 0.2 dB. This indicates that the box sizes used in the models are sufficient to avoid the edge effects on the sound radiation of the three sleepers.

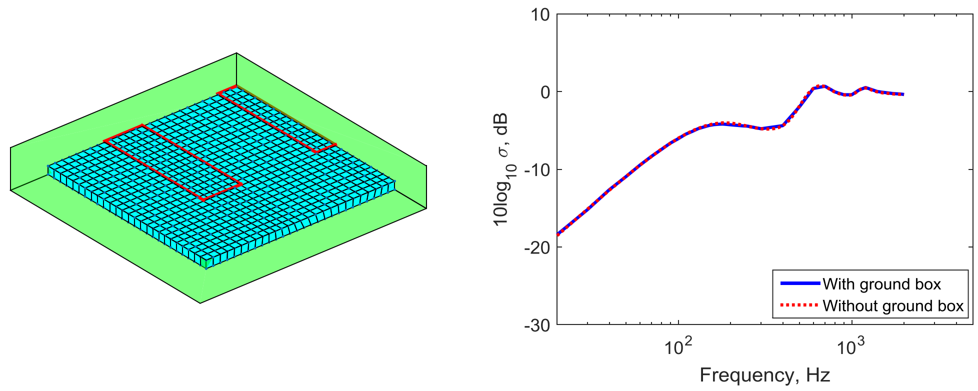

(a) Mesh of one quarter of domain for multiple sleepers embedded in rigid ground (high frequency model)

(b) Radiation ratio

Figure 4.23 Multiple sleepers embedded in rigid ground with ground box

The sound radiation of the sleepers vibrating vertically when they are embedded in an absorptive ground is next obtained for a ground with impedance obtained for various values of flow resistivity. Figure 4.24 shows the results. As for a single sleeper (Figure 4.11), it can be seen that the ground will absorb more noise if it has a lower flow resistivity. For example, the sound radiation will be reduced by up to 5 dB for the ground with flow resistivity of 3×10^3 Pa.s/m^2, compared with a rigid ground. However, the reduction will be much smaller at high frequency and is negligible above 1 kHz. In the same way as for the single sleeper, at very low frequencies the results tend towards those for a rigid ground as the impedance increases.

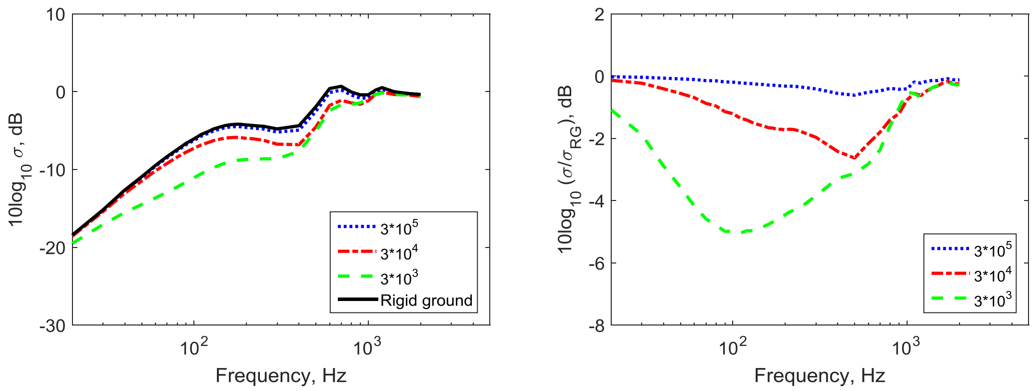

Figure 4.24 Radiation ratio of multiple sleepers embedded in an absorptive ground with different flow resistivity (in Pa.s/m^2)

The increase in radiation ratio for multiple sleepers embedded in an absorptive ground is also predicted, as shown in Figure 4.25, compared with a single sleeper embedded in an absorptive ground. As can be seen, for an absorptive ground, the increase trend due to the multiple sleepers is similar to that for multiple sleepers embedded in rigid ground, as shown in Figure 4.21.

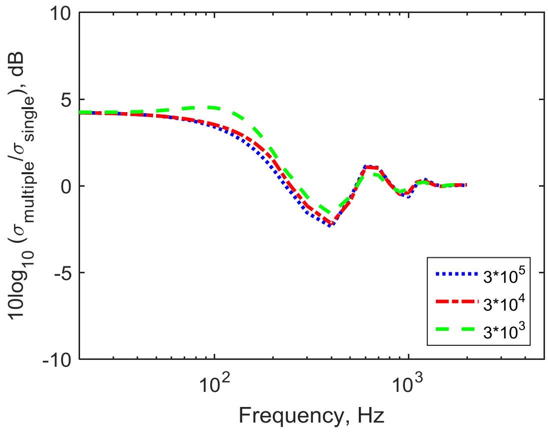

Figure 4.25 Increase in sleeper radiation ratio due to multiple sleepers embedded in absorptive ground compared with a single sleeper embedded in absorptive ground

4.4 Summary

The acoustic characteristics of railway sleepers undergoing vertical vibration have been predicted using a three-dimensional boundary element model. It has been shown that a single sleeper in free space exhibits the behaviour of a point dipole at low frequencies, but follows the behaviour of a line dipole at intermediate frequencies before tending to unity at high frequency. When the sleeper is embedded in a rigid ground the corresponding behaviour is that of a point monopole at low frequencies and a line monopole at intermediate frequencies. When the sleeper flexibility and support stiffness are taken into account, the radiation ratio of a flexible sleeper of length 2.5 m can be approximated by that for a rigid half-sleeper of length 1.25 m. Furthermore the effect of ground absorption has been taken into account and shown to reduce the radiation from the vertical motion of the sleeper especially in the mid-frequency region below 1 kHz. It is also shown that the sleeper radiation ratio does not change much, especially above 280 Hz, if the sleeper is flush or standing out of the ground.

When multiple sleepers are excited through the rail, their sound radiation is greater than would be obtained from the same sleepers treated independently. This increase in sound radiation has been calculated for cases where the sleeper is embedded in a rigid or partially absorptive ground. It is shown that it is sufficient to consider only three sleepers in determining their radiation ratio when installed in track. At low frequencies, although more sleepers lie within an acoustic wavelength, the vibration of the track is localised to the three sleepers nearest the excitation point. At higher frequencies, where more sleepers have significant vibration, the distance between them is large enough compared with the acoustic wavelength for them to be treated independently. Consequently the sound radiation increases by up to 5 dB below 100 Hz whereas above 300 Hz the result can be approximated by that for a single sleeper.

Chapter 5 Measurements of acoustic properties of porous materials

In a railway track, the rails and sleepers are usually laid in ballast. The gaps between the ballast particles mean that the ballast can be viewed as a kind of porous material, which is acoustically absorbing to some extent. The ballast absorption will have an influence on the rail and sleeper radiation which needs to be quantified; it is, therefore, necessary to investigate its acoustic properties experimentally and theoretically.

Taking the size and weight of ballast into account, reduced scale ballast is studied for convenience. A 1:5 scale model track, including ballast has been constructed in an undergraduate project by Lawrence [89]. The flow resistivity of this 1:5 scale ballast is determined initially, followed by the measurement of the porosity. The absorption of the scale ballast is next measured by different measurement methods. Finally, a model of ballast absorption is proposed. In order to test the accuracy of the measurement methods, a melamine foam is measured as well. Some of these results have been obtained in conjunction with an undergraduate project by Lewis [90].

5.1 Measurements of basic material properties

Before investigating the acoustic behaviour of porous materials, it is first necessary to determine two important and fundamental quantities: flow resistivity and porosity. Measurements of the flow resistivity and porosity of the scale ballast are presented in this section as well as those for a melamine foam.

5.1.1 Measurements of the flow resistivity

Flow resistivity is a measure of how easily air can enter a porous material and the resistance that air flow meets when passing through a structure [102]. The flow resistivity of a porous material is the most important parameter determining its surface impedance and absorption coefficient.

For the measurement of flow resistivity, there is an international standard ISO 9053: 1991 available [103], where further details can be found about the procedure. The direct airflow method is used here, which is based on the definition of the flow resistivity. Specifically, for a slice of the porous material with a thickness h, the pressure drop through the sample Δp is measured, when it is subject to a mean steady flow velocity U; the flow resistivity σ_f can be given by [102]:

$$\sigma_f = \frac{\Delta p}{Uh} \tag{5.1}$$

Figure 5.1 shows the corresponding experimental set up based on the equipment arrangement described in [104]. A steady air supply pushes the air through the test specimen. A flow meter and a pressure meter are used to measure the volume flow rate and the pressure drop to the atmospheric pressure.

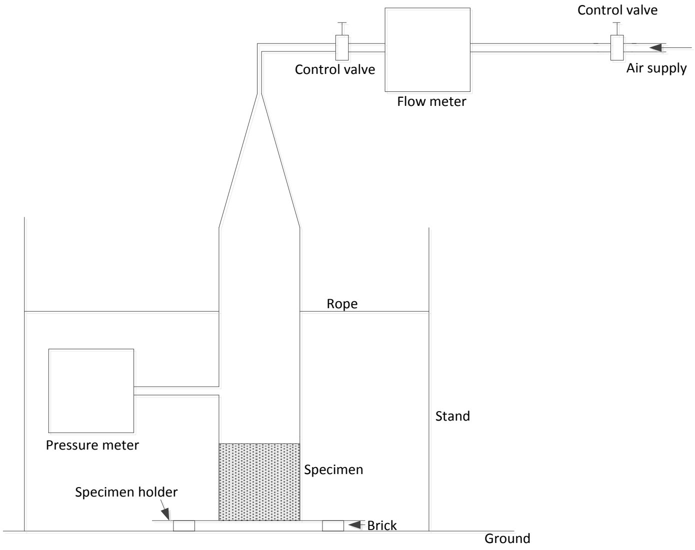

Figure 5.1 Experimental set up for the flow resistivity measurement

In the current measurements, the specimen is contained in a cylinder of internal diameter 146 mm which is connected by a conical element to the air supply. This ensures that the flow through the specimen has a low velocity and a smooth flow. Figure 5.2 presents the corresponding experimental set up. The specimen holder is a 1.5 mm-thick perforated steel plate, which has a perforation ratio of 0.31. The diameter of the holes in the plate is 3 mm. It is expected that the plate will not contribute to the flow resistivity. It not only can support the weight of the specimen above, but also let the air pass through the tube smoothly.

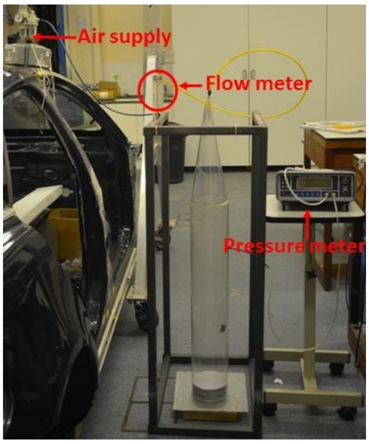

Figure 5.2 Experimental facility arrangements for flow resistivity

It is important to note that the flow velocity should be small, otherwise the relationship between the flow velocity and the pressure drop will be non-linear. Flow velocities between 5×10^{-4} and 5×10^{-2} m/s are recommended by Bies and Hansen [104]. The flow resistivity can be calculated as:

$$\sigma_f = \frac{\rho_0 \Delta p A}{mh} \tag{5.2}$$

where ρ_0 is the density of the air, A is the cross-sectional area of the specimen, h is its thickness, Δp is the pressure drop and m the air mass flow rate (kgs^{-1}).

5.1.1.1 *Melamine foam*

The flow resistivity of a sample of melamine foam, shown in Figure 5.3, was tested first. One, two and three layers of the melamine foam, with corresponding thicknesses of 17 mm, 34 mm, 51 mm, were measured. The diameters of the foam are slightly larger than the diameter of the conical cylinder (146 mm) in order to avoid leakage of the flow around the edge. Figure 5.4 presents the flow resistivity of the melamine foam, obtained from Equation (5.2), in different configurations. Measured values of flow resistivity are presented as a function of flow velocity of the air supply. As can be seen, different thicknesses of the material or different flow velocities affect the measured values of the flow resistivity slightly. However, these differences are relatively small. The error bars indicates the precision of the flow resistivity estimation from the precision of Δp and m. The mean value for the measured flow resistivity of this melamine foam is 9400 Pa.s/m^2. It is slightly smaller than the published values in [105], which will be demonstrated in Table 5.1 later. This is probably because the melamine foams in [105] are different from the current melamine foam as well with different thicknesses.

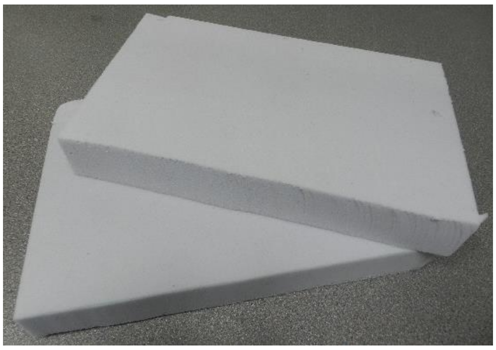

Figure 5.3 Melamine foam

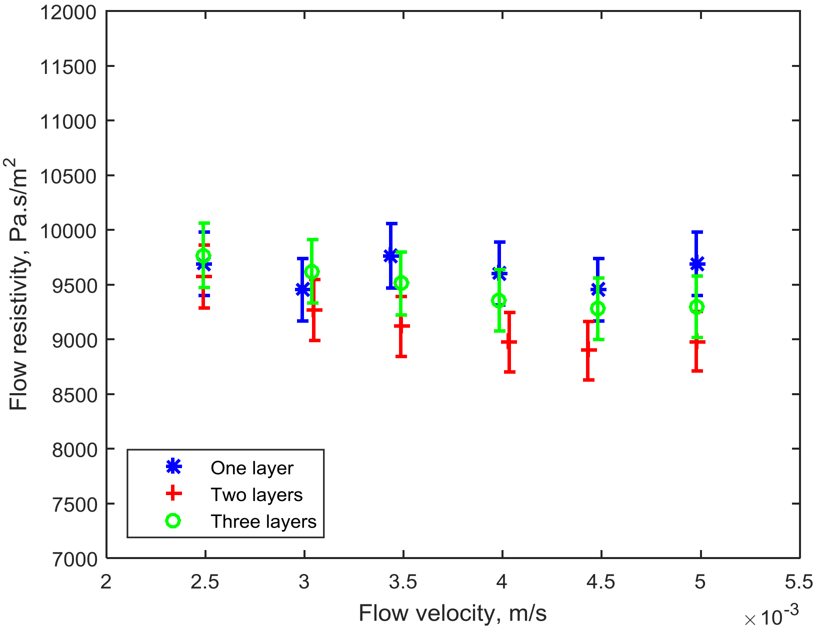

Figure 5.4 Measured flow resistivity for the melamine foam

5.1.1.2 *Reduced scale ballast*

The flow resistivity of 1:5 scale ballast has also been measured. Two thicknesses of the ballast were measured: 30 cm and 60 cm. Figure 5.5 shows the apparatus containing the 60 cm layer. Figure 5.6 presents the corresponding measured results for the ballast. As can be seen, there is little difference between the flow resistivity from these two thicknesses. The fact that the two thicknesses give the same results confirms that the specimen holder does not influence the results. The mean value of the flow resistivity for the 1:5 scale ballast is determined as 280 Pa.s/m^2. This is close to the flow resistivity of 200 Pa.s/m^2 for the full scale ballast obtained by Attenborough et al. [79].

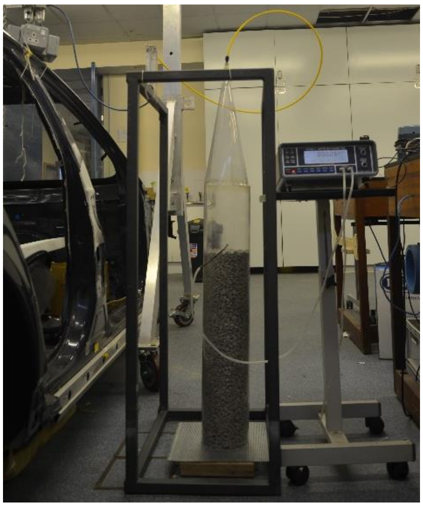

Figure 5.5 Set up for measuring the flow resistivity of one fifth scale ballast

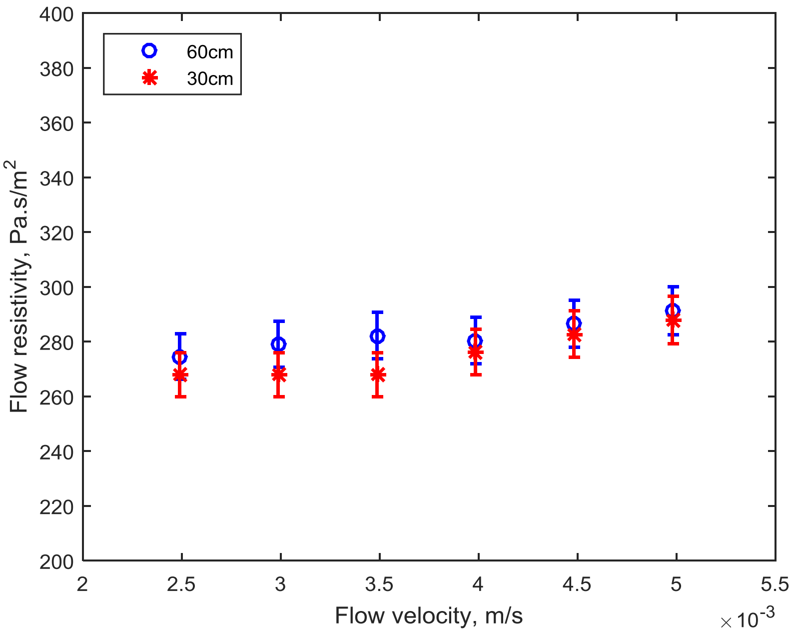

Figure 5.6 Measured flow resistivity for the 1:5 scale ballast

5.1.2 Measurements of the porosity

Porosity is the other important and fundamental parameter required to describe the acoustic property of porous materials. It is a ratio of the total pore volume to the total volume of the porous absorbers. A measurement method has been devised to determine the porosity of the 1:5 scale ballast based on its definition. A bucket containing ballast, with a total volume of 14.7 L, was filled with water as shown in Figure 5.7. When the water was flush with the surface of the ballast, the volume of the water used was recorded, which can be treated as the volume of the pores inside the ballast. A weighing scale underneath the bucket was also used to record the changes of the weight before and after the bucket is totally filled with water. This procedure was repeated 5 times with new dry samples. Finally, the porosity of this scale ballast is calculated as 0.463 ± 0.006, which is also close to the porosity value of 0.491 for full scale ballast given in [79]. The density of the stones is deduced as 2640 kg/m^3.

Figure 5.7 Measurement of the porosity of the scale ballast

The porosity of the melamine foam was not determined here. However, a previous study by Kino and Ueno [105] showed that the value of porosity changes very little for three different melamine foam samples, whose properties are presented in Table 5.1. As can be seen, the porosity of melamine foams is similar in each case although the flow resistivity and tortuosity vary.

Table 5.1 Non-acoustical parameters of melamine foam [105]

	Foam 1	Foam 2	Foam 3
Density, kg/m^3	8.6	10.3	13.27
Thickness, mm	32	25.5	10.5
Flow resistivity, Pa.s/m^2	10500	13100	17500
Tortuosity	1.0059	1.0053	1.0055
Porosity	0.995	0.993	0.992

5.2 Measurements of absorption

The absorption coefficient is an important parameter to characterize acoustic absorbers. It is defined as a ratio of the energy absorbed by the surface of the absorbers to the incident energy [102]. Three common techniques are available for the measurements of the absorption coefficient: impedance tube measurement, free field measurement and reverberation chamber method. The corresponding methods are reviewed here.

The impedance tube method enables the normal incidence absorption coefficient and surface acoustic impedance to be measured under well-defined and controlled conditions, hence it is commonly used in validating prediction models for porous materials [102]. This method can be carried out with relatively simple apparatus in a normal room and does not need specialist acoustic chambers. However, small samples of the porous materials are needed for this method. Therefore, problems will arise if the small sample is not representative of the behaviour of a large sample.

For the free field measurement, it is most straightforward for homogeneous, isotropic materials [102]. This technique needs not only a large sample but also an anechoic or hemi-anechoic space for the measurements. Also, it readily allows the absorption to be measured for oblique incidence.

The random incidence absorption coefficient, which is most used in the design of rooms, can be measured by reverberation chamber method. This test technique requires large samples and a specialist test room, thus it is expensive to undertake [102]. It only gives absorption coefficients; the impedance cannot be obtained.

Different measurement methods can be selected based on specific purpose in practice. For example, for developers of porous materials, the impedance tube method is convenient to first understand the acoustic properties of porous material with a small sample before undertaking a large test in reverberation chamber. Conversion between the absorption coefficients obtained by different measurement methods is described in [102].

The absorption measurements of the melamine foam and the 1:5 scale ballast by using the three test techniques were preliminarily conducted in an undergraduate project [90]. It was found that the free field measurement method works poorly for the two porous materials. Possible reasons are the small sample area in the tests or the time window in the signal processing. It was also found that the measured results were very sensitive to the time window used.

Two of the most common techniques: the impedance tube method and the reverberation chamber method, are explored here for the absorption measurements. The measurement of the melamine foam for the purpose of validation is carried out using both methods; this is followed by the absorption measurement of scale ballast by only using the reverberation chamber method.

5.2.1 Impedance tube

Measurements can be performed using either the standing wave method or the transfer function method. Detailed information is given in BS EN ISO 10534: 2001 [106, 107]. The corresponding methodology is described in Appendix C.

5.2.1.1 *Absorption of melamine foam*

The absorption of a sample of 50 mm thick melamine foam was tested using both methods in an impedance tube. The tube is shown in Figure 5.8. The diameter of the tube is 100 mm and therefore the upper limit of usable measurements is 2 kHz. For the transfer function method, a Dataphysics signal analyser and data acquisition system was used to generate the random noise signals with a bandwidth of 2 kHz. The measured data was averaged over 10 samples with a length of 10.2 s, to determine the transfer function. Two sets of microphone locations were used: 150 and 210 mm and 200 and 260 mm from the sample. This adhered to the minimum distance required from the test specimen surface (approximately 100 mm) [107] and separation distance between the microphones (approximately 70 mm). The mean absorption coefficient obtained for the two sets of microphone locations is shown in Figure 5.9, which is also compared with results from the standing wave method. Good agreement can be seen between the two methods, especially at high frequency. At low frequency, the signal is a bit noisy, which may be because 10 averages are not enough. Dips can also be seen in the curves at around 900-1000 Hz, which are due to the elastic resonances of the frame of the porous material [108, 109].

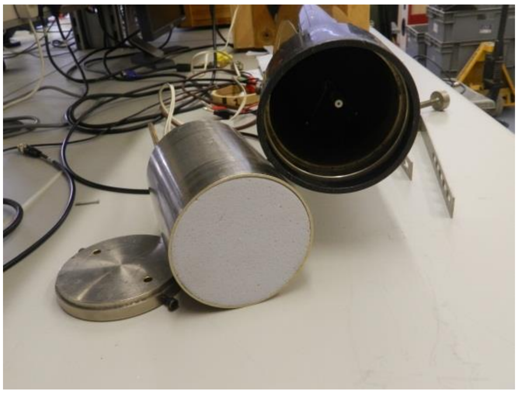

Figure 5.8 Melamine foam tested in the impedance tube

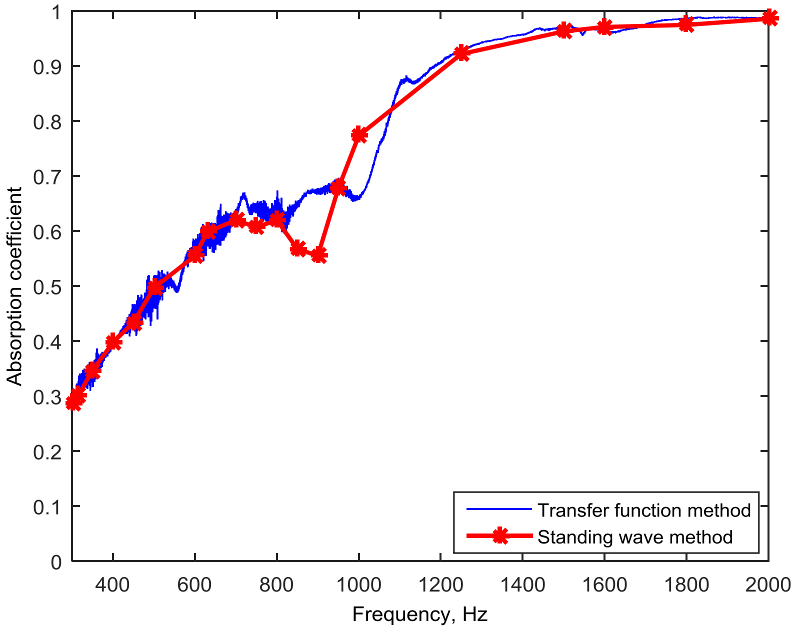

Figure 5.9 Absorption coefficient of the melamine foam measured in impedance tube

5.2.1.2 *Acoustic impedance of melamine foam*

According to Equation (C.9), the non-dimensional surface normal impedance can be deduced from the measurements by the transfer function method. This is shown in Figure 5.10. The Delany-Bazley model [56] is used here for comparison between the estimated impedance and the measurements.

Based on the Delany-Bazley model, the impedance can be expressed in terms of flow resistivity σ_f as

$$z_n' = 1 + 9.08\left(\frac{1000f}{\sigma_f}\right)^{-0.75} - 11.9i\left(\frac{1000f}{\sigma_f}\right)^{-0.73} \tag{5.3}$$

where z_n' is the normalised impedance $z_n/\rho_0 c_0$ and f is frequency.

If the performance of a relatively thin layer is required, the impedance z of a rigidly-backed layer of thickness l may be calculated from the equation

$$z = z_n' \coth \gamma_p l \tag{5.4}$$

where γ_p is the propagation coefficient. This can be given by

$$\gamma_p = 10.3k\left(\frac{f}{\sigma_f}\right)^{-0.59} + i\left[1 + 10.8k\left(\frac{f}{\sigma_f}\right)^{-0.7}\right] \tag{5.5}$$

where $k = \omega / c_0$; c_0 is the velocity of sound.

Using the measured value for the flow resistivity of the melamine foam, 9400 Pa.s/m^2, obtained in Section 5.1.1.1, the result from the Delany-Bazley model is compared with the measured impedance in Figure 5.10. It can be seen the theoretically estimated results, the dotted line, agree well with the measurement.

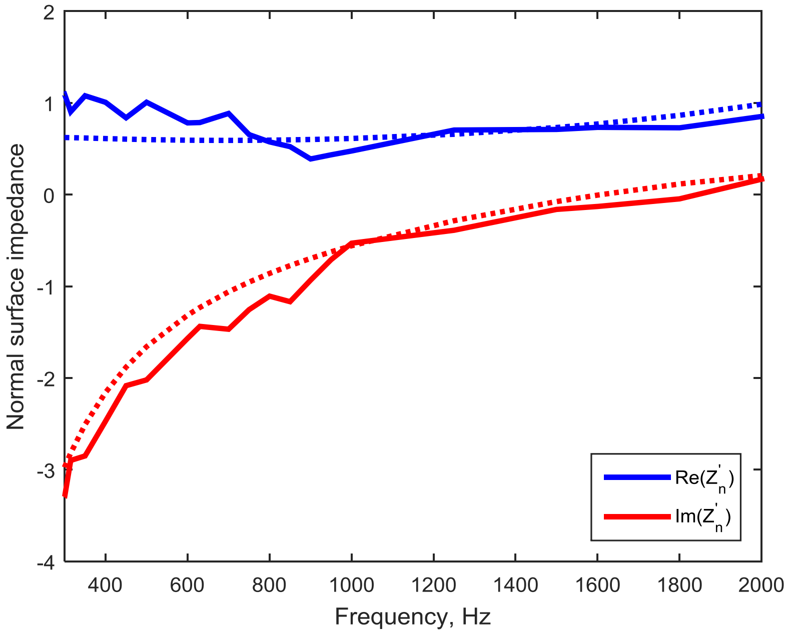

Figure 5.10 Measured non-dimensional surface normal impedance for melamine foam (solid lines) and comparison with Delany-Bazley model (dotted lines)

5.2.2 Reverberation chamber method

Although the measurement procedure using the impedance tube method is relatively straightforward, the ballast absorption could not be measured in this way. For such a measurement, a very large impedance tube would be needed. The diameter would need to be larger than the tube used in Section 5.2.1 in order to contain a representative sample of ballast. Swenson et al. in [82] studied the propagation of acoustic waves through gravel in a 7.5 m long impedance tube with a diameter of 0.76 m. Results were found up to 200 Hz. Equation (C.1) indicates that the frequency range that can be tested in such a tube limits its usefulness. Another limitation of the impedance tube method is it can only be used to obtain the normal incidence absorption coefficient. The reverberation chamber method is therefore used to obtain the ballast absorption. In order to determine the measurement effectiveness, the melamine foam is measured first, which is then compared with the results obtained by the impedance tube method. Next, the 1:5 scale ballast and a 1:√5 scale ballast are measured. Comparisons are made with previous measurements of the absorption of full scale ballast [83]. More details of this measurement method are presented in Appendix D.

5.2.2.1 *Melamine foam*

According to the standard ISO354: 2003 [110], the volume of the room should not be less than 150 m^3 and not more than 500 m^3 for measurements over a frequency range 100 ~ 5000 Hz. Due to the small area of the melamine foam and the scale ballast available, a small reverberation chamber has been used, which has a volume of 15.6 m^3 (2.5 m × 2.4 m × 2.6 m). This will not give valid results at low frequency so attention should be given to the Schroeder frequency. According to Equation (C.4), for the empty chamber used, the Schroeder frequency is around 800 Hz. For the chamber containing absorptive material, it should be lower, and has been calculated as approximately 630 Hz for a reverberation time of 1.58 s.

The sound sources, which include a high frequency horn and a low frequency hemispherical speaker, were positioned in separate corners of the room as shown in Figure 5.11. Two source and three receiver positions were used to average the results to reduce the effect of non-diffuseness, when the samples are tested.

One, two and four pieces of the melamine foam, with corresponding dimensions of 1 m × 0.39 m, 1 m × 0.78 m, and 2 m × 0.78 m, were tested. Figure 5.11 shows the corresponding experimental set up for the four pieces of foam in the reverberation chamber. Figure 5.12 presents the absorption coefficient of the melamine foam measured in different configurations. The Schroeder frequency is also marked for reference. As can be seen, for one piece of foam, the results are found to exceed 1, which is probably because the absorbing area of the foam was too small so that edge effects are important. Improvement can be seen for the results with two and four pieces of foam. The agreement between them, however, is still not ideal. This may because the absorption area of the foam is still too small.

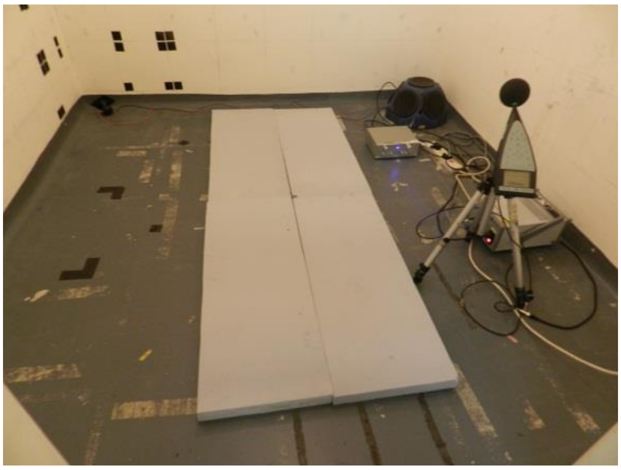

Figure 5.11 Experimental set-up for four pieces of melamine foam

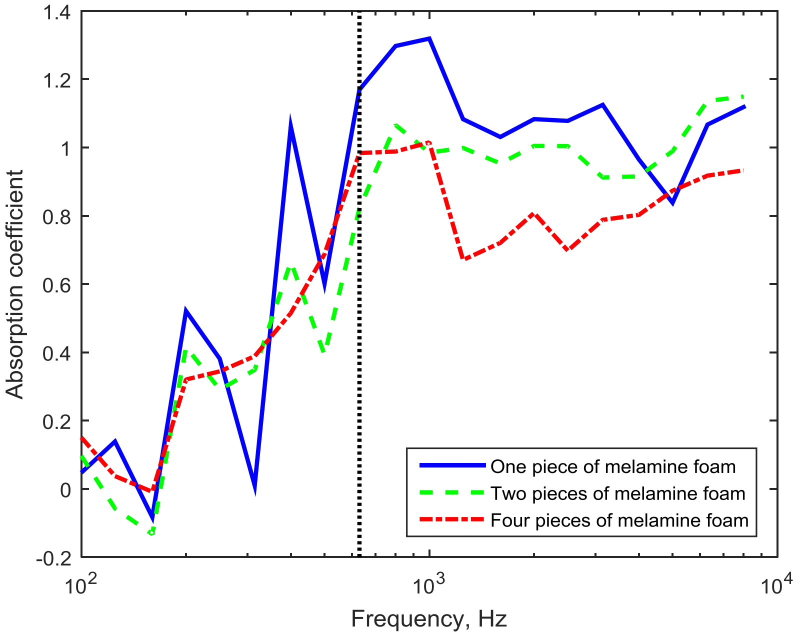

Figure 5.12 Absorption coefficient of 50 mm melamine foam in different configurations. The Schroeder frequency is shown as the vertical dotted line

The reverberation chamber method gives the random incidence absorption coefficient, whereas the impedance tube method gives the normal incidence absorption coefficient. Therefore, in order to compare the results, the results obtained from the impedance tube using the transfer function method were converted using the diffuse field conversion given in Annex D of [106]. Figure 5.13 shows the corresponding results. The agreement is quite poor. This may be due to measurement errors in the reverberation chamber method, or due to the difficulties in using the correction formula in this case. A potential problem in the reverberation chamber was that the melamine foam did not have a flat bottom surface in each configuration, so that small air gaps existed between the foam and the floor. This would increase the absorption coefficient compared with the foam alone in the tube. Moreover, there were small gaps between the pieces, as seen in Figure 5.11, which may cause additional edge diffraction.

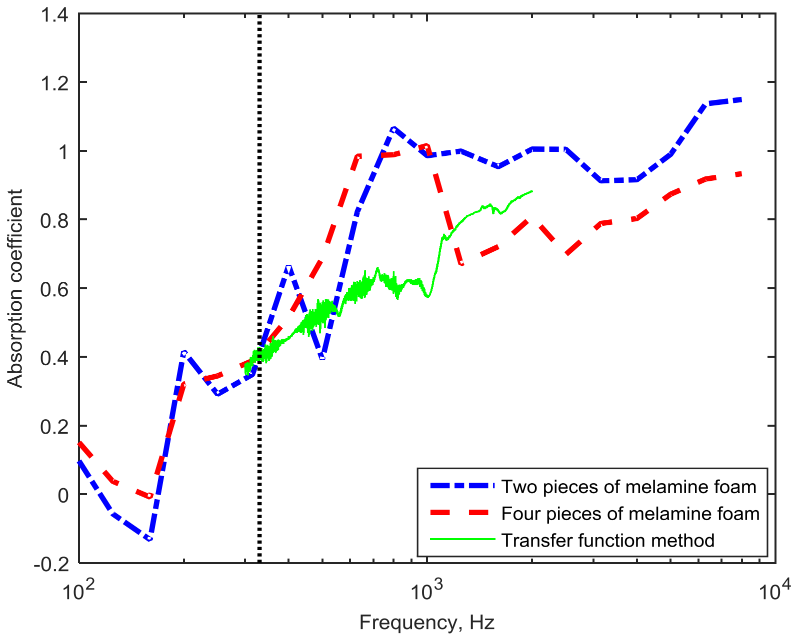

Figure 5.13 Comparison of the absorption coefficient for melamine foam using reverberation chamber method and transfer function method

Overall, the melamine foam was tested first to verify the measurement methods; however the agreement for the absorption of the melamine foam between the different methods is poor. More work will be needed in the future to obtain more convincing results and resolve these differences.

5.2.2.2 *Scale ballast*

According to the scaling law presented in [91], although the sample thickness scales properly with the frequency, it is the 'number of interstices' per area rather than the pore diameter that provides the correct scaling of the absorption as discussed in Section 1.8. This scaling law would suggest that tests should be performed with stone dimensions scaled at 1:√5 while the thickness is scaled by 1:5.

Ballast samples with a scale factor of 1:√5 have been constructed. The construction procedure of this scale ballast is described in Appendix E. The absorption coefficient of this 1:√5 scale ballast is then measured in the small reverberation chamber, as shown in Figure 5.14. A layer of ballast with an area of 1.6 m × 1.6 m was placed on the floor of the chamber. Two ballast thicknesses were tested: 30 mm and 60 mm, which correspond to thicknesses of 150 mm and 300 mm at full scale. The results are shown in Figure 5.15. Comparison is also made with the absorption measured for the corresponding thicknesses of full scale ballast from [83]. The frequency range of the full scale measurements has been increased by a factor of 5 in this plot. Generally good agreement can be seen. The ballast absorption increases with thickness, and similar peaks and dips are found in the reduced scale and full scale results. The absorption coefficient for the thicker layer exhibits a peak at 1250 Hz, which is where the thickness is roughly equal to a quarter of the acoustic wavelength [83]. There is a corresponding dip at 2500 Hz, where the thickness is approximately equal to half the acoustic wavelength. Similarly for the thinner layers a peak occur at 2500 Hz and a dip at 5000 Hz. In summary, Figure 5.15 shows that, although there is not a perfect match, the absorption coefficients for full scale and reduced scale ballast follow a similar trend and the main features of the curves (maxima and minima) are correctly reproduced.

Figure 5.14 Experimental set-up for the 1:√5 scale ballast

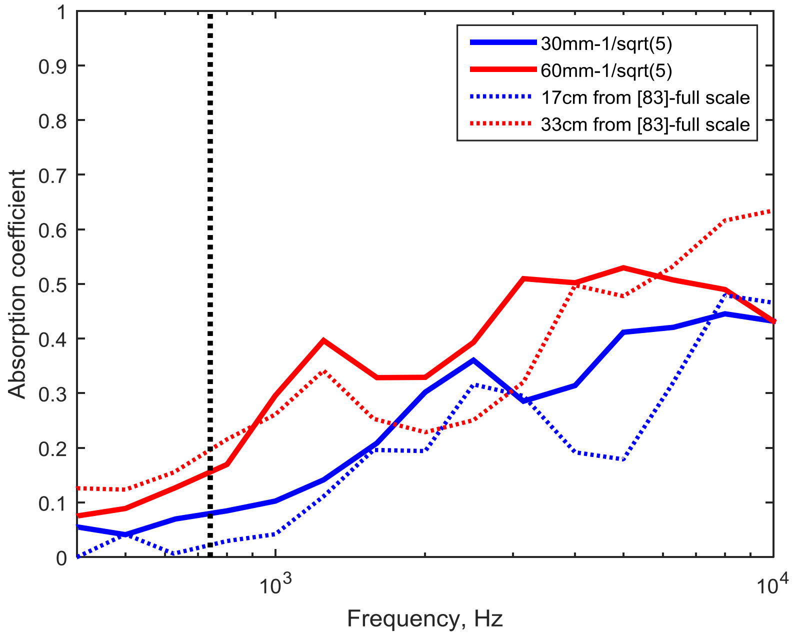

Figure 5.15 Absorption coefficient for the 1:√5 scale and full scale ballast in reverberation chamber (results at full scale are shifted in frequency). Vertical line corresponds to the Schroeder frequency of the room for 1:√5 ballast

Within the Track 21 project [111], different ballast gradations have been studied in relation to track settlement. It is therefore of interest to study the absorption of the ballast with such a different gradation. This ballast will have more small particles than the standard gradation. Samples of 1:√5 ballast with this new gradation have also been constructed. The detailed information on this new scale ballast and its construction is presented in Appendix E. The absorption of the ballast with the new gradation was measured in the reverberation chamber for thicknesses of 30 mm and 60 mm. The results are shown in Figure 5.16, where a comparison is also made with the absorption of the 1:√5 ballast with standard gradation (gradation 1 in the figure). As can be seen, the absorption changes more for the 60 mm-thick ballast due to the different gradations than for the ballast with 30 mm thickness. This may be due to the existence of more small particle sizes in the ballast with bigger thicknesses. The increase in absorption for the 60 mm thickness is promising.

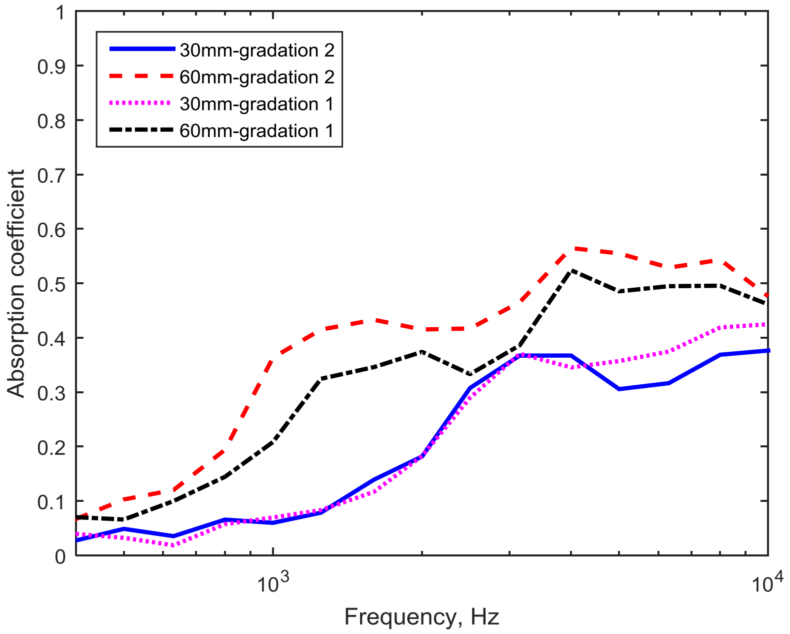

Figure 5.16 Comparison of the absorption for the 1:√5 scale ballast with two different gradations

The absorption of 1:5 scale ballast has also been measured. Figure 5.17 presents a comparison of the absorption coefficient of the two scale ballasts based on the standard gradation. Both were tested at 30 mm and 60 mm thickness. The difference between these two results is not very significant and it is on average smaller than the difference between the 1:√5 scale and the full scale ballast. Nevertheless it can be seen that the absorption increases slightly with the use of smaller particles, consistent with the results found in Figure 5.16. The difference between the results for the two different scale factors is smaller for the larger thickness than for the smaller thickness. It was therefore considered sufficient to use the 1:5 scale ballast to assess acoustic properties. This also avoids a particular problem with the 1:√5 scale ballast, which is that the stone size is quite large compared with the layer thickness.

The absorption coefficient of this 1:5 scale ballast is finally compared with the corresponding results for the full scale ballast, as shown in Figure 5.18. Acceptable agreement can be seen between them for these two thicknesses, except at the frequencies around the dips (5 kHz for the 30 mm-thick ballast and 2.5 kHz for the 60 mm ballast). It is found that the average differences of the absorption coefficient for these two ballast samples is a factor of 2.4 for the 30 mm ballast, and a factor of 1.15 for the 60 mm ballast. However, again the absorption coefficients for full scale and this reduced 1:5 scale ballast give a similar trend and the main features of the curves are similar. Therefore, it is assumed to be acceptable to use the 1:5 scale ballast to assess the acoustic properties of the ballast in the scale model experiments.

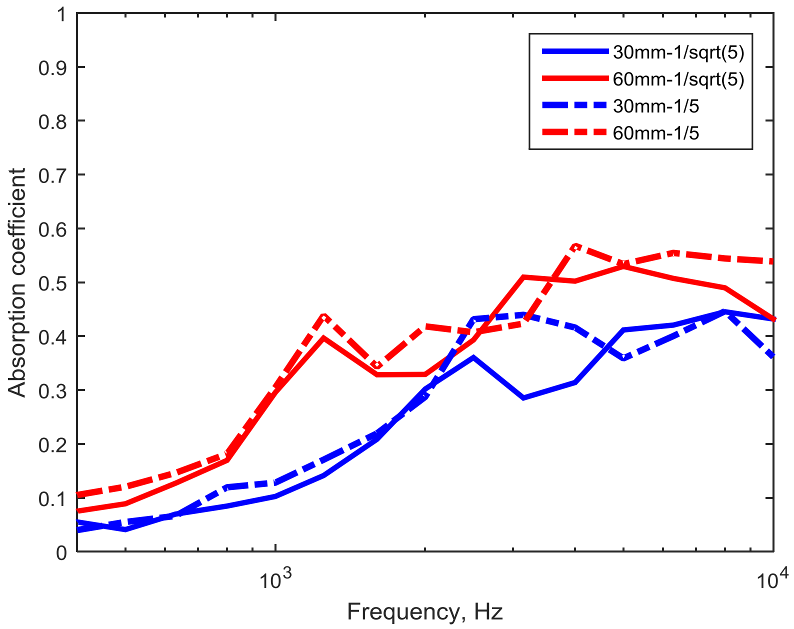

Figure 5.17 Comparison of the absorption for the 1:5 and 1:√5 scale ballast obtained in reverberation chamber

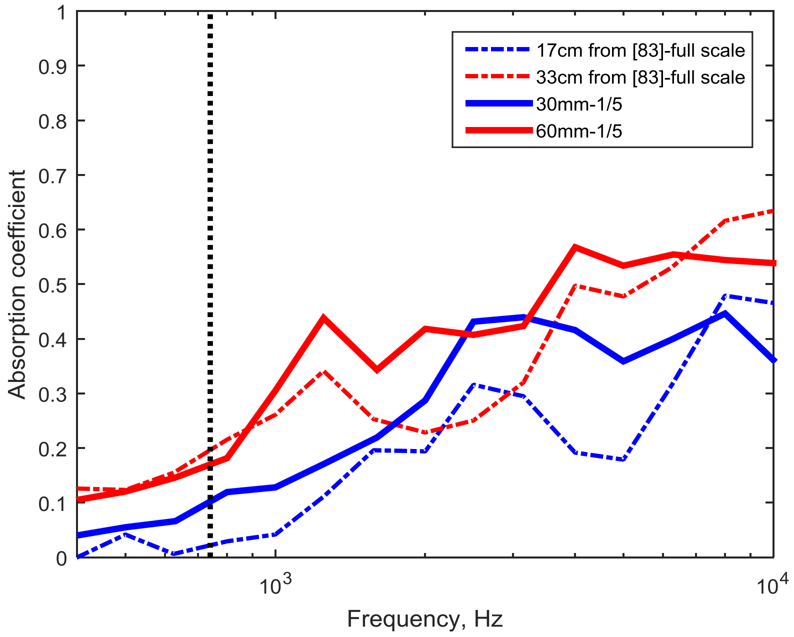

Figure 5.18 Absorption coefficient for the 1:5 scale and full scale ballast in reverberation chamber (results at full scale are shifted in frequency). Vertical line corresponds to the Schroeder frequency of the room for 1:5 ballast

5.3 Modelling of ballast absorption

As mentioned in Section 5.1, the flow resistivity can be used to deduce the absorption coefficient of a porous material. The measured flow resistivity of the scale ballast is around 280 Pa.s/m^2, which is not in the range of flow resistivity values for the Delany-Bazley model. Instead the Johnson-Allard local reacting model [60, 61] is used here to represent the absorption of the ballast. This model is summarized here.

For a porous material with flow resistivity σ_f, the effective density of the porous material is given by:

$$\rho_e = q\rho_0\left(1+\frac{\sigma_f\Omega}{i\omega q\rho_0}\sqrt{1+\frac{4iq^2\eta\rho_0\omega}{\sigma_f^2\Lambda^2\Omega^2}}\right) \tag{5.6}$$

where q and Ω are the tortuosity and the porosity of the porous material, while ρ_0 and η are the density and viscosity of the air. Λ is the viscous characteristic length, a weighted ratio of the volume to surface area of the pores. According to Cox & D’Antonio [102], for simple pore shapes, it can be approximated as

$$\Lambda = \frac{1}{\tau}\sqrt{\frac{8\eta q}{\Omega\sigma_f}} \tag{5.7}$$

where τ is a ‘constant’ usually between 0.3 and 3. For circular pores it takes the value 1 and this is a good approximation for other shaped pores. The thermal characteristic length Λ' is given approximately by Cox & D’Antonio [102] as $\Lambda' \approx 2\Lambda$.

The effective or dynamic bulk modulus of the air within the material is

$$K_e = \frac{\gamma P_0}{\gamma-(\gamma-1)/\Gamma} \tag{5.8}$$

where the term Γ is given by

$$\Gamma = 1+\frac{8\eta}{i\Lambda'^2 N_p\omega\rho_0}\sqrt{1+\frac{i\Lambda'^2 N_p\omega\rho_0}{16\eta}} \tag{5.9}$$

In these expressions, the ratio of specific heats, $\gamma = 1.4$, and the atmospheric pressure, $P_0 = 1.013\times10^5$ Pa. N_p is the Prandtl number, which is 0.709 [112].

The characteristic impedance is then given by

$$z_c = \sqrt{K_e \rho_e} \tag{5.10}$$

and the wavenumber is

$$k_{we} = \omega \sqrt{\rho_e / K_e} \tag{5.11}$$

Then the surface normal impedance of the porous material with a thickness *l* can be calculated as

$$z_n = -i \frac{z_c}{\Omega} \coth\left(k_{we} l\right) \tag{5.12}$$

The Johnson-Allard model is used to predict the absorption coefficient of the 1:5 scale ballast and this will be compared with the measured absorption coefficient in the reverberation chamber. In the prediction model, the random incidence absorption coefficient α is obtained by using Paris's formula [101]:

$$\alpha = \int_0^{\pi/2} \alpha\left(\theta\right) \sin\left(2\theta\right) d\theta \tag{5.13}$$

where $\alpha(\theta)$ is the absorption coefficient at an incident angle θ. $\alpha(\theta)$ can be written in terms of the surface normal impedance [101]:

$$\alpha\left(\theta\right) = \frac{4\,\mathrm{Re}\left(z_n'\right)\cos\theta}{\left(\mathrm{Re}\left(z_n'\right)\cos\theta + 1\right)^2 + \left(\mathrm{Im}(z_n')\cos\theta\right)^2} \tag{5.14}$$

where $z_n' = z_n / \rho_0 c_0$.

The parameters for this scale ballast are listed in Table 5.2. The viscous characteristic length is determined by using Equation (5.7). The constant term 'τ' in the equation has been adjusted for the best fitting with the measured results; a value of 2.5 is taken in the predictions. This gives a value of 482 μm for the viscous characteristic length. In Figure 5.19, the predictions of the absorption coefficient of the scale ballast with thicknesses of 30 mm and 60 mm are compared with the corresponding measurement results. As can be seen, they agree well with each other.

Table 5.2 Parameters used for the 1:5 scale ballast

Flow resistivity	280 Pa.s/m^2
Porosity	0.46
Tortuosity	1.3
Viscous characteristic length	482μm
Viscosity of air	1.82×10^{-5} Ns/m^2
Prandtl number	0.709
Atmospheric pressure	1.013×10^5 Pa
Ratio of specific heats	1.4
Speed of sound in air	343 m/s
Density of air	1.21 kg/m^3

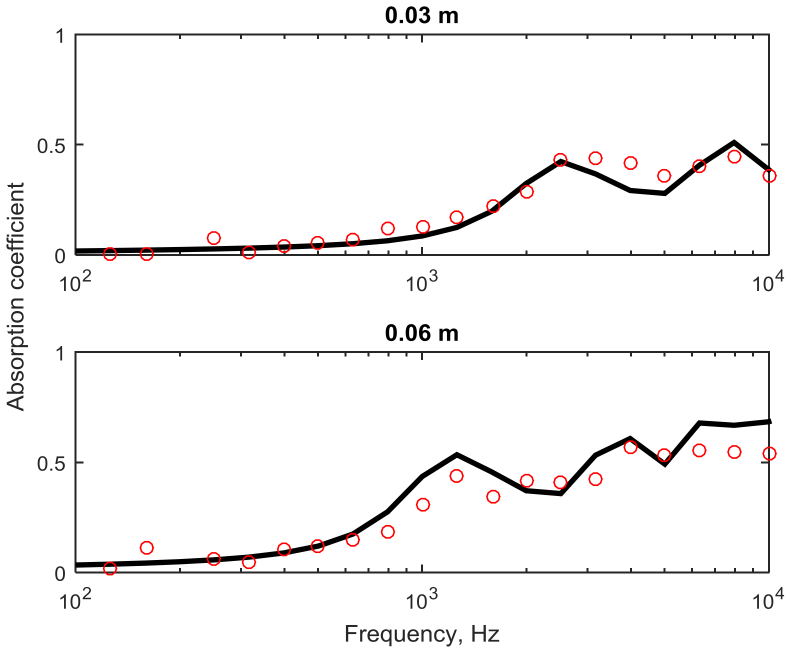

Figure 5.19 Absorption coefficient of the 1:5 scale ballast. Comparisons between reverberation chamber measurements and predictions using the parameters given in Table 5.2. o, Measurements; –, Predictions by Johnson-Allard model

This Johnson-Allard model is also used for the modelling of the absorption coefficient of the full scale ballast, and compared with the measured absorption from [83]. In the predictions, the tortuosity is taken as 1 and 0.65 is used as the constant term 'τ' in Equation (5.7) to give a value of 1627 μm for the viscous characteristic length. All the other parameters for the full scale ballast are the same as those for the 1:5 scale ballast in Table 5.2. The comparisons between the absorption coefficient predicted and the measured are shown in Figure 5.20. Good agreement can also be seen between them for the full scale ballast.

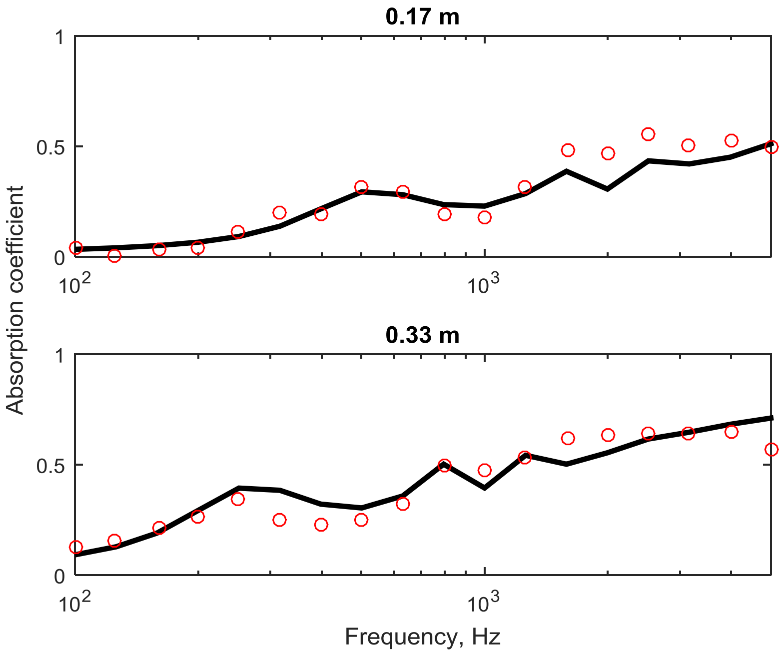

Figure 5.20 Absorption coefficient of the full scale ballast. Comparisons between the measured results from [83] and predictions. o, Measurements; –, Predictions by Johnson-Allard model

5.4 Summary

Measurements of the acoustic properties of a melamine foam and 1:5 scale ballast are presented in this chapter. Specifically, the flow resistivity of the melamine foam is measured by the direct airflow method, followed by that of 1:5 scale ballast. The porosity of this scale ballast is also measured.

Next, the impedance tube method and reverberation chamber method have been used to test the absorption properties of the melamine foam. Comparisons have been made between the measured data obtained by the different methods. Poor agreement has been found between the measurements performed with different methods for the melamine foam. This may be due to measurement errors in the reverberation chamber method due to air gaps between the rear of the foam and the floor of the chamber.

Only the reverberation chamber method has been used for the absorption measurement of the ballast. Both 1:5 scale ballast and a 1:√5 scale ballast have been tested. Quite good agreement was found between the reverberation room measurements on the two scale ballasts and with previous measurements on full scale ballast. It is concluded that the 1:5 scale ballast is sufficient to represent acoustic properties of the full size ballast, although its absorption is slightly higher. Tests on a revised gradation containing more small particles suggest this can increase the absorption somewhat.

Finally, the Johnson-Allard model is used for modelling the ballast absorption. Quite good agreement is found between the predictions and measured results for both the 1:5 scale ballast and the full scale ballast.

Chapter 6 Measurements of the sound radiation of the rail and sleeper

To validate the BEM modelling of the rail and sleeper radiation, measurements of the sound radiation have been carried out. A 1:5 scale model facility has been used, as shown in Figure 6.1, which was developed by Lawrence [89]. The rails have a length of 2 m. They are commercially available steel rails used for miniature railways and are approximately 1:5 scale replicas of the CEN60E1 section. Concrete sleepers have been specially constructed. By testing at 1:5 scale, the corresponding frequencies are increased by a factor of 5 compared with full scale. Tests for the rail and sleeper in different configurations have been conducted for comparison with the numerical modelling results of the rail and sleeper radiation given in Chapter 3 and Chapter 4.

Figure 6.1 1:5 scale model track [89]

6.1 Theory of experimental method

Based on Equation (1.1), the radiation ratio can be measured. Specifically, the sound power can be obtained by exciting the structure, for example using a shaker, and scanning using a sound intensity probe. The mean square velocity can be measured using accelerometers or a scanning laser vibrometer. This is viewed as a direct method. A weakness of this technique, however, is the noise from the shaker which may affect the results.

Another way to carry out this measurement is to use a reciprocal method [113] in which the sound power is measured in a reverberant room by acoustically exciting the structure and measuring its vibration levels. The transfer mobilities of the structure are measured separately. The validity of the reciprocity method has been checked against direct methods and numerical calculations for various test specimens in [113].

The approach is summarised here. Equation (1.1) can be rearranged as

$$\sigma = \frac{W \big/ \overline{F^2}}{\rho_0 c_0 \sum_j \left| v_j / F \right|^2 dS_j} \tag{6.1}$$

where $W \big/ \overline{F^2}$ is the radiated sound power normalised by the mean-square force $\overline{F^2}$ and $\left| v_j / F \right|^2$ is the squared mobility from the force position to a response position j. dS_j is the surface area of the structure associated with position j.

According to Equation (6.1), two measurements are required. One is used to measure the transfer mobilities, while the other is used to obtain the sound power for a given squared force. According to the reciprocity principle for the vibro-acoustic behaviour of an elastic structure by Lyamshev [114, 115], the acoustic pressure at a point A in the fluid due to a vibrating structure excited by a harmonic mechanical force at a point B is the same as the vibration that is produced at the point B on the structure due to an acoustic excitation by a point source located in the fluid at the point A. Hence, the radiated sound power normalised by the mean-square force could be determined reciprocally by measuring the acceleration response to a sound pressure field caused by an acoustic source. Moreover, this can be carried out in a reverberation chamber allowing the source strength to be measured in terms of the mean square pressure in the chamber. Then, the sound power W radiated by a vibrating structure, normalised by the mean-square force $\overline{F^2}$ exciting the structure, is equivalent to [113]

$$\frac{W}{\overline{F^2}} = \frac{\rho_0 \overline{a_Q^2}}{4\pi c_0 \left\langle \overline{p_Q^2} \right\rangle} \tag{6.2}$$

where $\overline{a_Q^2}$ is the mean-square acceleration of the structure at the original forcing position when excited acoustically and $\left\langle \overline{p_Q^2} \right\rangle$ is the spatially averaged mean-square pressure in the room. Note that it is not necessary to determine the reverberation time of the chamber, it is only necessary that the sound field is diffuse.

6.2 Measurements of sound radiation from the rail

To validate the BEM modelling of the rail radiation described in Chapter 3, measurements have been carried out using a 1:5 scale freely suspended rail. The dimensions of the full size and reduced scale rail cross-sections are presented in Figure 6.2. Note that the web is thicker than its full size counterpart and the head is slightly wider but otherwise the main dimensions are correct to a scale 1:5. The behaviour of this scale rail is therefore approximately that of a full size rail at five times the frequency. Nevertheless, for comparison with the measurements, new BE calculations have been carried out for this 1:5 scale cross-section.

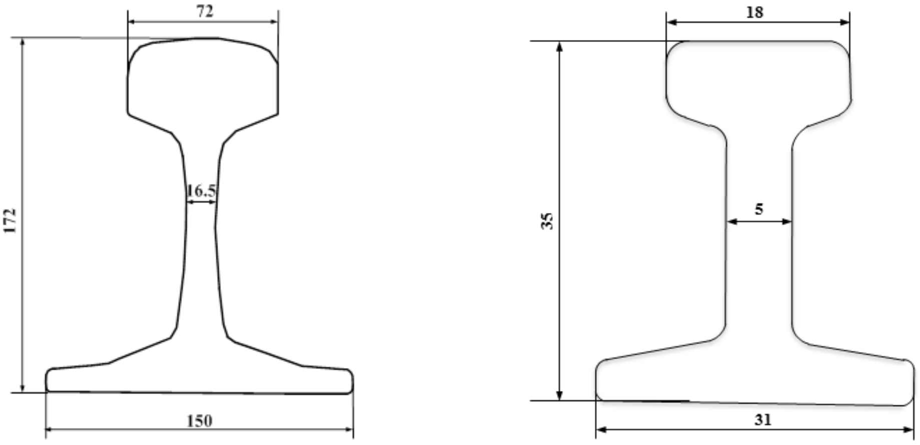

(a) Full size rail (b) 1:5 scale rail

Figure 6.2 Comparison of rail cross-section: dimensions in mm

Before carrying out the tests, thin strips of a constrained layer damping treatment with a thickness of 1 mm have been attached to the bottom of the rail foot. This increases the damping ratio of the rail and simplifies testing by reducing the dynamic range of the frequency response. Overall, the damping treatment increases the damping ratio of the free rail to an average value of around 0.013.

The transfer mobility has been measured at 41 points, equally spaced along the rail, for three different excitation positions, which are indicated in Figure 6.3. A small PCB 086C03 impact hammer (mass of 0.16 kg) with a titanium tip was used to allow the rail to be excited for frequencies up to 10 kHz. For each position of input force, the data obtained was averaged five times. Structural reciprocity has been used during the mobility tests, so that the hammer is moved along the length of the rail and the response is measured at the three fixed 'excitation' positions.

The acceleration response of the structure to a measured sound pressure field has been obtained in a reverberation chamber of volume 348 m^3. Four loudspeakers, excited by white noise over the frequency range up to 10 kHz, were used to create the sound field. The spatially averaged sound pressure $\left\langle \overline{p_Q^2} \right\rangle$ in the room has been obtained with a microphone placed on a rotating boom.

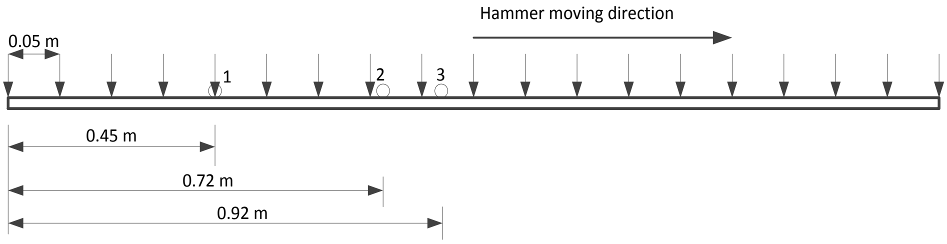

Figure 6.3 Hammer (↓) and accelerometer (o) positions for rail, length 2m - dimensions in m

The scale rail was tested in free space, above a rigid ground and above an absorptive ground, for both vertical and lateral vibration. The case of the rail on the ground, however, is not considered as it was found to be difficult to realize the same boundary conditions as in the BE model where the bottom of the rail foot was fixed to the rigid ground.

As the rails are tested in free condition structurally, it is necessary to determine the critical frequency f_c of the scaled rail, which is the same as that defined for an infinite rail given in Equation (3.4). A corresponding FE model has been made for the scale rail from which it is found that the critical frequency is 285 Hz for vertical motion and 700 Hz for lateral motion. The experimental results are compared with numerical predictions obtained for the scale rail in following sections.

6.2.1 Rail in free space

The rail was initially suspended by elastic cords 1 m above the floor of the chamber. This is far enough to consider the rail as being in free space for frequencies above 150 Hz, at which the distance is more than half the acoustic wavelength (similarly in ISO 3741 [116] sources should be at least 1.5 m from the walls of the chamber for measurements above 100 Hz). The corresponding experimental set-up is shown in Figure 6.4.

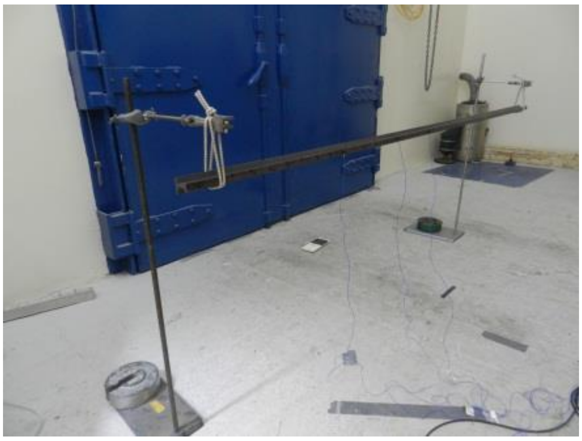

Figure 6.4 Rail in free space

6.2.1.1 Vertical motion of the rail

The rail acceleration was measured in the vertical direction in the centre of the rail head. A comparison of the measured sound pressure level with the background noise is shown in Figure 6.5(a). All results are shown in one-twelfth octave bands. This provides some smoothing of the measured data, while retaining a finer resolution than the more usual one-third octaves. Figure 6.5(b) shows equivalent results for the vertical acceleration signal. As can be seen, an adequate signal-to-noise ratio was achieved for the sound pressure, and at most frequencies above 300 Hz for the acceleration. Figure 6.6(a) presents the normalised power obtained by the reciprocity method according to Equation (6.2). The spatially averaged transfer mobility of the rail is shown in Figure 6.6(b), which shows a series of peaks corresponding to the bending modes of the finite length of rail.

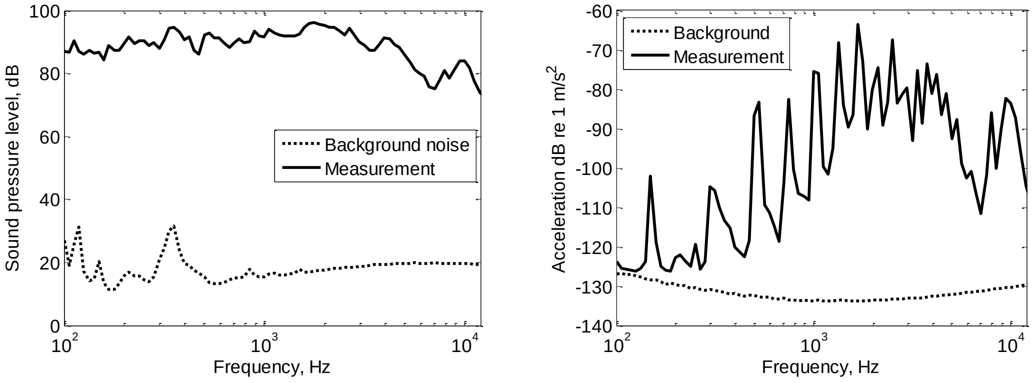

(a) Sound pressure level (b) Acceleration

Figure 6.5 Comparison of measurement and background noise signals for rail in reverberation chamber: vertical motion in one-twelfth octave bands

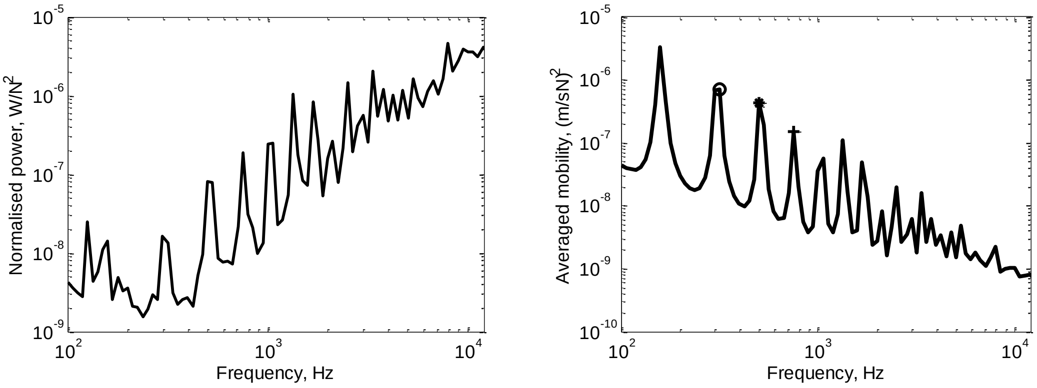

(a) Normalised power (b) Averaged mobility

Figure 6.6 Normalised sound power and averaged mobility of 1:5 scale rail in free space for vertical motion in one-twelfth octave bands

Figure 6.7 compares the numerical results and measurements of the radiation ratio for vertical vibration of the rail in free space. The line dipole behaviour ($\sigma \sim f^3$) can be seen at low frequency, rising to unity (0 dB) above 5 kHz (or 1 kHz for full scale). Above the critical frequency, it can be seen that the measured curve has some peaks and dips between 300 Hz and 900 Hz, not found in the numerical results. The largest dips, indicated by markers, correspond to modes of the rail, as also indicated in Figure 6.6(b). Clearly the acoustic behaviour of these low frequency modes can differ from that of the simple line dipole even above the critical frequency. The measured results at the dips agree better with the predictions including the wavenumber correction (see Section 3.4).

In the frequency range 900 Hz ~ 4 kHz, the experimental results agree very well with the numerical predictions with or without correction. However, the measurement results are larger than the numerical ones above 4 kHz, probably because of the influence of cross-sectional deformation of the rail which occurs at high frequency, whereas the predictions are based on a rigid vertical motion of the rail.

At around the critical frequency, the radiation ratio from the corrected 2D prediction drops dramatically. At and below the critical frequency, the measured result is strongly affected by the end effects of the finite length of the rail, which are not considered in the model. These are similar to corner and edge modes on a plate [27].

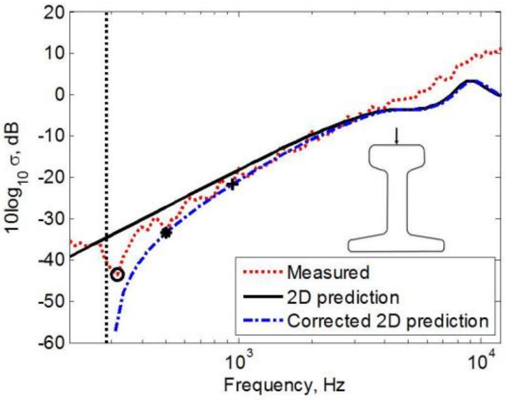

Figure 6.7 Comparison of numerical results and measurements for 1:5 scale rail in free space (the critical frequency is marked by a dotted vertical line)

6.2.1.2 Lateral motion of the rail

For the lateral motion of the rail, the accelerometer positions were at the centre of the web, and the mobility was measured for excitation at the corresponding web position. This was used, instead of an excitation at the rail head, in order to minimise the contribution of torsional vibration of the rail and to give a better comparison with the boundary element results which are based on rigid lateral motion.

Figure 6.8 demonstrates that an adequate signal-to-noise ratio is achieved for both the sound pressure and the vertical acceleration, at least above 300 Hz. Figure 6.9 shows the normalised power and averaged mobility. Compared with the equivalent data for the vertical rail vibration, the lateral vibration has more vibration modes in the same frequency range.

Figure 6.10 presents the comparison of the measured radiation ratio and the results obtained by BEM. As can be seen, good agreement is achieved up to 7 kHz. Between the critical frequency of 700 Hz and about 2 kHz the measurement follows the trend of the corrected BEM predictions, especially at the dips associated with rail modes. At very high frequencies, the measured radiation ratio is greater than the predictions, which is again likely to be due to the neglect of cross-sectional deformation of the rail in the numerical model. Web bending is expected to occur at about 1.5 kHz for the full scale rail [18], which corresponds to 7.5 kHz for the 1:5 scale rail. Below the critical frequency, the sound radiation will be again determined by end effects of the finite length rail, not included in the model.

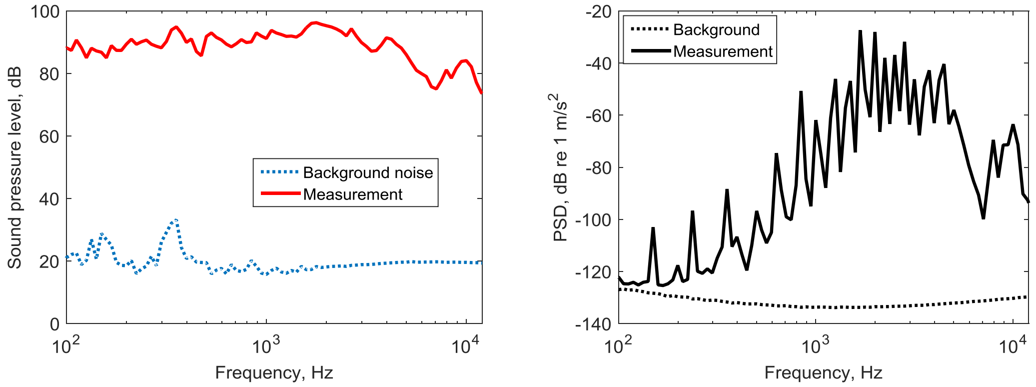

(a) Sound pressure level (b) Acceleration

Figure 6.8 Comparison of measurement and background noise signals for rail in reverberation chamber: lateral motion in one-twelfth octave band

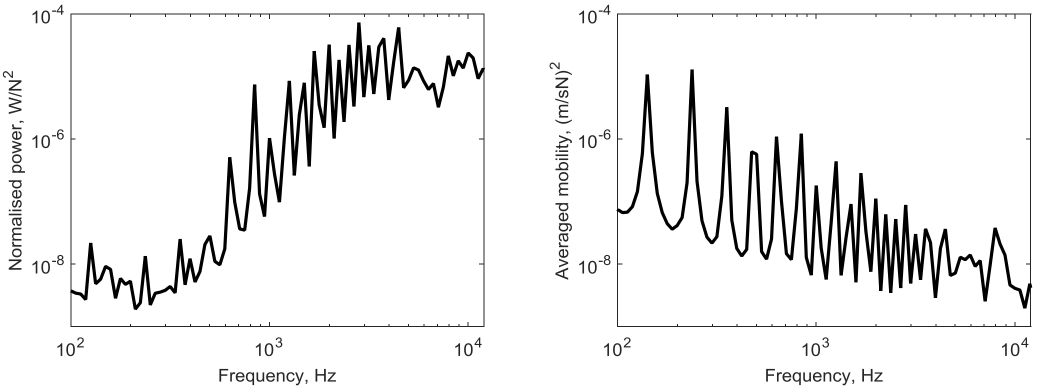

(a) Normalised power (b) Averaged mobility

Figure 6.9 Normalised sound power and averaged mobility of the rail in free space for lateral motion

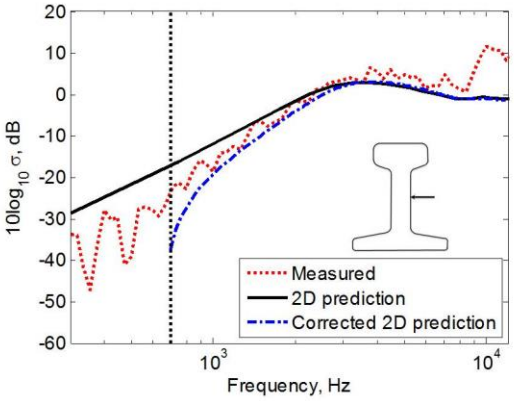

Figure 6.10 Comparison of numerical results and measurements for 1:5 scale rail in free space (the critical frequency is marked by a dotted vertical line)

6.2.2 Rail above rigid ground

The rail was next suspended 20 mm ± 3 mm above the rigid floor of the chamber, as shown in Figure 6.11. It should be noted that the rail was not exactly straight and the ground is not completely flat either. Figure 6.12 presents the effect of introducing the ground in the form of the level difference between the radiation ratio of the rail above the rigid ground and that in free space. Results are given for the measurements and for the predictions with and without the wavenumber corrections.

For vertical motion, in Figure 6.12(a), very good agreement can be seen between the experimental results and the numerical results, especially with the corrected 2D prediction. The markers correspond to the vibration modes indicated in Figure 6.7. It can be seen that the scale rail will radiate more noise than that in free space between 1.5 and 3.5 kHz. The peak observed in the predictions at 9 kHz is not seen in the measurements, possibly due to the variations in the distance above the ground.

In Figure 6.12(b), for the rail vibrating laterally, the same trends are seen in the measurements and the numerical predictions and good agreement is seen, particularly between the experimental results and the corrected 2D prediction. Below 2 kHz, the level difference is greater than 0 dB, which means the rail above the rigid ground will radiate slightly more noise than that in free space.

Figure 6.11 Rail suspended above rigid ground

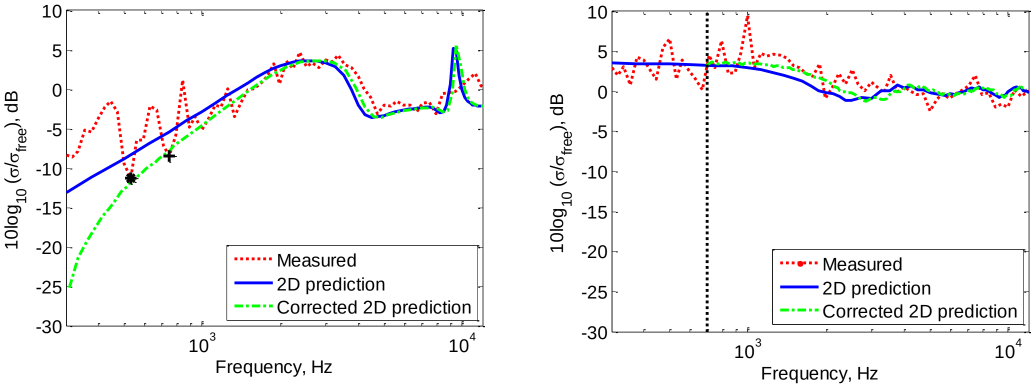

(a) Vertical motion (b) Lateral motion

Figure 6.12 Comparison of numerical results and measurements for 1:5 scale rail 20 mm above rigid ground (the critical frequency is marked by a dotted vertical line)

6.2.3 Rail above absorptive ground

The effects of an absorptive ground on the sound radiation of the rail have been tested by using a layer of melamine foam, with dimensions 2 m × 0.4 m × 50 mm. Again the rail was suspended 20 mm above the foam. The corresponding set-up of the rail is presented in Figure 6.13. Its non-dimensional surface normal impedance was measured in an impedance tube (see Chapter 5) and an equivalent value of the flow resistivity has been deduced as 9400 Pa.s/m^2 by measurement, which is shown in Figure 5.10 in Chapter 5. Note that the presence of the foam in the chamber will modify the reverberation time but since this is not present in Equation (6.2) this will not influence the sound power measurements.

Figure 6.13 Rail 20 mm above absorptive material

A comparison of the measured radiation ratio with the numerical calculations is shown in Figure 6.14. Again these results are normalised to the case of a rail in free space. Figure 6.14(a) compares the measurement with the prediction for vertical motion. The measured results agree well with the predictions above 600 Hz. Above 1500 Hz the absorptive ground causes the rail to radiate less noise than in free space. Figure 6.14(b) shows the corresponding results for lateral vibration of the rail. Here the noise radiation is reduced by the presence of the absorptive ground for all frequencies above 900 Hz. Similar trends are seen in the predictions.

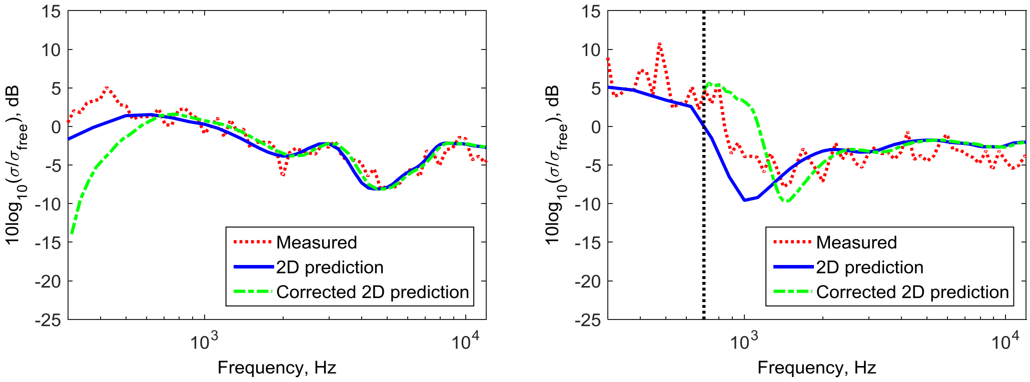

(a) Vertical motion (b) Lateral motion

Figure 6.14 Comparison of numerical results and measurements for 1:5 scale rail 20 mm above absorptive ground (the critical frequency is marked by a dotted vertical line)

6.3 Measurements of sound radiation from the sleeper

Corresponding measurements have been carried out to investigate the sound radiation of a single sleeper and three connected sleepers by using the same reciprocal method [113]. Scale model sleepers, as shown in Figure 6.15, are used. They have dimensions corresponding to 1:5 of the sleeper considered in Chapter 4 and were cast from concrete [89]. The sleeper radiation has been determined experimentally in different configurations for vertical vibration. Measurements have been carried out for a single sleeper in free space, a sleeper embedded in melamine foam to represent an absorptive ground and finally for three sleepers connected by a short length of rail and resting on the foam. In each case comparisons are made between the measured results and numerical predictions carried out for the 1:5 scale model.

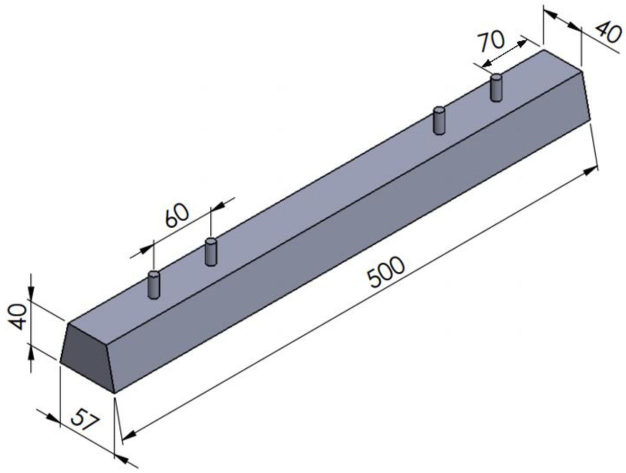

Figure 6.15 Scale model sleeper, dimensions in mm

6.3.1 A single sleeper in free space

The sound radiation of a single sleeper has been measured first with the sleeper hanging in free space. To simulate a sleeper in free space, the scale model sleeper was suspended 1 m above the floor of the large reverberation chamber using elastic cords, as shown in Figure 6.16. Structural reciprocity has been used during the mobility tests, so that the PCB 086C03 impact hammer (mass of 0.16 kg) with a titanium tip is moved along the length of the sleeper and the response is measured at a fixed 'excitation' position. For the spatially averaged mobility, 11 excitation points were used, spaced equally along the sleeper, and one accelerometer position, located at 0.1 m from one end of the sleeper; this corresponds to the rail seat. The corresponding locations are shown in Figure 6.17. For each force position, the frequency response function was obtained as an average over 5 impacts. The input spectrum for the force is found to reduce by 30 dB at 7 kHz, therefore the results for the sleeper will be shown up to 7 kHz.

Figure 6.16 Freely suspended sleeper

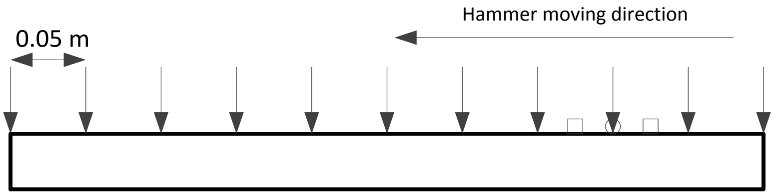

Figure 6.17 Hammer (↓) and accelerometer (o) positions for sleeper, length 0.5 m (dimensions in m)

A comparison of the measured sound pressure level with the background noise in the chamber is shown in Figure 6.18(a). Figure 6.18(b) presents corresponding results for the vertical acceleration signal on the sleeper. As can be seen, an adequate signal-to-noise ratio is achieved for both the sound pressure and the acceleration between about 160 Hz and 7 kHz, although the signal-to-noise ratio for the acceleration is only around 10 dB below 1 kHz. Figure 6.19(a) presents the normalised power obtained by the reciprocity method. The spatially averaged transfer mobility of the sleeper is shown in Figure 6.19(b). These results are again all shown in one-twelfth octave bands. Peaks can be seen in the normalised power and average mobility at the natural frequencies of the 1:5 scale sleeper: 550 Hz, 1500 Hz, 2800 Hz, 4400 Hz, etc.

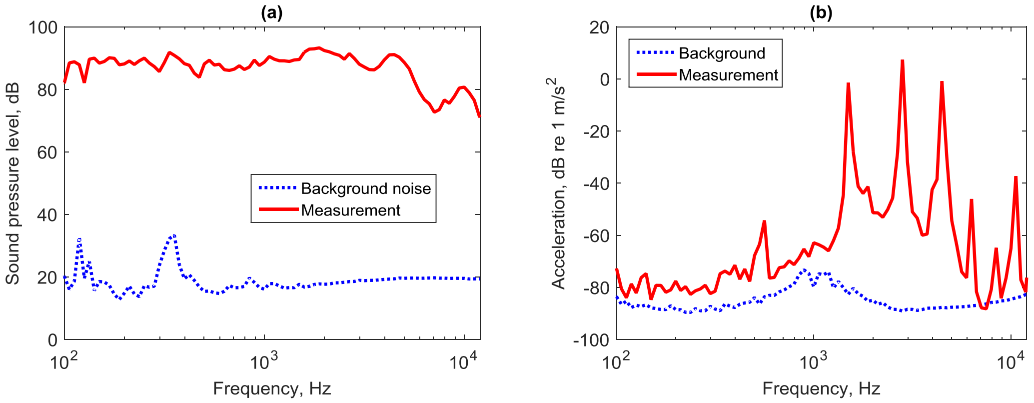

Figure 6.18 Comparison of measured spectra and background noise signals in one-twelfth octave bands for sleeper in reverberation chamber. (a) Sound pressure level; (b) acceleration

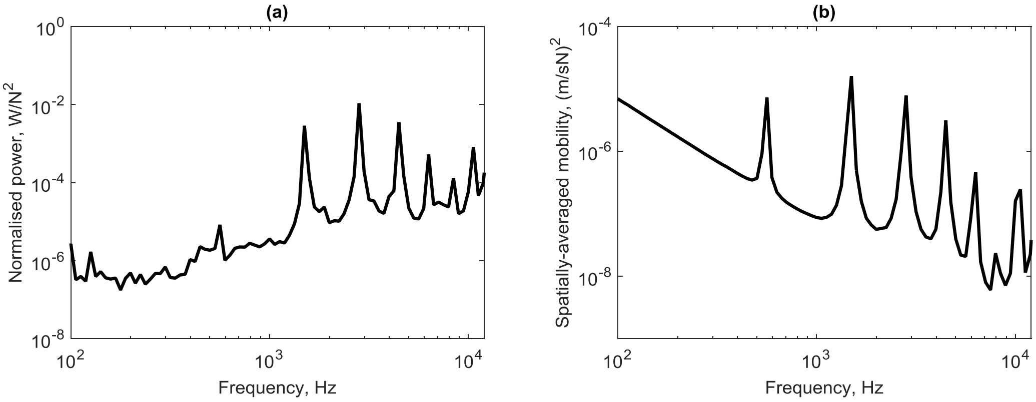

Figure 6.19 (a) Normalised sound power and (b) spatially-averaged mobility of sleeper in one-twelfth octave bands for single sleeper in free space

The effects of the sleeper flexibility have also been taken into account in the numerical model. For the numerical prediction of the sleeper radiation, the discrete bending resonances are important, so its vibration is modelled as a free-free beam and its sound radiation is modelled using a three-dimensional boundary element model using this vibration as input. An analytical model of a finite Timoshenko beam, as in Section 4.1, is used here to represent the freely suspended scale sleeper in the experiment. The driving point mobility is predicted by the Timoshenko beam model, when the excitation point is at 0.1 m from one end. This is compared with the corresponding measured result in Figure 6.20. It can be seen that the analytical predictions agree very well with the measurement results. To achieve this agreement, the Young's modulus was adjusted to a value of 2.76×10^{10} N/m^2 and the density is set to 2200 kg/m^3. A value of 0.01 is used for the sleeper damping loss factor in the model. The peaks in the measurements at around 2 kHz are probably the torsion modes of the sleeper excited, which are ignored in the analytical model.

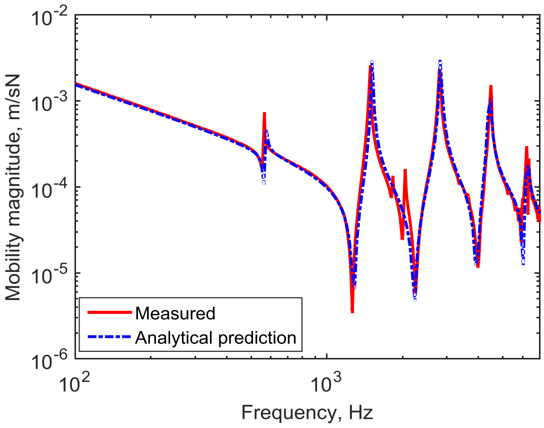

Figure 6.20 Comparison of measured point mobility and analytical prediction

Figure 6.21 presents the measured radiation ratio of the sleeper obtained from the above results. Predictions using the 3D BE model are given for both rigid vertical motion and for a flexible sleeper. The rigid scale sleeper has the full length of 0.5 m × 0.04 m. It can be seen that the experimental results agree well with the numerical predictions. At low frequency, the sleeper sound radiation is overestimated by the rigid sleeper model, especially at around 550 Hz. The dip in the radiation ratio at around 550 Hz corresponds to the first bending mode of the sleeper. It can be seen that the radiation ratio determined with the flexibility effects agrees very well with the measurements, with the dip in the measurements at around 550 Hz reproduced in the numerical predictions. Above 5 kHz, where the radiation ratio should tend to unity, the measured results appear too high. The reason for this is unclear.

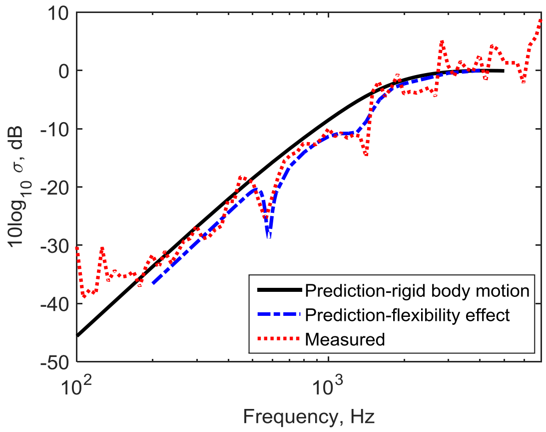

Figure 6.21 Comparison of radiation ratio from numerical prediction and measurement for the scale model sleeper in free space

6.3.2 A single sleeper embedded in foam

The effect of an absorptive ground on the sleeper radiation has been tested by embedding the sleeper in melamine foam, as shown in Figure 6.22. For this purpose, pieces of foam were cut to shape to match the profile of the sleeper. The overall dimensions of the foam were 1 m × 0.4 m × 0.1 m.

Figure 6.23 shows the boundary element model for the sleeper embedded in melamine foam, while Figure 6.24 presents the measurement results and the corresponding numerical predictions. The sleeper has a length of 0.25 m × 0.04 m before the symmetry planes are implemented in the numerical model in order to approximate the flexible behaviour of the sleeper. Quite good agreement can be seen between them. Above 5 kHz, the measured results again appear too high.

Figure 6.22 Sleeper embedded in melamine foam

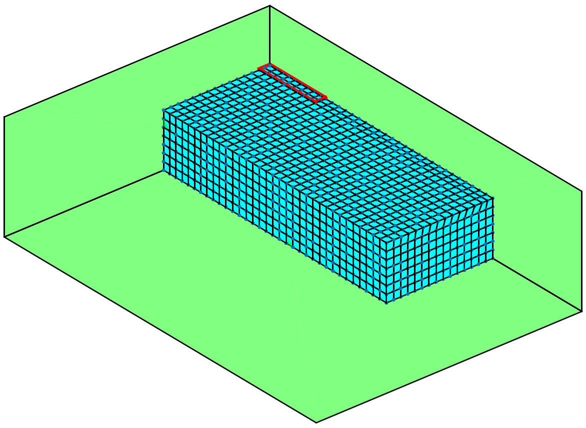

Figure 6.23 One quarter mesh for numerical predictions of the sound radiation of the sleeper embedded in melamine foam (high frequency model)

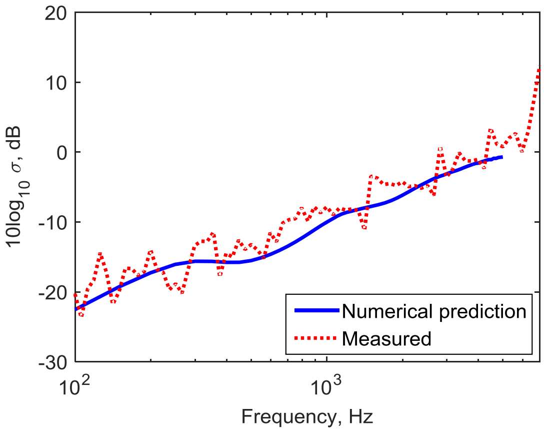

Figure 6.24 Comparison of measured radiation ratio and numerical predictions for a single sleeper embedded in melamine foam

6.3.3 Multiple sleepers

The sound radiation from three sleepers has also been investigated experimentally. Three sleepers were connected by two short 1:5 scale rails of length 0.36 m. These were attached to the sleepers using spring clips; there were no rail pads between the rails and the sleepers in order to maximise the vibration transmission from the rails to the sleepers. The sleepers rested on melamine foam with dimensions 1.2 m × 1 m × 0.05 m, as shown in Figure 6.25. The assembly was measured in the reverberation chamber using the same method as previously. The transfer mobility was measured for excitation at 13 points spaced equally along each rail and 11 points spaced equally along each sleeper, with two accelerometers located at the centre of the railhead, above the central sleeper on each rail. By reciprocity these measurements represent the transfer mobility from a force at the railhead to the velocity on the rail or sleeper.

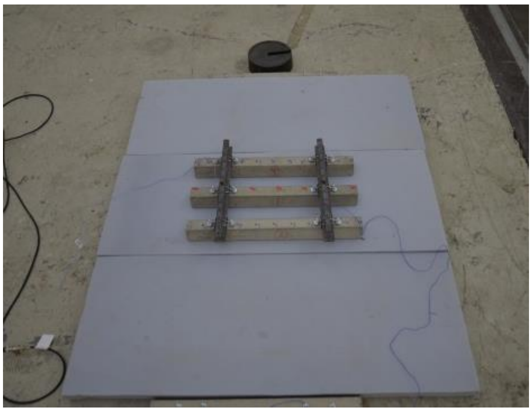

Figure 6.25 Experimental set-up for three sleepers resting on foam

Figure 6.26 shows the ratio of the averaged mobility amplitude of the outer sleepers to that of the middle one. As can be seen, this mobility ratio differs from those shown in Figure 4.15, mainly because of the short length of the rails used in the measurement.

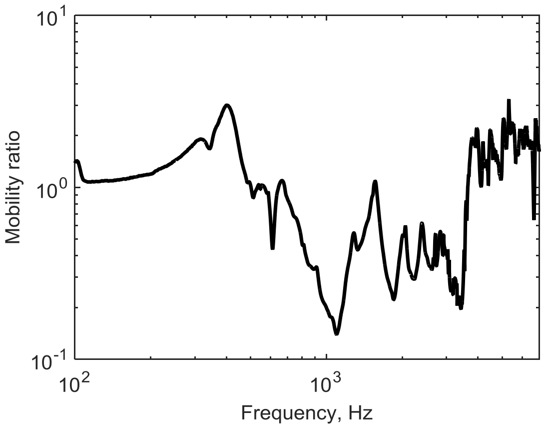

Figure 6.26 Averaged mobility amplitude of the outer sleepers relative to the central one

Figure 6.27 presents the measured sound power from the three sleepers and two short rails normalised by the mean square velocity of the central sleeper. Comparison is made with the sound power from the rails estimated by using Equation (1.1). For these predictions, a weighted average of the radiation ratio of a rail attached to a rigid ground and a rail above an absorptive ground is used, as shown in Figure 6.28. Specifically, out of the distance 0.12 m between sleepers, 0.04 m is directly above the sleeper and the remaining 0.08 m is above the foam at a distance of 0.04 m. Thus, the radiation ratio of a rail attached to a rigid ground is then taken with a weight of 1/3 and the radiation ratio of a rail above an absorptive ground with a weight of 2/3 give the weighted average radiation ratio of the rail in this case. Although this is an approximation it is used here to indicate the frequency region where the rail may influence the measurement. The predicted sound power from the rails is again shown normalised by the mean square velocity of the central sleeper. As can be seen, the sound power from the rail gives the dominant contribution at high frequency, especially above 2.2 kHz, whereas it is mostly at least 10 dB less than the total noise below this frequency, indicating that the sleeper radiation dominates at low frequency. Thus it may be concluded that the contribution from the rails can be ignored below 2 kHz.

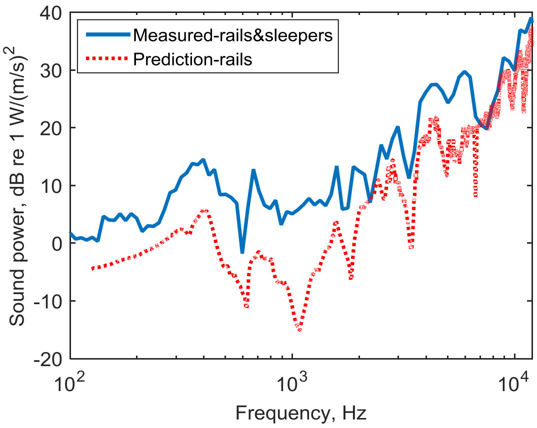

Figure 6.27 Measured sound power for three sleepers connected by rails resting on melamine foam. The power is shown normalised by the mean square velocity of the central sleeper. For comparison the estimated sound power from the rails is also shown

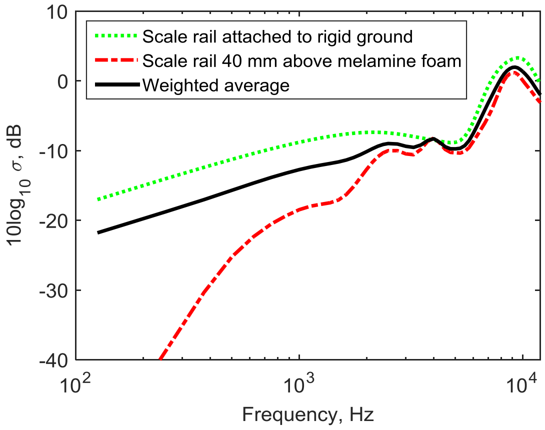

Figure 6.28 Averaged radiation ratio for the rail connected to the sleepers in the measurement

Finally, the sound power from the three connected sleepers is compared with the power that would be radiated by the three single sleepers with the same vibration levels. Numerical and experimental results are shown in Figure 6.29 in the form of the ratio between the power from the connected sleepers and that from the same sleepers radiating individually. In the predictions the vibration of the outer sleepers is assigned an amplitude equal to the measured mobility ratio from Figure 6.26 while the central sleeper has unit vibration amplitude. The phase of the three sleepers are assumed to be in phase. Measured results are not shown below 160 Hz, where the signal-to-noise ratio in the sound power measurement was very low. As can be seen, reasonable agreement is found between the numerical and measured results, which both show a similar tendency to the earlier predictions in Figure 4.21. Above 2 kHz the measured results are higher than the predictions, due to the dominant contribution of the rails.

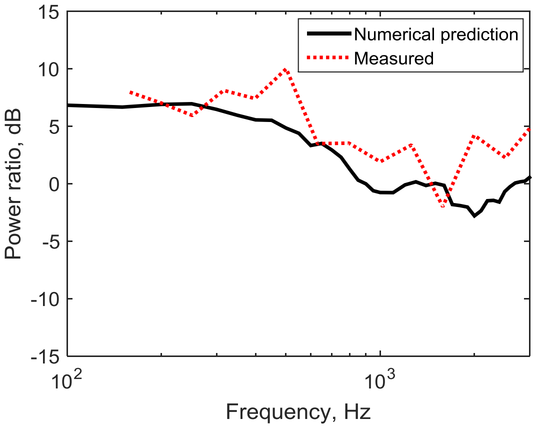

Figure 6.29 Ratio of sound power radiated by three connected sleepers to that obtained for the three sleepers separately

6.4 Effects of ballast absorption on the sound radiation from the rail and sleeper

In Chapter 5, it has been shown that the ballast has the acoustic properties of a porous material and the Johnson-Allard local reaction model has been proposed for the modelling of its absorption. The effects of ballast absorption on the sound radiation from the rail and sleeper are, therefore, investigated here. The 1:5 scale rail was measured when it is freely suspended above the ballast for both vertical and lateral excitation. This is followed by measurements of the scale sleeper (one single sleeper and multiple sleepers) embedded in ballast. For each case, comparison is made with numerical predictions obtained by considering the ballast absorption in the BEM models.

6.4.1.1 *Effects of ballast on rail radiation*

The effects of ballast absorption on the sound radiation of the rail have been tested by using a layer of 1:5 scale ballast, with dimensions 2.1 m × 1.25 m × 60 mm. The rail was supported an average of 20 mm above the ballast surface and the radiation ratio was measured by using the reciprocal method for excitation in both vertical and lateral directions in the large reverberation chamber. The corresponding set-up of the rail is presented in Figure 6.30. The surface normal impedance of the scale ballast in this case is predicted by using Equation (5.12), which presented in Figure 6.31. This impedance is next introduced into the BEM model to obtain numerical predictions of the rail radiation in this configuration.

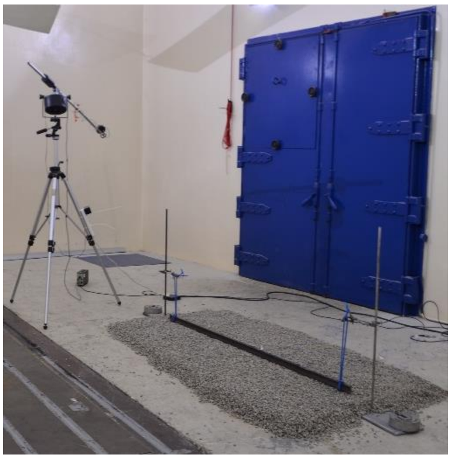

Figure 6.30 Rail 20 mm above the scale ballast on the rigid ground

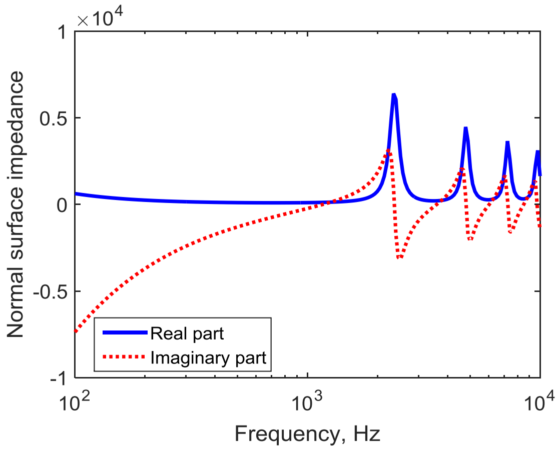

Figure 6.31 Predicted surface normal impedance for the scale ballast with the depth of 60 mm

A comparison of the numerical calculations with the measured radiation ratio is shown in Figure 6.32. These results are normalised to the case of a rail in free space. Figure 6.32(a) compares the measurement with the prediction for vertical motion. The measured results agree reasonably well with the predictions, especially above 1800 Hz. The dip in the predictions at 1.5 kHz for the impedance used in the Johnson-Allard model is due to the thickness of the ballast. When the thickness is one quarter of the wavelength the absorption is maximum. Above 3 kHz the absorptive ground causes the rail to radiate less noise than in free space, whereas at low frequencies it generally radiates more noise than in free space. Figure 6.32(b) shows the corresponding results for lateral vibration of the rail. As can be seen, the noise radiation is reduced by the presence of the ballast for all frequencies above 1 kHz. Similar trends are seen in the predictions, although the measured results are around 6 dB lower than the predictions above 1.5 kHz. The reason for this is unclear, but may be related to the use of a locally reacting model for the ballast.

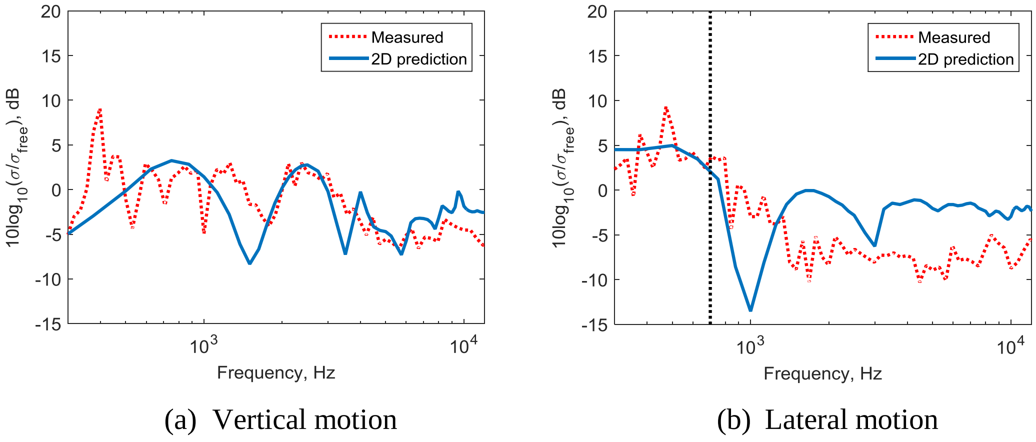

(a) Vertical motion (b) Lateral motion

Figure 6.32 Comparison of numerical results and measurements for 1:5 scale rail 20 mm above absorptive ground (the critical frequency is marked by a dotted vertical line)

6.4.1.2 *Effects of ballast on sleeper radiation*

The effects of the ballast on the sleeper radiation are studied by first embedding a single sleeper in the ballast on rigid ground. The dimensions of the ballast are again 2.1 m × 1.25 m × 60 mm. The corresponding experimental set-up is presented in Figure 6.33. The top surface of the ballast is flush with the top of the sleeper.

Figure 6.33 Sleeper embedded in the ballast

The radiation ratio of the sleeper was measured for vertical excitation. The results are shown in Figure 6.34, and are compared with those for the scale sleeper suspended in free space. In the numerical model for the sleeper embedded in ballast, the sleeper is moving rigidly but the dimensions of the sleeper are 0.25 m × 0.04 m in order to approximate the effect of the flexible behaviour of the sleeper. The peak at around 300 Hz in the measurement is probably contaminated by the vibration of the floor. The source of this vibration is unknown but it was seen in a number of the measurements. As it is shown, the sound radiation for the sleeper embedded in ballast is higher than that of the sleeper in free space, especially at low frequency. There are various possible reasons for the higher radiation ratio of the embedded sleeper compared with the case of a sleeper in free space. Firstly the sleeper tends to have the characteristics of a monopole when it is embedded in ballast instead of a dipole when in free space. This changes the slope of the radiation ratio curve at low frequencies and is seen in the predictions. Secondly the vibration of the ballast itself may increase the radiated noise. This will be investigated in Section 6.5. As can also be seen, for the sleeper embedded in ballast, there are some dips, marked as 'o', in the measured curve, which correspond to the vibration modes of the sleeper, whereas the dips in the numerical predictions are caused by the thickness in the Johnson-Allard impedance model.

Comparison is also made with the predictions for the ballast embedded in rigid ground, which takes the effect of the flexible behaviour of the sleeper into account by using 0.25 m × 0.04 m for the dimensions of the sleeper in the model. Reasonable agreement in the predictions can be seen between the sleeper embedded in ballast and the sleeper embedded in rigid ground, except in the frequencies around the dips for the sleeper embedded in ballast.

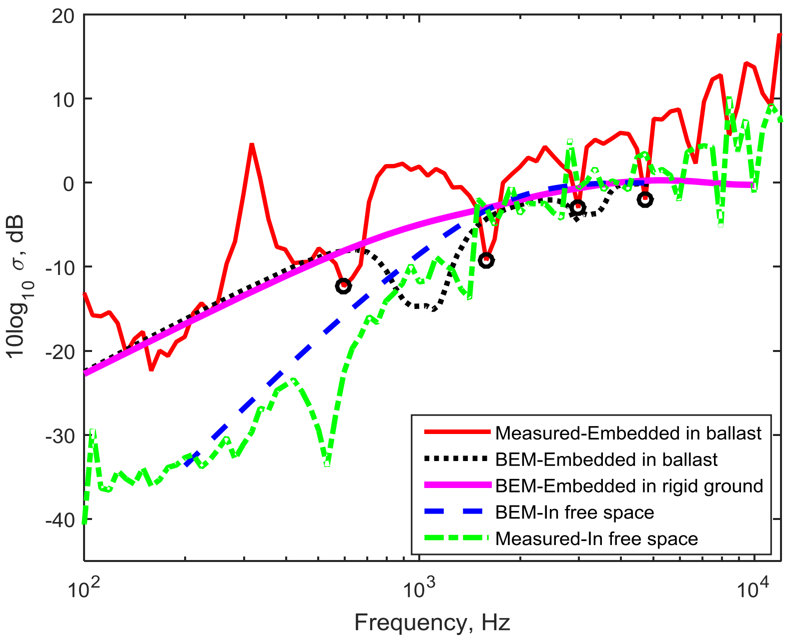

Figure 6.34 Comparison of measured radiation ratio and numerical predictions for a single sleeper embedded in the ballast

The influence of the ballast for multiple sleepers is also investigated experimentally, as shown in Figure 6.35. The three sleepers used in this configuration are the same as those used in Section 6.3.3, connected by short sections of rails. Again, there were no rail pads between the rails and the sleepers in order to maximise the vibration transmission from the rails to the sleepers. The dimensions of the ballast were 2 m × 0.8 m × 100 mm.

Figure 6.35 Experimental set-up for three sleepers embedded in ballast

Figure 6.36 presents the measured sound power from the three sleepers and two short rails. For comparison the sound power from the rails has been estimated by using the corresponding radiation ratio from Section 6.4.1.1 and Chapter 4. Specifically, in this case, a weighted average of the radiation ratio of a rail attached to a rigid ground (a weight of 1/3) and a rail 20 mm above the absorptive ballast (a weight of 2/3) is used. The corresponding averaged radiation ratio is shown in Figure 6.37. It shows that the sound power from the rails gives no dominant contributions except at the frequencies of around 2.5 kHz and 7.5 kHz. Therefore, the radiation ratio of the sleepers can be obtained by using Equation (6.1) in this configuration at least up to 2 kHz.

Figure 6.38 shows the measured result expressed as a radiation ratio and compared with the numerical predictions. Again, the peak at around 300 Hz in the measurement is probably due to the contamination from the vibration of the floor. In the boundary element model, the dimensions of the sleeper are set to 0.25 m × 0.04 m in order to approximate the effect of the flexible behaviour of the sleepers. The vibration of the three sleepers is assumed to be in the ratio 0.5:1:0.5. As can be seen, the measured results are generally higher than the predictions. The results above 2 kHz are probably affected by the rail noise but at lower frequency this is not the case. One possible reason is that the vibration of the ballast itself again increase the radiated noise. Dips again are caused by the thickness in the Johnson-Allard model.

The numerical prediction for the three sleepers embedded in a rigid ground is also shown in this figure. Again, in the frequencies around the dips for the sleeper embedded in ballast, the agreement between these two predictions is poor.

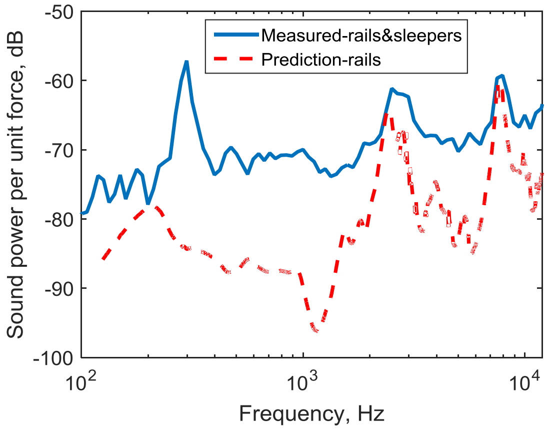

Figure 6.36 Measured sound power for three sleepers connected by rails embedded in the ballast. For comparison the estimated sound power from the rails is also shown

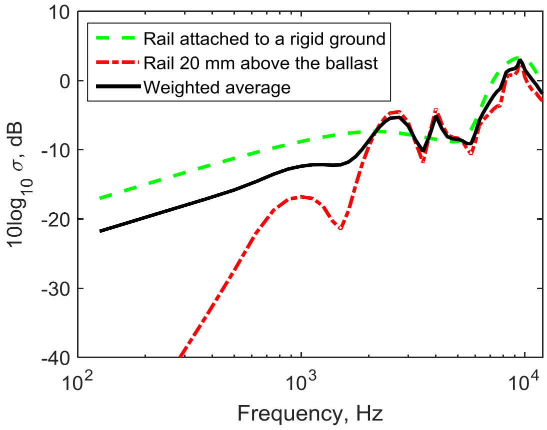

Figure 6.37 Averaged radiation ratio for the rail connecting three sleepers embedded in the ballast

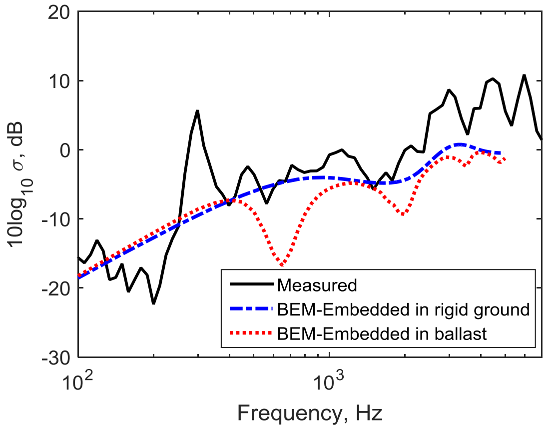

Figure 6.38 Comparison of measured radiation ratio and numerical predictions for three sleepers embedded in the ballast

6.5 Effects of ballast vibration on the sound radiation from railway sleepers

It has been seen in Section 6.4 that more noise is radiated when the sleeper is embedded in ballast. Although this is partly due to the presence of the ground, another possible reason is that the ballast vibrates, induced by the sleeper vibration, and this radiates sound. The ballast vibration is explored in this section. A scanning laser vibrometer has been used to measure the vibration of the ballast in the 1:5 scale model when the sleeper was excited using an instrumented hammer. The effect of ballast vibration on the sleeper radiation is then estimated.

6.5.1 Measurements of ballast vibration

6.5.1.1 *A single sleeper*

The first case considered is where a single sleeper is embedded in ballast located on a wooden base. Figure 6.39 shows the corresponding experimental set up. The 1:5 ballast was 60 mm thick below the sleeper and 100 mm deep overall. It was resting on a layer of 1 mm neoprene on a thick wooden base with dimensions of 2 m × 0.8 m. In order to improve the reflection of the ballast to the laser scan, small pieces of reflective strip were attached to some of the ballast particles measured.

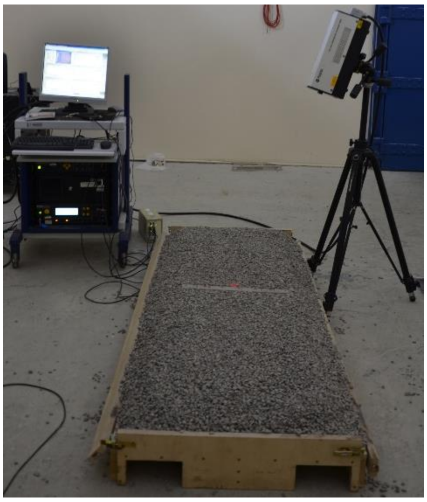

Figure 6.39 Sleeper embedded in ballast

In the tests, two excitation points were used on the sleeper. One is at the point where the rail would be connected to the sleeper; the other is in the middle of the sleeper. The ballast surface was scanned to one side of the sleeper to obtain transfer mobilities between the force on the sleeper and the vibration of the ballast. Figure 6.40 shows the grid of measurement points.

Approximately 100 points were used to capture the ballast vibration, while 7 points were used for sleeper.

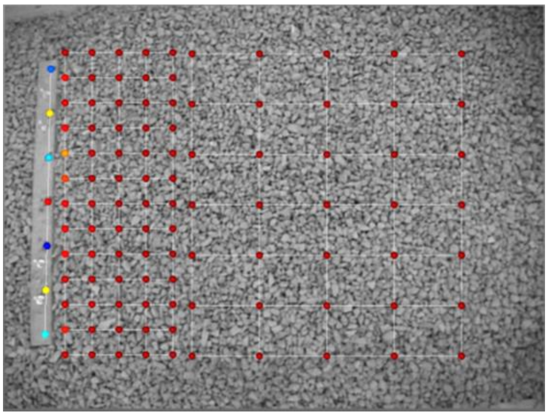

Figure 6.40 Measurement grid for ballast and sleeper vibration for sleeper embedded in ballast located on a wooden base

Figure 6.41 shows the averaged mean square velocity of the sleeper and ballast at different distances away from the sleeper when the sleeper is excited at the two different points. Each line corresponds to the average over positions at a certain distance from the sleeper. The values in the figure legend are the distances away from the sleeper centre. As can be seen, in Figure 6.41(a), the vibration level of the sleeper is larger than that of the ballast. Generally speaking, below 1 kHz the vibration level becomes smaller as the distance increases. At low frequencies, some influence of vibration modes of the wooden box can be seen. Above 1 kHz, the measurements are contaminated by background noise particularly at the larger distances. Results around 1 kHz have been omitted due to an obvious contamination with background noise. The peak in the sleeper vibration at around 1.68 kHz is the second vibration mode of the sleeper (the first is not excited in this case as the excitation point is close to a nodal point).

In Figure 6.41(b), a similar trend can be seen for the comparison of sleeper vibration and ballast vibration for the excitation point at the centre of the sleeper. The sleeper vibration level is larger than that of the ballast. As well as the second mode of the sleeper, the first mode of the sleeper at around 630 Hz is excited. This is at a higher frequency than for the free sleeper (550 Hz) due to the influence of the ballast stiffness. It also can be seen that, below 630 Hz, the reduction of the ballast vibration at a certain distance away from the sleeper is less when the sleeper is excited at point 2 than excitation point 1.

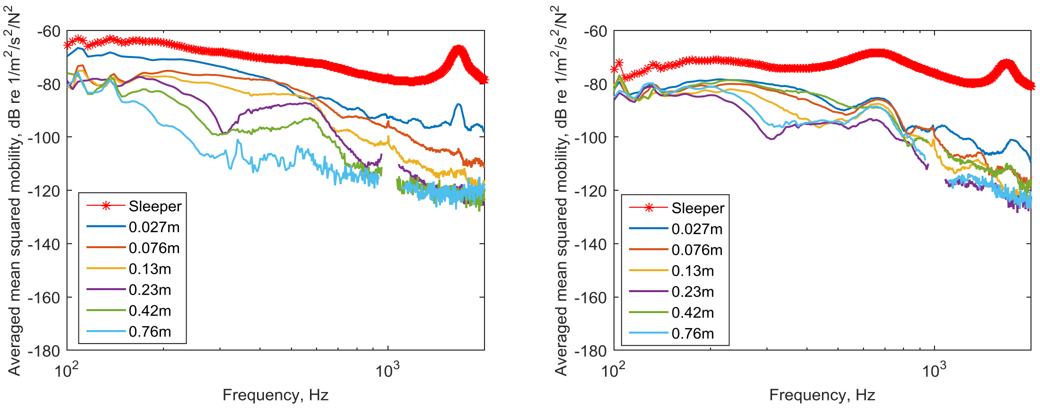

(a) Excitation point 1 (b) Excitation point 2

Figure 6.41 Comparison of sleeper vibration and ballast vibration at different distances for sleeper embedded in ballast located on a wooden base

Taking the sleeper vibration as the reference value, the ballast vibration is presented at various frequencies in Figure 6.42 as a function of the distance from the sleeper. As can be seen, the ballast vibration decays with distance over the whole frequency range, but the decay is more gradual at low frequency.

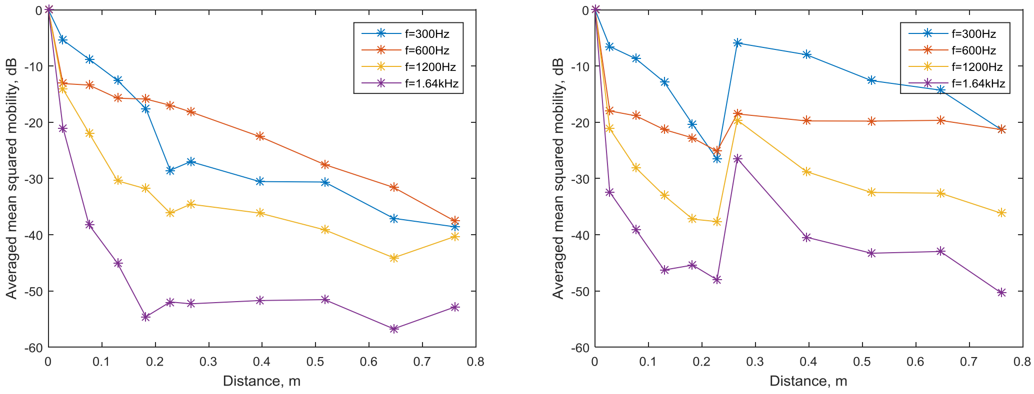

(a) Excitation point 1 (b) Excitation point 2

Figure 6.42 Vibration decay with distance for sleeper embedded in ballast located on a wooden base

Overall, the results are very similar for the two excitation points. It is sufficient, therefore, to present results for the sleeper excited at the point where the rail is connected in the following sections.

Next the experiment has been repeated with the ballast laid directly on the floor of the reverberation room without neoprene. Again the sleeper was embedded in the ballast with 60 mm of ballast beneath the sleeper.

Figure 6.43 shows the averaged mean square mobility of the sleeper and the ballast at different distances away from the sleeper on the rigid ground. As can be seen, again, the vibration level of the sleeper is much higher than that of the ballast. Compared with the results for the ballast in the wooden box, the ballast vibration at a certain distance away from the sleeper is smaller when the ballast is located on the rigid ground. It is also can be seen that, for the rigid ground, the ballast vibration drops dramatically below 300 Hz compared with that of the sleeper, whereas in the box, below 200 Hz, the ballast vibration drops very little beyond 0.1 m. Clearly at low frequencies the ballast vibration is strongly affected by the stiffness of the foundation.

Figure 6.44 presents these results as a decay with distance of the ballast vibration at different frequencies. The average sleeper vibration is taken as the reference value. As can be seen, for both cases, the ballast vibration decays with distance over the whole frequency range, but the decay is smaller at low frequency. Also, at a given frequency, the decay of the ballast vibration with distance when the ballast is contained in the wooden box (see Figure 6.42(a)) is lower than on the rigid ground.

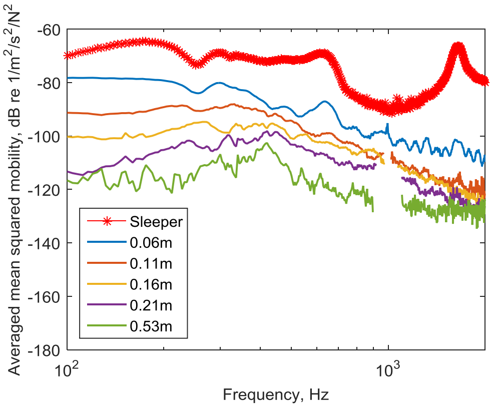

Figure 6.43 Comparison of sleeper vibration and ballast vibration at different distances for sleeper embedded in ballast

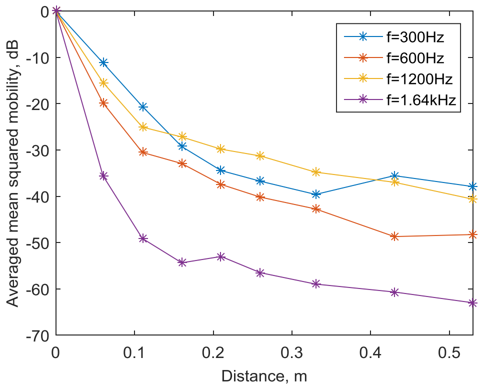

Figure 6.44 Vibration decay with distance for sleeper embedded in ballast

6.5.1.2 *Multiple sleepers*

The same test procedure has been applied to three sleepers embedded in ballast with a 100 mm depth (60 mm beneath the bottom of the sleeper) when the centre of the railhead above the central sleeper was excited by an impact hammer. A railpad, with a stiffness of 18 MN/m, was located between the rails and the concrete sleepers (details of the railpad are given in Section 7.1). This arrangement was located on the rigid ground. Figure 6.45 shows the corresponding mesh points on the ballast and sleepers.

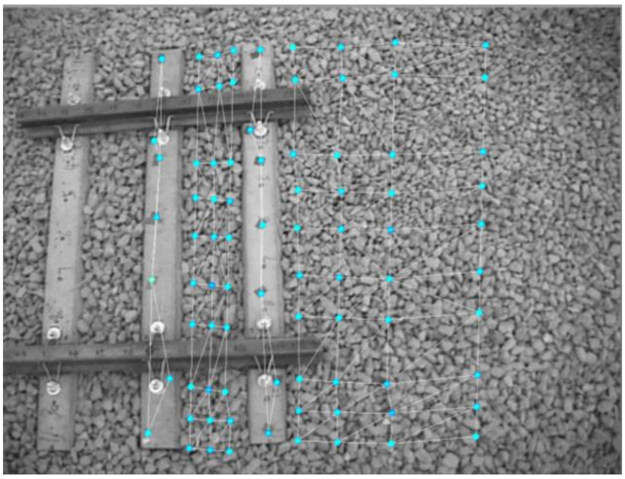

Figure 6.45 Measurement grid for ballast and sleeper vibration for three sleepers embedded in ballast

The averaged mean square mobilities of the sleepers and the ballast at different distances away from the sleepers are presented in Figure 6.46. Sleeper 1 corresponds to the central one, whereas Sleeper 2 is one of the outside sleepers. Similar results are found to those for the single sleeper embedded in ballast. The vibration of the sleepers is generally higher than that of the ballast, whereas the vibration level of the ballast decreases as the distance away from the sleeper increases.

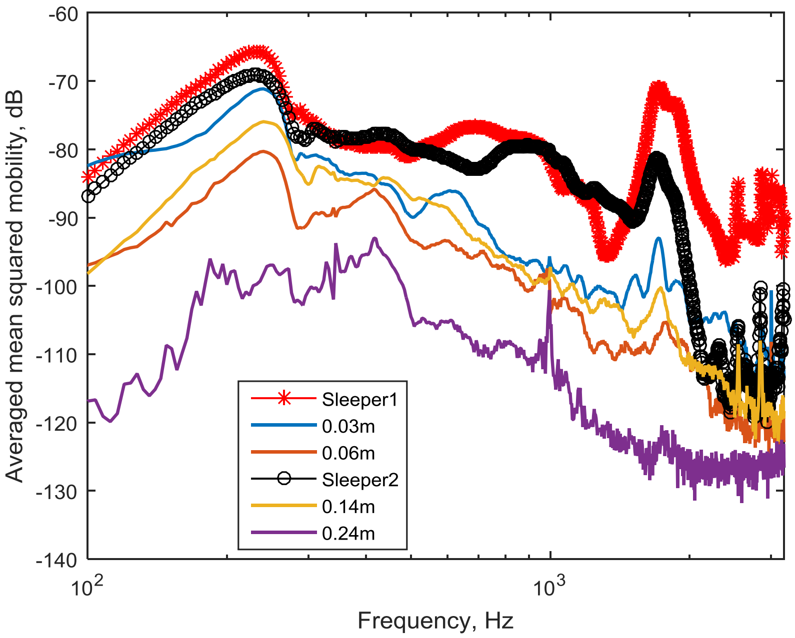

Figure 6.46 Comparison of sleeper vibration and ballast vibration at different distances for three sleepers embedded in ballast

The ballast vibration and the sleeper vibration at various frequencies, normalised by that of the central sleeper, is presented in Figure 6.47. As can be seen, the vibration level of the ballast between the two sleepers is lower than the sleeper vibration. The decay of the ballast vibration on the outside of the sleeper 2, is similar to that in Figure 6.44 for a single sleeper.

In order to validate the experimental results, the measured vibration of the scale ballast 0.03 m away from the central sleeper is compared with the vibration of the full size ballast 0.2 m way from a sleeper on site[2]. For the measurements of the full size system on site, the vibration of the ballast and sleepers was recorded when a Javelin train with 6 cars ran over the track with a speed of 60 m/s; detailed information on this measurement can be found in [117]. Figure 6.48 shows the results, where the frequency range from the scale ballast is shifted to the original one by dividing by a factor 5. In both cases, the ballast vibration is normalised by that of the corresponding sleepers. As can be seen, quite good agreement is found between them. From this it can be concluded that the scale ballast on the rigid base is representative of a practical situation.

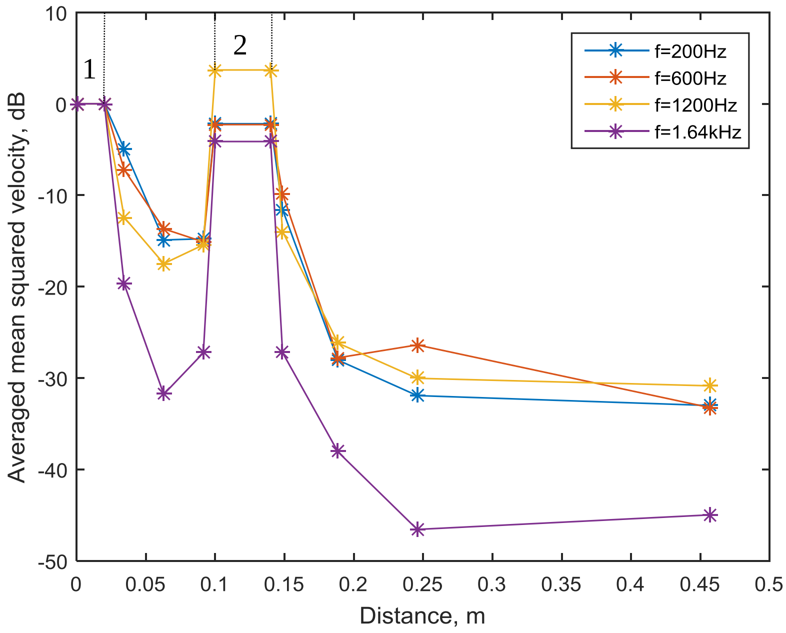

Figure 6.47 Vibration decay with distance for three sleepers embedded in ballast. The numbers 1 and 2 in the figure indicate the positions of sleeper 1and sleeper 2

---

[2] These measurements were taken by David Milne using an instrumented ballast stones.

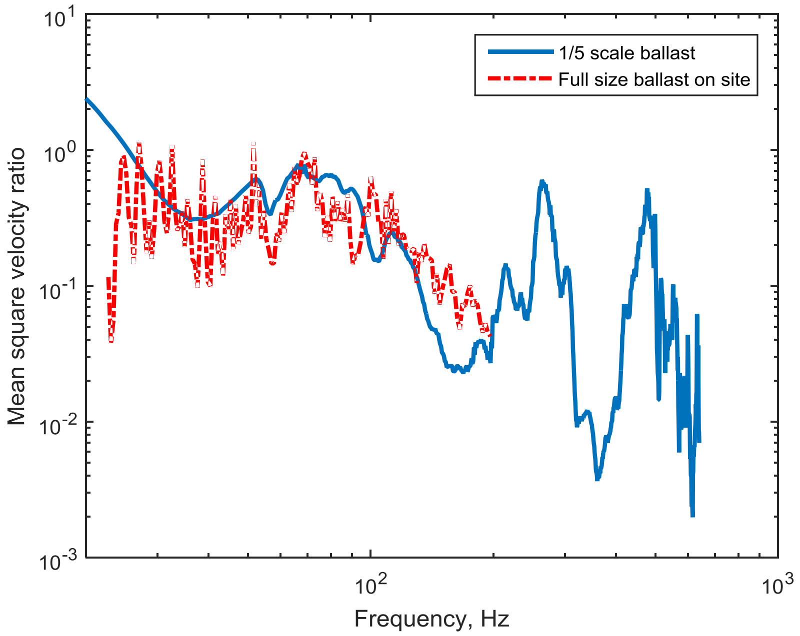

Figure 6.48 Comparison of ballast vibration normalised by the central sleeper vibration between the 1:5 scale model and the full size model (results at frequencies corresponding to full size scale)

6.5.2 Estimation of effects of ballast vibration on sleeper radiation

Although the ballast has a lower vibration level than the sleeper, it may still contribute to the noise due to its larger radiating area. Therefore, the sound power caused by the ballast vibration is estimated here.

The effect of the ballast vibration on the sleeper radiation has been evaluated based on the Rayleigh integral [95]. This is based on the assumption that the surface is non-absorptive which will give an over-estimate of the radiation in this case. The radiated power is calculated when including an increasing area of the ballast in the Rayleigh integral. The measured ballast vibration levels per unit force obtained using the scanning laser vibrometer are used in this calculation, although the phase is ignored for simplicity initially. This will yield an upper bound for the radiated sound.

The influence of the ballast vibration on the sound radiation from a single sleeper is evaluated first. The results are shown in Figure 6.49 for the cases studied in Section 6.5.1.1. The values in the legend indicate the width of the ballast on one side of the sleeper included in the calculation; symmetry is adopted to consider the ballast on the non-measured side of the sleeper as well. As can be seen, for both cases, the ballast vibration has an impact on the sound power of the system below about 1500 Hz (300 Hz at full scale). Above 500 Hz (100 Hz at full scale), only the ballast vibration close to the sleeper (0.076 m) contributes significantly to the sound power and the increase in noise is less than 5 dB. Below this frequency an increase of around 9 dB is found due to the ballast.

When the ballast is located on the rigid ground, the increase in the sound power due to the ballast is smaller than when it is located in the wooden box and only the area within 0.11 m contributes significantly. The ballast radiates more noise in the former case because of the compliance of the elastic base so that a greater area of ballast is involved.

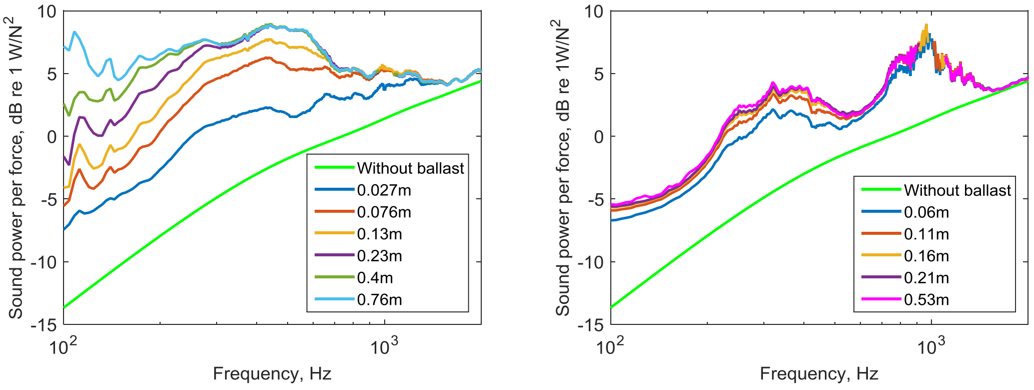

(a) In wooden box (b) On rigid ground

Figure 6.49 Sound power of the sleeper embedded in ballast without phase information on the ballast

The effect of ballast vibration on the sound radiation is also evaluated for multiple sleepers, for the case when the three sleepers are embedded in ballast, as shown in Figure 6.45. In this case, the influence of the ballast between the sleepers on the sleeper radiation is estimated. The phase information of the ballast vibration is also taken into account in the prediction. Specifically, the phase of the ballast vibration at positions, which are in a line perpendicular to one end of the central sleeper with distances of 0.03 m, 0.06 m and 0.08 m away from the sleepers, is normalised by that of the sleeper at the excitation point. This relative phase is shown in Figure 6.50. As can be seen, the phase of the ballast at these three points does not show a regular pattern, especially at high frequencies. Thus, the phases of 1 rad, -1.5 rad and -0.5 rad (mean values for the phase differences based on observation) are assigned to all the ballast at these three distances away from the middle sleeper.

Figure 6.51 shows the estimated contribution of the ballast vibration to the sound power in this system. As can be seen, when the ballast phase is not included in the estimation, below 1.2 kHz (240 Hz at full scale), the ballast vibration at different distances affects the sound power. Above this frequency, the ballast vibration close to the sleeper makes the biggest contribution to the sound power of the system. If the phase of the ballast is considered in the predictions, the evaluations are around 2 dB lower than the result neglecting phase details for the same radiating area only below 1 kHz (200 Hz at full size).

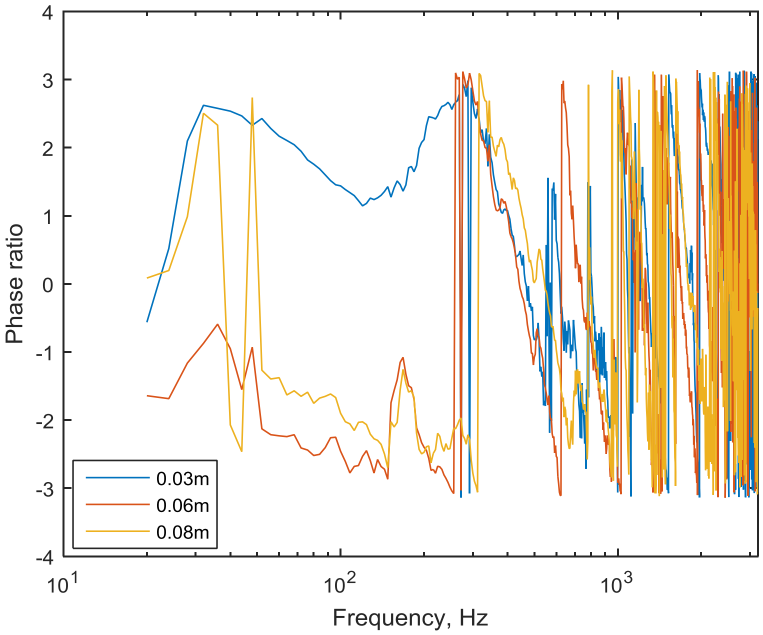

Figure 6.50 Phase of the ballast normalised by that of the central sleeper at the excitation point

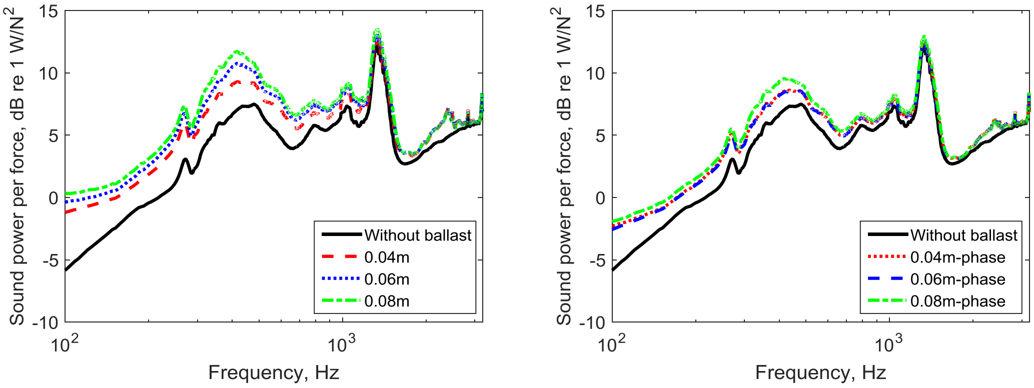

(a) Without phase (b) With phase

Figure 6.51 Sound power of the sleeper embedded in ballast with and without phase of the ballast

The evaluated effects of the ballast vibration on the sleeper radiation for multiple sleepers embedded in the ballast are shown in dB in Figure 6.52. Only the distance of 0.08 m away from the sleeper centre is used to present the maximum influence. As can be seen, the differences made by the ballast vibration to the sleeper radiation is less than 4 dB in the frequency range 100 ~ 3200 Hz (20 ~ 640 Hz at full scale). The influence caused by the ballast vibration on the sleeper radiation is larger below 700 Hz (140 Hz at full scale) than that above 1 kHz, which is no more than 1.5 dB. Also, the effects of ballast vibration for multiple sleepers are less than for a single sleeper (0.11 m away from the sleeper centre in Figure 6.49(b), for example), this is because the radiation ratio is already higher due to multiple sleepers.

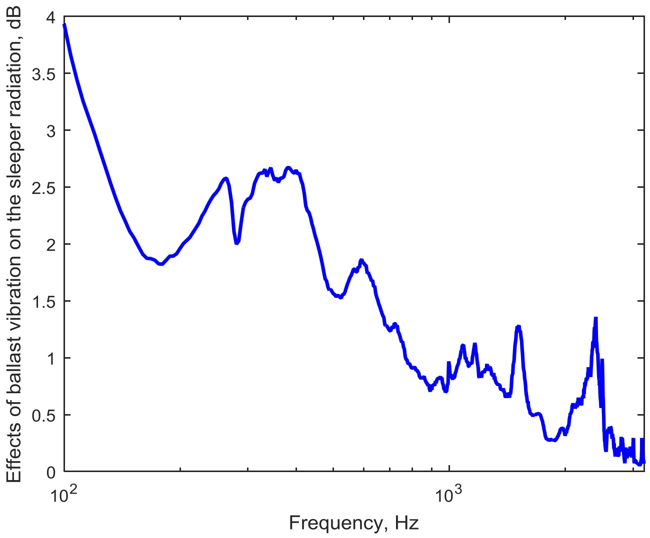

Figure 6.52 Estimation of effects of the ballast vibration on the sleeper radiation for the three sleepers embedded in ballast with phase of the ballast vibration

6.6 Summary

In order to measure the sound radiation of a rail and a sleeper in realistic conditions, various configurations of 1:5 scale rail and 1:5 scale sleeper have been tested using a reciprocal method. For the rail radiation, tests have been carried out for both vertical and horizontal excitation, when the rail is in free space and above rigid and absorptive ground. Quite good agreement for all the configurations is found between the boundary element predictions and the measured radiation ratio above the corresponding critical frequency. At high frequency, however, it is found that the experimental results are always higher than the numerical predictions. This could be because of neglect of the cross-sectional deformation of the rail in the numerical modelling, but this requires further investigation.

The sleeper radiation has been measured for vertical excitation, when a single sleeper is in free space and embedded in an absorptive ground. It has been found that the numerical predictions agree quite well with the measured results in all the configurations. Also, calculations have been included in which the flexible modes of the sleeper are taken into account. Good agreement can be seen between the measured radiation ratio and numerical results in this case. Moreover, multiple sleepers connected by a short length of rail and resting on the foam have been tested showing reasonable agreement with corresponding numerical predictions.

Next, the effects of 1:5 scale ballast absorption on the sound radiation from the rail and sleeper have been measured. For the sound radiation of a rail above the ballast, the measured results agree well with the predictions for the rail vibrating vertically, whereas poor agreement is found for the rail moving laterally. For the influence of the ballast on the sleeper radiation (a single sleeper embedded in ballast and multiple sleepers embedded in ballast), it is shown that the measured results are always higher than the numerical predictions. One possible reason for this is the vibration of the ballast, induced by the sleeper vibration, increases the radiated noise. The other reason is the use of locally reacting model for the ballast absorption, which gives higher noise prediction at low frequencies.

Finally, the effects of ballast vibration on the sound radiation from the sleepers have been quantified. The one-fifth scale model of the track has been used again to carry out acoustic and vibration measurements. For a single sleeper embedded in ballast, it is shown that vibration of the ballast affects the sleeper radiation below 1500 Hz for the scale model (300 Hz at full scale). Above 500 Hz (100 Hz at full scale), only the region of ballast close to the sleeper (within 0.076 m) contributes significantly to the sound power and the increase in noise is less than about 3 dB. At lower frequencies the sound power has been estimated to increase by around 7 dB for the ballast with a rigid base, and 12 dB for the ballast on an elastic base.

For the ballast vibration when multiple (three) sleepers are embedded in ballast, comparison with field measurements suggests the rigid base gives the best agreement. It is also shown that vibration of the ballast, which is assumed in phase, affects the sleeper radiation below 1.2 kHz for the scale model (240 Hz at full scale). It is also shown that those effects are less than 2 dB when including the phase of ballast vibration below 1 kHz (200 Hz at full scale).

Chapter 7 Complete prediction model for track sound radiation

The rail, the sleeper and the ballast are three of the most important components in the railway track system. The sound radiation from the rail and the sleeper has been investigated numerically by using the boundary element method in Chapter 3 and Chapter 4. The corresponding experimental validation of the numerical results was presented in Chapter 6. Moreover, the influence of both the acoustic and mechanical properties of the ballast on the rail and sleeper radiation has also been explored experimentally in Chapter 6 and compared with the numerical predictions. In the present chapter the complete prediction of the track sound radiation is considered by drawing together these various components.

The sound radiation from the complete 1:5 scale track model is measured reciprocally in the reverberation chamber and the results are compared with the corresponding numerical results. The models for the sound radiation from the rail and the sleeper developed in this thesis are then implemented together with the TWINS software to give a prediction of the sound radiation from an operational track. The differences between the results of the existing TWINS models and the updated models are shown.

7.1 Connection between the rail and sleeper

Before the experimental investigation of the sound radiation from the complete track model, it is necessary to connect the rails to the sleepers. As also used in Chapter 6, spring clips are used here to attach the rails to the transverse sleepers, as shown in Figure 7.1. Rubber rail pads are also located between the rail foot and the sleepers. These consisted of pieces of neoprene with a thickness of 2.5 mm and dimensions 45 mm × 35 mm. Rail pads have a considerable influence on the rolling noise and their thickness has been carefully defined so that stiffness correspond to commonly used values on real track; their stiffness has therefore been measured. The corresponding measurement method is described below.

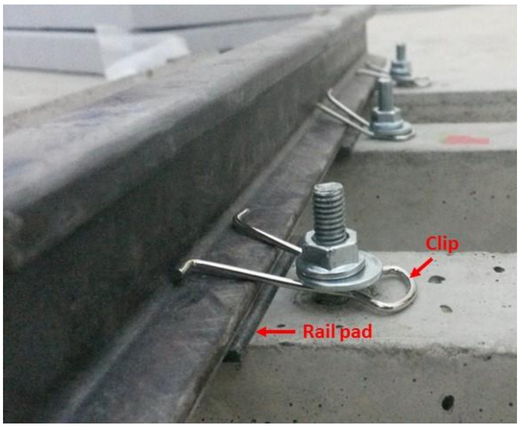

Figure 7.1 Fastening system in the measurements

Following the experimental set-up shown in Figure 7.2, the transmissibility between the rail head and sleeper has been measured with different rubber samples fitted as railpads. During these measurements, a 0.114 m-long scale rail was connected to one scale sleeper. A strip of a damping layer has been attached to the bottom of the rail foot to correspond to the arrangement used in the measurements for the rail in Section 6.2. This system was resting on the melamine foam, which can be assumed to be sufficiently soft that it can be neglected. The transmissibility was measured as the transfer function between the accelerometer attached to the sleeper and the one on the rail, for a force given at the rail head with an impact hammer. In order to estimate the stiffness of the pads a two-degree-of-freedom model was established to represent the measurement set-up of Figure 7.2. The stiffness was estimated by fitting the calculated transmissibility to the measured ones.

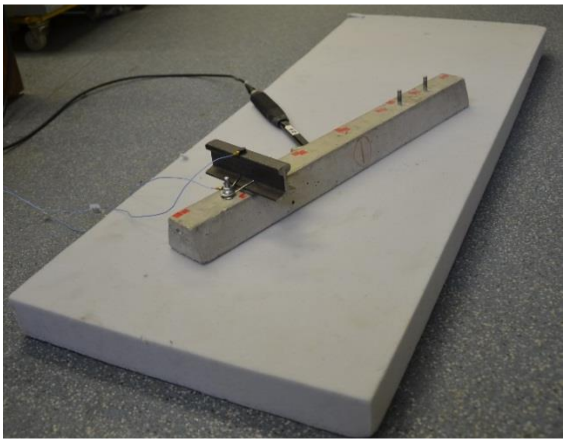

Figure 7.2 Experimental set-up for the stiffness measurement of the rail pad

7.1.1 Experimental method for determining the railpad stiffness

The measurement set-up is represented by a two-degrees-of-freedom system, as shown in Figure 7.3. A vertical harmonic force of amplitude F with time dependence $e^{i\omega t}$ acts on the rail. m_r and m_s denote, respectively, the masses of the rail and the sleeper, whereas u_1 and u_2 are their corresponding vertical complex displacement amplitudes, which have the forms of $u_1=U_1e^{i\omega t}$ and $u_2=U_2e^{i\omega t}$, where U_1 and U_2 are the amplitudes of the displacements for the rail and the sleeper, respectively. k_{ps} represents the railpad stiffness, which is to be measured, while k_{fs} corresponds to the elastic foundation beneath the sleeper. k_{fs} is much softer than k_{ps} in this system.

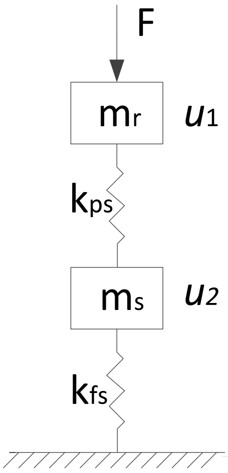

Figure 7.3 Two-degrees-of-freedom model representing the measurement

The equations of motion for this two-degrees-of-freedom system can be expressed as

$$\begin{bmatrix} m_r & 0 \\ 0 & m_s \end{bmatrix}\begin{Bmatrix} \ddot{u}_1 \\ \ddot{u}_2 \end{Bmatrix}+\begin{bmatrix} k_{ps} & -k_{ps} \\ -k_{ps} & k_{fs}+k_{ps} \end{bmatrix}\begin{Bmatrix} u_1 \\ u_2 \end{Bmatrix}=\begin{bmatrix} F \\ 0 \end{bmatrix} \tag{7.1}$$

Substituting the forms of $u_1=U_1e^{i\omega t}$ and $u_2=U_2e^{i\omega t}$ into the above matrix equation, the displacement amplitudes of the two objects are given by

$$\begin{Bmatrix} U_1 \\ U_2 \end{Bmatrix}=\left\{-\begin{bmatrix} m_r & 0 \\ 0 & m_s \end{bmatrix}\omega^2+\begin{bmatrix} k_{ps} & -k_{ps} \\ -k_{ps} & k_{fs}+k_{ps} \end{bmatrix}\right\}^{-1}\begin{bmatrix} F \\ 0 \end{bmatrix} \tag{7.2}$$

Solving this for each frequency, the transmissibility U_2/U_1 can then be obtained as a function of frequency. As the masses m_r and m_s are known, the stiffness can be determined by fitting the transmissibility to the measured results.

7.1.2 The stiffness of the railpad

Due to its bending resonances, the sleeper will not act purely as a mass at high frequency. To allow for this, the point accelerance $H(\omega)$ of the sleeper alone resting on the foam was measured and this is shown in Figure 7.4. The resonance at around 550 Hz is the first mode of the sleeper.

This accelerance is then used to obtain the apparent mass of the sleeper, as a function of frequency

$$m_s(\omega) = \frac{1}{H(\omega)} \tag{7.3}$$

where ω is the angular frequency.

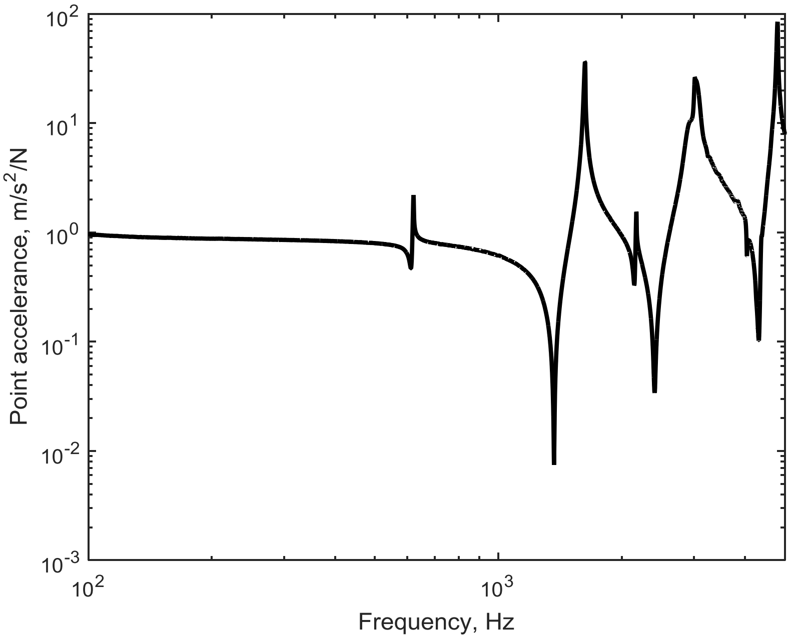

Figure 7.4 Accelerance of the sleeper for the point at the railseat

The apparent mass is then substituted into Equation (7.2). Because this apparent mass already accounts for the stiffness of the foam that the sleeper was resting on, Equation (7.2) is modified as

$$\begin{Bmatrix} U_1 \\ U_2 \end{Bmatrix} = \left\{ \begin{bmatrix} m_r & 0 \\ 0 & m_s(\omega) \end{bmatrix} \omega^2 + \begin{bmatrix} k_{ps} & -k_{ps} \\ -k_{ps} & k_{ps} \end{bmatrix} \right\}^{-1} \begin{bmatrix} F \\ 0 \end{bmatrix} \tag{7.4}$$

which can be solved to find the transmissibility U_2/U_1. The railpad stiffness is varied until a result is obtained that gives a good fit to the measured transmissibility (U_2/U_1). For the prediction, the mass of the scale rail (m_r) is 0.39 kg, which was obtained from measurement.

The first attempt was made with a thicker piece of neoprene rubber railpad the dimensions of which are 45 mm × 35 mm × 5 mm. Figure 7.5 shows a comparison between the measured and predicted transmissibility, when the rail pad stiffness is set to 8 MN/m and the loss factor is set to 0.13. Good agreement can be seen between them, especially at low frequency. The peak at 390 Hz is the resonance of the rail above the rail pad, and it is mostly determined by the pad stiffness and loss factor.

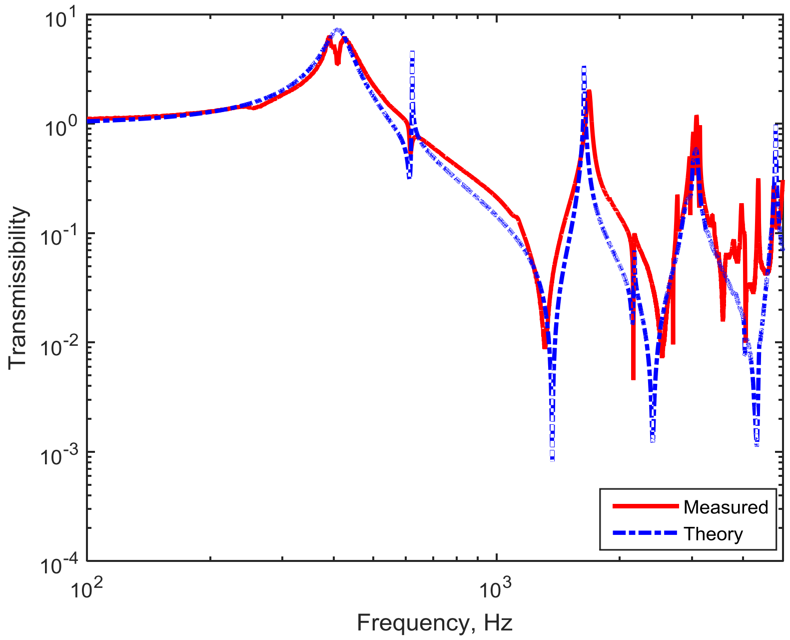

Figure 7.5 Comparison of the measured and predicted transmissibility between the rail and the sleeper

This tested rail pad, which has a stiffness of 8 MN/m at 1:5 scale (40 MN/m at full scale), is too soft to represent a realistic full scale track. A second rail pad was therefore made by slicing the previous test rail pad into half to make it thinner. The same measurement procedure was applied to this rail pad.

The measured transmissibility between the rail and the sleeper in this case is compared with the predicted one by Equation (7.4) in Figure 7.6. The best-fitting rail pad stiffness is found to be 18 MN/m. The first peak at around 570 Hz is still due to the first sleeper bending mode. The second peak at around 730 Hz is due to the rail bouncing on the rail pad stiffness. As stated above, the thickness of this second rail pad is half that of the first one, which should give a stiffness of 16 MN/m (twice 8 MN/m) instead of 18 MN/m. This is probably because it is difficult to halve the thickness of the rail pad exactly.

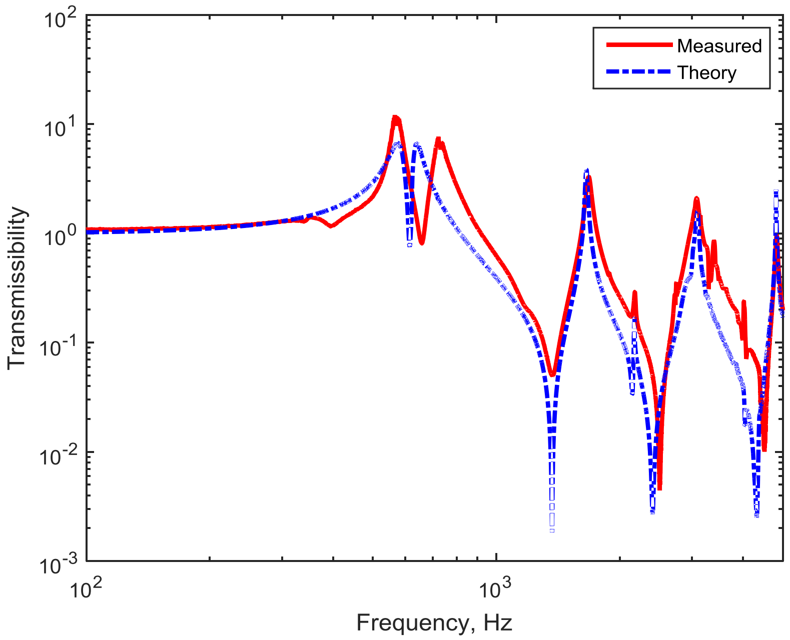

Figure 7.6 Comparison of the measured and predicted transmissibility between the rail and the sleeper for the second rail pad

The model track has also been used without fitting any rail pads. The contact stiffness between the rail and the sleeper is estimated by using the same procedure described above. Figure 7.7 presents the corresponding transmissibility. A value of 100 MN/m is used in the prediction. Reasonable agreement can be seen between them. The first peak in the measured results is again the first mode of the sleeper. The prediction, however, does not show this peak. Besides, the predicted peak values at the resonance frequencies are a bit lower than the corresponding measured results.

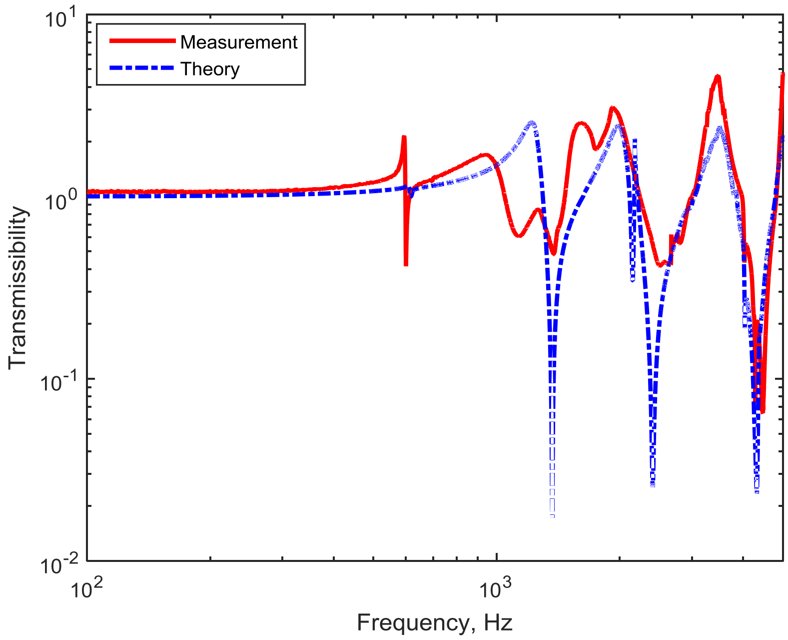

Figure 7.7 Comparison of the measured and predicted transmissibility between the rail and the sleeper for the contact stiffness

In summary, three kinds of stiffness have been estimated in this section by using the same measurement procedure. The second rail pad with a stiffness of 18 MN/m will be used in the scale whole track system in this chapter. Note that the corresponding stiffnesses at full scale for the measured scale models are: 40 MN/m, 90 MN/m and 500 MN/m, which correspond to very soft, soft, and stiff rail pads at full scale.

7.2 Measurements on the whole 1:5 scale track model

Measurements have been carried out of the dynamic properties and sound radiation of the whole track system using the 1:5 scale model. The scale model track used for the measurements consisted of two 2 m-long rails attached to 17 sleepers. These were arranged with a spacing of 0.12 m (corresponding to a full scale distance of 0.6 m). The central sleeper was located at the mid-point of the rails. The whole track system was embedded in 1:5 scale ballast, with dimensions 2 m × 0.8 m × 100 mm, located on the floor of the large reverberation chamber; the depth of ballast beneath the sleepers was 60 mm. The corresponding set up is presented in Figure 7.8.

Two cases are considered: one with the rail pads between the rails and sleepers and one without, which gives a stiffer connection between the rails and sleepers and therefore a different balance between rail and sleeper radiation. The dynamic properties and the sound radiation of this scale track in these conditions are measured, and compared with the corresponding predictions.

Figure 7.8 Experimental set up for the scale whole track embedded in ballast

7.2.1 Point mobility

For the scale track with rail pads, the driving point mobility of both left and right rails is presented in Figure 7.9, where the mobility magnitude from the measurements is shown in Figure 7.9(a), and the corresponding phase information is given in Figure 7.9(b). As can be seen, the point mobilities at the two rails are nearly the same above 2 kHz, but there are differences at lower frequency.

Comparison is also made in Figure 7.9(a) with the prediction of the mobility magnitude obtained by using a track model, which is a continuously supported infinite Timoshenko beam [1, 8]. This model is the same as that used for the prediction of the sleeper vibration in Section 4.3.1. The parameters used for the 1:5 scale track in the analytical model are listed in Table 7.1. The masses of the rail and the sleeper were obtained by using a weighting scale. Other parameters are from the quantities for the full scale track or scaled according to the scale factor 5 based on the physical properties of the parameters. Ballast stiffness and pad stiffness are adjusted to best fit the measured data. The pad stiffness used in the prediction is 15 MN/m, which is a bit different from the measured value of 18 MN/m in Section 7.1.2. This is probably because the rail pads used in the whole track are not the same as each other, it cannot be guaranteed, therefore, that the rail single pad used for the stiffness measurement in Section 7.1.2 is representative of the whole track, but the results are still close.

Quite good agreement can be seen between the prediction and the measured point mobility. The location of the peak at around 1 kHz is determined by the pad stiffness. The fluctuations in the measurements at high frequencies are due to the finite length of the rail.

Table 7.1 Parameters used for vertical motion of the track

Young's modulus	2.1×10^{11}
Rail bending stiffness	0.01 MNm^2
Rail mass per unit length	3.4 kg/m
Rail loss factor	0.05
Rail density	7850 kg/m^3
Pad stiffness	15 MN/m
Pad damping loss factor	0.2
Sleeper mass	2.42 kg
Sleeper spacing	0.12 m
Ballast stiffness	1.0 MN/m
Ballast loss factor	1.0

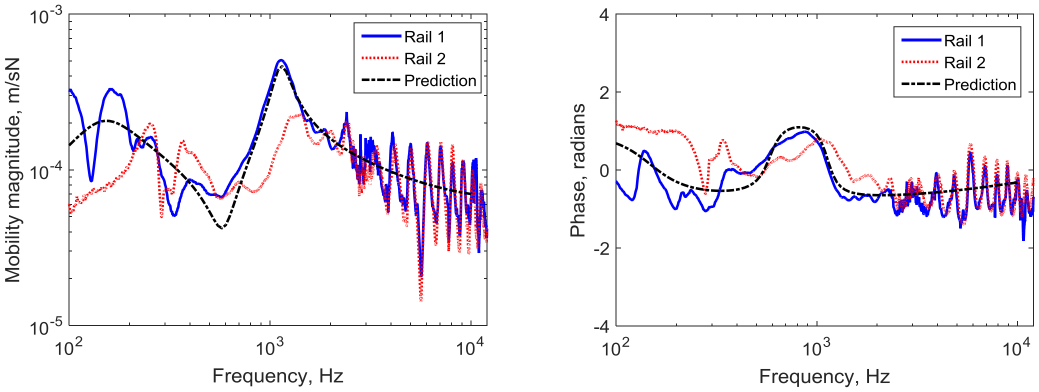

(a) Magnitude (b) Phase

Figure 7.9 Point mobility of the rails. There are rail pads in the system

The driving point mobility for the whole track without rail pads was also measured and compared with the predicted mobility, as presented in Figure 7.10. The pad stiffness is from the corresponding stiffness measurements in Section 7.1.2. A value of 100 MN/m is, therefore, used here for the system without rail pads. As can be seen, on average there is good agreement between the measured and predicted mobilities. The mobilities of the two rails are not identical, especially below 7 kHz. One possible reason is that the force applied to the clips for the connection of the rails to the sleepers are different.

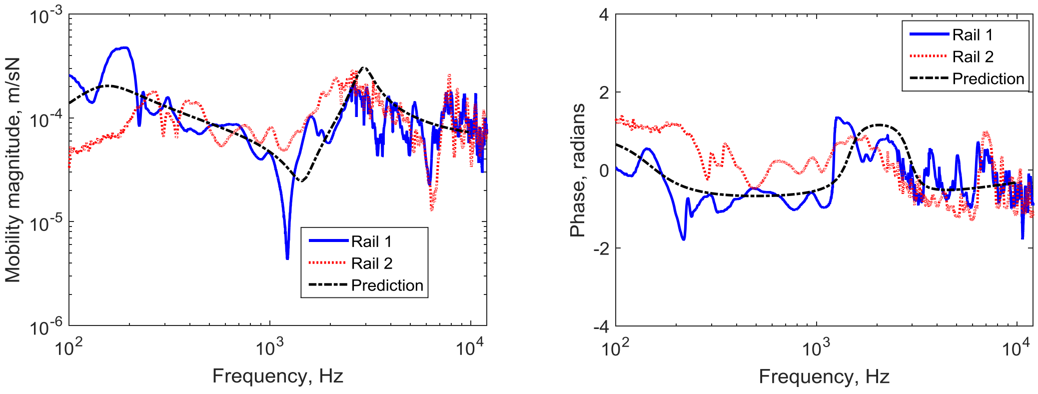

(a) Magnitude (b) Phase

Figure 7.10 Point mobility of the rails. There are no rail pads in the system

7.2.2 Decay rate

As stated in Section 1.2, the decay rate is important for the noise radiated by the rail. Hence, it is convenient to verify if the decay rate for the 1:5 scale track is representative of a real track.

For a single wave with a complex wavenumber $k = k_r + ik_i$ (k_i is negative), the decay rate in dB/m is given by [1]

$$\Delta = -20\log_{10}\left(\exp\left(k_i\right)\right) = -8.686k_i \tag{7.5}$$

7.2.2.1 *Measurement method for the decay rate of a track*

Two methods are used for the measurement of the decay rate of a track. One can be viewed as a direct method. Specifically, based on the definition of the decay rate, the vibration amplitude at the rail ends is measured directly by using two accelerometers attached to the each end of the rail, when one end of the rail is excited by an impact hammer. The decay rate is then obtained by the reduction of the vibration amplitude, which is normalised by the length of the track [118].

The other method is based on the measurement procedure given in the BS EN 15461 [26].

Figure 7.11 shows the corresponding grid locations of the excitation points on the track used in the current measurements. The decay rates on the track in each one-third octave band can be evaluated by:

$$\Delta = \frac{4.343}{\sum_{n=0}^{x_{\max}} \frac{\left|A\left(x_n\right)\right|^2}{\left|A\left(x_0\right)\right|^2} \Delta x_n} \tag{7.6}$$

where $A(x_n)$ and $A(x_0)$ are the measured mobilities or accelerances at the n and 0 positions, respectively. They should be given in the form of one-third octave band spectra. Δx_n is the corresponding distance between adjacent positions.

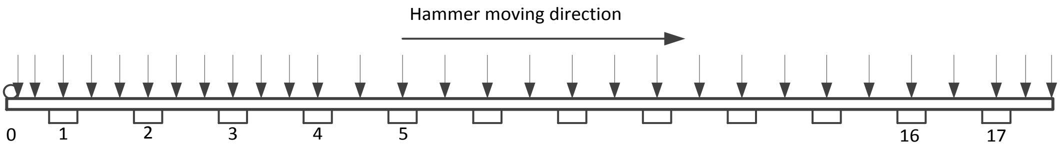

Figure 7.11 Decay rate on the track: grid of positions of the excitation points. Hammer (↓); accelerometer (o) positions on the rail and sleepers (□)

7.2.2.2 *Discussion*

The decay rate on the 1:5 scale track with and without rail pads has been measured by these two methods. In applying the method from the EN 15461 standard, the initial point was set at one end of the track. The mobility was measured reciprocally by moving the impact hammer, which was the same one as that used for the rail in Section 6.2, along the track.

For the scale track with rail pads, the decay rates in one-third octave band are shown in Figure 7.12, and also compared with the predictions by using the infinite track model shown in Section 4.3.1. In the prediction, the parameters used for the track are the same as those used for the prediction of the corresponding point mobility in Section 7.2.1. Method 1 is the direct method, whereas Method 2 the standard BS EN 15461. As can be seen, the agreement among them is not so good. This is because the theory behind these three kinds of decay rates are different. The prediction only takes the propagating wave into account by using an infinite track model. However, the track measured is 2 m-long, which means the reflected wave at the end of the track will affect the measured decay rate.

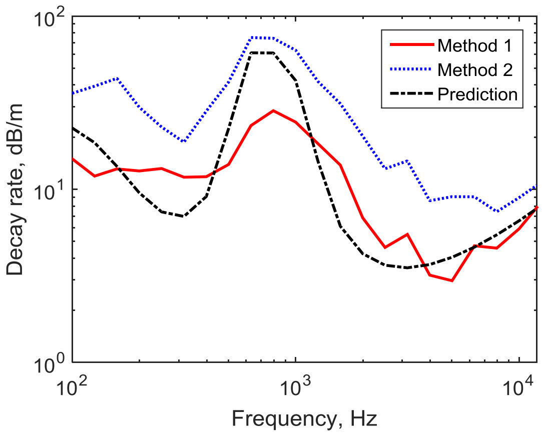

Figure 7.12 Decay rate for the whole scale track with rail pads

In order to improve the results of Figure 7.12, corrections are made to the measurements. Specifically, correction factors are calculated by using a finite Timoshenko beam on double elastic layer foundations (see Section 4.1) and an infinite Timoshenko beam on two layer foundations (see Section 4.3.1). From the ratio between the decay rates calculated with these two models, the measured decay rates on the 2 m-long track can be converted into their corresponding results for an infinite track. Detailed information on the calculation of the decay rate correction can be found in [118]. Figure 7.13 presents the decay rate measured after the conversion by using the corresponding correction factors. As it is shown the decay rate obtained by the two methods has better agreement. Good agreement can be seen now between the predicted decay rate and the one measured by using the standard BS EN 15461. The decay rate has a typical form, with a high value at low frequency, a peak in the region where the sleeper acts as a dynamic absorber, a sudden drop above the resonance of the rail on the pad before rising again at high frequency. Thus, it can be concluded that the 1:5 scale track with rail pads in the measurements is representative of a real 1:5 scale track, provided that corrections for end effect are taken into account.

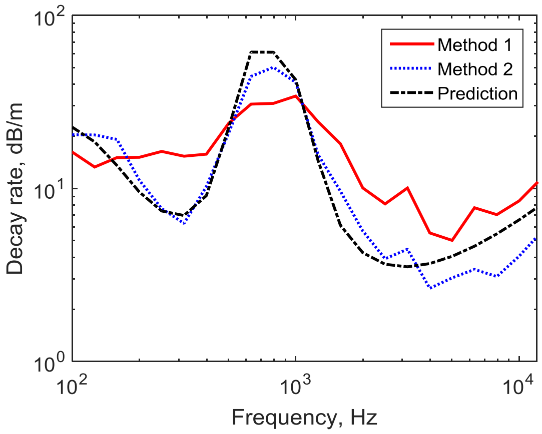

Figure 7.13 Decay rate on an equivalent scale infinite track for the whole scale track with rail pads

The same procedure is applied to measure and predict the decay rate on the scale track without rail pads. Figure 7.14 shows the corresponding results. Again, the agreement among them are not so good before the corrections are made for the decay rate measured, as shown in Figure 7.14(a). After converting the decay rate measured for the 2 m-long track into equivalent infinite tracks, as presented in Figure 7.14(b), the measurements agree better with each other and on average also with the predicted result for an infinite track.

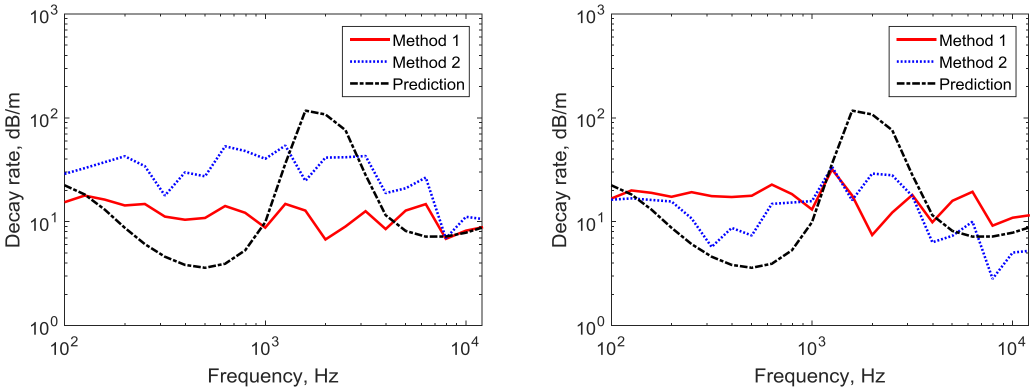

(a) Without corrections (b) With corrections

Figure 7.14 Comparison of the decay rate between the predictions and the measurements for the whole scale track without rail pads

7.2.3 Sound power from the whole track

Both the structural mobility of this whole track and the sound power for a unit force applied at the rail from this system have been measured by applying the reciprocal method. The transfer mobility was measured for excitation at 69 points along each rail (4 points spaced equally along the rail section in each sleeper span), 11 points spaced equally along the central three sleepers, and 3 points spaced equally along all the other sleepers. Two accelerometers were located vertically at the centre of the railhead above the central sleeper, one on each rail. By reciprocity these measurements represent the transfer mobility from a force at the railhead to the velocity of the rail or the sleeper.

The sound power from the whole track with and without rail pads was also measured reciprocally. Comparison will be made with the evaluation of the sound power from both the rails and the sleepers by using the corresponding radiation ratios, including the effect of the ballast absorption as studied in Chapter 5. Specifically, the sound power from the rails is estimated by using a weighted average radiation ratio (1/3 times the result for the rail attached to the rigid ground and 2/3 times that for the rail 20 mm above the ballast), as was presented in Figure 6.37. This is used in combination with the measured squared mobility for the two rails. For the sound power from the sleepers, the radiation ratio is based on three sleepers with vibration amplitudes in the ratio of 0.5:1:0.5 as discussed in Section 4.3.2. Two different models have been used due to the difficulties in modelling the absorption of the ballast: three sleepers embedded in a rigid ground, which can be treated as an extreme case, and three sleepers embedded in ballast based on the Johnson-Allard model. The sleeper dimensions are set to 0.25 m × 0.04 m (half of the 0.5 m-long sleeper) in order to approximate the behaviour of the flexible sleepers as discussed in Section 4.3.2.

Figure 7.15 presents the measured sound power from the assembly without rail pads normalised by the mean square force. The results are shown in 1/12 octave bands. These are compared with the estimation of the sound power from the two rails and 17 sleepers based on the measured vibration. As can be seen, the sound power from the sleepers dominates the noise up to 7500 Hz (1500 Hz at full size), due to the high vibration transmission from the rails to the sleepers without rail pads. The sound power from the sleepers predicted by using the radiation ratio of the sleepers embedded in rigid ground agree better with the measured sound power than that predicted using the ballast absorption, especially in the frequency range 500 ~ 2000 Hz. Conversely, the results using the radiation ratio of the sleepers embedded in ballast are lower than the measurements at around 650 Hz and 2000 Hz. This is related to the dips in the predicted radiation ratio of the three sleepers embedded in ballast, as shown in Figure 6.39. It appears that the impedance obtained from the Johnson-Allard model is not adequate for use in the BEM model, although good agreement was found between the results from the Johnson-Allard model and the measured ballast absorption shown in Chapter 5. It is likely that the model is less reliable at grazing incidence which will dominate the current case than for diffuse incidence.

Figure 7.16 presents the corresponding results for the track fitted with rail pads. Here, the sleepers are the dominant noise source only below 2000 Hz (400 Hz at full size) as the rail pads reduce the vibration transmission from the rails to the sleepers. Again, the sleeper sound power predicted by using the radiation ratio from the three sleepers embedded in ballast has dips at around 650 Hz and 2000 Hz and the radiation ratio based on a rigid ground gives a better agreement with the measured results.

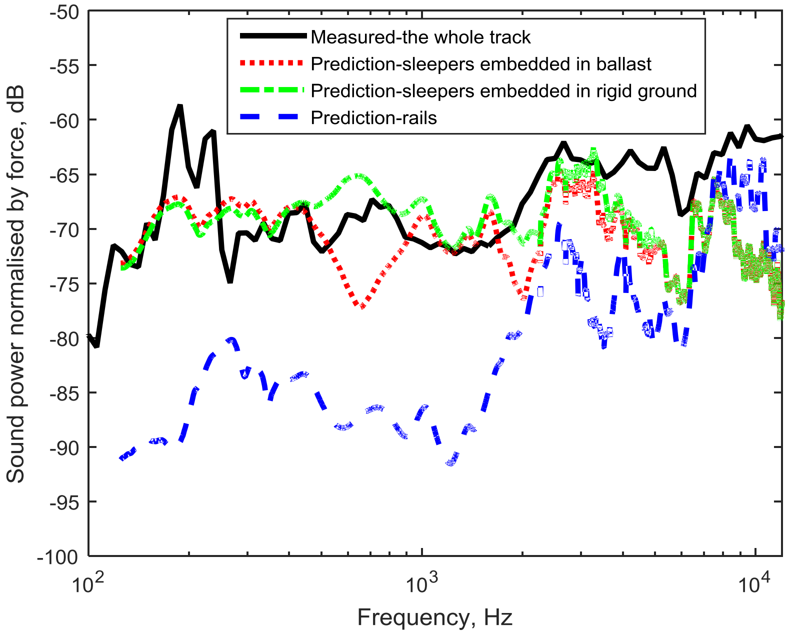

Figure 7.15 Comparison of measurements and the predictions for the sound power of the whole track shown in Figure 7.8. There are no rail pads in the system

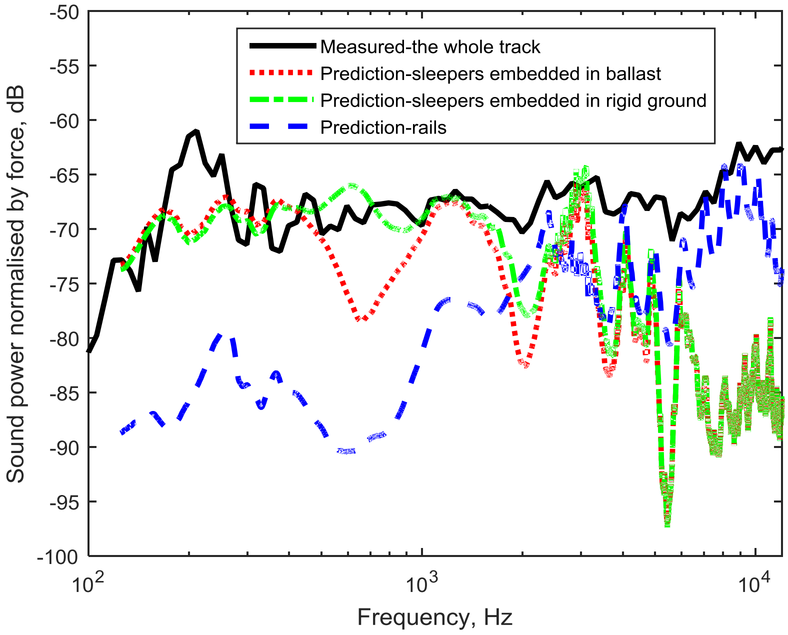

Figure 7.16 Comparison of measurements and the predictions for the sound power of the whole track shown in Figure 7.8. There are rail pads between the rails and the sleepers in the system

The influence of ballast vibration on the sleeper radiation has not been considered in the predictions in this section. According to the results in Section 6.5.2, it is shown that the ballast vibration has an influence on the sleeper radiation below 1.2 kHz. Thus, in Figure 7.15 and Figure 7.16, the measured sound power should include the sound power due to the ballast vibration to some extent at low frequency. It seems, therefore, that the prediction for the total sound power from the rails and sleepers below 1.2 kHz, obtained by using the radiation ratio of sleepers embedded in rigid ground, is slightly higher than expected. This is probably due to neglecting ballast absorption. Nevertheless, using the impedance from the Johnson-Allard model for the ballast appears to lead to predictions that are too low, especially in certain frequency ranges associated with the depth of the ballast. Hence, further work on the modelling of ballast absorption is necessary.

7.3 Prediction of track noise in practice

In order to check the application of the current models for the sound radiation from the rail and sleeper to an operational track, the complete prediction for a whole track is predicted in the TWINS software. These predictions will be compared with existing measurements obtained at Fishbourne, UK[3]. The sound pressure spectrum was measured at a point 7.5 m away from the track and 1.5 m above the ground in 2013 during the passage of Class 377 Electrostar EMUs at a speed of 118 km/h. The rail roughness and track decay rates were measured at the site and wheel roughness measurements were available from similar trains. The main parameters used in the predictions are listed in Table 7.2.

Apart from the measured data, results will be shown from the existing TWINS software and additionally two modified predictions by using the sound radiation from the rail and sleeper in this thesis. One of these modified predictions uses an impedance for the ballast based on the Johnson-Allard model [60, 61] introduced in Chapter 5. This impedance is used to determine the radiation ratios of the rail 50 mm above the ballast and the sleepers embedded in the ballast. In the second model, the ballast impedance is based on the Delany and Bazley model [56]. A value of 50 kPa.s/m^2 is used for the flow resistivity based on the recommendation for ballast in [76], even though it has been shown in the current work that the flow resistivity of the ballast is around 300 Pa.s/m^2. As before, the radiation ratio of the rail 50 mm above the ground and that of the sleepers embedded in the absorptive ground are used in the predictions. Detailed information on the differences among these radiation ratios and predictions will be discussed below.

---

[3] These measurements were carried out by Martin Toward as part of the Track 21 project.

Table 7.2 Parameters used in the TWINS predictions

Rail parameters	
Young's modulus	2.1×10^{11} N/m^2
Density	7850 kg/m^3
Rail mass per length	60 kg/m
Poisson's ratio	0.3
Vertical bending stiffness	6.42×10^6 Nm^2
Lateral bending stiffness	1.07×10^6 Nm^2
Shear coefficient	0.4
Loss factor	0.02
Rail pad	
Vertical stiffness	120 MN/m
Vertical loss factor	0.2
Lateral stiffness	13 MN/m
Lateral loss factor	0.2
Sleeper parameters	
Mass	280 kg
Young's modulus	4.13×10^{10} N/m^2
Density	2750 kg/m^3
Poisson's ratio	0.15
Shear coefficient	0.83
Loss factor	0.02
Length	2.6
Spacing between sleepers	0.6 m
Ballast parameters	
Vertical stiffness	Frequency dependent
Vertical loss factor	1.0
Lateral stiffness	3.5×10^7 N/m
Lateral loss factor	2.0

7.3.1 Radiation ratios of the rail and sleeper in TWINS

Before the prediction of the sound pressure component from the rail and sleeper, it is necessary to present the radiation ratios from the rail and sleeper used in the updated TWINS.

An assumption of the rail 50 mm above a ground (two models of ballast absorption) is made in the models. It has shown in Chapter 5 that the Johnson-Allard model can be used for the absorption coefficient modelling of the full scale ballast with thicknesses of 170 mm and 330 mm (see Figure 5.20). Therefore, it is considered here the parameters used in Johnson-Allard model for the absorption coefficient of the full scale ballast also works for the ballast with a 500 mm thickness. The radiation ratio of the rail 50 mm above a 500 mm-thick ballast bed is calculated in the numerical model, as shown in Figure 7.17. In order to have the gradation changes at the edges of the ballast, the lengths are 2 m and 3 m for the top and the bottom of the ballast bed, respectively. The dashed line is the symmetry axis in the numerical model.

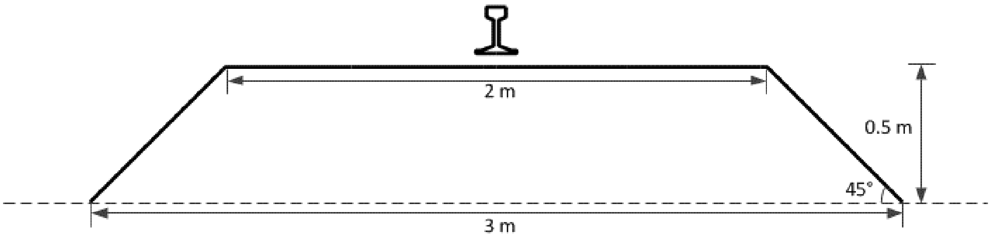

Figure 7.17 Illustration of the rail 50 mm above the ground (ballast)

The radiation ratio of the rail 50 mm above the ballast (Delany&Bazley model and Johnson-Allard model) is presented in Figure 7.18, when the rail is vibrating vertically and laterally. Dips again occur below 1 kHz in the results predicted by the Johnson-Allard model, which are due to the thickness effects in the impedance. These are not present in the results for the Delany and Bazley model. For the lateral motion of the rail, the radiation ratio is reduced by around 2 dB at high frequency because of the absorption of the ballast in either model.

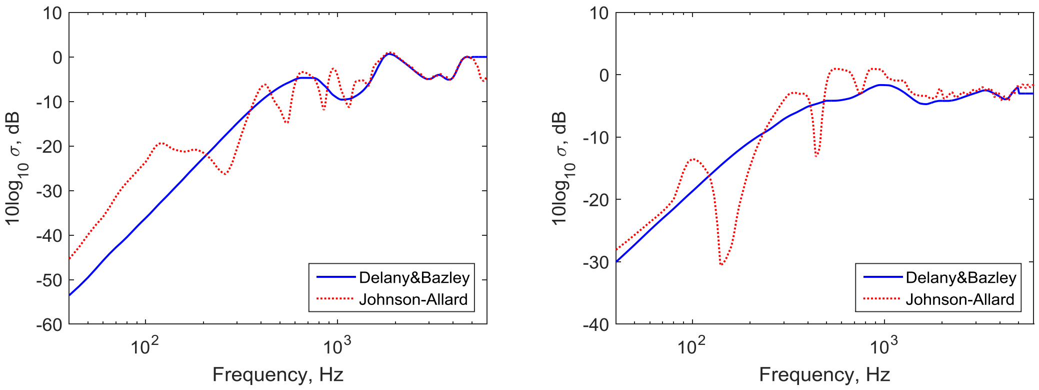

(a) Vertical motion (b) Lateral motion

Figure 7.18 Radiation ratio of the rail 50 mm above the ballast

The different radiation ratios used for the rail in the predictions are presented in Figure 7.19. In the original TWINS model, the radiation ratio of the rail is based on a rail in free space for both vertical and lateral motion. In current work, however, the effects of a rigid ground and an absorptive ground (ballast) are considered in the numerical models. Specifically, a weighted average radiation ratio, as was presented in Section 6.4, is used: a weight of 1/3 for the rail attached to the rigid ground (concrete sleeper) and 2/3 for the rail 50 mm above an absorptive ground or the ballast (in Figure 7.18). As shown in Figure 7.19, the differences between the original radiation ratios and the updated ones are greatest at low frequencies.

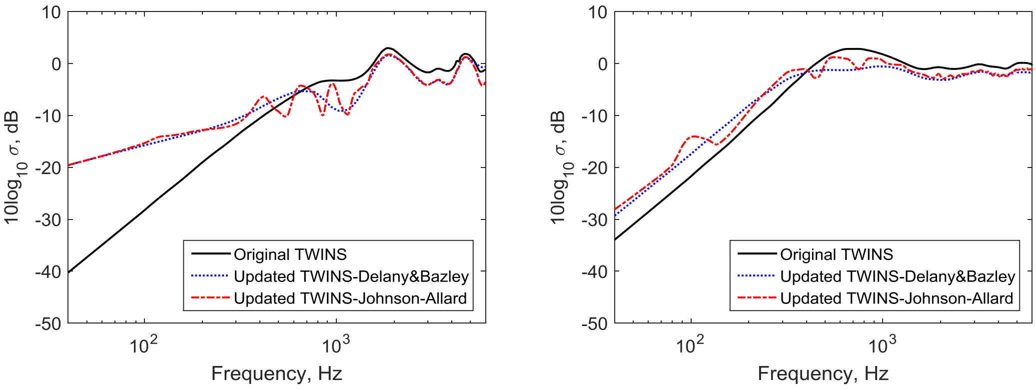

(a) Vertical motion (b) Lateral motion

Figure 7.19 Comparison of the radiation ratio of the rail in the predictions

In the updated TWINS, the radiation ratio of three sleepers embedded in a ground (the same two models for a ballast bed) is also used in the prediction models. These three sleepers with a vibration ratio of 0.5:1:0.5 are assumed to be fully embedded in the ground. For the case of a ballast bed, the width of the ballast top is 4 m, whereas it is 6 m for the bottom of the ballast. The height of the ballast bed is again 500 mm. The mesh of one quarter for the model is shown in Figure 7.20. The element size and dimensions of the ground box in different frequency ranges in Table 4.2 are used for the length of the ballast region along the track here.

Figure 7.21 shows the radiation ratio for multiple sleepers used in the different prediction models. The sleeper radiation ratio in the original TWINS is an approximation based on the radiation from a rectangular piston set in an infinite baffle with a heuristic correction for the fact that multiple sleepers are close together compared with the acoustic wavelength at low frequency [46]. The predicted radiation ratio from the sleeper in the current research has allowed for this effect in a more rigorous way and can therefore be considered to be more reliable. It also approximates the flexible behaviour of the sleeper when it is embedded in a ground by using half length of the sleeper (1.25 m × 0.2 m).

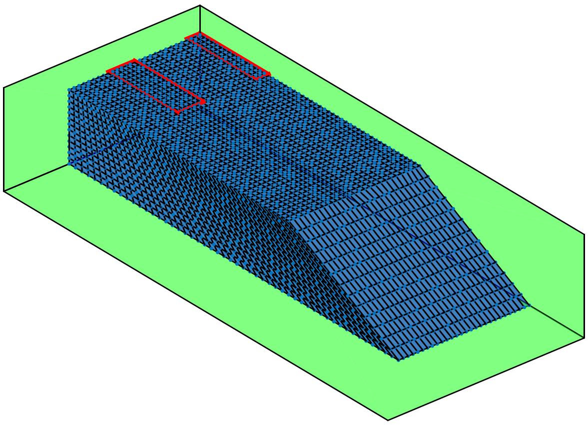

Figure 7.20 Mesh of one quarter of domain for multiple sleepers embedded in ballast (high frequency model)

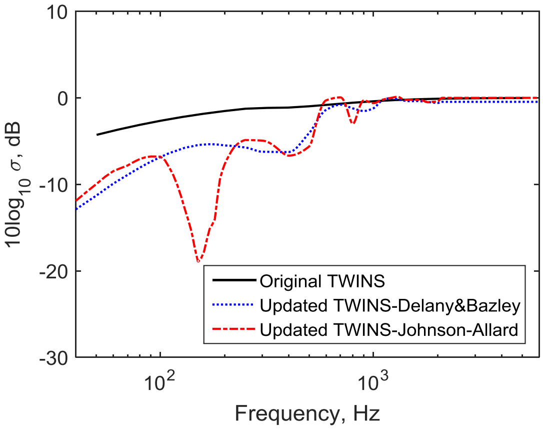

Figure 7.21 Comparison of the radiation ratio of the sleeper

7.3.2 Prediction of the sound radiation from different components in the track

The predicted sound pressure component from the rails is shown in Figure 7.22, for the original and updated models. As can be seen, there are great differences between the original TWINS and the updated TWINS at low frequency, where the sleeper is actually the dominant source. Hence, although the sound pressure level from the contributions of the rails is obviously different between the original TWINS and updated TWINS at low frequency, this difference does not make much contribution to the predicted total noise.

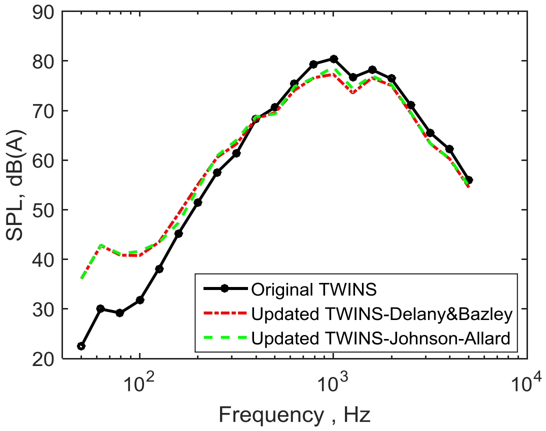

Figure 7.22 Comparison of the predicted A-weighted sound pressure level of the component from the rails in the track

Note that the sound pressure predicted for the rail is for a ballast track. For a slab track, however, the rail would be important at lower frequencies and would not be masked by the sleepers. Measurements on a slab track would allow verification of the rail radiation models to lower frequency.

The component of the sound pressure level from the sleepers in the whole track for each model is presented in Figure 7.23. As can be seen, the contribution from the sleeper obtained by using current sleeper radiation ratio is lower than that based on the original model. That is also the reason why the predicted total sound pressure level from the updated TWINS agrees better with the measured results at low frequencies. However, there is always a dip at 160 Hz for the case of the sleeper embedded in ballast based on the Johnson-Allard model.

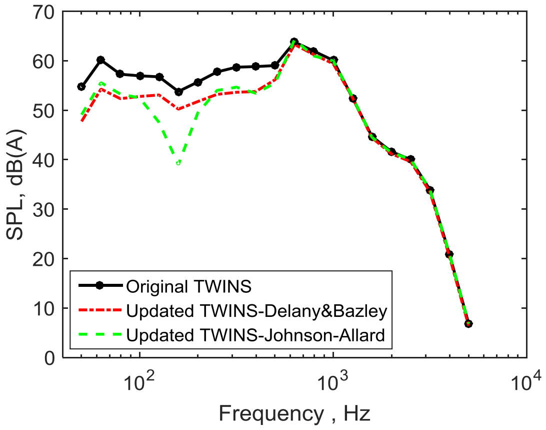

Figure 7.23 Predicted A-weighted sound pressure level

The sound pressure component from the wheels is also predicted in TWINS software for the track noise in Fishbourne, and is shown in Figure 7.24. There are no differences for the predictions between the original TWINS and updated TWINS, therefore, only the prediction from the original TWINS is presented. As can be seen by comparison with the other components, the wheel will become the dominant source at high frequencies.

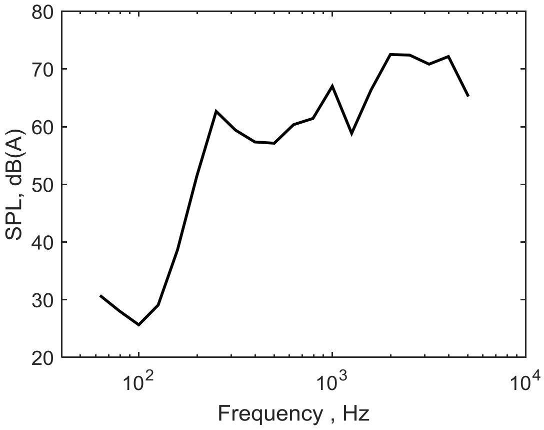

Figure 7.24 The predicted sound pressure level from the component of the wheels

7.3.3 Prediction of the sound radiation from the whole track

The A-weighted sound pressure level is shown in one-third octave bands in Figure 7.25. From [119] it is known that the measured results are subject to a variation of +/- 3 dB(A) in each 1/3 octave band due to variations in train speed, wheel roughness and temperature. Good agreement can be seen between the measurements and the predictions from both the original and updated versions of TWINS, especially above 200 Hz. The modification to the predictions from TWINS has a significant effect below 200 Hz, but the differences are much smaller at high frequencies. This is because the wheel component dominates the noise at high frequency, above 2 kHz, which remains invariant in the different predictions, while the changes in the rail component in mid frequencies are quite modest. The prediction for the rails and sleepers with a ballast bed based on Johnson-Allard model, is a bit lower than the prediction based on Delany&Bazley) due to the higher absorption of the ballast. The Johnson-Allard model gives an improved agreement with the measured sound pressure level below 1 kHz, apart from the dip at 125 Hz. This is a consequence of the dip in the predicted radiation ratio of multiple sleepers embedded in ballast, as shown in Figure 7.21. Besides, the predictions from the updated TWINS, which use the sound radiation models for the rail and the sleeper obtained in this thesis, are smaller than their counterparts from the original TWINS below 200 Hz, where the sleeper is the dominant noise source.

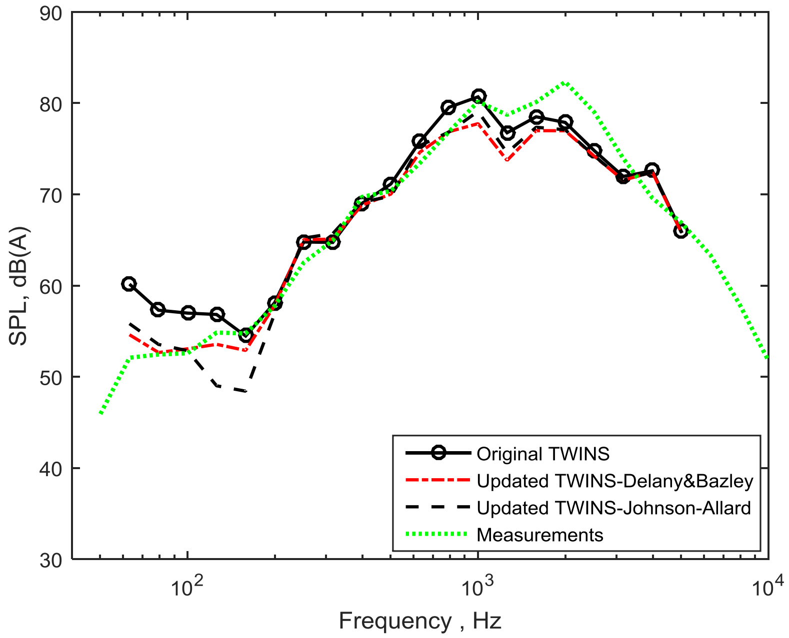

Figure 7.25 Comparison of A-weighted sound pressure spectra between different predictions and the measurements

Again the effects of the ballast vibration on the sound radiation from the sleeper have been ignored in the above predictions. The ballast vibration will increase the noise radiated at low frequency for multiple sleepers embedded in the ballast, as shown in Figure 6.52. For a full scale track, the effects of the ballast vibration on the sleeper radiation can be approximated by converting the results in Figure 6.52 (the results at 1:5 scale are shifted in frequency by dividing a factor of 5) into one-third octave bands and this is presented in Figure 7.26. As can be seen, the increase is less than 3 dB in this frequency range. The influence on the sleeper radiation caused by the ballast vibration can be included in the TWINS predictions by applying this increase at each one-third octave frequency (50 ~ 500 Hz) to the predictions; the effects of the ballast vibration on the sleeper radiation at frequencies above 500 Hz are assumed to be zero.

Figure 7.27 shows the influence of the ballast vibration on the predictions of the total rolling noise in TWINS, while Figure 7.28 presents its effects on the predictions of the sound radiation from the sleeper. Again both ballast impedance models are used. As can be seen, the ballast vibration has very little effect on the results above 200 Hz. The predictions based on the ballast impedance using the Johnson-Allard are underestimated at 160 Hz for both the total track noise and sleeper radiation. This is again because of the dip in the radiation ratio of the sleeper, as shown in Figure 7.21.

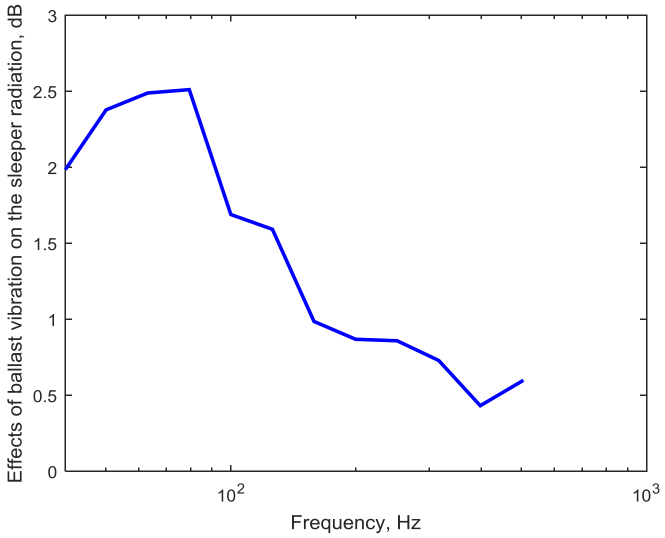

Figure 7.26 Effects of the ballast vibration on the sleeper radiation in one-third octave band at full scale frequency

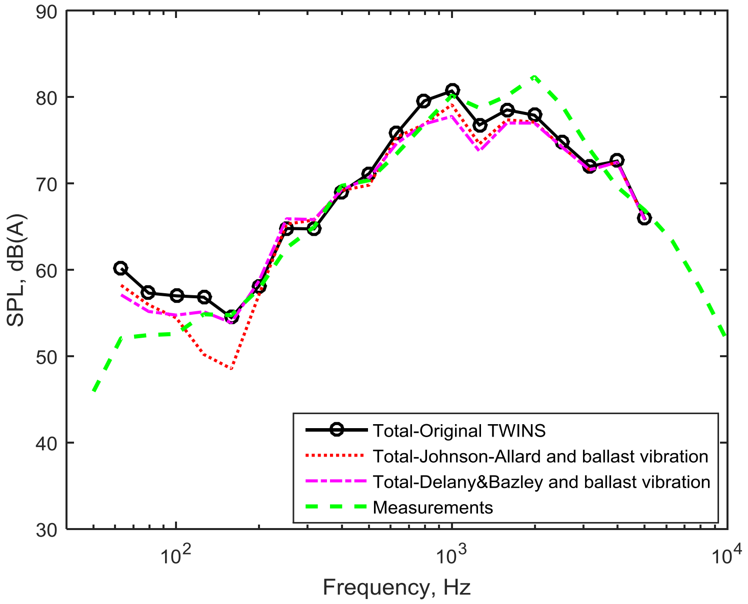

Figure 7.27 Effects of ballast vibration on the predictions of the sound pressure from the whole track

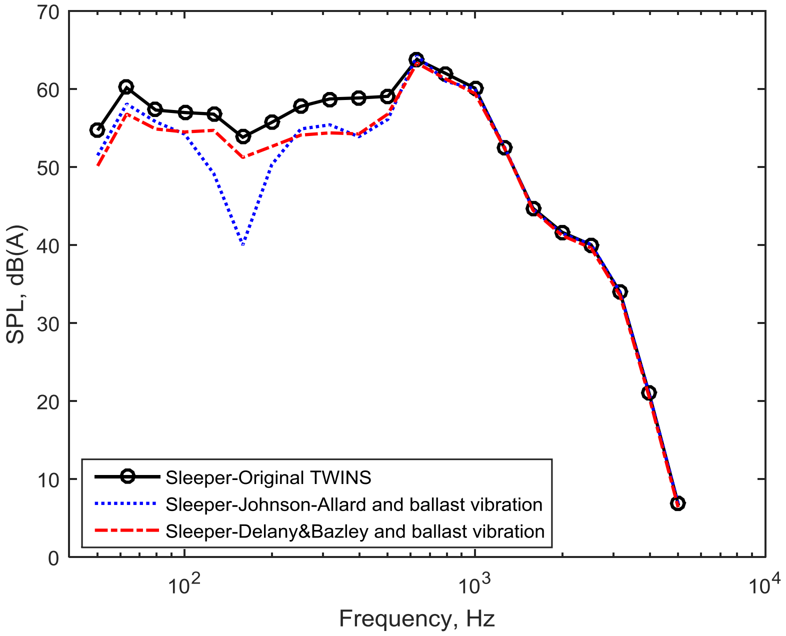

Figure 7.28 Effects of ballast vibration on the predictions of the sound pressure from the sleeper

Finally, for the complete prediction of the track sound radiation, there are some improvements which could be made, and are pointed out here. The TWINS predictions are based on models for the vibration of the rail and sleeper. For full validation of the radiation models, however, measurements of rail and sleeper vibration will be required, as differences may be caused by the vibration predictions as well as the radiation models. Besides, there may be other sources of noise from the trains: electric motors, fans, shoe gear etc. Hence, in order to improve the agreement between the prediction and the measured results, attention should be paid to the contributions from these other noise sources during the measurements as well. Moreover, there remains a dip in the prediction from the updated TWINS based on the radiation ratio of the rails and sleepers with a ballast bed, which is caused by the dip in the radiation ratio of the multiple sleepers embedded in ballast, as shown in Figure 7.21. This did not correspond to the measurements on the scale model (see section 6.4.1.2). More work is therefore needed to improve the models for the ballast absorption.

7.4 Summary

In this chapter the various models for the sound radiation from the track have been combined to predict the sound radiation from the whole track. First, the dynamic properties of the 1:5 scale track model used in the measurements was assessed, it has been found that this scale track is equivalent to a real track. The sound radiation from this scale track model has then been measured reciprocally in the reverberation chamber and comparison has been made with the corresponding numerical predictions. It is shown that the radiation ratio for the multiple sleepers embedded in rigid ground give better predictions than that from the radiation ratio for the multiple sleepers embedded in the ballast. This is probably due to inadequacies in using the impedance from the Johnson-Allard model for the ballast in the numerical models. Therefore, further work will be needed to deal with the impedance of the ballast, for example using an extended reaction model.

The models have then been applied to the prediction of the sound radiation from an operational track and comparisons have been made with existing field measurements. The predictions are conducted using a modification to the TWINS software by including the radiation ratio of the rails and the sleepers developed in this thesis. The effects of ballast vibration on the track sound radiation have also been included using the results from Chapter 6. It is shown that the predictions from current work give an improvement at low frequencies, where the sleeper is the dominant noise source.

Chapter 8 Conclusions and future work

8.1 Conclusions

This thesis is concerned with basic issues related to the rolling noise in the railway system: how the noise is generated by the rail and the sleepers. As both a mechanical supporting layer and a kind of porous material, how the ballast affects the sound radiation from the rail and the sleeper has also been investigated in the current research. Finally, the acoustic properties of these three components are all considered together with the TWINS software to give a complete prediction of the noise from the whole track. The conclusions from the work within this thesis can be summarised in terms of four main aspects, as described in the following.

8.1.1 Sound radiation from the rail

Sound radiation from the rail is explored by using a two-dimensional boundary element model in terms of the radiation ratio. The following conclusions are drawn:

1. The sound radiation from a rail in free space has the behaviour of a line dipole. For vertical motion above a rigid ground this is changed to that of a line quadrupole, while it becomes a line monopole when the rail is attached to the rigid ground. For lateral vibration of the rail, however, the radiation follows the characteristics of a line dipole for all three cases. Furthermore, if the rail is attached to an absorptive ground, the noise radiated by the rail reduces as the absorption is increased. For the rail above an absorptive ground, the ground absorption will reduce the sound radiated by lateral motion of the rail over the whole frequency range. For the rail vibrating vertically, however, at low frequency, an absorptive ground will make the rail radiate more noise than above a rigid ground but less than the rail in free space, whereas the rail radiation will be reduced at higher frequencies.
2. Corrections to the 2D predictions have been introduced to allow for the wavenumber in an unsupported rail, which are significant in the vicinity of the critical frequency of the rail. However, for a rail supported in track these corrections are not applicable. For vertical motion it is shown that no correction is required whereas for lateral motion, the specific correction required at low frequency will be less than that for an unsupported rail and will depend on the stiffness of the rail pad used in practice.

3. Corresponding measurements have been performed on a reduced scale rail to verify the numerical predictions for the rail in different configurations. For both vertical and lateral vibration, very good agreement has been found between the measured results and numerical predictions for all configurations. In general, however, the measured radiation ratio is somewhat greater than the numerical estimates at high frequency, which is probably due to the presence of cross-section deformation which has been neglected in the BEM calculations.

8.1.2 Sound radiation from the sleeper

The sound radiation from the sleeper (a single sleeper and multiple sleepers) undergoing vertical vibration is studied by using a three-dimensional boundary element model. It has been shown that:

1. A single sleeper in free space exhibits the behaviour of a point dipole at low frequencies, but follows the behaviour of a line dipole at intermediate frequencies before tending to unity at high frequency. When the sleeper is embedded in a rigid ground the corresponding behaviour is that of a point monopole at low frequencies and a line monopole at intermediate frequencies. When the sleeper flexibility and support stiffness are taken into account, the radiation ratio of a sleeper of length 2.5 m can be approximated by that of a rigid half-sleeper of length 1.25 m. Furthermore the effect of ground absorption has been taken into account and shown to reduce the radiation from the vertical motion of the sleeper especially in the mid-frequency region.
2. When multiple sleepers are excited through the rail, their sound radiation is greater than would be obtained from the same sleepers treated independently. This increase in sound radiation has been calculated for cases where the sleeper is embedded in a rigid or partially absorptive ground. It is shown that it is sufficient to consider only three sleepers in determining their radiation ratio when installed in track. At low frequencies, although more sleepers lie within an acoustic wavelength, the vibration of the track is localised to the three sleepers nearest the excitation point. At higher frequencies where more sleepers have significant vibration, the distance between them is large enough for them to be treated independently. Consequently the sound radiation increases by up to 5 dB below 100 Hz whereas above 300 Hz the result can be approximated by that for a single sleeper.

3. Measurements have been carried out on a 1:5 scale model railway track to verify the numerical predictions for various configurations. Good agreement has been found between the measured results and the numerical predictions for all configurations.

8.1.3 Ballast absorption and vibration

Both the absorption and vibration of the ballast are studied experimentally and theoretically by using a 1:5 scale ballast. The following conclusions are reached:

1. The flow resistivity, the porosity and the absorption coefficient of a 1:5 scale ballast have been measured. For the absorption measurement of the scale ballast, the scaling law for the porous material by Junger [81] is also tested by using a 1: √5 scale ballast. It has been shown that the absorption for these two scale ballasts does not show much difference. Besides, the effect of a change in gradation on the ballast absorption is measured, found to give an increase which is promising. Moreover, the Johnson-Allard model is used as the local reacting model for the prediction of the 1:5 scale ballast absorption by using the measured ballast properties. Quite good agreement is found between the predictions and the measurements for the 1:5 scale ballast.
2. The effects of ballast absorption on the sound radiation from the rail and the sleeper have also been measurement and compared with the corresponding predictions. For a rail above the ballast, the measured radiation ratio agree well with the predictions for the rail vibrating vertically, whereas poor agreement is found for the rail moving laterally. One possible reason is the local reacting model is less appropriate for grazing incidence. For the sleeper embedded in the ballast, it has been found the measured results are always larger than the predicted one, which is probably due to effects of the ballast vibration on the sleeper radiation.
3. The effects of the ballast vibration on the sleeper radiation has been estimated based on the measured vibration of the ballast. It has been shown that, for a single sleeper embedded in ballast, vibration of the ballast affects the sleeper radiation below 1500 Hz for the scale model (300 Hz at full scale). Above 500 Hz (100 Hz at full scale), only the region of ballast close to the sleeper (within 0.076 m) contributes significantly to the sound power and the increase in noise is less than about 3 dB. At lower frequencies the sound power has been estimated to increase by around 7 dB for the ballast with a rigid base, and 12 dB for the ballast on an elastic base. For multiple (three) sleepers embedded in ballast, it is found that vibration of the ballast, which is assumed in phase, affects the sleeper radiation below 1.2 kHz for the scale model

(240 Hz at full scale). It is shown that these effects will be less than 2 dB when including the phase of ballast vibration below 1 kHz (200 Hz at full scale).

8.1.4 Complete prediction for the sound radiation from the whole track

The complete prediction of the noise radiation from a whole track is carried out finally by using the sound radiation models for the rail and the sleeper from current work. Following conclusions have been drawn:

1. The sound radiation from the 1:5 scale track model has been measured which is compared with the corresponding numerical predictions. It is shown that the radiation ratio for the multiple sleepers embedded in rigid ground give better predictions than that from the radiation ratio for the multiple sleepers embedded in the ballast. This is probably due to the limitations of the impedance from the Johnson-Allard model for the ballast used in the numerical models.
2. The models have then been applied to the prediction of the sound radiation from an operational track and comparisons have been made with existing field measurements. The predictions are conducted using a modification to the TWINS software by including the radiation ratio of the rails and the sleepers developed in this thesis. It is shown that the predictions from current work give an improvement at low frequencies, where the sleeper is the dominant noise source.

8.2 Recommended future work

For extension of the current work, following would be of particular interest:

1. It is found that the measured radiation ratio of the rail at high frequency is always higher than the predicted results for the rail vibrating both vertically and laterally. This is probably due to the cross-section deformation at high frequencies. Therefore, it is important to explore the effects of cross-sectional deformation on rail radiation theoretically and experimentally in the future. The WANDS software can be used to obtain the amplitude of different wave types so as to include cross-sectional deformation effects, at high frequencies, on the radiation ratio. The possibility of experiments to verify this effect can be explored as well.

2. In Chapter 5, the melamine foam was tested first to verify the measurement methods of impedance tube method and the reverberation chamber method; however the agreement for the absorption of the melamine foam between the different methods is poor. More work will be needed to obtain more convincing results and to resolve these differences.
3. For the complete prediction of the 1:5 scale track, it is shown the impedance from the Johnson-Allard model for the ballast used in the numerical models caused the inaccuracy in the predictions compared with the corresponding measurements. Therefore, it will be necessary to deal with the impedance of the ballast, for example using an extended reaction model. This also requires measurements of ballast absorption for different angles of incidence. Besides, the effects of the ballast vibration on the track sound radiation should be taken into account in the numerical models. It would be possible to combine these two effects by using a finite element model of a poro-elastic material.
4. For the complete prediction of the track sound radiation in practice, the TWINS predictions are based on models for the vibration of the rail and sleeper. For full validation of the radiation models, however, measurements of rail and sleeper vibration are required. New field measurements will be necessary to verify the complete prediction of the whole track by using the sound radiation models for the rail and sleeper developed in this thesis. Also, measurements of radiation ratio from the rail on a slab track, where negligible radiation from the slab and sleepers is expected, would allow the validation of the rail radiation model at lower frequencies, especially the weighted average radiation from the rail. This can also be validated using the boundary element method in 3D.

Appendix A Publications

- **Journal papers**

1. G. Squicciarini, A. Putra, D.J. Thompson, **X. Zhang**, M.A. Salim. Use of a reciprocity technique to measure the radiation efficiency of a vibrating structure. *Applied Acoustics*, 89, 107-121, 2015.
2. **X. Zhang**, G. Squicciarini, D.J. Thompson. Sound radiation of a railway rail in close proximity to the ground. *Journal of Sound and Vibration*, 362, 111-124, 2016.
3. **X. Zhang**, D.J. Thompson, G. Squicciarini. Sound radiation of railway sleepers. *Journal of Sound and Vibration*, 369, 178-194, 2016.

- **Conference papers**

1. **X. Zhang**, D.J. Thompson, G. Squicciarini. Influence of ground impedance on the sound radiation of a railway track. *Proceedings of 21st International Congress on Sound and Vibration, Beijing, China*, 2014.
2. **X. Zhang**, G. Squicciarini, D.J. Thompson. Influence of ground impedance on the sound radiation of a railway sleeper. *The 169th Meeting of the Acoustical Society of America, Pittsburgh, USA*, 2015.
3. **X. Zhang**, D.J. Thompson, G. Squicciarini. Effects of railway ballast on the sound radiation from the sleepers. *Euronoise2015, Maastricht, Netherlands*, 2015.
4. **X. Zhang,** D.J. Thompson, G. Squicciarini. A new model for the prediction of track sound radiation. *International Workshop on Railway Noise, Terrigal, Australia,* 2016 (To be published).

Appendix B **Rayleigh integral**

The sound radiated by a vibrating structure mounted in a rigid coplanar baffle, as shown in Figure B.1, can be calculated by using the Rayleigh integral [95]. Specifically, the pressure at a point $\mathbf{r}=(r, \theta, \phi)$ can be expressed in terms of the structure surface complex velocity $v(x, y)$ as

$$p(\mathbf{r})=\frac{ik\rho_0 c_0}{2\pi}\int_S v(x,y)\frac{e^{-ikr'}}{r'}\mathrm{d}x\mathrm{d}y \tag{B.1}$$

where k is the acoustic wavenumber and $\mathrm{r}'=\left|\mathbf{r}-\mathbf{x}\right|$ represents the distance between a point $\mathbf{x}$ on the structure surface and a point in the medium at $\mathbf{r}=(r, \theta, \phi)$.

The sound power can then be obtained by integrating the acoustic intensity over a hemisphere in the far field as

$$W=\int_0^{2\pi}\int_0^{\pi/2}\frac{\left|p(\mathbf{r})\right|^2}{2\rho_0 c_0}r^2\sin\theta\mathrm{d}\theta\mathrm{d}\phi \tag{B.2}$$

where ρ_0 is the air density, c_0 is the speed of the sound and $p(\mathbf{r})$ is the complex acoustic pressure amplitude at $\mathbf{r}=(r, \theta, \phi)$.

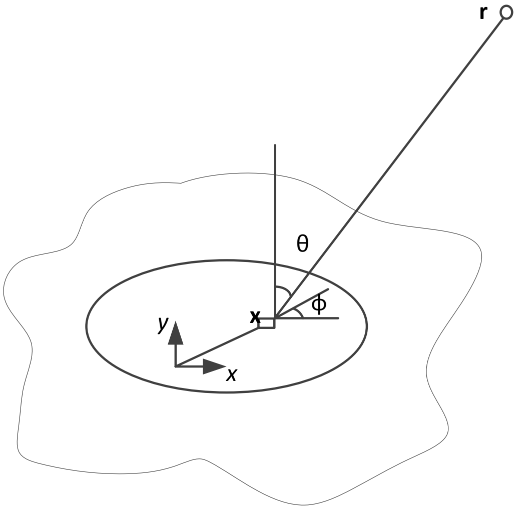

Figure B.1 A vibrating structure set in a rigid coplanar baffle

Appendix C Impedance tube

The impedance tube method is illustrated in Figure C.1. A sample of material is located at one end of a tube, whereas a loudspeaker is located at the opposite end of the tube to generate plane waves in the tube. A standing wave is formed in the tube by interference between incident and reflected waves. The impedance of the sample alters how the sound is reflected, and by measuring the standing wave using microphones, it is possible to calculate the normal incidence absorption coefficient and the surface impedance of the sample.

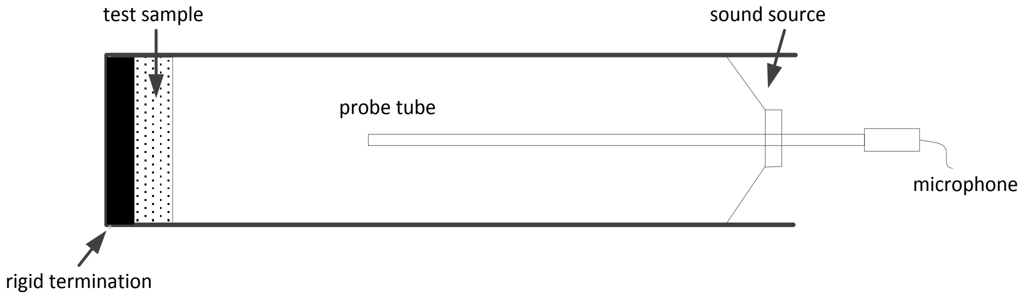

Figure C.1 Set-up for impedance tube measurement

The highest frequency, f_u, that can be measured in a circular tube is determined by [106]

$$f_u = \frac{0.58c_0}{d} \tag{C.1}$$

where d is the tube diameter or maximum width and c_0 the speed of the sound.

For the standing wave method, the tube is excited at a single frequency and both the maximum and the minimum pressure amplitudes, denoted by $p_{\max}$, $p_{\min}$ are measured. The standing wave ratio s_r is given by

$$s_r = \left| p_{\max} / p_{\min} \right| \tag{C.2}$$

If the sound pressure level in tube is measured in decibels, and the difference in level between the maximum and minimum pressures is ΔL dB, then

$$s_r = 10^{\Delta L/20} \tag{C.3}$$

Then the magnitude of the reflection coefficient R can be obtained as

$$|R| = \frac{s_r - 1}{s_r + 1} \tag{C.4}$$

The normal incidence sound absorption coefficient α can be given by

$$\alpha = 1 - |R|^2 = \frac{4s_r}{\left(s_r + 1\right)^2} \tag{C.5}$$

For the transfer function method, the tube is excited by a broadband signal and the transfer function H_{12} between microphone points 1 and 2 can be obtained as the ratio of complex pressures, $H_{12} = p\left(x_2\right) / p\left(x_1\right)$.

Then the complex pressure reflection coefficient is given by

$$R = \frac{H_{12} - H_{\mathrm{I}}}{H_{\mathrm{R}} - H_{12}} e^{ikx_1} \tag{C.6}$$

where x_1 is the distance between the sample and the further microphone location; $k=\omega/c_0$ is the acoustic wavenumber; H_{I}, H_{R} are the theoretical transfer functions between the two microphone locations for the incident wave and the reflected wave, respectively, given by

$$H_{\mathrm{I}} = e^{-ik\Delta x},\ H_{\mathrm{R}} = e^{ik\Delta x} \tag{C.7}$$

where $\Delta x = x_1 - x_2$ is the separation between the two microphone points.

The normal incidence absorption coefficient α can then be determined by

$$\alpha = 1 - |R|^2 \tag{C.8}$$

while the impedance is given by

$$z_n = \rho_0 c_0 \left(\frac{1 + R}{1 - R} \right) \tag{C.9}$$

Appendix D Reverberation chamber method for measuring absorption

The absorption coefficient can be obtained by measuring the reverberation time of a reverberation room before and after a sample of absorptive material is introduced. The reverberation time before the test specimen is introduced is given by

$$T_0 = \frac{55.3V}{c_0\alpha_0 S + 4Vm_1} \tag{D.1}$$

where V is the room volume, c_0 the speed of sound, α_0 the average absorption coefficient of the empty room, S the surface area of the room and m_1 the air absorption in the room.

When the sample is mounted in the chamber, the reverberation time is written as

$$T_1 = \frac{55.3V}{c_0\left(\alpha_0\left[S - S_s\right] + \alpha_s S_s\right) + 4Vm_1} \tag{D.2}$$

where S_s is the surface area and α_s the absorption coefficient of the sample.

If it is assumed that the air absorption, m_1, is unchanged and $S_s \ll S$, then the absorption coefficient of the sample can be calculated as

$$\alpha_s = \frac{1}{c_0 S_s}\left(\frac{55.3V}{T_1} - \frac{55.3V}{T_0}\right) \tag{D.3}$$

The measured absorption coefficients are often more inaccurate at low than high frequencies, due to modal effects in the room. The lower limit of the frequency range, for which the results from the reverberation chamber can be considered valid, is given by the Schroeder frequency of the room. It is given by

$$f_s = 2000\left(T/V\right)^{\frac{1}{2}} \tag{D.4}$$

where T is the reverberation time [120].

Appendix E Construction of 1:√5 scale ballast samples

The railway ballast is made up of aggregates graded according to particle size, which are obtained by passing the samples through a number of different sizes of sieve. According to the standard for the ballast aggregates used by Network Rail [121], there are a minimum and maximum distribution of the ballast particle sizes, which are shown in Table E.1.

Table E.1 Standard ballast aggregates used by Network Rail

Sieve size, mm	22.4	31.5	40	50	60
Minimum (cumulative), %	0	1	30	70	100
Maximum (cumulative), %	3	25	65	99	100

For the construction of a scale ballast, the distribution of the ballast particle sizes is calculated by dividing the actual sieve sizes by the scale factor and an optimum line is drawn according to the sieve sizes available. This line should be located between the minimum and maximum distribution of the ballast particle sizes according to the standard. According to the availability of sieve sizes for the sieving machine in the Heavy Structures Laboratory, as shown in Figure E.1, a 1:5 scale ballast has been constructed by Lawrence [89]. Table E.2 shows the minimum and maximum aggregates for this 1:5 scale ballast according to the standard, whereas Table E.3 presents the corresponding optimum aggregates. The construction of a 1:√5 scale ballast has been conducted in the current work. Table E.4 and Table E.5 give the aggregates according to standard and the optimum aggregates for the 1:√5 scale ballast, respectively. For the optimum aggregates, compared with that for the 1:5 scale ballast (Table E.3), this new scale ballast has more large particles.

Comparison is made between the optimum aggregates and the minimum and maximum standard aggregates for the 1:√5 scale ballast, as shown in Figure E.2. As can be seen, the optimum is between the minimum and maximum aggregate distribution. The construction of the 1:√5 scale ballast in the current research is based on this optimum aggregate distribution.

Figure E.1 Sieving machine (D450 Endecott Shaker) with different sieve sizes

Table E.2 Aggregates for the 1:5 scale ballast by the standard

Sieve size, mm	4.48	6.3	8	10	12.6
Minimum (cumulative), %	0	1	30	70	100
Maximum (cumulative), %	3	25	65	99	100

Table E.3 Optimum aggregates for the 1:5 scale ballast based on standard gradation

Sieve size, mm	4.75	6.7	8	9.5	11.2	13.2
Cumulative, %	0	20	45	75	95	100

Table E.4 Aggregates for the 1:√5 scale ballast by the standard

Sieve size, mm	10	14.1	17.9	22.4	28.2
Minimum (cumulative), %	0	1	30	70	100
Maximum (cumulative), %	3	25	65	99	100

Table E.5 Optimum aggregates for the 1:√5 scale ballast based on standard gradation

Sieve size, mm	8	9.5	11.2	13.2	16	22.4	25	31.5
Cumulative, %	0	0	3	11	27	87	95	100

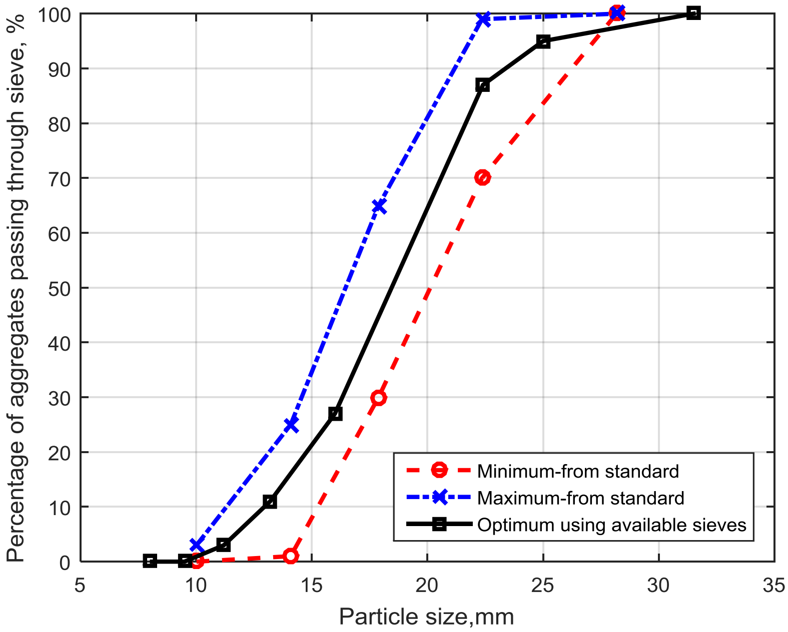

Figure E.2 Ballast minimum, maximum and optimum passing percentage for 1:√5 ballast according to the standard requirements

Another task required by the Track 21 project is to test the absorption of ballast with more small particle sizes. An assumed ballast aggregate distribution is presented in Table E.6. An optimum gradation for 1:√5 scale ballast is selected, as shown in Table E.7. Figure E.3 shows the comparison of the ballast passing percentages between the standard (Gradation 1) and the new gradation for the Track 21 project (Gradation 2). As can be seen, there are more small particle sizes for gradation 2. Also, the current optimum for the construction of 1:√5 scale ballast is close to the target.

Table E.6 Assumed aggregate distribution for railway ballast by Track 21 project

Sieve size, mm	4.75	9.5	11.2	13.2	16	22.4	25	31.5	37.5	40	50	63
Cumulative, %	1	2	3	6	17	41	48	63	80	87	95	100

Table E.7 Optimum aggregate distribution for 1:√5 scale ballast based on the gradation by Track 21 project

Sieve size, mm	3.35	4.75	6.7	8	9.5	11.2	13.2	16	22.4	25	31.5
Cumulative, %	0	0	10	23	33	46	61	76	96	99	100

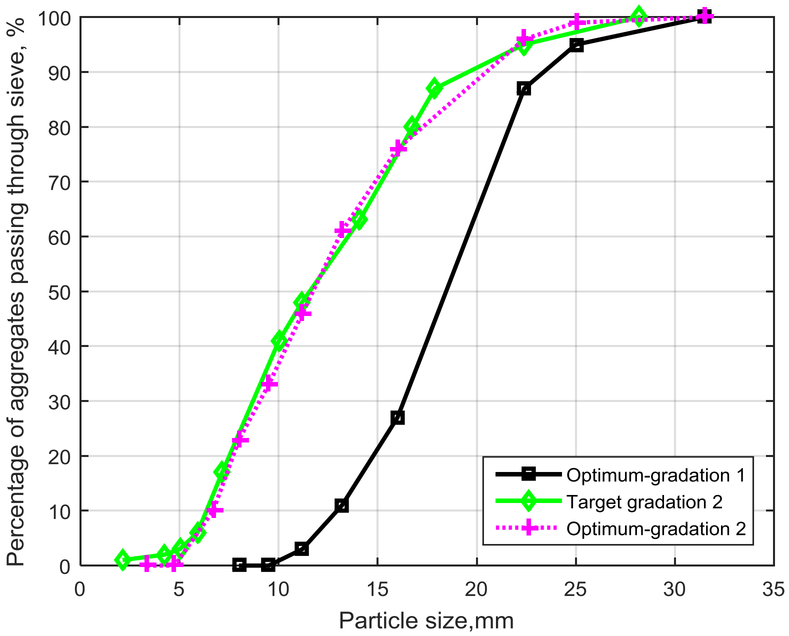

Figure E.3 Comparison of optimum passing percentages with the target in the project and the standard for 1:√5 scale ballast

List of References

[1] David Thompson. Railway noise and vibration mechanisms, modelling and means of control. Elsevier, 2008.

[2] D.J. Thompson, B. Hemsworth, N. Vincent. Experimental validation of the TWINS prediction program for rolling noise, Part 1: description of the model and method. Journal of Sound and Vibration, 193, 123-135, 1996.

[3] D.J. Thompson, P. Fodiman, H. Mahé. Experimental validation of the TWINS prediction program for rolling noise, part 2: results. Journal of Sound and Vibration, 193, 137-147, 1996.

[4] D. J. Thompson, C. J. C. Jones. Sound radiation from a vibrating railway wheel. Journal of Sound and Vibration, 253(2), 401-419, 2002.

[5] P. J. Remington. Wheel/rail noise-part 1 characterization of the wheel/rail dynamic system, Journal of Sound and Vibration, 46, 359-380, 1976.

[6] P. J. Remington. Wheel/rail rolling noise I: theoretical analysis. Journal of the Acoustical Society of America, 81, 1805-1823, 1987.

[7] K.F. Graff. Wave motion in elastic solids. Dover Publications, New York, 1991.

[8] S. L. Grassie, R. W. Gregory, D. Harrison and K. L. Johnson. The dynamic response of railway track to high frequency vertical excitation. Journal of Mechanical engineering science, 24, 77-90, 1982.

[9] R.A. Clark, P.A. Dean, J.A. Elkins and S. G. Newton. An investigation into the dynamic effects of railway vehicles running on corrugated track. Journal of mechanical engineering science, 24, 65-76, 1982.

[10] E. Tassilly. Propagation of bending waves in a periodic beam. International Journal of Engineering Science, 25, 85-95, 1987.

[11] K. Ono and M. Yamada. Analysis of railway track vibration. Journal of Sound and Vibration, 130, 269-297, 1989.

[12] J.C.O. Nielsen, A. Igeland. Vertical dynamic interaction between train and track-influence of wheel and track imperfections. Journal of Sound and Vibration, 187(5), 825-839, 1995.

[13] D. J. Thompson. Wheel-rail noise: theoretical modelling of the generation of vibrations. Ph. D. Thesis, University of Southampton, 1990.

[14] D. J. Thompson. Wheel-rail noise generation, Part iii: rail vibration. Journal of Sound and Vibration, 161(3), 421-446, 1993.

[15] K. Knothe, S.L. Grassie. Modelling of railway track and vehicle/track interaction at high frequencies. Vehicle System Dynamics, 22, 209-262, 1993.

[16] D.J. Thompson, N. Vincent. Track dynamic behaviour at high frequencies. Part 1: theoretical models and laboratory measurements. Vehicle System Dynamics Supplement, 24, 86-99, 1995.

[17] N. Vincent, D.J. Thompson. Track dynamic behaviour at high frequencies. Part 2: Experimental results and comparisons with theory. Vehicle System Dynamics Supplement, 24, 100-114, 1995.

[18] D. J. Thompson. Experimental analysis of wave propagation in railway tracks. Journal of Sound and Vibration, 203(5), 867-888, 1997.

[19] T.X. Wu, D.J. Thompson. A double Timoshenko beam model for vertical vibration analysis of railway track at high frequencies. Journal of Sound and Vibration, 224, 329-348, 1999.

[20] T.X. Wu, D.J. Thompson. Analysis of lateral vibration behaviour of railway track at high frequencies using a continuously supported multiple beam model. Journal of the Acoustical Society of America, 106, 1369-1376, 1999.

[21] T.X. Wu, D.J. Thompson. Application of a multiple-beam model for lateral vibration analysis of a discretely supported rail at high frequencies. Journal of the Acoustical Society of America, 108, 1341-1344, 2000.

[22] M.A. Heckl. Coupled waves on a periodically supported Timoshenko beam. Journal of Sound and Vibration, 252, 849-882, 2002.

[23] C.-M. Nilsson, C.J.C. Jones, D.J. Thompson and J. Ryue. A waveguide finite element and boundary element approach to calculating the sound radiated by railway and tram rails. Journal of Sound and Vibration, 321, 813-836, 2009.

[24] J. Ryue, D.J. Thompson, P.R. White and D.R. Thompson. Investigations of propagating wave types in railway tracks at high frequencies. Journal of Sound and Vibration, 315, 157-175, 2008.

[25] C.J.C. Jones, D.J. Thompson, R.J. Diehl. The use of decay rates to analyse the performance of railway track in rolling noise generation. Journal of Sound and Vibration, 293, 485-495, 2006.

[26] BS EN 15461:2008+A1:2010. Railway applications. Noise emission. Characterization of the dynamic properties of track selections for pass by noise measurements.

[27] F. Fahy, P. Gardonio. Sound and structural vibration: radiation, transmission and response. Second edition, Elsevier, Oxford, 2007.

[28] D.J. Thompson. Predictions of acoustic radiation from vibrating wheels and rails. Journal of Sound and Vibration, 120, 275-280, 1988.

[29] D.J. Thompson, C.J.C. Jones. Review of the modelling of wheel/rail noise generation. Journal of Sound and Vibration, 231, 519-536, 2000.

[30] E.K. Bender, P.J. Remington. The influence of rails on train noise. Journal of Sound and Vibration, 37, 321-334, 1974.

[31] P.J. Remington. Wheel/rail noise-part iv: rolling noise. Journal of Sound and Vibration, 46, 419-436, 1976.

[32] C. I. Chessell. Propagation of noise along a finite impedance boundary. Journal of the Acoustical Society of America, 62, 825-834, 1977.

[33] P. J. Remington. Wheel/rail rolling noise II: Validation of the theory, Journal of the Acoustical Society of America, 81, 1824-1832, 1987.

[34] D.J. Thompson. Wheel-rail noise generation, part 1 introduction and interaction model. Journal of Sound and Vibration, 161, 387-400, 1993.

[35] M.-F. Petit, M. Heckl, J. Bergemann, J. Baae. Calculation of the radiation efficiency of railway rails using multipole synthesis, proceedings DAGA, 997-1000, 1992.

[36] D.J. Thompson, C.J.C. Jones, N. Turner. Comparison of 2D and 3D rail radiation models. ISVR contract report No. 99/28, 1999.

[37] H.A. Schenck. Improved integral formulation for acoustic radiation problems. Journal of Acoustical Society of America, 44(1), 41-58, 1968.

[38] D.J. Thompson, C.J.C. Jones, N. Turner. Investigation into the validity of two-dimensional models for sound radiation from waves in rails. Journal of Acoustical Society of America, 113, 1965-1974, 2003.

[39] T. Kitagawa, D.J. Thompson. The horizontal directivity of noise radiated by a rail and implications for the use of microphone arrays. Journal of Sound and Vibration, 329, 202-220, 2010.

[40] X. Zhang, H. G. Jonasson. Directivity of railway noise sources. Journal of Sound and Vibration, 293, 995-1006, 2006.

[41] X. Zhang. The directivity of railway noise at different speeds. Journal of Sound and Vibration, 329, 5273-5288, 2010.

[42] C.J.C. Jones, D.J. Thompson. Extended validation of a theoretical model for railway rolling noise using novel wheel and track designs. Journal of Sound and Vibration, 267(3), 2003.

[43] B. Betgen, N. Vincent. Acoutrain project Deliverable D2.2. EC contract No. FP7-284877 (Confidential).

[44] S.L. Grassie, S.J. Cox. The dynamic response of railway track with flexible sleepers to high frequency vertical excitation. Proceedings of the Institution of Mechanical Engineers Part D, 198D, 117-124, 1984.

[45] S. L. Grassie. Dynamic modelling of concrete railway sleepers. Journal of Sound and Vibration. 187, 799-813, 1995.

[46] D.J. Thompson, M.H.A. Janssens. Track Wheel Interaction Noise Software. Version 2.4. Theoretical manual, TPD-HAG-MEMO-960343, 1996.

[47] A. M. David, D. J. Thompson. Measurements of the vibration and sound radiation of a concrete railway sleeper. ISVR Contract Report 98/22, September 1998.

[48] N. Vincent, P. Bouvet, D. J. Thompson and P. E. Gautier. Theoretical optimisation of track components to reduce rolling noise. Journal of Sound and Vibration. 193, 161-171, 1996.

[49] J. C. O. Nielsen. Acoustic optimization of railway sleepers. Journal of Sound and Vibration. 231, 753-764, 2000.

[50] T. Fernstrom. Structural dynamics optimisation of railway sleeper. Thesis for the degree of master of science, Sweden, 1997.

[51] J. C. O. Nielsen. Parametric study on low noise sleeper design. Brite/EuRam Silent track, 1998.

[52] LMS Numerical Technologies, Leuven, Belgium. SYSNOISE rev 5.3 User's Manual.

[53] C. Zwikker, C.W. Kosten. Sound absorbing materials, Elsevier, New York, 1949.

[54] M.A. Biot. Theory of propagation of elastic waves in a fluid-saturated porous solid. 1. Low-frequency range. Journal of Acoustical Society of America, 28, 168-178, 1956.

[55] M.A. Biot. Theory of propagation of elastic waves in a fluid-saturated porous solid. ii. Higher frequency range. Journal of Acoustical Society of America, 28, 179-191, 1956.

[56] M.E. Delany, E.N. Bazley. Acoustical properties of fibrous absorbent materials. Applied Acoustics, 3, 105-116, 1970.

[57] Yasushi Miki. Acoustical properties of porous materials-modifications of Delany-Bazley models. Journal of Acoustical society of Japan, (E)11, 19-24, 1990.

[58] Yasushi Miki. Acoustical properties of porous materials-Generalizations of empirical models. Journal of Acoustical society of Japan, (E)11, 25-28, 1990.

[59] K. Attenborough. Acoustical impedance models for outdoor ground surfaces. Journal of Sound and Vibration, 99, 521-544, 1985.

[60] D.L. Johnson, J.Koplik, R. Dashen. Theory of dynamic permeability and tortuosity in fluid-saturated porous media. Journal of Fluid Mechanics, 176, 379-402, 1987.

[61] J.F. Allard, N. Atalla. Propagation of Sound in Porous Media: modelling sound absorbing materials. Wiley, Chichester, 2009.

[62] D. Wilson. Relaxation-matched modelling of propagation through porous media, including fractal pore structure. Journal of Acoustical Society of America, 94(2), 1136-1145, 1993.

[63] M. Berengier, M.R. Stinson, G.A. Daigle, J.F. Hamet. Porous road pavements: acoustical characterization and propagation effects. Journal of Acoustical Society of America. 101(1), 155-162, 1997.

[64] J.F. Hamet, M. Berengier. Acoustical characteristics of porous pavements: a new phenomenological model. Internoise 93, Leuven, Belgium, 641-646, 1993.

[65] G. Taraldsen. The Delany-Bazley impedance model and Darch’s law. Acta Acustica united with Acustica. 91, 41-50, 2005.

[66] G. Taraldsen, H. Jonasson. Aspects of ground effect modelling. Journal of Acoustical Society of America, 129(1), 47-53, 2011.

[67] K. Attenborough, I. Bashir, S. Taherzadeh. Outdoor ground impedance models. Journal of Acoustical Society of America, 129(5), 2806-2819, 2011.

[68] B. Stallaert. Acoutrain project Deliverable D4.3. EC contract No. FP7-284877 (Confidential).

[69] W. M. Zhai, K. Y. Wang, and J. H. Lin. Modelling and experiment of railway ballast vibration. Journal of Sound and Vibration, 270, 673-683, 2004.

[70] K. Knothe, Gleisdynamic, Ernst & Sohn, Berlin, 2001.

[71] D. R. Ahlbeck, H. C. Meacham, R. H. Prause. The development of analytical models for railroad track dynamics. Railroad Track Mechanics & Technology, Pergamon Press, Oxford, 1978.

[72] Y. Sato, T. Odaka, H. Takai. Theoretical analyses on vibration of ballasted track. QR of RTRI 29, 30-32, 1988.

[73] W. M. Zhai, X. Sun. A detailed model for investigating vertical interaction between railway vehicle and track. Vehicle System Dynamics Supplement, 23, 603-615, 1994.

[74] N. Fremion, J.P. Goudard and N. Vincent. Improvements of ballast and sleeper description in TWINS. Step 1: experimental characterization of ballast properties. Vibratec report 072.028a, July 1996.

[75] G. W. C. Kaye, E. J. Evans. The sound absorbing properties of some common outdoor materials. Proceedings of the Physical Society, 52, 371-379, 1940.

[76] P. van der Stap, E. V. Practical data collection for the Harmonoise deliverable: HAR 12TR-031203-AEA12.doc, 2004.

[77] R. W. Morse. Acoustic propagation in granular media. Journal of Acoustic Society of America, 24, 696-700, 1952.

[78] K. M. Li, T. Waters-Fuller, K. Attenborough. Sound propagation from a point source over extended-reaction ground. Journal of Acoustic Society of America, 104, 679-685, 1998.

[79] K. Attenborough, P. Boulanger, Q. Qin and R. Jones. Predicted influence of ballast and porous concrete on rail noise. Internoise, Brazil, 2005.

[80] O. Umnova, K. Attenborough, K.M. Li. A cell model for the acoustical properties of packings of spheres. Acustica combined with Acta Acustica. 87, 226-235, 2001.

[81] K. Heutschi. Sound propagation over ballast surfaces. Acta acustica united with acustica, 95, 1006-1012, 2009.

[82] G. W. Swenson Jr, M. J. White, M. L. Oelze. Low-frequency sound wave parameter measurement in gravels. Applied Acoustics, 71, 45-51, 2010.

[83] R. A. Broadbent, D. J. Thompson, and C. J. C. Jones. The acoustic properties of railway ballast. EURONOISE, Edinburgh, 2009.

[84] J.W. Verheij. Multi-path sound transfer from resiliently mounted shipboard machinery. PhD thesis, Delft, 1982.

[85] I.L. Ver, C.S. Vertres, M.M. Myles. Wheel/rail noise-Part iii: impact noise generation by wheel and rail discontinuities. Journal of Sound and Vibration, 46(3), 395-417, 1976.

[86] T.D. Armstrong, D.J. Thompson. Use of a reduced scale model for the study of wheel/rail interaction. Journal of Rail and Rapid Transit, 220, 235-246, 2006.

[87] A. Jaschinski, H. Chollet, S. Iwnichi, A. Wickens, J. Wurzen. The application of roller rigs to railway vehicle dynamics. Vehicle System, Dynamics, 31(5-6), 345-392, 2010.

[88] ORE Report. Wheel/rail contact noise-Investigation into the application of a one-eighth scale wheel-rail roughness test rig. ORE, Question C163 Railway Noise, Report Number 11.

[89] B. Lawrence. Scale model facility for railway vibration and noise, ISVR MEng individual project, University of Southampton, 2013.

[90] J. Lewis. Scale model tests of acoustic behaviour of railway, ISVR MEng individual project, University of Southampton, 2014.

[91] M.C. Junger. Model scaling laws for sound absorptive boundaries. Journal of the Acoustical Society of America, 62, 209-211, 1977.

[92] D.J. Thompson, C.J.C. Jones, T.P. Waters and D. Farrington. A tuned damping device for reducing noise from railway track. Applied Acoustics, 68, 43-57, 2007.

[93] B. Asmussen, D. Stiebel, P. Kitson, D. Farrington, and D. Benton. Reducing the noise emission by increasing the damping of the rail: results of a field test, Noise and vibration mitigation for rail transportation systems. 2007.

[94] B. Croft, C. Jones. Modelling the effect of rail dampers on railway rolling noise and the rate of rail head roughness growth. SILENCE project, ISVR contract report, CR07/17.

[95] J.W. Strutt (Lord Rayleigh). Theory of Sound, 2nd edition. Dover Publications, New York, 1945.

[96] T.W. Wu. Boundary element acoustics: Fundamentals and computer codes. WITpress, Southampton, 2000.

[97] M. Petyt, C.J.C, Jones. Numerical methods in acoustics, Chapter 2 in F. Fahy, J. Walker (editors). Advanced applications in acoustics, noise and vibration. Spon Press, London, 2004.

[98] David T. Blackstock. Fundamentals of physical acoustics. A Wiley-interscience publication, New York, 2000.

[99] Philip M. Morse, K. Uno Ingard. Theoretical acoustics. Princeton University Press Princeton, 1986.

[100] T.F.W. Embleton, J.E. Piercy, and G.A. Daigle. Effective flow resistivity of ground surfaces determined by acoustical measurements. Journal of the Acoustical Society of America, 74, 1239-1244, 1983.

[101] D.J. Thompson. Noise control, Chapter 5 in F. Fahy, D.J. Thompson (editors). Fundamentals of sound and vibration. CRC Press, Cornwall, UK, 2015.

[102] T.J. Cox, P.D’Antonio. Acoustic absorbers and diffusers theory, design and application. Second edition, Taylor & Francis, London, 2009.

[103] Acoustics-Materials for acoustical applications-Determination of airflow resistance (ISO9053: 1991). International Standards Organisation.

[104] D.A. Bies, C.H. Hansen. Flow resistance information for acoustical design. Applied Acoustics, 13, 357-391, 1980.

[105] N. Kino, T. Ueno. Comparisons between characteristic lengths and fibre equivalent diameters in glass fibre and melamine foam materials of similar flow resistivity. Applied Acoustics, 69, 325-331, 2008.

[106] BS EN ISO 10534-1. Determination of sound absorption coefficient and impedance in impedance tubes: Part 1 Method using standing wave ratio. British Standards Institution, 2001.

[107] BS EN ISO 10534-2. Determination of sound absorption coefficient and impedance in impedance tubes: Part 2 Transfer function method. British Standards Institution, 2001.

[108] C. Langlois, R. Panneton, N. Atalla. Polynomial relations for quasi-static mechanical characterization of isotropic poroelastic materials. Journal of the Acoustical Society of America. 110(6), 3032-3040, 2001.

[109] Y. Atalla, R. Panneton. Inverse acoustical characterization of open cell porous media using impedance tube measurements. Canadian Acoutics, 33, 11-24, 2005.

[110] BS EN ISO 354: 2003. Acoustics-Measurement of sound absorption in a reverberation room. British Standards Institution, 2003.

[111] Track 21 project website-http://track21.org.uk/

[112] M.J. Brennan, W.M. To. Acoustic properties of rigid-frame porous materials-an engineering perspective. Applied Acoustics. 62, 793-811, 2001.

[113] G. Squicciarini, A. Putra, D. J. Thompson, X. Zhang and M. A. Salim. Use of a reciprocity technique to measure the radiation efficiency of a vibrating structure. Applied Acoustics, 89, 107-121, 2015.

[114] LM. Lyamshev. A method for solving the problem of sound radiation by thin elastic shells and plates. Sov Phys Acoust. 5, 122-4 1959.

[115] LM. Lyamshev. A question in connection with the principle of reciprocity in acoustics. Sov Phys Dokl. 4, 406, 1959.

[116] Acoustics-Determination of sound power levels and sound energy levels of noise sources using sound pressure-Precisions methods for reverberation test rooms (ISO 3741:2010). International Standards Organisation.

[117] D. Milne, L.M. Le Pen, G. Watson, D.J. Thompson, W. Powrie, M. Hayward and S. Morley. Measuring Acceleration of Ballast Particles at Track Level. The Third International Conference on Railway Technology: Research, Development and Maintenance. Stirlingshire, UK, 2016.

[118] G. Squicciarini, M.G. R. Toward and D.J. Thompson. Experimental procedures for testing the performance of rail dampers. Journal of Sound and Vibration, 359, 21-39, 2015.

[119] G. Squicciarini, D.J. Thompson, M.G.R. Toward and R.A. Cottrell. The effect of temperature on railway rolling noise. Journal of Rail and Rapid Transit, doi: 10.1177/0954409715614337, 2015.

[120] F. Fahy. Foundations of engineering acoustics. Academic Press, London, 2001.

[121] BS EN 13450: 2013. Aggregates for railway ballast.